

WL - TR - 95 - 2143

NOZZLE GEOMETRY EFFECTS ON STRUT
INJECTION INTO A SUPERSONIC FLOW



DIANA D. GLAWE
ABDOLLAH S. NEJAD
MOHAMMAD SAMIMY

EXPERIMENTAL RESEARCH BRANCH
ADVANCED PROPULSION DIVISION
AEROPROPULSION AND POWER DIRECTORATE
AIR FORCE MATERIEL COMMAND

SEPTEMBER 1995

FINAL REPORT : SEPTEMBER 1993 - SEPTEMBER 1995

APPROVED FOR PUBLIC RELEASE; DISTRIBUTION IS UNLIMITED.

AEROPROPULSION AND POWER DIRECTORATE
WRIGHT LABORATORY
AIR FORCE MATERIEL COMMAND
WRIGHT PATTERSON AFB OH 45433-7251

19961028 044

DTIC QUALITY INSPECTED 1

NOTICE

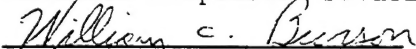
WHEN GOVERNMENT DRAWINGS, SPECIFICATIONS, OR OTHER DATA ARE USED FOR ANY PURPOSE OTHER THAN IN CONNECTION WITH A DEFINITE GOVERNMENT-RELATED PROCUREMENT, THE UNITED STATES GOVERNMENT INCURS NO RESPONSIBILITY OR ANY OBLIGATION WHATSOEVER. THE FACT THAT THE GOVERNMENT MAY HAVE FORMULATED OR IN ANY WAY SUPPLIED THE SAID DRAWINGS, SPECIFICATIONS, OR OTHER DATA, IS NOT TO BE REGARDED BY IMPLICATION, OR OTHERWISE IN ANY MANNER CONSTRUED, AS LICENSING THE HOLDER, OR ANY OTHER PERSON OR CORPORATION; OR AS CONVEYING ANY RIGHTS OR PERMISSION TO MANUFACTURE, USE, OR SELL ANY PATENTED INVENTION THAT MAY IN ANY WAY BE RELATED THERETO.

THIS REPORT IS RELEASABLE TO THE NATIONAL TECHNICAL INFORMATION SERVICE (NTIS). AT NTIS, IT WILL BE AVAILABLE TO THE GENERAL PUBLIC, INCLUDING FOREIGN NATIONS.

THIS TECHNICAL REPORT HAS BEEN REVIEWED AND IS APPROVED FOR PUBLICATION.



DIANA D. GLAWE, PhD
Aerospace Engineer (WL/POPT)
Advanced Propulsion Division



WILLIAM C. BURSON, PhD
Acting Chief (WL/POP)
Advanced Propulsion Division

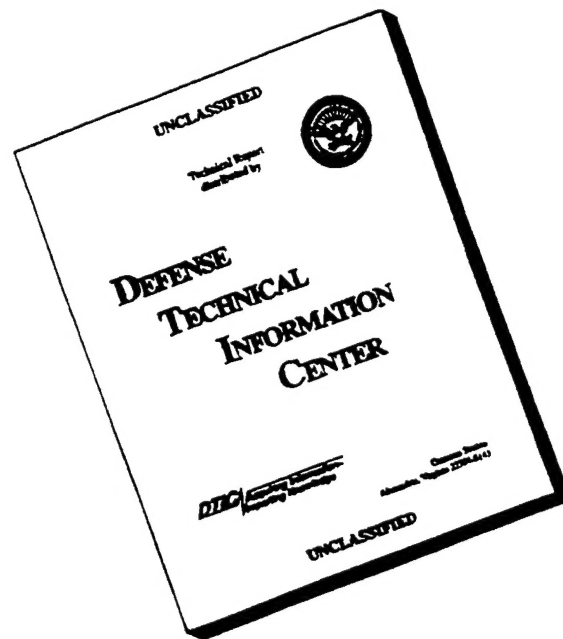


ABDOLLAH S. NEJAD, PhD
Acting Chief, (WL/POPT)
Advanced Propulsion Division

IF YOUR ADDRESS HAS CHANGED, IF YOU WISH TO BE REMOVED FROM OUR MAILING LIST, OR IF THE ADDRESSEE IS NO LONGER EMPLOYED BY YOUR ORGANIZATION PLEASE NOTIFY WL/POP WRIGHT-PATTERSON AFB OH 45433-7251 TO HELP MAINTAIN A CURRENT MAILING LIST.

Copies of this report should not be returned unless return is required by security considerations, contractual obligations, or notice on a specific document.

DISCLAIMER NOTICE



**THIS DOCUMENT IS BEST
QUALITY AVAILABLE. THE
COPY FURNISHED TO DTIC
CONTAINED A SIGNIFICANT
NUMBER OF PAGES WHICH DO
NOT REPRODUCE LEGIBLY.**

REPORT DOCUMENTATION PAGE

Form Approved
OMB No. 0704-0188

Public reporting burden for this collection of information is estimated to average 1 hour per response, including the time for reviewing instructions, searching existing data sources, gathering and maintaining the data needed, and completing and reviewing the collection of information. Send comments regarding this burden estimate or any other aspect of this collection of information, including suggestions for reducing this burden, to Washington Headquarters Services, Directorate for Information Operations and Reports, 1215 Jefferson Davis Highway, Suite 1204, Arlington, VA 22202-4302, and to the Office of Management and Budget, Paperwork Reduction Project (0704-0188), Washington, DC 20503.

1. AGENCY USE ONLY (Leave blank)		2. REPORT DATE September 1995		3. REPORT TYPE AND DATES COVERED Final Report: Sep 93 - Sep 95	
4. TITLE AND SUBTITLE Nozzle Geometry Effects on Strut Injection into a Supersonic Flow				5. FUNDING NUMBERS PE 61102 PR2308 TA S1 WU 01	
6. AUTHOR(S) Diana D. Glawe, PhD Abdollah S. Nejad, PhD Mohammad Samimy, PhD					
7. PERFORMING ORGANIZATION NAME(S) AND ADDRESS(ES) Aero Propulsion and Power Directorate Wright Laboratory Air Force Materiel Command Wright-Patterson AFB OH 45433-7251				8. PERFORMING ORGANIZATION REPORT NUMBER WL-TR-95-2143	
9. SPONSORING/MONITORING AGENCY NAME(S) AND ADDRESS(ES) Aero Propulsion and Power Directorate Wright Laboratory Air Force Materiel Command Wright-Patterson AFB OH 45433-7251				10. SPONSORING/MONITORING AGENCY REPORT NUMBER WL-TR-95-2143	
11. SUPPLEMENTARY NOTES Technical Monitor - Dr. Abdollah S. Nejad (WL/POPT, WPAFB OH 45433-7251)					
12a. DISTRIBUTION/AVAILABILITY STATEMENT Approved for public release; distribution is unlimited.				12b. DISTRIBUTION CODE	
13. ABSTRACT (Maximum 200 words) <p>Fuel injection from the base of a two-dimensional extended strut bounded above and below by Mach 1.92 freestreams was investigated. Without injection, a nominally two-wake flow exists behind the base of the strut. When fuel, simulated with helium, was injected parallel to the Mach 2 freestream, a highly three-dimensional complex flowfield results. The behavior of the flowfield generated by a circular injection nozzle was compared to the results obtained with two asymmetric nozzle geometries - an elliptic nozzle and a circular nozzle with vortex-generating tabs.</p> <p>Flow visualization and LDV results show that the jets, for all the injection cases, are confined to the region which is marked by the wake region in the flow without injection, thus limiting the jet spread in the transverse direction.</p> <p>The jet emanating from the circular-with-tabs jet, with two tabs oriented on a vertical line, exhibits the most complete mixing downstream. The second best mixing was exhibited by the elliptic nozzle, with its major axis along a vertical line. The circular-with-tabs nozzle with tabs oriented along a horizontal line and the elliptic nozzle with major axis along a horizontal line exhibited the poorest mixing.</p>					
14. SUBJECT TERMS nozzle, geometry, parallel injection, base flow, fuel-air mixint, strut				15. NUMBER OF PAGES 327	
				16. PRICE CODE	
17. SECURITY CLASSIFICATION OF REPORT UNCLASSIFIED	18. SECURITY CLASSIFICATION OF THIS PAGE UNCLASSIFIED	19. SECURITY CLASSIFICATION OF ABSTRACT UNCLASSIFIED	20. LIMITATION OF ABSTRACT SAR		

Foreword

This study explores parallel fuel injection as a possible candidate for a supersonic air breathing propulsion device and also explores the possibility of enhancing fuel-air mixing by varying injector nozzle geometry. An extended two-dimensional strut, with the base generating a recirculation zone for flame stabilization, was used to support a fuel injector. Helium, used to simulate gaseous hydrogen fuel, was injected from the base of the strut into a Mach 1.92 freestream air flow. Three converging nozzle geometries, circular, circular-with-tabs, and elliptic, were evaluated.

Schlieren photography, Laser Doppler Velocimetry (LDV), Planar Laser Induced Fluorescence (PLIF) and Rayleigh/Mie scattering diagnostic techniques were used to characterize the aerodynamics of this fuel injection scheme. An innovative image analysis scheme was developed to characterize mixing for the different nozzle geometries, addressing the long term research issue of characterizing mixing. A shape factor was used to describe the mixing potential of the jets in the near base region where large-scale structures dominate mixing. A mixedness index was used downstream to evaluate the quality of small-scale mixing for each nozzle configuration.

Flow visualization and LDV results show that the jets, for all the injection cases, are confined to the region which is marked by the wake region in the flow without injection. It appears that compressibility effects limit the jet spread in the transverse direction. Observation and mixing analysis show that the jet emanating from the circular-with-tabs jet, with two tabs oriented on a vertical line, has the largest mixing potential

(large shape factor) and undergoes the most complete mixing downstream (high mixedness index). The second best mixing was exhibited by the elliptic nozzle, with its major axis along a vertical line. This nozzle produced a disturbance in the wake flow surrounding the jet proper which may improve flame holding in combustion applications. The circular-with-tabs nozzle with tabs oriented along a horizontal line and the elliptic nozzle with major axis along a horizontal line exhibited the poorest mixing.

ACKNOWLEDGMENTS

Many thanks are in order to those who supported the work presented in this technical report. Charlie Smith, Kevin Kirkendall and Gary Haines assisted with experimental operations. Dave Schomer and Dr. Tzong Chen provided computer support. Useful insight was gained from technical discussions with Dr. Stephen A. Arnette, Dr. Gregory S. Elliott, Dr. Mark Reeder, Dr. Vince Belovich, Dr. Cam Carter, Dr. Charbel Raffoul, Jeff Donbar, Dr. Mark Gruber and Dr. Rodney Bowersoxs. Dr. Anna Creese, Dr. Cam Carter, Dr. Stephen A. Arnette and Dr. Mark Reeder assisted with technical editing. Jan Solari helped create the graphics. Thanks to USAF Palace Knight Program for their financial sponsorship. Also, thanks to AIAA Journal, Journal of Fluid Mechanics, Physics of Fluids Journal, and TSI Incorporated for granting permission to reprint several figures from articles in their publications.

TABLE OF CONTENTS

	page
FOREWORD	iii
ACKNOWLEDGMENTS	v
LIST OF TABLES	ix
LIST OF FIGURES	x
NOMENCLATURE.....	xxii
 CHAPTER	
1. INTRODUCTION	1
2. BACKGROUND	4
2.1 Injection schemes.....	4
2.2 Planar mixing layer structures.....	8
2.3 Axisymmetric shear layers.....	14
2.4 Noncircular nozzle geometries.....	19
2.4.1 Elliptic Nozzles.....	20
2.4.2 Circular-with-tabs nozzles	24
2.5 Base flow.....	27
3. FACILITY AND EXPERIMENTAL APPARATUS.....	43
4. EXPERIMENTAL TECHNIQUES AND INSTRUMENTATION.....	58
4.1 Schlieren photography	59
4.2 Rayleigh and Mie scattering	60
4.2.1 Rayleigh and Mie scattering technique.....	60
4.2.2 Scattering particles.....	62

5.3.3 Baseline helium injection case using circular (C) nozzle	146
5.3.3.1 LDV profiles in the (X,Y) plane	148
5.3.3.2 LDV profiles in the (X,Z) plane.....	153
5.3.4 Helium injection cases using circular-with tabs (T1) and elliptic (E1) nozzle.....	159
5.3.4.1 LDV profiles in the (X,Y) plane for the circular- with-tabs (T1) and elliptic (E1) nozzles.....	161
5.3.4.2 LDV Profiles in the (X,Z) plane	166
6. SUMMARY AND CONCLUSIONS	280
7. REFERENCES.....	285
APPENDIX A: FREESTREAM MACH NUMBER.....	295
APPENDIX B: HELIUM EXIT PRESSURE.....	296
APPENDIX C: LDV DATA REDUCTION EQUATIONS.....	297
APPENDIX D: BOUNDARY LAYER CALCULATIONS	298
APPENDIX E: STANDARD DEVIATION FOR A STREAM-SEPARATED FLOW	300

LIST OF TABLES

TABLE 1.	Nozzle dimensions	50
TABLE 2.	Operating conditions for helium injection into Mach 1.92 freestream air	50
TABLE 3.	Parameters of large-scale mixing	171

LIST OF FIGURES

2.1.	Illustration of: a) normal, b) oblique, and c) parallel injection of an underexpanded jet into a supersonic primary flow.....	31
2.2.	Crown nozzle with four teeth	32
2.3.	Circular nozzle with two delta tabs oriented at a 135° angle to the nozzle wall	32
2.4.	Simplified schematic of large spanwise (Kelvin-Helmholtz type) "roll-up" structures in an incompressible planar shear layer	33
2.5.	Laser induced fluorescence (Y,Z) cross section through the braid region of an incompressible planar mixing layer. The entire channel span of 11 cm is shown (from Bernal and Roshko [1986]).....	33
2.6.	Schematic of the physical structure of a transitional incompressible axisymmetric jet (from Yule [1978]).....	34
2.7.	Cross-sectional view (Y,Z) at $X/d = 3.25$ of a low Reynolds number ($Re = 5500$) circular free jet showing: a) the braid region and b) the primary vortical ring surrounded by streamwise vortex pairs as they pass through the image plane (from Liepmann [1991]).....	34
2.8.	Filtered Rayleigh/Mie scattering image at $X/d = 2.0$ of an underexpanded free jet (from Arnette et al. [1992]).....	35
2.9.	Illustration of axis-switching and vortex evolution process for an incompressible low Reynolds number jet emanating from an elliptic nozzle (from Husain and Hussain [1991]).....	35

2.10.	The effect of tab location for a Mach 1.63 air free jet is shown by flow visualization (left) and pressure contours (right) for: a) no tab, and b) $X/q = -1.5$, c) $X/q = 0.5$, and d) $X/q = 1.5$. Data for $X/d = 2$ where q is the cylindrical tab diameter (from Reeder and Zaman [1994]).....	36
2.11.	Laser sheet illuminated cross section of a Mach 1.63 air free jet at $X/d = 2$ for the indicated number of tabs (from Zaman et al. [1994]).....	37
2.12.	Streamwise (U) velocity contours (in m/s) taken at $X/d = 0.5$ for an incompressible jet ($Re = 1950$) with two delta tabs positioned on the Y-axis (at $Z/d = 0$) (from Reeder [1994])	38
2.13.	Spanwise (W) velocity contours (in m/s) taken at $X/d = 0.5$ for an incompressible jet ($Re = 1950$) with two delta tabs positioned on the Y-axis (at $Z/d = 0$) (from Reeder [1994]).....	38
2.14.	Transverse (V) velocity contours (in m/s) taken at $X/d = 0.5$ for an incompressible jet ($Re = 1950$) with two delta tabs positioned on the Y-axis (at $Z/d = 0$) (from Reeder [1994])	39
2.15.	Illustration of primary and secondary flow patterns of fluid emanating from a circular nozzle with two delta tabs at 135° to the nozzle wall.....	40
2.16.	Illustration of primary counter rotation vortices and secondary "horseshoe" vortices for flow around a delta tab at a 135° angle to the nozzle wall.....	40
2.17.	Schematic of two-dimensional base flow with equal supersonic primary flows on both sides of the strut	41
2.18.	Three-dimensional simulated Mach contours for an underexpanded ($\Psi = 4$) sonic circular helium jet (from Chen et al. [1995]).....	42
3.1.	Schematic of supersonic combustion facility	51
3.2.	Schematic of extended strut and reference coordinate system	52
3.3.	Nozzle and nozzle extension tube mounted in base retainer plate.....	53
3.4.	Wind tunnel with side wall removed, showing the nominal Mach 2 nozzle, extended strut, and beginning of the test section	54

3.5.	Photographs of the tips of the injector nozzles: a) circular, b) elliptical, and c) and d) circular-with-tabs	55
3.6.	Design specifications for circular-with-tabs nozzle.....	56
3.7.	Schematic of nozzle orientations. No injection (N) case and injection cases: circular (C), circular-with-tabs (T1, T2, T3), elliptic (E1, E2, E3)	57
4.1.	Schematic of schlieren photography system.	77
4.2.	Schematic of flow visualization system to obtain Rayleigh/Mie scattering images of the streamwise (X,Y) plane of view	78
4.3.	Schematic of flow visualization system to obtain Rayleigh/Mie scattering images of the face-on (Y,Z) plane of view	79
4.4.	Schematic of flow visualization system to obtain Rayleigh/Mie scattering images of the plan (X,Z) plane of view	80
4.5.	Schematic of acetone Planar Laser Induced Fluorescence (PLIF) imaging system to obtain PLIF image of the streamwise (X,Y) plane of view.....	81
4.6.	Schematic of two-component Laser Doppler Velocimetry (LDV) measurement volume.....	82
4.7.	Schematic of experimental instrumentation for Laser Doppler Velocimetry (LDV) measurements.....	83
5.1.	Schlieren photograph of streamwise (X,Y) plane of view without injection...	172
5.2.	Illustration of Prandtl-Meyer expansion wave theory at base of the extended strut without injection.....	173
5.3.	Instantaneous Rayleigh/Mie images of boundary layer . Streamwise (X,Y) plane of view located on the centerline of the strut ($Z = 0$) for the no injection (N), and helium injection ($\Psi=4$) through circular (C) nozzle.....	174
5.4.	Instantaneous acetone PLIF images of helium injection through circular nozzle (C) at static pressure ratios $\Psi = 1$, $\Psi = 2$, and $\Psi = 4$. Streamwise (X,Y) plane of view located on centerline of the jet ($Z = 0$).....	175

5.5.	Schematic of instantaneous Rayleigh/Mie scattering images for the: a) streamwise (X,Y), b) plan (X, Z) and c) face-on (Y,Z) planes of view	176
5.6.	Instantaneous Rayleigh/Mie images of streamwise (X,Y) plane of view located on the centerline of injector nozzle ($Z=0$) for the no injection (N) case and helium injection ($\Psi = 4$) cases (C, T1, T2 ,T3 ,E1 ,E2 ,E3). Upstream view.....	177
5.7.	Average Rayleigh/Mie images of streamwise (X,Y) plane of view located on the centerline of injector nozzle ($Z=0$) for the no injection (N) case and helium injection ($\Psi = 4$) cases (C, T1, T2 ,T3 ,E1 ,E2 ,E3). Upstream view.....	178
5.8.	Instantaneous Rayleigh/Mie images of streamwise (X,Y) plane of view located on the centerline of injector nozzle ($Z = 0$) for the no injection (N) case and helium injection ($\Psi = 4$) cases (C, T1, T2 ,T3 ,E1 ,E2 ,E3). Downstream view	179
5.9.	a) Original and b) corrected image of scale used for Rayleigh/Mie scattering images of the face-on (Y,Z) plane of view. Grid is 2.54 x 2.54 mm.	180
5.10.	a) Original and b) corrected instantaneous Rayleigh/Mie image of the face-on (Y,Z) plane of view located at $X/h = 2$ for helium injection ($\Psi = 4$) using circular (C) nozzle.	181
5.11.	Instantaneous Rayleigh/Mie images of face-on (Y,Z) plane of view located at $X/h = 1$ for the no injection (N) case and helium injection ($\Psi = 4$) cases (C, T1, T2 ,T3 ,E1 ,E2 ,E3)	182
5.12.	Average Rayleigh/Mie images of face-on (Y,Z) plane of view located at $X/h = 1$ for the no injection (N) case and helium injection ($\Psi = 4$) cases (C, T1, T2 ,T3 ,E1 ,E2 ,E3)	183
5.13.	Instantaneous Rayleigh/Mie images of face-on (Y,Z) plane of view located at $X/h = 2$ for the no injection (N) case and helium injection ($\Psi = 4$) cases (C, T1, T2 ,T3 ,E1 ,E2 ,E3)	184
5.14.	Average Rayleigh/Mie images of face-on (Y,Z) plane of view located at $X/h = 2$ for the no injection (N) case and helium injection ($\Psi = 4$) cases (C, T1, T2 ,T3 ,E1 ,E2 ,E3)	185

5.15.	Instantaneous Rayleigh/Mie images of face-on (Y,Z) plane of view located at $X/h = 4$ for the no injection (N) case and helium injection ($\Psi = 4$) cases (C, T1, T2 ,T3 ,E1 ,E2 ,E3)	186
5.16.	Average Rayleigh/Mie images of face-on (Y,Z) plane of view located at $X/h = 4$ for the no injection (N) case and helium injection ($\Psi = 4$) cases (C, T1, T2 ,T3 ,E1 ,E2 ,E3)	187
5.17.	Instantaneous Rayleigh/Mie images of face-on (Y,Z) plane of view located at $X/h = 6.8$ for the no injection (N) case and helium injection ($\Psi = 4$) cases (C, T1, T2 ,T3 ,E1 ,E2 ,E3)	188
5.18.	Average Rayleigh/Mie images of face-on (Y,Z) plane of view located at $X/h = 6.8$ for the no injection (N) case and helium injection ($\Psi = 4$) cases (C, T1, T2 ,T3 ,E1 ,E2 ,E3)	189
5.19.	Instantaneous Rayleigh/Mie images of face-on (Y,Z) plane of view located at $X/h = 10$ for the no injection (N) case and helium injection ($\Psi = 4$) cases (C, T1, T2 ,T3 ,E1 ,E2 ,E3)	190
5.20.	Average Rayleigh/Mie images of face-on (Y,Z) plane of view located at $X/h = 10$ for the no injection (N) case and helium injection ($\Psi = 4$) cases (C, T1, T2 ,T3 ,E1 ,E2 ,E3).....	191
5.21.	Illustration depicting the second most dominant component of mean flow velocity of the jet issuing from the circular with tabs nozzle configurations T1, T2, and T3. The most dominant component of the mean flow velocity is the streamwise component directed out of the plane of the page.....	192
5.22.	Instantaneous Rayleigh/Mie images of plan (X,Z) plane of view located on the centerline of injector nozzle ($Y = 0$) for the no injection (N) case and helium injection ($\Psi = 4$) cases (C, T1, T2 ,T3 ,E1 ,E2 ,E3)	193
5.23.	Average Rayleigh/Mie images of plan (X,Z) plane of view located on centerline of injector nozzle ($Y = 0$) for the no injection (N) case and helium injection ($\Psi = 4$) cases (C, T1, T2 ,T3 ,E1 ,E2 ,E3)	194
5.24.	Standard deviation of Rayleigh/Mie images of face-on (Y,Z) plane of view located at $X/h = 1$ for the no injection (N) case and helium injection ($\Psi = 4$) cases (C, T1, T2 ,T3 ,E1 ,E2 ,E3)	195

5.25.	Standard deviation of Rayleigh/Mie images of face-on (Y,Z) plane of view located at $X/h = 2$ for the no injection (N) case and helium injection ($\Psi = 4$) cases (C, T1, T2 ,T3 ,E1 ,E2 ,E3)	196
5.26.	Standard deviation of Rayleigh/Mie images of face-on (Y,Z) plane of view located at $X/h = 4$ for the no injection (N) case and helium injection ($\Psi = 4$) cases (C, T1, T2 ,T3 ,E1 ,E2 ,E3)	197
5.27.	Example of a standard deviation of Rayleigh/Mie image of face-on (Y,Z) plane of view with corresponding schematic of high standard deviation map and visually approximated contour of highest standard deviation values.	198
5.28.	Plot of cross-sectional areas of the helium jet ($\Psi = 4$) determined from Rayleigh/Mie scattering images of face-on (Y,Z) planes of view located at $X/h = 1,2$ and 4.....	199
5.29.	Plot of shape factors for helium jet ($\Psi = 4$) calculated from cross-sectional area and perimeter calculations	200
5.30.	Hypothetical fuel concentration measurements at a point in a two segregated-stream flow of pure air and pure fuel.....	201
5.31.	Hypothetical fuel concentration measurements at a point in a two segregated-stream flow of 60% and 40% fuel to air ratio mixtures.....	201
5.32.	Graphical representation of Konrad's unmixedness parameter.....	202
5.33.	Example of concentration trace about local mean value $\chi_a = 0.3$	203
5.34.	Example of concentration trace about local mean value $\chi_a = 0.3$	203
5.35.	Mixedness maps of face-on (Y,Z) plane of view located at $X/h = 2, 4, 6.8$ and 10 for the helium injection ($\Psi=4$) case using circular (C) nozzle.....	204
5.36.	Mixedness maps of face-on (Y,Z) plane of view located at $X/h = 10$ for the no injection (N) case and the helium injection ($\Psi=4$) cases (C, T1, T2, T3, E1, E2, E3).....	205

5.37.	Mixedness contours along a vertical line passing through the center pixel of the mixedness maps shown in Figure 5.36.....	206
5.38.	Mixedness contours along a horizontal line passing through the center pixel of the mixedness maps shown in Figure 5.36.....	207
5.39.	Normalized mean streamwise velocity in (X,Y) plane at $X/h = -2, -1, 0$. One component ($\blacktriangle \bar{U}/U_{ref}$) and two component ($\bullet \bar{U}/U_{ref}$) measurements....	208
5.40.	Normalized streamwise turbulence intensity in (X,Y) plane at $X/h = -2, -1, 0$. One component ($\Delta \sigma_u/U_{ref}$) and two component ($O \sigma_u/U_{ref}$) measurements.	209
5.41.	Boundary layer velocity profiles from one- and two- component Laser Doppler Velocimetry (LDV) measurements at $X/h = -1$ superimposed on Wall-Wake Law calculated boundary layer profile assuming $\delta = 5.6$ mm and $C_f = 0.0016$	210
5.42.	Generalized velocity defect in boundary layer for present study superimposed on profiles for compressible, adiabatic flat-plate boundary layers (from Maise and McDonald[1968]).....	211
5.43.	Turbulence intensity measurements in the boundary layer of the present study superimposed on measurements from previous studies for various Mach numbers (from Kuntz et al.[1973]).....	212
5.44.	Normalized mean streamwise velocity in (X,Y) plane for the no injection (N) case	213
5.45.	Normalized mean streamwise velocity on centerline of strut (X-axis) for the no injection (N) case	214
5.46.	Normalized mean streamwise velocity in (X,Y) plane for the no injection (N) case. Composite plot.....	215
5.47.	Normalized mean transverse velocity in (X,Y) plane for the no injection (N) case	216
5.48.	Normalized mean transverse velocity in (X,Y) plane for the no injection (N) case. Composite plot.....	217

5.49.	Velocity map of two-component LDV data in (X,Y) plane on centerline of strut without injection	218
5.50.	Streamwise turbulence intensity in (X,Y) plane for the no injection (N) case	219
5.51.	Streamwise turbulence intensity in (X,Y) plane for the no injection (N) case. Composite plot.....	220
5.52.	Transverse turbulence intensity in (X,Y) plane for the no injection (N) case	221
5.53.	Transverse turbulence intensity in (X,Y) plane for the no injection (N) case. Composite plot.....	222
5.54.	Ratio of streamwise to transverse turbulence intensities in (X,Y) plane for the no injection (N) case	223
5.55.	Ratio of streamwise to transverse turbulence intensities in (X,Y) plane for the no injection (N) case. Composite plot.....	224
5.56.	Turbulent shear stress in (X,Y) plane for the no injection (N) case	225
5.57.	Turbulent shear stress in (X,Y) plane for the no injection (N) case. Composite plot.....	226
5.58.	Turbulent shear stress correlation coefficient in (X,Y) plane for the no injection (N) case	227
5.59.	Turbulent shear stress correlation coefficient in (X,Y) plane for the no injection (N) case. Composite plot.	228
5.60.	Normalized mean streamwise velocity in (X,Z) plane for the no injection (N) case	229
5.61.	Normalized mean transverse velocity in (X,Z) plane for the no injection (N) case	230
5.62.	Streamwise turbulence intensity in (X,Z) plane for the no injection (N) case	231

5.63.	Transverse turbulence intensity in (X,Z) plane for the no injection (N) case	232
5.64.	Ratio of streamwise to transverse turbulence intensities in (X,Z) plane for the no injection (N) case	233
5.65.	Turbulent shear stress in (X,Z) plane for the no injection (N) case	234
5.66.	Turbulent shear stress correlation coefficient in (X,Z) plane for the no injection (N) case	235
5.67.	Illustration of the mixing interaction between the nominally two-dimensional mixing layers formed between the primary flow and the recirculating flow at the base of the strut and the helium jet.....	236
5.68.	Normalized mean streamwise velocity in (X,Y) plane for the no injection (N) case (---) and the helium injection case using circular (C) nozzle (●).....	237
5.69.	Normalized mean streamwise velocity on centerline of strut (X-axis) for the no injection (N) case.....	238
5.70.	Normalized mean transverse velocity in (X,Y) plane for the no injection (N) case (---) and the helium injection case using circular (C) nozzle (●).....	239
5.71.	Streamwise turbulence intensity in (X,Y) plane for the no injection (N) case (---) and the helium injection case using circular (C) nozzle (●).....	240
5.72.	Transverse turbulence intensity in (X,Y) plane for the no injection (N) case (---) and the helium injection case using circular (C) nozzle (●).....	241
5.73.	Ratio of streamwise to transverse turbulence intensities (X,Y) plane for the no injection (N) case (---) and the helium injection case using circular (C) nozzle (○).....	242
5.74.	Turbulent shear stress in (X,Y) plane for the no injection (N) case (---) and the helium injection case using circular (C) nozzle (▲).....	243
5.75.	Turbulent shear stress correlation coefficient in (X,Y) plane for the no injection (N) case (---) and the helium injection case using circular (C) nozzle (▲)	244

5.76.	Normalized mean streamwise velocity in (X,Z) plane for the no injection (N) case and the helium injection case using circular (C) nozzle	245
5.77.	Normalized mean transverse velocity in (X,Z) plane for the no injection (N) case and the helium injection case using circular (C) nozzle	246
5.78.	Streamwise turbulence intensity in (X,Z) plane for the no injection (N) case and the helium injection case using circular (C) nozzle	247
5.79.	Transverse turbulence intensity in (X,Z) plane for the no injection (N) case and the helium injection case using circular (C) nozzle	248
5.80.	Ratio of streamwise to transverse turbulence intensities in (X,Z) plane for the no injection (N) case and the helium injection case using circular (C) nozzle	249
5.81.	Turbulent shear stress in (X,Z) plane for the no injection (N) case and the helium injection case using circular (C) nozzle	250
5.82.	Turbulent shear stress correlation coefficient in (X,Z) plane for the no injection (N) case and the helium injection case using circular (C) nozzle	251
5.83.	Normalized mean streamwise velocity in (X,Y) plane at $X/h = 2$ for all cases	252
5.84.	Normalized mean streamwise velocity in (X,Y) plane at $X/h = 6.8$ for all cases	253
5.85.	Normalized mean transverse velocity in (X,Y) plane at $X/h = 2$ for all cases	254
5.86.	Normalized mean transverse velocity in (X,Y) plane at $X/h = 6.8$ for all cases	255
5.87.	Streamwise turbulence intensity in (X,Y) plane at $X/h = 2$ for all cases	256

5.88.	Streamwise turbulence intensity in (X,Y) plane at $X/h = 6.8$ for all cases....	257
5.89.	Transverse turbulence intensity in (X,Y) plane at $X/h = 2$ for all cases....	258
5.90.	Transverse turbulence intensity in (X,Y) plane at $X/h = 6.8$ for all cases ...	259
5.91.	Ratio of streamwise to transverse turbulence intensities in (X,Y) plane at $X/h = 2$ for all cases	260
5.92.	Ratio of streamwise to transverse turbulence intensities in (X,Y) plane at $X/h = 6.8$ for all cases	261
5.93.	Turbulent shear stress in (X,Y) plane at $X/h = 2$ for all cases	262
5.94.	Turbulent shear stress in (X,Y) plane at $X/h = 6.8$ for all cases	263
5.95.	Shear stress correlation coefficient in (X,Y) plane at $X/h = 2$ for all cases .	264
5.96.	Shear stress correlation coefficient in (X,Y) plane at $X/h = 6.8$ for all cases.	265
5.97.	Normalized mean streamwise velocity in (X,Z) plane at $X/h = 2.0$ for all cases	266
5.98.	Normalized mean streamwise velocity in (X,Z) plane at $X/h = 6.8$ for all cases	267
5.99.	Normalized mean transverse velocity in (X,Z) plane at $X/h = 2$ for all cases	268
5.100.	Normalized mean transverse velocity in (X,Z) plane at $X/h = 6.8$ for all cases	269
5.101.	Streamwise turbulence intensity in (X,Z) plane at $X/h = 2$ for all cases.....	270
5.102.	Streamwise turbulence intensity in (X,Z) plane at $X/h = 6.8$ for all cases.....	271
5.103.	Transverse turbulence intensity in (X,Z) plane at $X/h = 2$ for all cases.....	272
5.104.	Transverse turbulence intensity in (X,Z) plane at $X/h = 6.8$ for all cases.....	273

5.105. Ratio of streamwise and transverse turbulence intensities in (X,Z) plane at $X/h = 2$ for all cases.....	274
5.106. Ratio of streamwise and transverse turbulence intensities in (X,Z) plane at $X/h = 6.8$ for all cases.....	275
5.107. Turbulent shear stress in (X,Z) plane at $X/h = 2$ for all cases.....	276
5.108. Turbulent shear stress in (X,Z) plane at $X/h = 6.8$ for all cases.....	277
5.109. Shear stress correlation coefficient in (X,Z) plane at $X/h = 2$ for all cases....	278
5.110. Shear stress correlation coefficient in (X,Z) plane at $X/h = 6.8$ for all cases.....	279

NOMENCLATURE

Roman symbols

A	cross-sectional area of jet
a	speed of sound
C	circular nozzle
C_f	coefficient of skin friction
c_p	specific heat at constant pressure
$D_{e^{-2}}$	diameter of laser beam at which the intensity is equal to e^{-2} of the beam centerline amplitude
d	diameter of a circular nozzle exit
d_b	distance between parallel beams entering lens system in mm
d_e	equivalent diameter
d_f	fringe spacing in LDV measurement volume in mm
d_m	diameter of LDV measurement volume in mm
d_p	diameter of particles
E1	elliptic nozzles oriented with major axis along Y axis
E2	elliptic nozzle oriented with major axis at a 45 degree angle to Y axis (counter clockwise)
E3	elliptic nozzle oriented with major axis along Z axis
f	focal length of lens in mm
g	variance
h	strut thickness or step height
I	pixel intensity

\bar{I}	average pixel intensity
I_1	maximum pixel intensity
I_2	minimum pixel intensity
I_s	scattering intensity
K	constant in the law of the wall
K_n	Knudsen number
k	kinetic energy of fluctuating motion, thermal conductivity
l	unit length
l_m	length of LDV measuring volume in mm
M	Mach number
M_c	convective Mach number
M_I	mixedness parameter for digitized images
m	mixedness parameter
\dot{m}	mass flow rate
N	no injection
N_{fr}	number of fringes in LDV measurement volume
n	total number of samples in a summation set
P	static pressure
\dot{P}	momentum
P_o	stagnation pressure
Pr	Prandtl number
p	perimeter
q	cylindrical tab diameter (Figure 2.102)
r_p	radius of a particle
R	universal gas constant
R_o	effective radius of jet cross-sectional area

R_{uv}	correlation coefficient between u and v
Re	Reynolds number
S	shape factor
St	Stokes number
s	segregation
T	static temperature
T_o	stagnation temperature
T1	circular-with-tabs nozzle oriented with tabs along Y axis
T2	circular-with-tabs nozzle oriented with tabs at a 45 degree angle to Y axis (counter clockwise)
T3	circular-with-tabs nozzle oriented with tabs along Z axis.
t	time
U	streamwise velocity
\bar{U}	mean streamwise velocity
U_c	convection velocity
U_{eff}	effective velocity
U_{ref}	calculated Mach 2 freestream air velocity
u	streamwise velocity fluctuation
um	unmixedness
um_e	unmixedness with mean value consideration
\overline{uu}	turbulent normal stress in streamwise direction
\overline{uv}	turbulent (Reynolds) shear stress
V	velocity in transverse direction
\bar{V}	mean velocity in transverse direction
v	velocity fluctuation in the transverse direction
\overline{vv}	turbulent normal stress in transverse direction

W	velocity in the spanwise direction
\overline{W}	mean velocity in spanwise direction
X	streamwise distance measured from nozzle exit and coincident end of strut
Y	transverse distance measured from center of injection nozzle
Z	spanwise distance measured from center of injection nozzle

Greek symbols

α	semi-major axis of an ellipse, fraction of time
β	semi-minor axis of an ellipse, fraction of time
δ	boundary layer thickness
δ_w	size of largest eddies or width of flow
γ	specific heat ratio
κ	lens half angle in degrees
λ	wavelength of radiation or light
μ	absolute fluid viscosity
η	Kolmogorov microscale of length
π	3.14159
ρ	density
ρ_p	density of particle
ϕ	observation angle
σ_I	standard deviation of pixel intensity
σ_u	standard deviation of streamwise velocity
σ_v	standard deviation of transverse velocity
σ_x	standard deviation of mole fraction
τ	shear stress
τ_p	particle time scale
τ_f	flow time scale

τ_{uv}	Normalized turbulent (Reynolds) shear stress
$\vec{\omega}$	vorticity vector
χ	mole fraction
χ_a	mole fraction of air
Ψ	ratio of calculated static pressure of the jet at nozzle exit to the static pressure of freestream air

Mathematical Symbols

∇	gradient operator
Δ	differential operator
\cong	approximately equal to
$ \quad $	absolute value of enclosed value

Subscripts

1	high speed free stream or fluid 1
2	low speed freestream or fluid 2
e	injector nozzle exit values
o	stagnation values
i	ICCD camera pixel array row
j	ICCD camera pixel array column
k	index of summation
w	wall values
∞	freestream values

CHAPTER 1

INTRODUCTION

Gaseous injection into supersonic flows has many engineering applications. One which concerns the aerospace industry and combustion engineers in particular is injection of gaseous hydrogen or hydrocarbon fuels in supersonic combustion ramjet (SCRAMJET) engines. It has been argued that air breathing supersonic combustion engines offer the best performance for a single-stage-to-orbit flight vehicle [Heppenheimer 1989]. However, the challenges involved in the realization of such a vehicle are still beyond present engineering capabilities.

In a conventional ramjet engine, the air flow is captured by an inlet and decelerated to subsonic speed before entering the combustor. There is a vast pool of engineering experience in the design of ramjet powered systems, perhaps because the mechanisms involved in the transport and mixing of fuel and air in these systems are not much different from those encountered in gas turbine combustors. Ramjets have demonstrated excellent performance and are the engines of choice for flight in the Mach number range 3 to 6 [Heiser and Pratt 1994]. At higher flight speeds however, the reduction in the total pressure recovery of the inlets, combined with a rise in the static temperature of the air entering the combustor chamber, degrades the performance of conventional ramjets [Curran and Stull 1963].

At hypersonic flight speeds, the performance of the ramjet engine can be increased if combustion is allowed to take place at supersonic velocities rather than decelerating to subsonic velocities. Scramjet propulsion systems employ three-

dimensional compression inlets, geometrically complex fuel injection systems, and two- or three-dimensional exhaust nozzles. During operation, these components, both individually and as a system, generate spatially and temporally complex flow fields that contain viscous/inviscid interactions with thermochemical effects. Adding to the complexity of the flow field is the fact that the fore and aft sections of the vehicle are necessarily used as compression and expansion surfaces. The resulting vehicle is a highly integrated flight vehicle/engine configuration which must operate efficiently as a single element over a wide flight-speed envelope in very challenging thermodynamic environments [Heiser and Pratt 1994]. General lack of engineering experience with scramjet powered vehicles, together with the currently limited understanding of the physics of mixing and heat release in supersonic flows, have made the engineering realization and implementation of an efficient hypersonic vehicle a formidable task.

Designing a fuel injection scheme to produce optimal fuel-air mixing and combustion within the space and time constraints of a supersonic combustor remains one of the primary engineering challenges in scramjet technology. Enhancement and control of fuel-air mixing in supersonic flows suffers from very short time scales and inherently low mixing rates at higher Mach numbers [Papamoschou and Roshko 1988, Samimy and Elliott 1990]. Normal, oblique, and parallel fuel injection schemes have all been considered in past studies. Normal injection produces the best mixing but incurs a significant total pressure loss, primarily due to the generation of a strong bow shock [King et al. 1989]. Injection at an oblique angle has shown an improved total pressure recovery as compared to normal injection and an improved mixing and fuel distribution when compared to parallel injection [McClinton 1972, Mays et al. 1989, Fuller et al. 1992]. Parallel injection of fuel can provide a significant component of the engine thrust in high flight Mach numbers, but has only limited mixing capability.

Parallel fuel injection shows promise in terms of thrust addition and absence of significant thrust losses, provided that mixing can be increased. The need to mechanically support the parallel injection nozzle and connected fuel lines can be fulfilled by a variety of designs. Two of the proposed design configurations are struts extending across the primary flow channel separating the flow into discrete air streams [Heppenheimer 1989], and wall mounted ramp injectors that protrude a limited distance into the freestream [Waitz et al. 1992a]. Ramp injectors produce vortex shedding and shock waves, both of which enhance mixing of the jet and freestream flow. However, the ramps are intrusive to the supersonic flow, causing excessive pressure loss and requiring extensive cooling at high flight Mach numbers. Despite numerous base flow studies [Samimy and Addy 1986, Amatucci et al. 1992, Dutton et al. 1995], to date, there is no detailed experimental study of injection from the base of a two-dimensional strut into a turbulent supersonic flow. Nonetheless, parallel injection from a strut is expected to incur minimal shock losses and mixing may be enhanced by such means as modified nozzle geometry.

The objectives of this investigation were to determine the fundamental characteristics of parallel fuel injection from an extended strut into a supersonic freestream and to explore passive mixing enhancement through the use of different nozzle geometries. The configuration designed for experiments in this study consisted of a two-dimensional strut spanning a nominal Mach two combustion wind tunnel. The strut extended into the settling chamber, well upstream of the supersonic nozzle, to eliminate leading edge shocks and to produce a well behaved two stream Mach 1.92 flow upstream of the bluff-body separation point. Gaseous helium was injected into the Mach 1.92 air flow through three converging nozzles of different geometry: circular, circular-with-tabs, and elliptic.

CHAPTER 2

BACKGROUND

Injection from the base of a strut, as in the present experimental program, results in a complex three-dimensional flow field. The use of various nozzle geometries for injection compounds the complexity. This section describes the basic structures and characteristics of the flow field components that are combined in the configuration used for the current experimental program.

2.1 Injection schemes

Overcoming the inherently low mixing rates in supersonic flows is one of the key engineering challenges for the design of supersonic combustors. The overall goal is to produce optimal mixing and combustion with minimal thrust loss within the spatial and temporal constraints of the combustion chamber. Molecular mixing of the initially segregated fuel and air streams must occur in order to produce the chemical reaction and heat release of combustion which yields the expansion of hot gases and produces thrust. The failure of fuel and oxidizer to mix fully results in incomplete combustion and lost chemical/heating energy of the fuel [Glassman 1987].

In addition to fuel/air mixing, age mixing or back mixing of partially or wholly burned gases into the uncombusted fuel/air mixture is necessary in order to achieve sustained self-ignition without the aid of an external energy source such as a pilot flame, spark plug or ignition point [Pratt 1975]. Age mixing in supersonic combustion

istypically achieved by the use of a bluff body. The function of a bluff body is to create a turbulent wake in which age mixing occurs, thereby sustaining or "holding" the flame.

Mixing enhancement in supersonic combustion applications thus involves two components -- initial fuel/air mixing and age mixing. Fuel injection parallel, normal [e.g., Schetz and Billig 1966, Papamoschou et al. 1991] and at an oblique angle [e.g. McClinton 1972, Mays et al. 1989, and Fuller et al. 1992] to the mean freestream air flow have all been considered as possible configurations for mixing capability in supersonic combustion applications. Figure 2.1 shows schematics of underexpanded jets injected normal, at an oblique angle, and parallel to a supersonic freestream. Normal or oblique injection through flush mounted wall injectors is an attractive method of fuel injection, because it avoids the need for cooling and protection of the injectors. However, in these configurations, the thrust component of the fuel is not aligned with the flight direction, flame holding is a problem, and the presence of the fuel jet causes bow shocks in the air stream, resulting in thrust losses [King et al. 1989]. Parallel fuel injection on the other hand, actually adds thrust to the air stream, due to the momentum associated with the fuel stream. It also avoids the strong bow shocks caused by normal injection, and can provide an integrated flame holder. However, parallel injection results in less effective mixing of the jet with the freestream fluid as compared to normal injection.

Considering the trade-offs between thrust, shock losses, flame holding, mixing and fuel distribution in parallel, normal and oblique injection, parallel injection seems promising in terms of thrust realization and flame holding, provided that mixing can be increased. Acoustic excitation, variations in nozzle geometry or shock induced mixing are potential mixing enhancement techniques. Of these methods, the passive method of variation in nozzle geometry appears most practical for applications in combustors, since shock waves induce losses and acoustic excitation requires additional hardware.

Noncircular nozzle geometries have been used in incompressible and compressible flow research to promote better mixing between the jet and freestream fluids. Several of the basic nozzle geometries previously tested include circular, triangular, square, rectangular and elliptic. The oblong shapes of the ellipse and the rectangle create an azimuthal variation of initial conditions which results in a phenomenon referred to as "axis-switching." Axis-switching has been shown to significantly increase mixing in both subsonic [Ho and Gutmark 1987, Quinn 1989, Shih et al. 1992] and supersonic jets [Schadow and Gutmark 1989]. Three-dimensional, irregular nozzle geometries incorporating 'teeth' [Wlezien and Kibens 1987, Longmire et al. 1992] and tabs [Samimy et al. 1993, Zaman et al. 1994] at the nozzle exit have been shown to create streamwise vortices which increase mixing. A representative illustration of a nozzle with teeth is shown in Figure 2.2 and a nozzle with delta tabs in Figure 2.3.

The present investigation examines helium injection from circular, elliptic, and circular-with-tabs nozzles into a supersonic flow. The circular nozzle was chosen as the baseline geometry. The elliptic nozzle was chosen to explore the effects related to an oblong geometry. The circular-with-tabs nozzle was chosen to examine effects of vortex generators mounted at the exit of a nozzle.

The need to mechanically support the parallel injection nozzle and connected fuel lines can be fulfilled by a variety of designs, each with its own flow patterns. Two of the configurations proposed in recent studies are struts extending across the primary flow channel separating the flow into discrete air streams [Heppenheimer 1989], and wall mounted ramp injectors that protrude a limited distance into the freestream from one of the channel walls [Waitz et al. 1991]. An advantageous consequence of injection from the base of either the strut or ramp injector is the recirculation zone typical of flow around a bluff body, which in combustion applications enables flame holding.

Wall mounted ramp injectors have been the focus of several recent parallel injection endeavors. The wall mounted ramp injectors have been designed to fit on one wall of a square channel [Davis and Hingst 1991, Waitz et al. 1991, 1992a, and 1992b] or around the circumference of an axisymmetric channel [Yu et al. 1992]. Ramp injectors produce vortex shedding and local separation behind the ramp's base. In some designs, shock waves are employed to enhance mixing by generating a shock wave that passes at an oblique angle through the jet of injected fluid. Vorticity is created at any point in a flow field where a pressure gradient interacts with a nonparallel density gradient. Thus, when a shock wave passes obliquely through a column (jet) of low density fluid surrounded by a higher density primary flow (air), vorticity is created precisely where it is desired: at the gas/air interface [Jacobs 1992, Waitz et al. 1992b]. The mechanism generating vorticity is referred to as baroclinic torque and can be seen in the source term of the vorticity equation:

$$\rho \frac{D}{Dt} \left(\frac{\varpi}{\rho} \right) = \frac{1}{\rho^2} \bar{\nabla} \rho \times \bar{\nabla} P, \quad 2.1$$

where ρ is density, P is pressure and ϖ is vorticity. Continued research on ramp injectors focuses on exploiting the mixing enhancement capabilities of the flow patterns inherent in the various parallel injection configurations.

Despite numerous base flow investigations [Samimy and Addy 1986, Amatucci et al. 1992, Dutton et al. 1995, Raffoul 1995] there has as yet been no detailed experimental study of injection from the base of a two dimensional strut. However, numerical simulations have been performed. The symmetry of a two-dimensional strut with the injector nozzle mounted at the center lends itself to numerical analysis, because the configuration for the strut can be divided into four identical quadrants about the center of

the nozzle, whereas the asymmetric ramp injector configuration can only be divided into two identical quadrants. A two-dimensional numerical simulation by Sullins et al. [1982] highlighted the basic characteristics of the flow field resulting from injection from a two-dimensional slot injector at the base of a strut. More complex three-dimensional analysis evolved with the increase in computational power of more recent super computers. A very recent three-dimensional numerical simulation by Chen et al. [1995] provides calculated thermodynamic properties of a jet issuing from a 3.5 mm circular nozzle mounted in the base of a strut with thickness (h) equal to 1.27 cm.

The simplicity of the strut with its well defined initial conditions makes it attractive for experimental as well as numerical studies. Thus, parallel injection from the base of a strut, like that explored by Chen, is the configuration chosen for the present experimental program. Three different injector nozzle geometries were used: circular, circular-with-tabs, and elliptic.

2.2 Planar mixing layer structures

The following summary of previous work in planar free shear layers is intended as background on the shear layer structures present in incompressible and compressible flows. Although the free shear layers, also referred to as mixing layers, originating at the base of the strut experience compressibility effects, incompressible planar shear layers are presented here in order to introduce the organized structures present in incompressible flows that are affected under compressible conditions.

Incompressible mixing layers

A simple two-dimensional incompressible shear layer consists of two fluid streams of equal pressure traveling parallel to one another at different subsonic velocities. Shear stress arises at the interface between the two streams, due to the velocity difference

between the flows. The shear stress generates a Kelvin-Helmholtz instability at the mixing interface, that produces large-scale vortices.

Research on the large-scale structures in planar mixing layers was initiated by Brown and Roshko [1974] and later reviewed by Ho and Huerre [1984]. Large-scale structures are the primary mixing mechanism in a two-dimensional incompressible mixing layer and appear as a rolling up of the plane at the interface of the two streams (Figure 2.4). The rolling motion engulfs fluid from both streams and stretches the mixing interface. This stretching of the mixing interfacial area simultaneously increases the local concentration gradients and increases the area of interaction between the two fluids. The smallest scale mixing achieved is on the molecular level at the interface between the two fluids and is thus accelerated with the increase of the area of contact between the two fluids.

In addition to the primary large spanwise vortices, secondary streamwise structures can evolve in mixing layers. Numerous observation of streamwise streaks in flow visualizations [Konrad 1976, Breidenthal 1981], "mushroom" shaped ejected fluid structures [Bernal 1981], and shear layer deformation [Jimenez 1983] were early indicators of the presence of streamwise structures which prompted further research.

Detailed analysis of subsonic mixing layers by Lasheras et al. [1986] showed that small-scale streamwise vortices evolve in the braid region between larger spanwise vortices. The region between the vortex pairs is referred to as the "braid" region because of the entwined, thin ligaments of vorticity linking adjacent vortex structures. Lasheras and Maxworthy used a water tunnel to produce a turbulent reacting mixing layer between a 6.5 cm/s stream a 3.5 cm/s stream of aqueous solution, one being acidic and one being basic. They captured the generation and development of streamwise vortical structures and their interaction with the spanwise structures using Planar Laser-Induced Fluorescence (PLIF) and a direct color based visualization of an acid/base reaction

between the two streams. The mechanism of axial vorticity production was identified as the response of spanwise vortex lines in the braid region to small three-dimensional perturbations. The spanwise vortex cores cause a strong positive strain rate in the braid region which results in three-dimensional instabilities that are sensitive to perturbations. The counter-rotating streamwise vortex pairs grow as they propagate downstream and deform as they pass through each spanwise vortex core. A follow-up study with the same experimental setup, using a sinusoidal trailing edge attached at the end of the splitter plate to induce spanwise vortices, provided more details on the nonlinear interaction between the primary spanwise and secondary streamwise structures [Lasheras and Choi 1988].

Bernal and Roshko [1986] performed similar water tunnel experiments along with a helium-nitrogen shear layer experiment. The water tunnel experiments clearly showed spatially organized counter-rotating vortex pairs on the top and bottom of streamwise vortex cores (Figure 2.5). These streamwise vortices produced a well-defined spanwise entrainment pattern in which fluid from each stream is preferentially entrained at different spanwise locations. This study also showed the existence of streamwise streaks in schlieren images of a high Reynolds number helium-nitrogen mixing layer, indicative of the presence of streamwise vortices. The streaks are fixed with each flow condition but changed in number and location when the upstream flow was changed by replacing upstream flow conditioning screens. This suggests that the streamwise vortices are associated with flow instabilities that amplify upstream disturbances.

Later, Bell and Metha [1990] showed that the streamwise vortical structures that appear in laminar two-stream mixing layers, as in the aforementioned studies, disappear when the boundary layers were tripped to induce turbulence. This signifies that the turbulent motion in the boundary layer typically found in high Reynolds number flows prohibits the formation of organized streamwise structures without substantial artificial

disturbances. Furthermore, they found that both the near and far field growth rate to be significantly higher for the untripped case. This was attributed to the presence of streamwise vortices that result in additional entrainment in the mixing layer.

Compressibility

In cases where at least one of the fluids is traveling at supersonic velocity, the large-scale spanwise vortices evolve as in subsonic flows, but compressibility effects decrease their growth and their entraining ability (seen as a decrease in the shear layer spread rate). Bogdanoff [1983] and Papamoschou and Roshko [1988] have developed a parameter to describe the compressibility effects in supersonic shear layers between two pressure matched streams of fluid. This parameter, referred to as the convective Mach number, M_c , is defined as the convection speed of the large-scale structures in the shear layer relative to the velocity of one of the streams, normalized by the speed of sound of the same stream:

$$\begin{aligned} M_{c1} &= \frac{U_1 - U_c}{a_1} \\ M_{c2} &= \frac{U_c - U_2}{a_2} \end{aligned} \tag{2.2}$$

Where U_1 and U_2 ($U_1 > U_2$) are the velocities of the two streams forming the shear layer (Figure 2.4), U_c is convective velocity, a_1 and a_2 are the speed of sound, and M_{c1} and M_{c2} are the convective Mach numbers with respect to these two streams. With the assumption of a common stagnation point between the two streams [Coles 1981], implying equal total pressures in the two streams at the stagnation points, one can state:

$$\left(1 + \frac{\gamma_1 - 1}{2} M_{c1}^2\right)^{\frac{\gamma_1}{\gamma_1 - 1}} = \left(1 + \frac{\gamma_2 - 1}{2} M_{c2}^2\right)^{\frac{\gamma_2}{\gamma_2 - 1}} \tag{2.3}$$

where γ_1 and γ_2 are the specific heat ratios for the fluid in stream 1 and stream 2, respectively. When M_{c1} and M_{c2} are not very large and γ_1 and γ_2 are not greatly different, equation 2.3 can be approximated by:

$$\frac{U_c}{U_1} = \frac{1 + \frac{U_2}{U_1} \left(\frac{\rho_2}{\rho_1} \right)^{\frac{1}{2}}}{1 + \left(\frac{\rho_2}{\rho_1} \right)^{\frac{1}{2}}} \quad 2.4$$

Where ρ_1 and ρ_2 are the densities of the fluid in stream 1 and stream 2, respectively. Together with the defining equation (2.2), this becomes:

$$M_{c2} = \left(\frac{\gamma_1}{\gamma_2} \right)^{\frac{1}{2}} M_{c1} \quad 2.5$$

For $\gamma_1 = \gamma_2$, $M_{c1} = M_{c2}$ (simply written M_c), U_c can be expressed in the simplified form:

$$U_c = \frac{a_2 U_1 + a_1 U_2}{a_1 + a_2} \quad 2.6$$

Frequently M_{c1} or M_{c2} is not specified; rather, M_c is written without reference to either stream, in which case either M_{c1} is equal to M_{c2} (i.e., $\gamma_1 = \gamma_2$) or M_c is assumed to be equal to the value of M_{c1} , since the high speed fluid provides the driving force for the mixing layer.

It is important to note that although compressibility effects are present in all types of injection into supersonic flow, the convective Mach number is defined solely for mixing layers between two parallel, **pressure matched** streams of fluid. Nonpressure

matched conditions involve quickly changing velocities and pressure conditions not addressed in the convective Mach number derivation.

Papamoschou and Roshko [1988] showed that the normalized growth rate of the shear layers decreases for $M_c > 0.6$ and reaches an asymptotic value of about 20% of the incompressible spread rate for high convective Mach numbers (i.e., $M_c > 1.5$ or 2.0). More recent studies in planar shear layers have investigated such factors as shear stress and turbulence intensity [Elliott and Samimy 1990, Samimy and Elliott 1990, Goebel and Dutton 1991]. These studies indicate that both small and large-scale mixing decrease with increased convective Mach number.

When the flow velocities are increased to a level where compressibility effects are significant, the spanwise large-scale structures become highly three-dimensional and disorganized [Elliott et al. 1992, Samimy et al. 1992]. Clemens and Mungal [1992] examined the change in characteristics of the large-scale structures in the shear layer as the convective Mach number was increased from a low compressible case ($M_c = 0.28$) to high compressible cases ($M_c = 0.62, 0.79$). Planar Mie scattering images and schlieren photographs showed the two-dimensional, organized, spanwise structures in the low compressibility, $M_c = 0.28$, shear layer (characteristic of incompressible shear layers) to become highly convoluted, three-dimensional structures lacking spatial regularity with the increase of M_c to 0.62 and 0.79. The differences between the $M_c = 0.28$ and $M_c = 0.62$ cases are attributed to compressibility effects rather than to Reynolds number effect because the Reynolds numbers were nearly matched in these two cases. There was no obvious difference between the $M_c = 0.62$ and $M_c = 0.79$ cases. Clemens and Mungal observed small jets of mixed fluid being ejected from the mixing layers; these jets may be initiated by small-scale counter-rotating vortices. They conjecture that three-dimensionality may impact the ability to force and control compressible mixing layers.

Summary

Incompressible shear layers exhibit well organized spanwise large-scale structures. In addition to these spanwise structures, organized secondary streamwise structures are evident in incompressible flows with incoming laminar boundary layers. These secondary structures are absent with an incoming turbulent boundary layer, typical of high Reynolds number flows, upstream of the shear layer. As the velocities of the freestreams are increased, compressibility effects reduce the spread of the mixing layer. Compressibility effects also cause the two-dimensional spanwise large vortices to become highly three-dimensional and disorganized.

2.3 Axisymmetric shear layers

The following summary of previous work in free jets and coaxial jets provides background concerning the structure and characteristics of the mixing layer around the circumference of the jet, and highlights the specific characteristics of an underexpanded jet. Although the helium jet in the present study encounters a complex flow field due to the wake flow behind the strut, an understanding of the well documented structure of jets in simple flow conditions provides a basis for an understanding of the complex interactions of the jet in the present study.

Incompressible flows

In axisymmetric incompressible shear layers, the vorticity roll-up caused by the Kelvin-Helmholtz instability results in axisymmetric vortex rings (Figure 2.6). These vortex rings are the counterpart of spanwise vortices formed in a planar shear layer. As the jet exits the circular nozzle it encounters a velocity gradient (along with temperature, pressure, and density gradients) that cause flow instabilities. These instabilities result in a migration of vorticity to form periodic, circumferentially coherent concentrations in the

axisymmetric shear layer. Thus it appears that the laminar shear layer rolls up to form a periodic row of discrete vortex rings [Yule 1978].

These vortex rings, in general, grow three-dimensionally as they move downstream, by entraining ambient fluid. The rolling motion engulfs fluid from both streams and stretches the mixing interface. This stretching of the mixing interfacial area simultaneously increases the local concentration gradients and increases the area of interaction between the two fluids. The smallest scale mixing is on the molecular level at the interface between the two fluids and is thus accelerated with the increase of the area of contact between the two fluids. Any nonequality of spacing, strength, or speed of two (or more) adjacent vortices induces them to amalgamate and form a single, larger vortex; the process repeats itself in the downstream direction. The vortices may become turbulent during the first coalescence or soon thereafter, but they retain their large-scale identities downstream. The turbulent large-scale eddies are highly three-dimensional and less organized than the vortex pairs from which they evolve [Hussain and Zedan 1978].

Unlike the planar mixing layer, the growth of an axisymmetric mixing layer causes it to converge radially inward on itself at the jet centerline. The location where the mixing layers converge at the center of the jet marks the end of the jet core and thus serves to establish the length of the jet core. The length of the jet core changes in an unstable manner similar to the vibration of a column and thus termed "jet column" instability. The jet core has a natural frequency at which it can be acoustically excited to generate organized and amplified structures. Lepicovsky et al. [1987] showed this preferred excitation frequency for a high Reynolds number and fully expanded Mach 1.4 free air jet to correspond to a Strouhal number of 0.4. In addition to column instability, which affects the core length, PLIF studies of turbulent water jets have shown that structures in the jet flow evolve from both helical and axisymmetric instability modes

[Dimotakis et al. 1983, Yoda et al. 1992]; the flow appears to switch between these two modes.

As in planar shear layers, secondary streamwise vortices have been observed in axisymmetric shear layers. Figure 2.7 shows a cross-sectional view and accompanying images of a very low Reynolds number jet shows structures projecting radially from the jet core [Liepmann 1991]. The cross-sectional views in Figure 2.7 were taken using PLIF at a downstream distance (X) from the nozzle exit equivalent to 3.25 nozzle exit diameters (d). These streamwise structures result from azimuthal instability. They significantly impact the instantaneous entrainment of freestream fluid and therefore effect the overall mixing process of the jet. In high Reynolds number flows, a similar type of streamwise structure may be generated by artificial means such as tabs or "teeth" mounted at the exit of the nozzle (refer to Figures 2.2 and 2.3). The streamwise vortices induced by tabs will be discussed in detail in Section 2.4.2.

The strength of the streamwise vortices depends on the presence and nature of the disturbance(s) in the jet flow along with the magnitude of amplification of the disturbance caused by instabilities in the flow. Subtle perturbations from upstream flow conditions or nonideal nozzle surfaces may cause irregularities in the jet contour depending on the operating regime. For example, Novopashin and Perepelkin [1989] used Rayleigh scattering cross-sectional images to show that an angular rotation of a circular sonic nozzle results in an equivalent rotation of the indentation pattern around the circumference of the jet operating in the underexpanded regime. This indicates a direct relation between the nozzle shape and the streamwise vortex pattern around the jet. Upon inspection, the indentation pattern was linked to fine scratches on the nozzle internal surface, thus indicating that disturbances were amplified by a Taylor-Görtler type instability mechanism.

King et al. [1994] also showed equivalent rotation between the nozzle and streamwise structures. They also showed that polishing the nozzle surface to remove a discovered flat spot removed the largest disturbances, but some fluctuations were still present. Even when the nozzle is machined to a smooth surface finish, there is still sufficient irregularity, however minute, in flow conditions or nozzle surface or contour to initiate perturbations. This follows the suggestion of Bernal and Roshko [1986] and Lasheras et al. [1986] that in incompressible plane mixing layers, streamwise structures are initiated by a disturbance within the separating boundary layer. Once the perturbation is generated, the magnitude of its effect depends upon the stability or instability of the flow. The generation of vortices capable of increasing mixing by disturbances in the nozzle suggests the placement of intentional vortex generators in the nozzle.

Along these lines, King et al. [1994] attached triangular pieces of tape to the inside surface of a circular nozzle to explore the effects of a substantial disturbance located at the inner surface of the nozzle. Total pressure measurements and flow visualizations showed the presence of streamwise vortices at the locations in a fully expanded jet corresponding to the locations of the triangular pieces of tape in the nozzle.

Instability in underexpanded jets

A jet static pressure which is higher than the surrounding flow static pressure results in instabilities due to flow curvature of the jet. As an underexpanded jet exits a nozzle it initially expands and undergoes a process of pressure equalization with the surrounding flow. The streamwise curvature of the jet along with a radial velocity gradient inherent in underexpanded jets causes a significant instability which amplifies even the minute disturbances from the roughness of the inner nozzle surface.

Pitot pressure measurements and planar flow visualizations by Arnette et al. [1993b] and Krothapalli et al. [1991] have confirmed earlier observations of counter rotating stationary streamwise vortices by Zapryagaev and Solotchik [1988] in the near

field of an underexpanded jet and by Novopashin and Perepelkin [1989] in a highly underexpanded jet which were not present in underexpanded and fully expanded jets. Arnette et al. [1993b] used total pressure measurements and flow visualization to show the azimuthal variations characteristic of streamwise vortices present in axisymmetric jets. Figure 2.8 shows streamwise vortices between the jet flow of an underexpanded jet and the ambient air. The strength and organization of these structures in an underexpanded supersonic jet, as compared to a fully expanded and overexpanded jet, are believed to originate from the instability arising from streamline curvature and a radial velocity gradient which are characteristic of a Taylor-Görtler type instability [Arnette et al. 1993b].

Schlieren images [Zapryagaev and Solotchin 1988] and Mie scattering images [Arnette et al. 1993b, Novopashin and Perepelkin 1989, Krothapalli et al. 1991, King et al. 1994] have shown that the initially spatially stationary streamwise vortices in underexpanded jets merge and become less organized and nonstationary downstream. The vortices act to entrain ambient fluid and eject jet fluid in a radially inward or outward motion, depending on the rotation sense of the particular vortex pair. For the streamwise vortices to arise, both an instability and a perturbation must be present in the flow field.

Compressible axisymmetric mixing layers

As observed in planar shear layers, the spread rate of axisymmetric shear layers formed between two supersonic coaxial jets decreases with an increase in convective Mach number. In a study by Schadow et al. [1989b], the convective Mach number was varied between $0.25 < M_c < 2.25$ for a fully expanded Mach 3 jet, centered inside an outer jet of Mach 1.8. The spreading rate of the center circular jet was found to decrease with an increasing convective Mach number until it reached a constant value of 20% to 30% of the incompressible spreading rate for $M_c > 1.4$. This study was extended to rectangular jets by Gutmark et al. [1991]. Pressure matched axisymmetric and plane

shear layers exhibit the same effect of a 20-30% reduction in spread rate for compressible shear layers as compared to incompressible shear layers. This is not the case for underexpanded jets in which static pressure between the jet and ambient flow is different.

Summary

Incompressible shear layers in low Reynolds numbers (laminar) jets exhibit well organized vortex ring structures characteristic of a Kelvin-Helmholtz instability. In addition, streamwise vortex structures originate between the large-scale vortex ring structures. In high Reynolds number jets, the magnitude of the streamwise vortices depends on the presence and nature of disturbances in the flow and the magnitude of amplification caused by instabilities in the flow. Overexpanded and fully expanded high Reynolds number jets exhibit streamwise vortices only with the addition of a substantial disturbance such as vortex generators placed on the inner surface of the nozzle. On the other hand, additional instabilities (believed to be Taylor-Görtler type [Arnette et al. 1993b]) in underexpanded jets amplify the minute disturbances caused by the surface roughness on the inside of the jet nozzle to produce significant streamwise vortices. As in planar shear layer studies, the spread rate of axisymmetric shear layers decreases with increased convective Mach number due to compressibility effects.

2.4 Noncircular nozzle geometries

Noncircular nozzle geometries have been used in incompressible and compressible flow research to promote better mixing between the jet and freestream fluids. Several of the basic nozzle geometries tested include circular, triangular, square, rectangular and elliptic. The oblong shapes of the ellipse and the rectangle create an azimuthal variation of initial conditions which results in a phenomenon called "axis-switching." Axis-switching has been shown to significantly increase mixing in both subsonic [Ho and Gutmark 1987, Gutmark et al. 1989, Quinn 1989, Shih et al. 1992] and

supersonic jets [Schadow and Gutmark 1989]. Three-dimensional, irregular nozzle geometries that incorporate "teeth" [Wlezien and Kibens 1987, Longmire et al. 1992] and tabs [Samimy et al. 1993, Zaman et al. 1994] at the nozzle exit have been shown to create streamwise vortices which increase mixing. A representative illustration of a nozzle with teeth is shown in Figure 2.2 and a nozzle with delta tabs in Figure 2.3.

The present investigation examines helium injection from circular, elliptic, and circular-with-tabs nozzles, located at the base of an extended strut, into a Mach 1.92 freestream air flow. The circular nozzle was chosen as the baseline geometry. The elliptic nozzle was chosen to explore the effects related to an oblong geometry. The circular-with-tabs nozzle was chosen to examine effects of vortex generators mounted at the exit of a nozzle. The following two sections summarize earlier research involving elliptic and circular-with-tabs nozzles.

2.4.1 Elliptic Nozzles

The evolution of a jet issuing from an elliptic shape nozzle is significantly different than a jet issuing from a circular nozzle. The variation in azimuthal curvature of the elliptic vortical structures causes axis-switching and a three-dimensional entanglement process of elliptic vortex pairs.

A nonuniform variation in momentum thickness along the jet exit perimeter influences the vorticity in the roll-up structures and the subsequent joining of coherent structures. In contrast to the mechanisms of circular jets, where pairing occurs nearly uniformly around the entire perimeter of the vortical structures [Reynolds and Bouchard 1981], pairing in elliptic jets occurs only on the major-axis sides of the vortical structures, through an entanglement process [Husain and Hussain 1991]. The schematic in Figure 2.9 illustrates this entanglement process and also shows how the large separation of interacting vortices in the minor plane of elliptic jets hinders pairing; and that instead of

pairing, the trailing vortex rushes through the leading vortex and subsequently breaks down. This entanglement process causes greater stretching of interacting vortices, resulting in greater entropy production and vorticity diffusion than in a circular jet. The three-dimensional motion of the elliptical vortices produces considerably greater entrainment and mixing in elliptic jets than is found in circular or plane jets.

It is evident from Figure 2.9 that the jet cross section contracts in the direction of major axis and expands along the minor axis, so that after a certain distance downstream the two axes are interchanged. This phenomenon is referred to as axis-switching and occurs as follows: initially, when an elliptic vortex ring rolls up, the plane of the vortex ring is parallel to the nozzle exit plane. Because of their higher curvature, the major-axis sides move ahead of the minor-axis sides. In this process the vortex configuration soon takes on the shape of the seam of a tennis ball as illustrated in Figure 2.9 [Hussain and Husain 1989]. The forward inclination of the major-axis sides acts to fold the initial minor-axis sides. As a result, the induced velocity on the minor-axis sides, now directed outward based on curvature orientation, increases, and the minor-axis sides move outward. Consequently, the vortex again takes an elliptic shape; but now the major-axis of the vortex is in the plane of the minor-axis. The jet may repeatedly switch axes downstream, depending on the rate of vorticity diffusion. As the major-axis side shrinks, it brings in ambient fluid toward the jet centerline and, simultaneously, jet core fluid is carried outward on the minor-axis side. The elliptic structures thus act as a pumping device to entrain ambient fluid and eject core fluid.

Momentum thickness is believed to be the primary cause of axis-switching seen in noncircular jets, such as elliptic [Hussain and Husain 1989], rectangular [Krothapalli et al. 1981, Shih et al. 1992], and triangular jets [Gutmark et al. 1985, Koshigoe et al. 1989]. Koshigoe et al. [1989] compared the development of triangular and elliptic jets to demonstrate the influence of momentum thickness on the deformation of noncircular jets

that leads to axis-switching. The momentum thickness at the vertex in the developing region of a triangular jet core is typically larger than that at the flat sides, and in this situation, all of the calculated instability modes are concentrated on the flat sides. This is accompanied by the generation of large-scale coherent structures at the flat sides and turbulent, predominantly fine-scale eddies at the vertex. Numerical simulations have shown that in the case where a uniform azimuthal momentum thickness distribution evolves, one of the instability modes switches to the vertex, while the other remains at the flat side. This combination acts to deform the initially coherent structures of the jet by bending the vertex section in the streamwise direction (similar to the deformation of an elliptical jet described by Husain and Hussain [1991]). These computational results were verified experimentally using different triangular orifices to create jets with equal and unequal momentum thicknesses. The jet that evolved to have equal momentum thickness at the vertices and flat sides switched axes, while the other jet retained a larger momentum thickness at the vertex and did not switch axes.

The aspect ratio of oblong jets was discovered to influence physical characteristics of the jet evolution. Aspect ratio is defined as the ratio of the semimajor axis (a) to the semi-minor axis (b) dimension (i.e., a/b). By using elliptic sharp-edged slot nozzles, Lee and Baek [1993] found that the cross-over point and minimum jet half width were linear functions of nozzle aspect ratio. Hussain and Husain [1989] found that for aspect ratios above about 3.5, the jet undergoes one axis-switch and then bifurcates into two nearly circular vortices by a cut-and-connect interaction.

Downstream, the centerline mean velocity of jets issued from various nozzle shapes appear to be a function of the equivalent diameter. Hussain and Husain [1989] found that the equivalent diameter is the appropriate length scale to collapse the velocity data downstream for jets of various geometries. The equivalent diameter (d_e) is defined as the diameter of a circle with an area equal to that of an ellipse with semimajor and

semi-minor axes a and b respectively; i.e., $d_e = 2(ab)^{1/2}$. When they plotted the centerline mean velocity against the axial downstream distance, nondimensionalized by the equivalent diameter, the plotted data collapsed to form a single line beyond about 15 diameters downstream of the nozzle exit. This region downstream of the collapse is sometimes referred to as the "self-similar" region and its initiation is dependent on initial conditions. However, since the jets change drastically around the centerline, off-axis measurement must also be considered in order to obtain a complete picture of the jet development.

The preceding discussion involved results and conclusions from free jet experiments. Further information on subsonic jets emanating from elliptic nozzles into ambient air can be found in a series of in-depth studies of elliptic jets, including a comprehensive survey of previous research, published by Hussain and Husain [Hussain and Husain 1989, Husain and Hussain 1991 and 1993].

Studies by Schadow et al. [1989a] showed that the superior mixing characteristics of elliptic jets as compared to circular jets, discovered in previous works on subsonic free jets, prevails with sonic injection and are further augmented by the shock structures of the supersonic underexpanded free jet. They observed that the major and minor axes switched at a distance of three diameters from the exit of the elliptic, aspect ratio 3:1, nozzle for an underexpanded $M = 1.3$ free jet. This was much closer to the nozzle exit than the axis switch for the subsonic $M=0.15$ condition using the same elliptic nozzle. Furthermore, the spreading rate of the minor axis side for the underexpanded free jet was twice that of the subsonic free jet.

Studies of supersonic Mach 3 jet issuing from a 3:1 aspect ratio rectangular nozzle into a Mach 1.8 co-flowing stream, $0.5 < M_c < 2.2$ demonstrated superior spreading rate relative to a circular jet, but no axis-switch [Gutmark et al. 1991]. As with the co-flowing jets, injection from the base of a strut or ramp into a supersonic

freestream adds additional forces on the jet which alter axis-switching. Studies of Mach 1.63 injection from a slot injector, behind the base of a ramp injector, into a Mach 2 freestream air flow showed that the rectangular jet, switched axes at a distance of 0.75 ramp heights downstream of the exit of the injection nozzle [Haimovitch et al. 1994] when oriented in either the horizontal or vertical positions. The various responses of the axis-switching phenomenon to various external flow conditions warrants further research on the mechanisms involved.

2.4.2 Circular-with-tabs nozzles

A vortex generator configuration referred to as a delta tab (Figure 2.3), has been found to substantially increase jet mixing with a relatively small thrust penalty [Zaman 1994b]. An added attraction of these tabs is that they can be inserted into the flow when needed and withdrawn when not desired. A series of free jet studies has shown that flow structures generated by tabs mounted at the jet exit distort the downstream jet cross-section and increase the jet spread rate [Samimy et al. 1993, Reeder 1994, Reeder and Zaman 1994, and Zaman et al. 1994]. These studies have shown that tabs mounted at the exit of a nozzle of subsonic and supersonic free jets generate a pair of counter-rotating vortices which engulf ambient fluid. The generation of the vortices has been attributed to a pressure "hill" upstream of the tab and a lower pressure downstream of the tab. The strength of the pressure gradient was seen to increase with an increasing jet-to-freestream pressure ratio [Zaman et al. 1994].

Varying the tab shape, size, orientation, and location with respect to the nozzle exit and changing the number of tabs produces marked effects on the jet. Studies by Samimy et al. [1993] in a Mach 1.63 free air jet showed that it is necessary for the tab to protrude beyond the boundary-layer thickness in order to produce a significant distortion of the jet. However, variation of the length beyond the boundary-layer thickness, for a

given width, did not seem to have a noticeable effect. It was also found that with approximately the same flow blockage, the distortion was greater when the tab width was larger.

An experiment by Reeder and Zaman [1994] using simple peg shaped tabs showed that the location of the tabs relative to the nozzle exit in the streamwise direction dictates the sense of rotation of the vortices at the exit of the nozzle that propagate downstream. The distortion of a Mach 1.63 free air jet resulting from a cylindrical peg shaped tab mounted inside the nozzle exit, at the nozzle exit, and at the nozzle exit with a gap are shown in Figure 2.10. Placing the cylindrical tabs inside the jet just upstream of the nozzle exit causes a noticeable ejection of core fluid, whereas ambient fluid is ingested into the core when cylindrical tabs are placed at the nozzle exit. Furthermore, the influence of the tabs virtually vanishes when there is a gap between the nozzle exit and the tabs.

Although modifying the shape of the tip of a rectangular tab had an insignificant effect on the flow distortion, the overall shape of the tab does influence the strength of the vortices [Samimy et al. 1993]. Triangular "delta" tabs oriented with their apex extending into the jet flow downstream of the nozzle exit plane (pointed downstream), as shown in Figure 2.3, caused the strongest vortices of the tab configurations tested in the series of studies by Samimy, Reeder, and Zaman [Zaman et al. 1994]. Mounting the delta tabs with their apex pointed upstream of the nozzle exit plane causes another vortex pair with an opposite sense of rotation at the tip of each tab.

The number of tabs around the nozzle exit circumference dictates the resulting jet shape and mixing characteristics. Figure 2.11 shows the cross section of a Mach 1.63 free air jet with no tab and with from one to six tabs. Four delta tabs appear to cause the greatest mixing, perhaps because of an increase in the area of the mixing layer exposed to the ambient air, or because increased vortices and vortex breakdown result in increased

entrainment and jet spread. One notable effect of the presence of two tabs mounted at the nozzle exit of Mach 1.63 jet is that flow visualizations indicate the jet bifurcated and the jet distortion persisted further downstream than in the four tab configuration [Samimy et al. 1993].

To capture details of the dynamic involved in vortex generation about a tab, Reeder [1994] performed extensive subsonic water tunnel experiments. Detailed results for a nozzle with two delta tabs (oriented as in Figure 2.3) showed that besides the primary flow out of the nozzle in the streamwise direction, the tabs produce a nearly symmetric secondary flow away from the tabs (i.e., perpendicular to a line connecting the two tabs). Figures 2.12 and 2.13 show the streamwise and lateral components of velocity resulting from the subsonic water jet study. It is significant to note that the maximum lateral velocity of 0.020 m/s is nearly 13% of the streamwise velocity in the jet core of 0.16 m/s. Figure 2.14 shows the third component of velocity along the spanwise direction. Considering these three components of velocity it can be seen that the configuration with two delta tabs pumps jet fluid away from the axis of the tabs and pumps freestream fluid into the jet core along the tab axis, as is graphically illustrated in the schematic in Figure 2.15. In addition to the stronger vortices which cause the bifurcation of the water jet, the tabs generated two additional, weaker vortices just outside the stronger ones. The rotation and location of these secondary vortices are consistent with those of the legs of the "horseshoe" vortex which forms on a boundary layer with a protuberance as illustrated in Figure 2.16 [Reeder 1994]. Although these experiments were performed in a subsonic water tunnel, the results for tabs mounted at the nozzle exit were remarkably similar to those in supersonic free air jets. Furthermore, these water channel experiments offer a better forum for obtaining detailed data as compared to supersonic flow experiments.

Aside from the increased mixing achieved with tabs, another positive consequence of the use of tabs in supersonic jets is the reduction in screech noise that adds to the overall noise level of supersonic aircraft in flight today. The coupling of the shear layer instabilities and acoustic field adjacent to a supersonic jet create a screech tone which has been observed to closely match that of the most amplified instability wave of the jet [Tang and Ko 1993]. Tabs located at the exit of a supersonic jet drastically alter the near field shock structure and eliminate this screech noise.

2.5 Base flow

Since injection from a strut into a flow over the strut involves a more complex flow field than injection from a free single or coaxial jet, it is important to understand the flow patterns around the strut itself without injection. Figure 2.17 shows a schematic of supersonic streams flowing over a thick base. The primary flow components are: the initial two shear layers originating at the base of the strut, the recirculation zone, the expansion waves, and the recompression shocks.

Amatucci et al. [1992] characterized the flow in a thick plate wake through experimental studies of a two-stream, supersonic wake flow behind a 2.54 cm thick base plate. The flow was Mach 2.05 on one side of the plate and Mach 2.56 on the other side. Using schlieren photography, pressure measurements and one- and two-component LDV, they found the near-wake interaction flow field to be characterized by steep velocity gradients, high turbulence intensities, and viscous mixing in the presence of an adverse pressure gradient. The separated flow showed vigorous recirculation with a maximum reverse flow velocity equaling 23% of the Mach 2.05 freestream velocity and strong turbulent interactions with the edge of the shear layer bordering the recirculation zone. This is consistent with earlier results of Samimy and Addy [1986]. The vector representation of the velocity data of Amatucci et al. [1992] showed two large, counter-

rotating, separation bubbles. The two shear layers merged in the reattachment region at a distance of about 1.37 base heights downstream. Both streamwise and transverse turbulence intensities increase gradually from relatively low initial values in the boundary layer to maximum levels in the vicinity of reattachment and then decrease downstream. The turbulent mixing which occurs during recompression quickly reduces the mean velocity deficit. This is consistent with the results of Samimy and Addy [1986].

Dutton et al. [1995] collected detailed Mie images of a base flow around a 2.5 cm thick strut. The flow above the strut was Mach 2.5 and the flow below the strut was Mach 2.56. The images show the behavior and evolution of the large-scale turbulent structures inherent to supersonic base flows. Large-scale structures remain fairly consistent in size and shape during recompression, but appear to bloom immediately after the reattachment. Large sweeping motions into the wake were evident. Absence of condensed water downstream of reattachment point clearly indicates that the base fluid is being pumped into the wake flow. Observed dominant organized motions with smaller-scale structures residing on the larger-scale structures.

An early two-dimensional computational analysis of a 2.54 cm thick strut configuration with Mach 2.54 air streams on both sides was performed by Sullins et al. [1982]. This was the first detailed numerical calculation of a compressible, viscous base flow in such a configuration with and without gas injection. It clearly showed the recirculation flow behind the base of the strut, the expansion fan over the edge of the strut, and the recompression shock wave. The study suggested that the recirculation zone ended where the two shear layers merged, at approximately 1.5 base thicknesses downstream.

In addition to computations of flow around the strut, Sullins performed a two-dimensional computational analysis of air injection at sonic velocity from a slot injector at 10 times the static pressure of the freestream air flow. The expansion and shock wave

patterns were weakened considerably by the presence of a jet plume. The two mixing layers originating at the base of the strut were clearly displaced by the presence of the jet as compared to the flow without injection. The results show that the plume acts as an "effective body" that masks the base from the main flow.

A recent three-dimensional computational simulation performed by Chen et al. [1995] portrays a three-dimensional flow field created by injection from the base of a strut using a circular nozzle. These computations involved an intricate three-dimensional grid as compared to the two-dimensional grid used by Sullins. Figure 2.18 shows the Mach number profiles computed for an underexpanded circular jet with static pressure ratio of 4. This plot shows the rapid expansion of the jet exiting the nozzle to reach supersonic velocities.

Contribution of the present study

Free jet studies have shown the effect of nozzle geometry on jet development, shape, and mixing enhancement. However, the effect of nozzle geometry on parallel injection into a supersonic freestream with practical aspects of a recirculation zone has seen limited consideration. To date, there has been to date only one study of the effects of nozzle geometry on injection into a base flow. This study by Haimovitch et al. [1994] examined a swept ramp injector with a circular, stepped circular, elliptic, trapezoidal slot, circular, and circular with four tabs nozzle. Ethanol vapor was used for planar Mie scattering flow visualization. The jet appeared to be dominated by the strong vortical flow field generated by the swept ramp.

The extended strut used in the present experiment replaces the three-dimensional expansion around the base of the swept ramp with a simpler symmetric, two-dimensional expansion around the base of a strut. In addition, the extended strut avoids the leading edge or ramp induced shock waves incurred in bluff body struts and ramp injectors. Thus, the present experimental program was designed as a more generic study of parallel

injection into a supersonic base flow. This will isolate the effects of nozzle geometry from asymmetric effects and shock induced mixing incurred during injection from a ramp. Furthermore, the symmetry of the strut configuration allows the strut to be divided into four equal quadrants about the center of the jet, thus greatly simplifying computational studies.

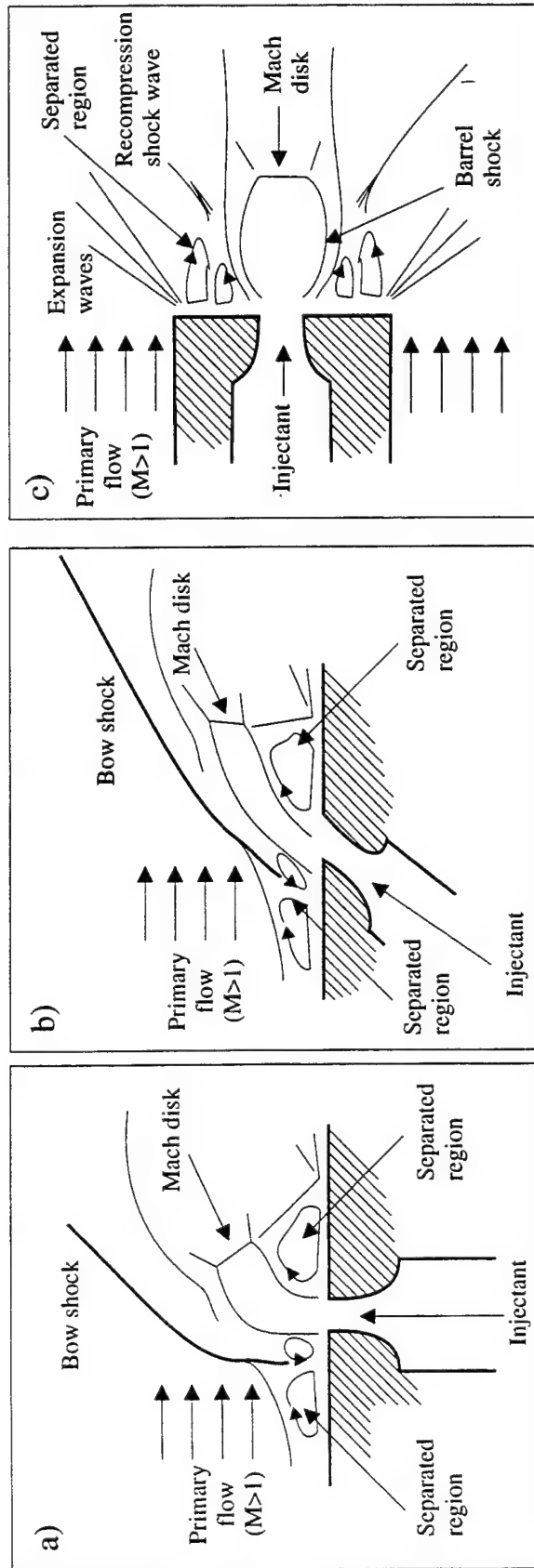


Figure 2.1. Illustration of: a) normal, b) oblique, and c) parallel injection of an underexpanded jet into a supersonic primary flow.

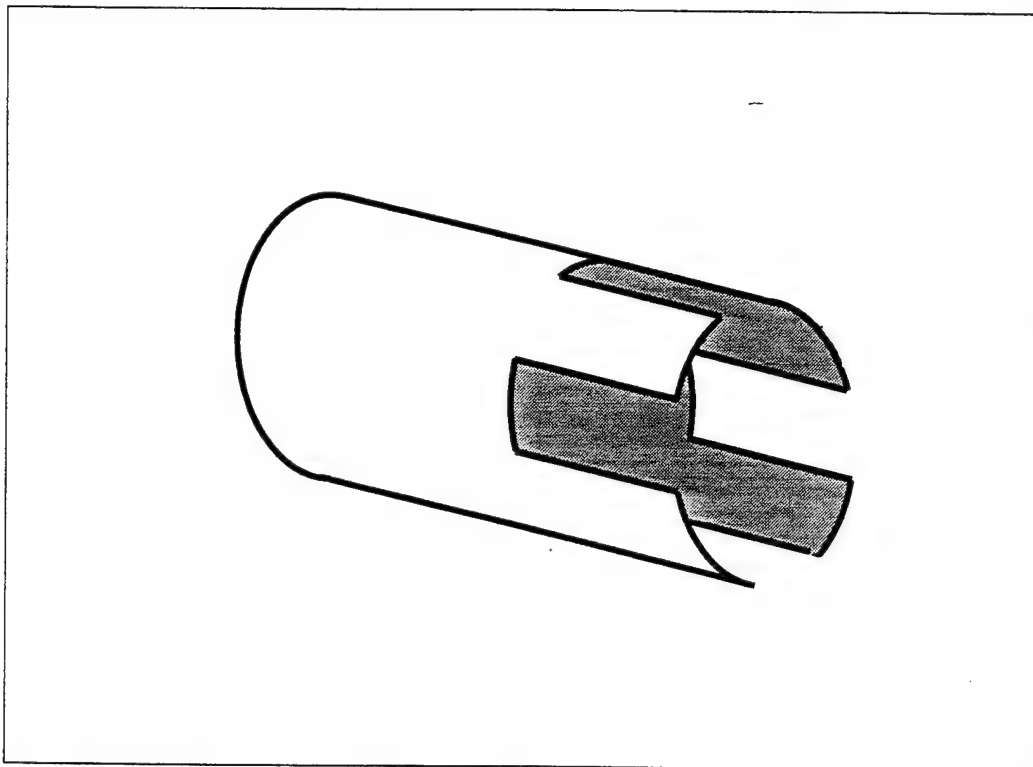


Figure 2.2. Crown nozzle with four teeth.

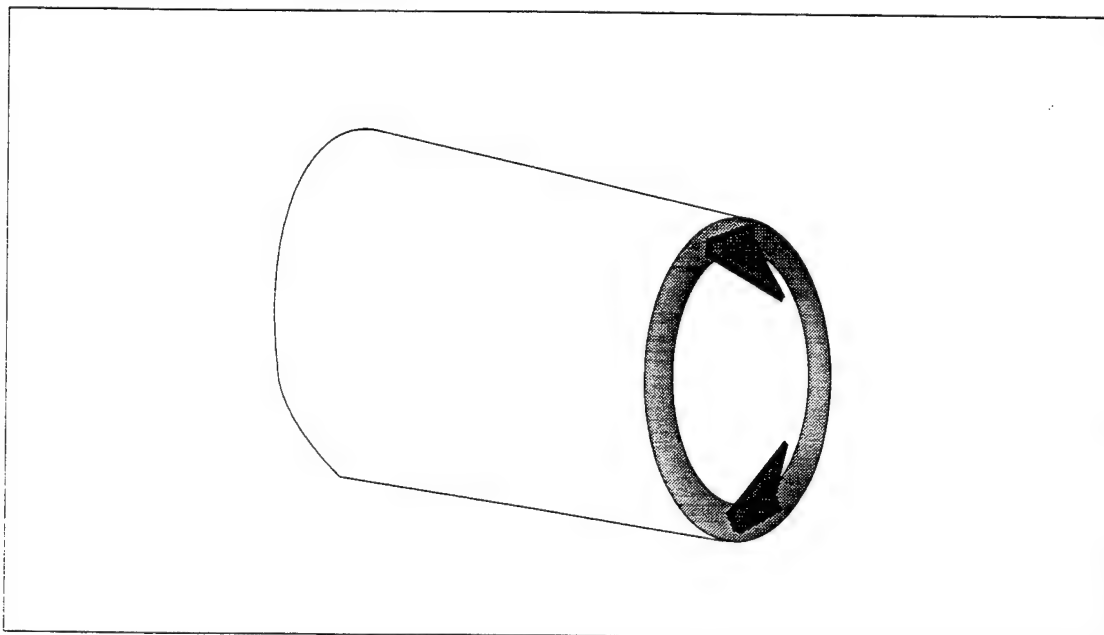


Figure 2.3. Circular nozzle with two delta tabs oriented at a 135° angle to nozzle wall.

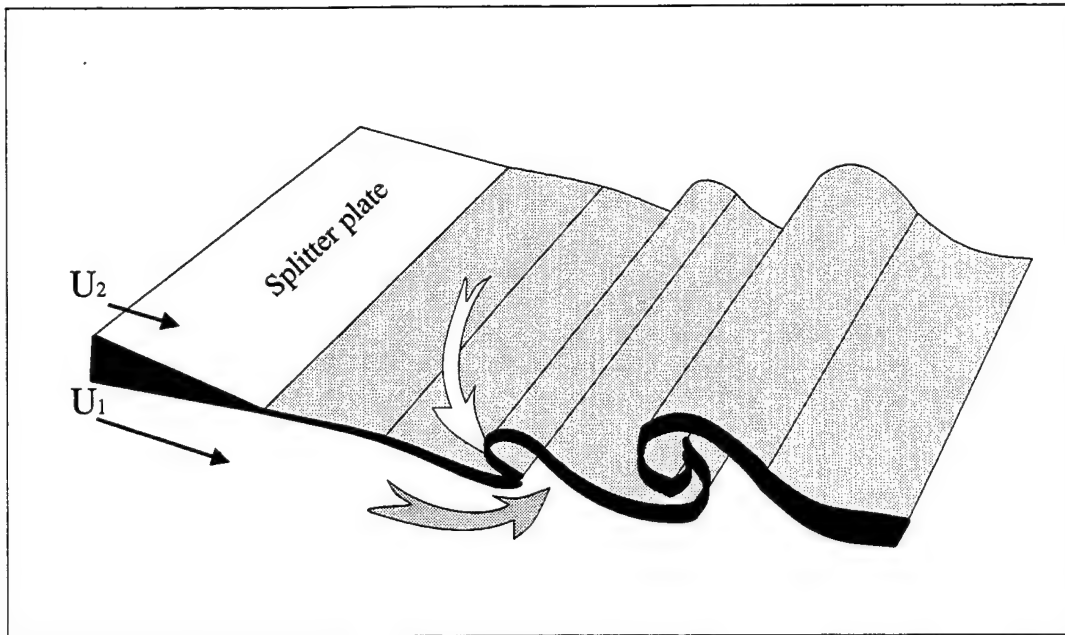


Figure 2.4. Simplified schematic of large spanwise (Kelvin-Helmholtz type) "roll-up" structures in an incompressible planar shear layer.



Figure 2.5. Laser-induced fluorescence (Y, Z) cross-section through the braid region of an incompressible planar mixing layer. The entire channel span of 11 cm is shown (from Bernal and Roshko [1986]).

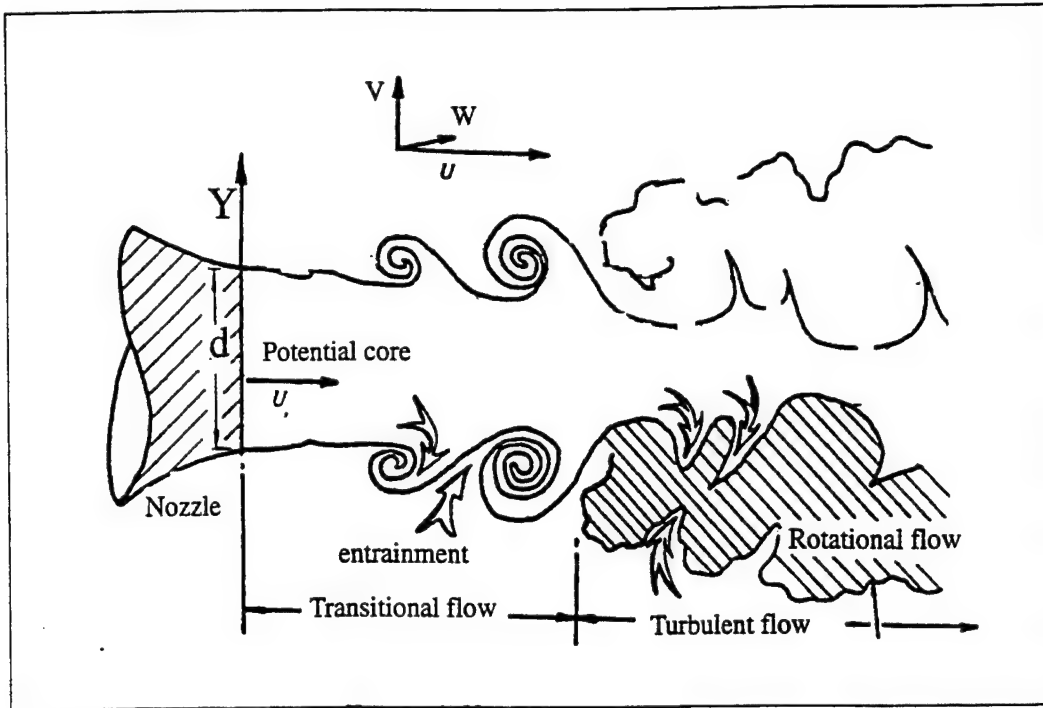


Figure 2.6. Schematic of the physical structure of a transitional incompressible axisymmetric jet (from Yule [1978]).

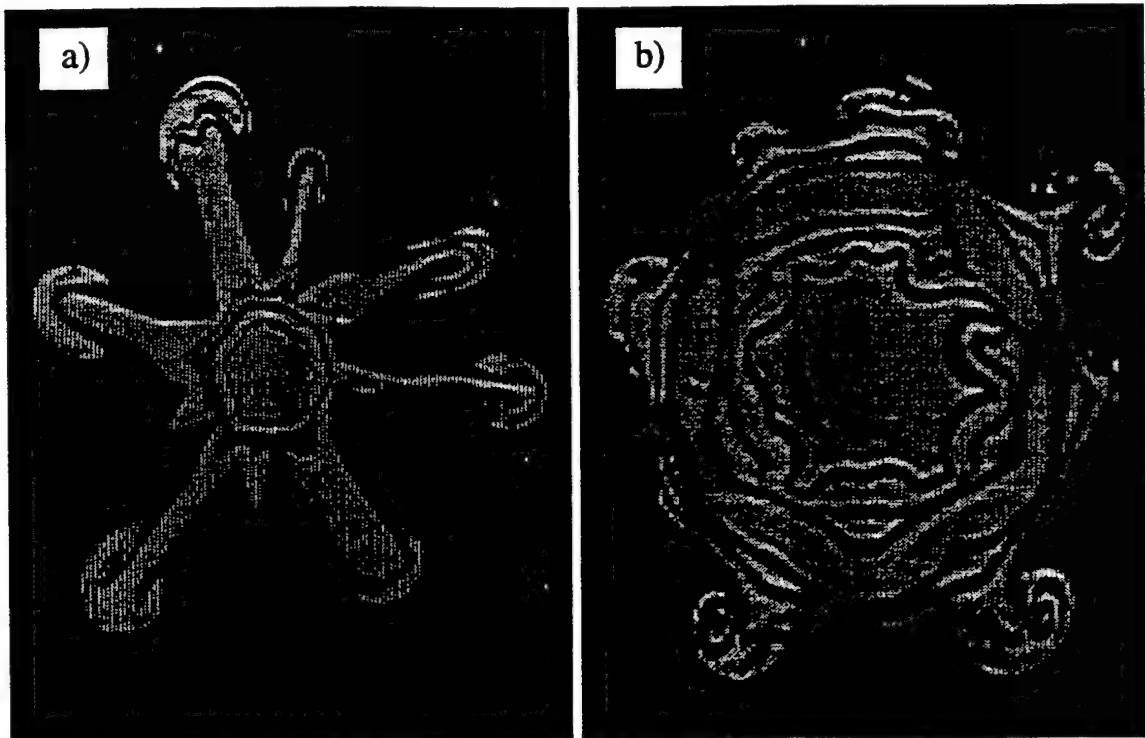


Figure 2.7. Cross-sectional view (Y, Z) at $X/d=3.25$ of a low Reynolds number ($Re=5500$) circular free jet showing: a) the braid region and b) the primary vortical ring surrounded by streamwise vortex pairs as they pass through the image plane (from Liepmann [1991]).

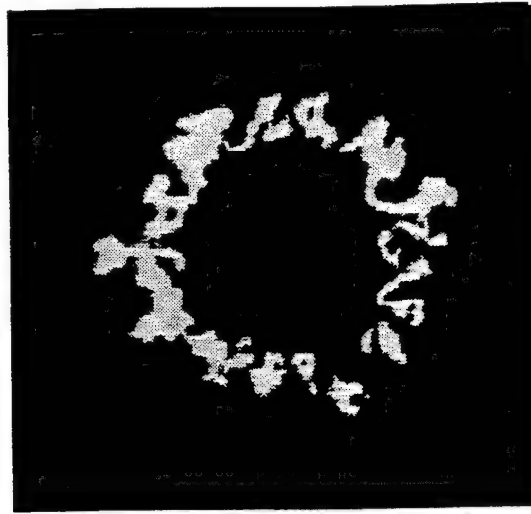


Figure 2.8. Filtered Rayleigh/Mie scattering image at $X/d=2.0$ of an underexpanded free jet (from Arnette et al. [1992]).

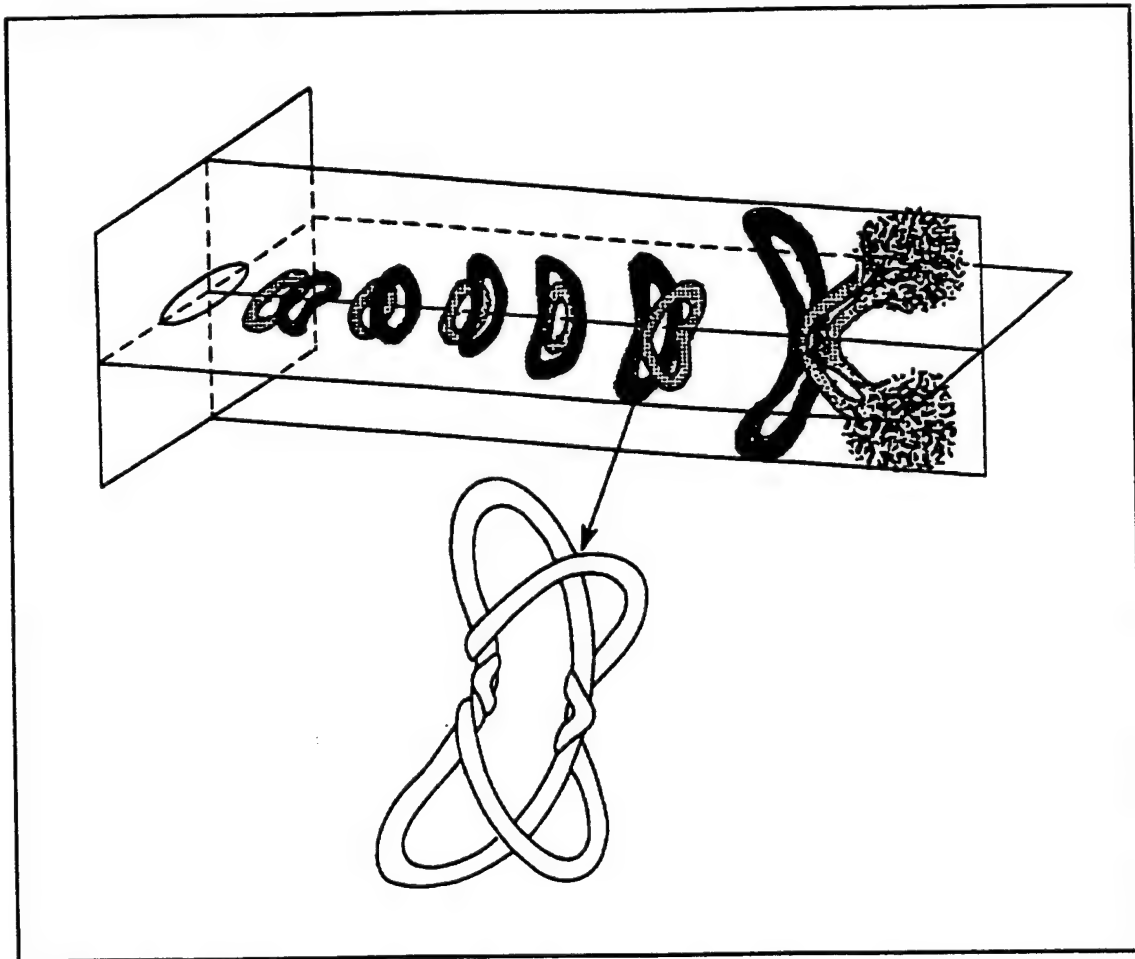


Figure 2.9. Illustration of axis-switching and vortex evolution process for an incompressible low Reynolds number jet emanating from an elliptic nozzle (from Husain and Hussain [1991]).

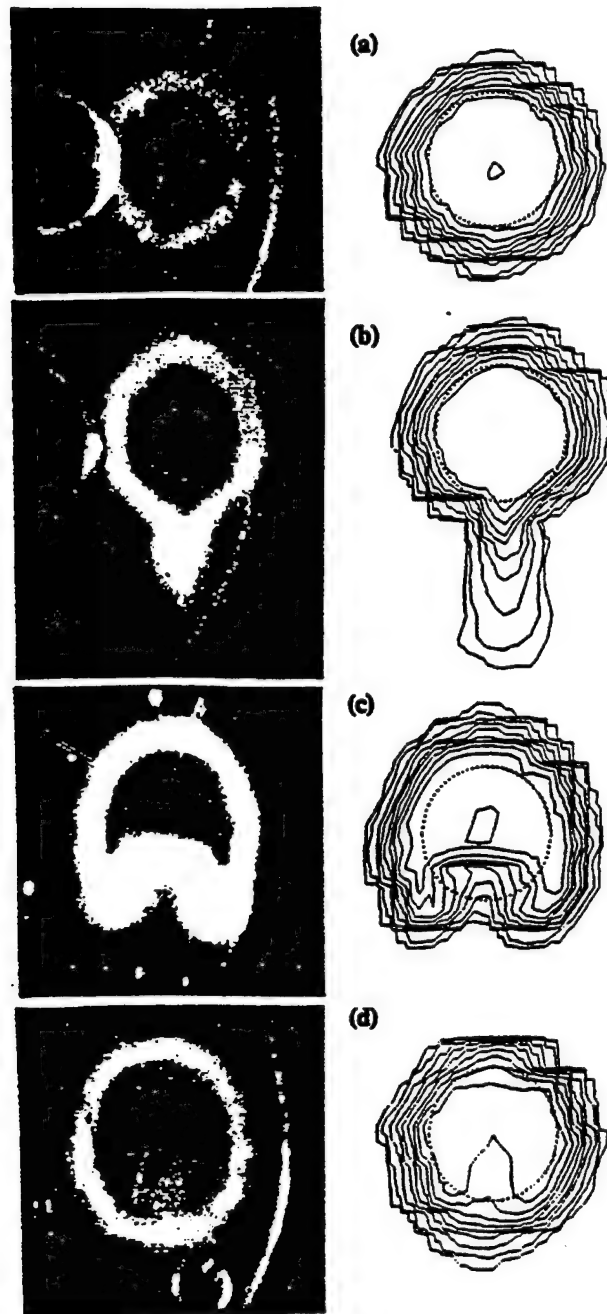


Figure 2.10. The effect of tab location for a Mach 1.63 air free jet is shown by flow visualization (left) and pressure contours (right) for: a) no tab, and b) tab at $X/q = -1.5$, c) tab at $X/q = 0.5$, and d) tab at $X/q = 1.5$. Data for $X/d = 2$, where q is the cylindrical tab diameter (from Reeder et al. [Copyright © 1994 AIAA - reprinted with permission]).

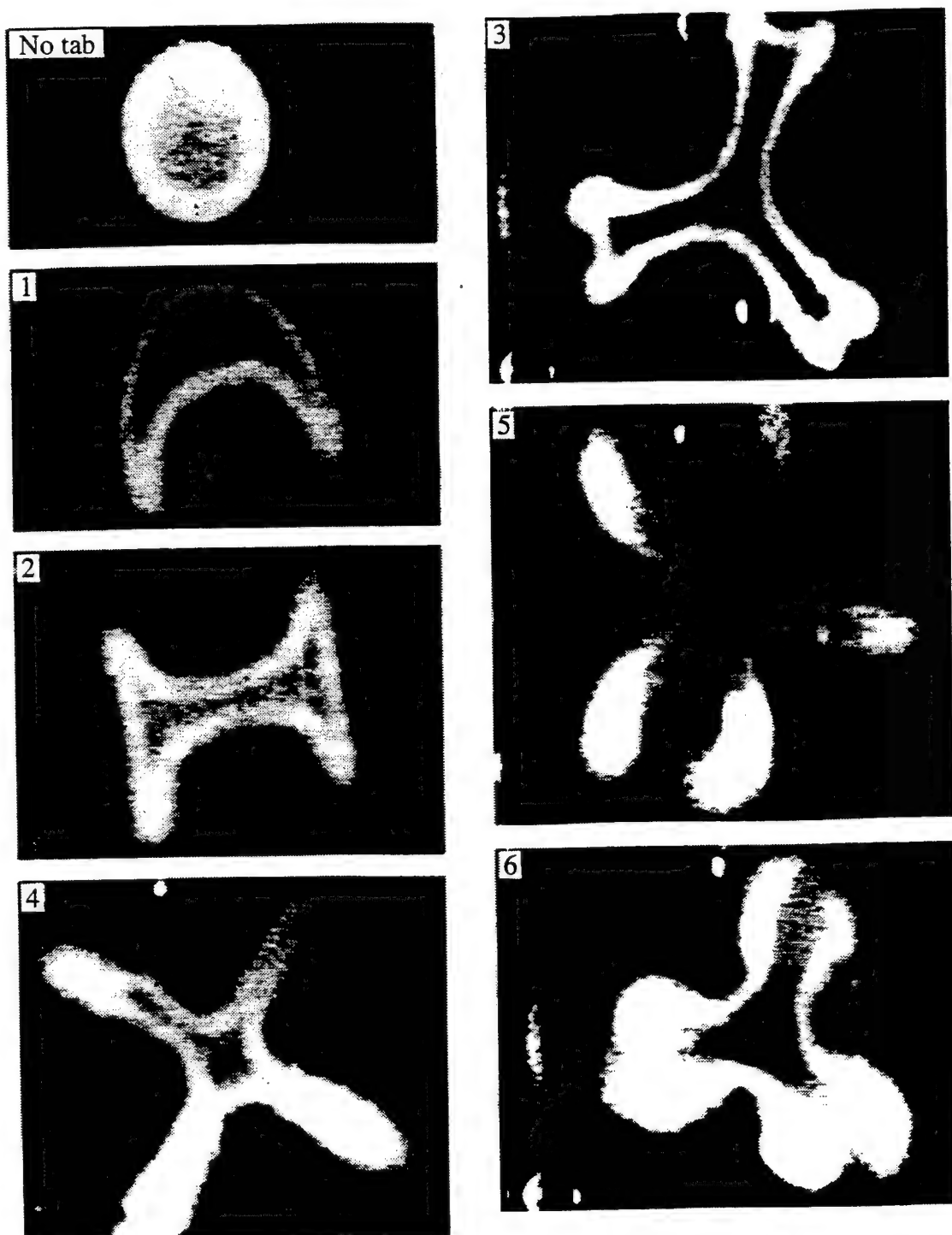


Figure 2.11. Laser sheet illuminated cross section of a Mach 1.63 air free jet at $X/d=2$ for the indicated number of tabs (from Zaman et al. [1994]).

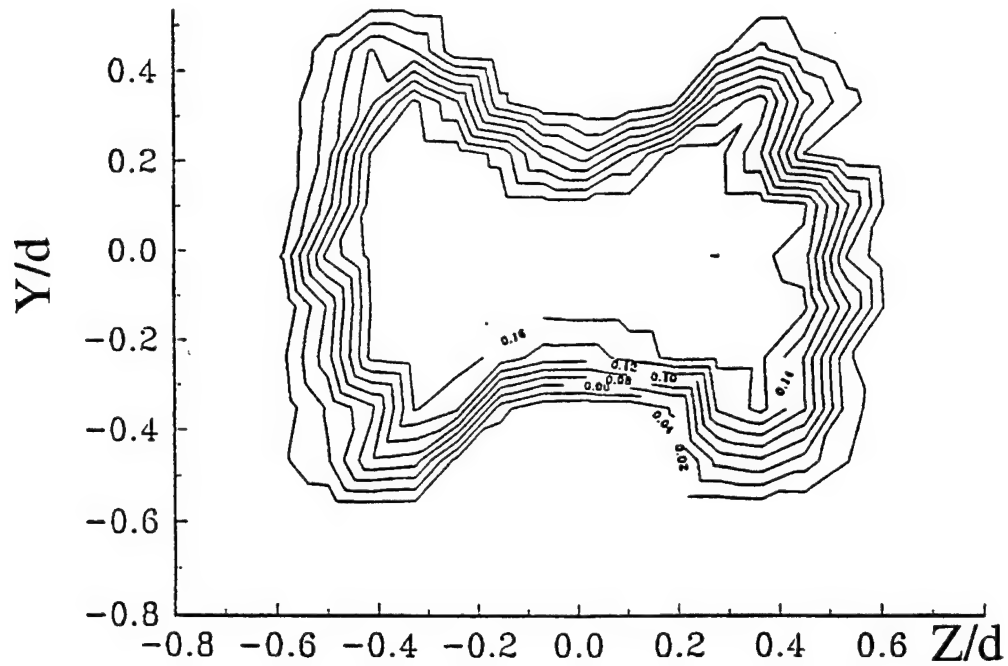


Figure 2.12. Streamwise (U) velocity contours (in m/s) taken at $X/d=0.5$ for an incompressible jet ($Re=1950$) with two delta tabs positioned on the Y -axis (at $Z/d=0$) (from Reeder [1994]).

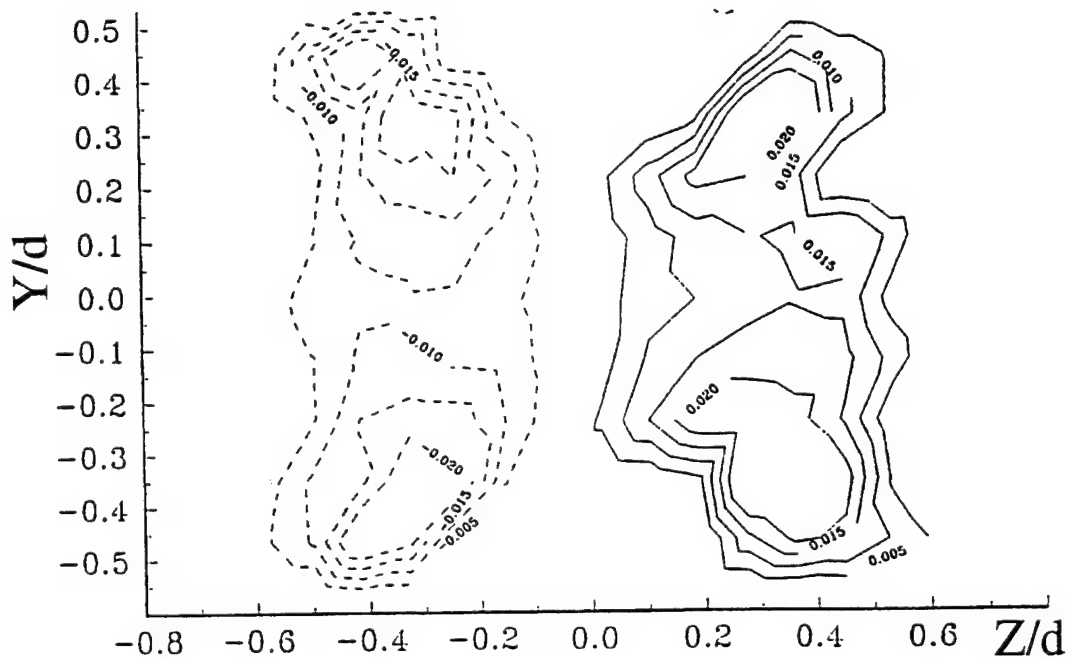


Figure 2.13. Spanwise (W) velocity countours (in m/s) at $X/d=0.5$ for the incompressible jet ($Re=1950$) with two delta tabs positioned on the Y -axis (at $Z/d=0$) (from Reeder [1994]).

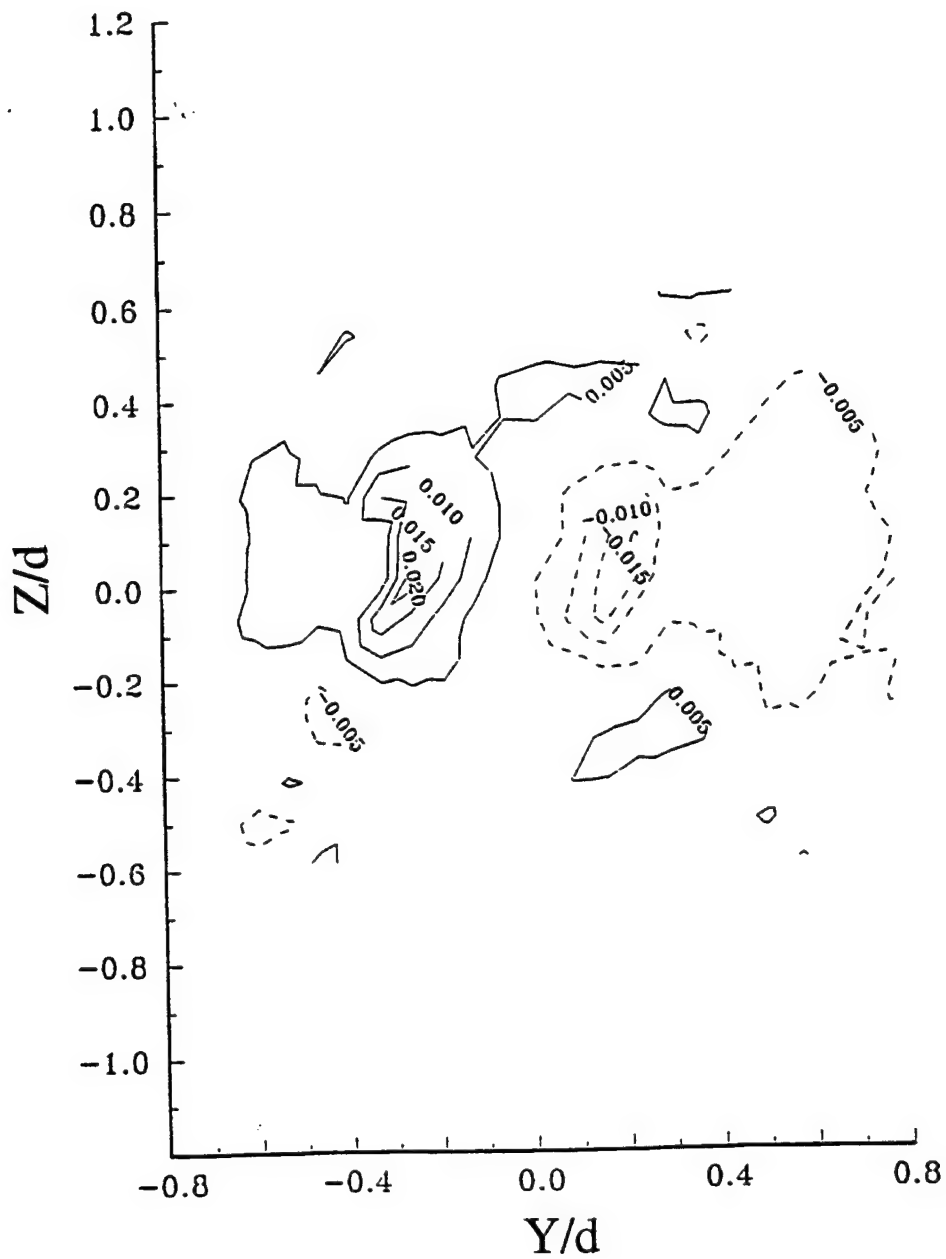


Figure 2.14. Transverse (V) velocity contours (in m/s) at $X/d=0.5$ for the incompressible jet ($Re=1950$) with two delta tabs positioned on the Y -axis (at $Z/d=0$) (from Reeder [1994]).

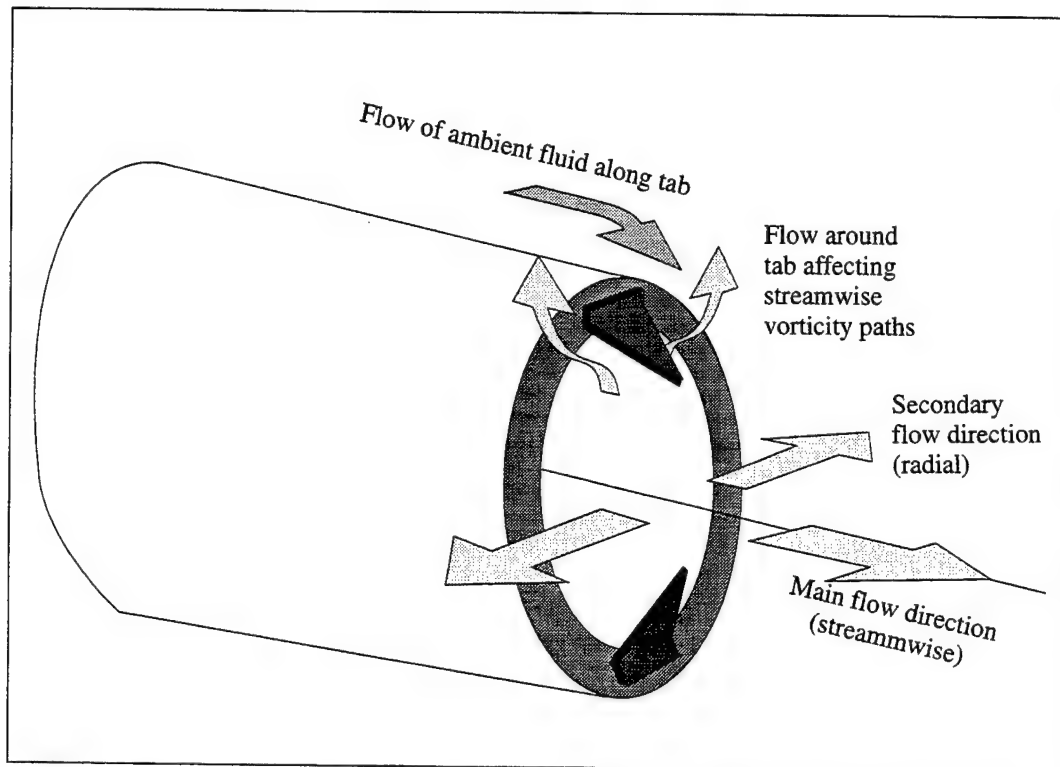


Figure 2.15. Illustration of primary and secondary flow patterns of fluid emanating from a circular nozzle with two delta tabs oriented at 135° to the nozzle wall.

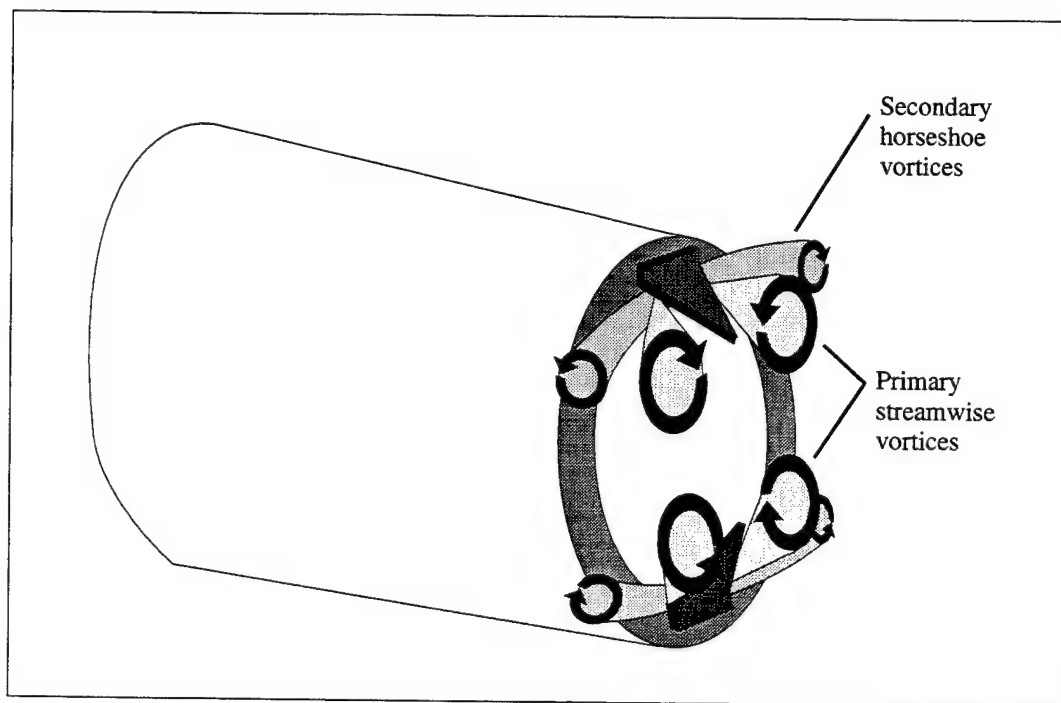


Figure 2.16. Illustration of primary counter rotation vortices and secondary horseshoe vortices for flow around a delta tab oriented at a 135° angle to the nozzle wall.

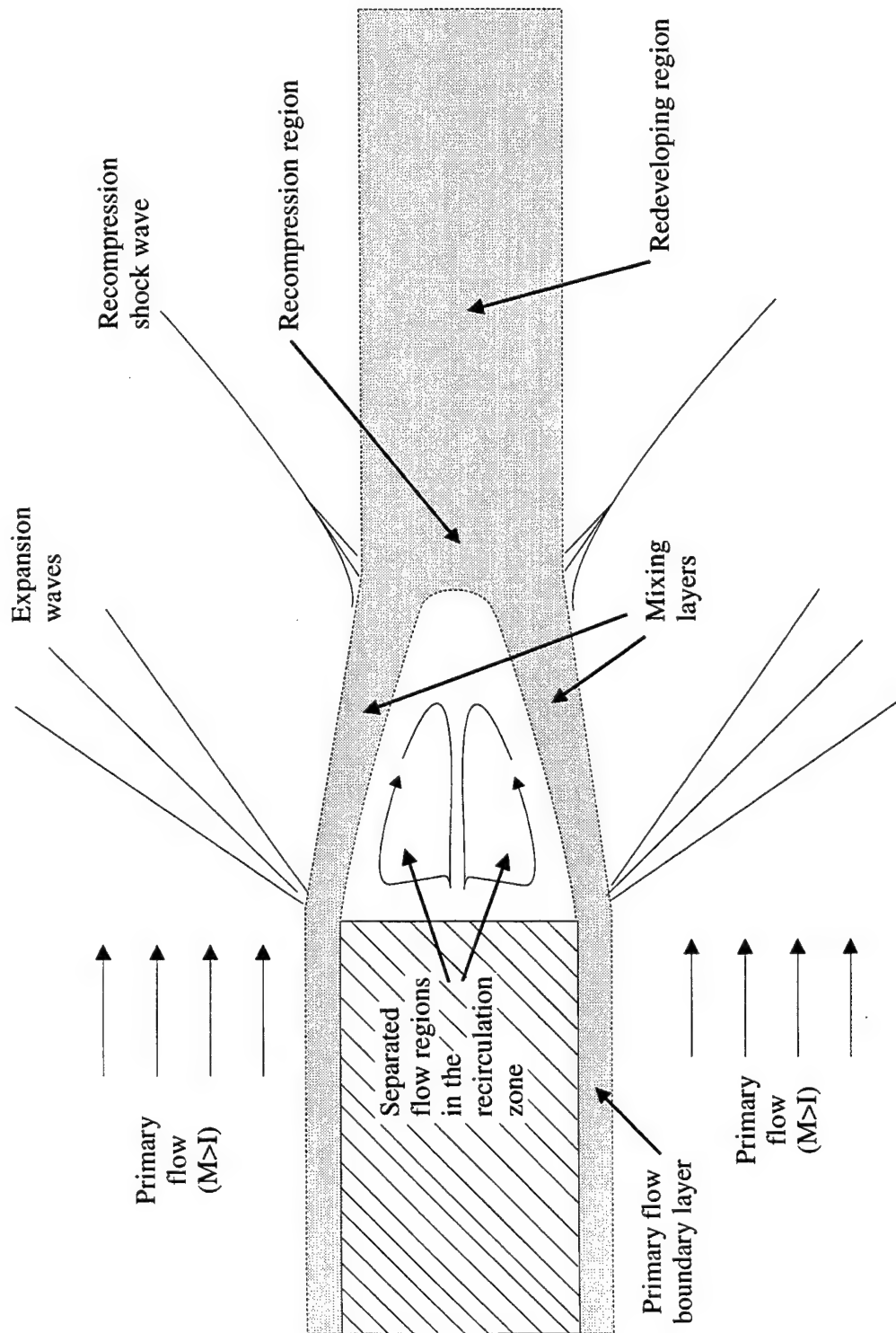


Figure 2.17. Schematic of two-dimensional base flow with equal supersonic primary flows on both sides of the strut.

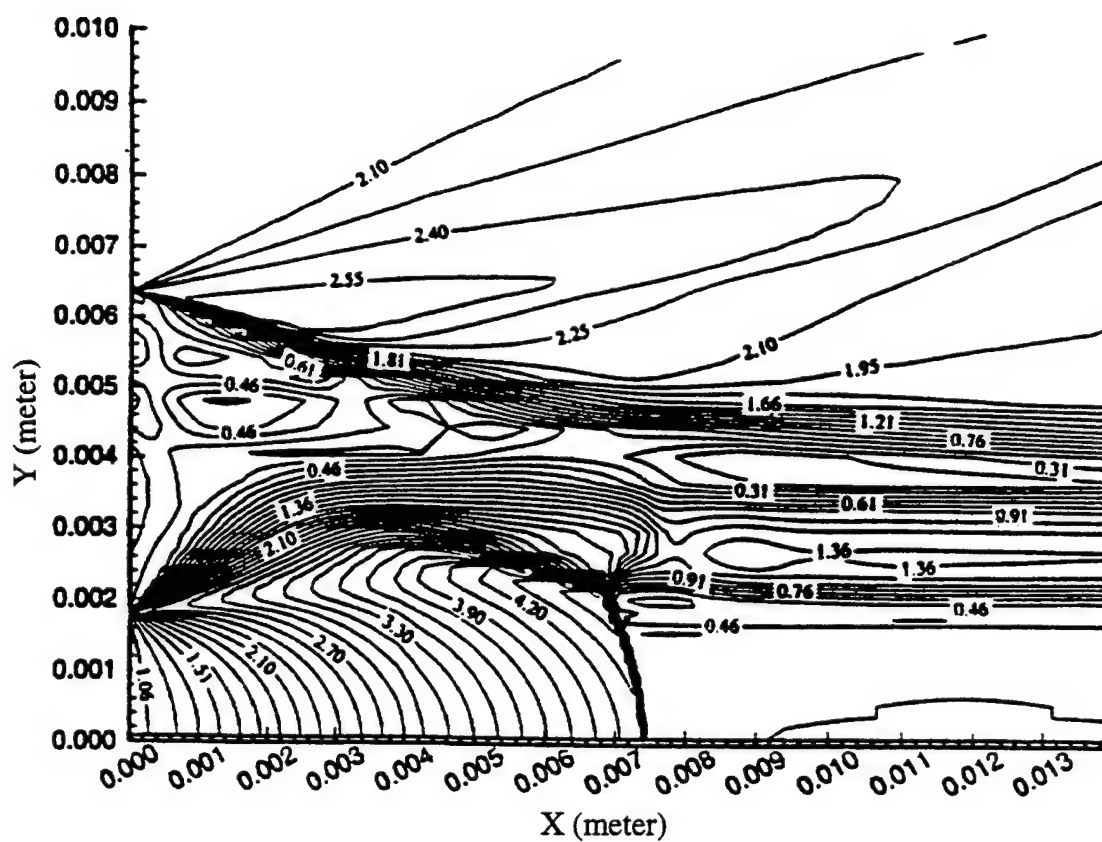


Figure 2.18. Three-dimensional simulated Mach contours for an underexpanded ($\Psi=4$) sonic circular helium jet (from Chen et al. [Copyright © 1995 AIAA - Reprinted with permission]).

CHAPTER 3

FACILITY AND EXPERIMENTAL APPARATUS

The present research was conducted in the supersonic combustion research facility at the Aero Propulsion and Power Directorate, Wright-Patterson Air Force Base, Dayton, Ohio. Various turbine and reciprocating compressors are available to produce a continuous flow of approximately 15.5 kg/s of clean, compressed air at a maximum supply pressure of 5 MPa to the wind tunnel. Half of this air can be heated to a maximum stagnation temperature of 920 K using a gas-fired heat exchanger. Two supply lines, one suited for high temperatures and one for ambient temperatures, transport the air to the wind tunnel supply manifold in the test cell. The test section temperature and pressure conditions are adjusted by mixing air from the hot and cold supply lines in controlled quantities.

The five major components that comprise the supersonic tunnel are the inlet section, the settling chamber, the nozzle section, the test section, and the diffuser (Figure 3.1). The inlet section transports air from the supply manifold to the settling chamber. A seed injection port on the inlet section provides a convenient means for the addition of seed media for laser sheet lighting diagnostics, such as Mie scattering, and other laser based measurement systems, such as Laser Doppler Velocimetry (LDV). Since injection of seed media from this port occurs upstream of the settling chamber, the entire primary flow is seeded uniformly. Finally, the expansion section of the inlet houses a rearward-facing perforated cone to provide a means of distributing the flow as it enters the settling chamber.

The settling chamber conditions the air using an array of three mesh screens, one coarse (30 x 30 x 0.05 cm) and two fine (51 x 51 x 0.03 cm), and a section of honeycomb (0.64 cm cell size) to break up large-scale turbulence and straighten the flow before acceleration by the supersonic nozzle. This chamber withstands pressures up to 2.75 MPa at temperatures of 920 K. Pressure and temperature sensors installed in the chamber provide stagnation temperature and pressure measurements to the control system for regulation and documentation of the flow conditions. The entire chamber is mounted on a support stand (fixed at the downstream end, rolling at the upstream end) which supports the weight of the chamber and the force experienced due to the subatmospheric pressure of the exhaust system.

The nozzle section is composed of two identical planar two-dimensional nozzles; one on either side of the strut. The nozzles were designed using a method of characteristics code developed by Carroll, et al. [1986] to produce the desired expansion to a nominal Mach number of 2.0 on either side of the strut at the entrance to the test section.

The constant area test section, 15.2 cm-wide by 13.1 cm-high, is depicted in Figure 3.2. A pair of fused silica windows mounted in the side walls and a single fused silica window mounted in the top wall provide the desired optical access. The side windows allow direct viewing of the entire transverse dimension of the test section and approximately 44 cm in the streamwise dimension. The top window provides the same access length in the streamwise dimension with approximately 7 cm along the spanwise dimension. Because each window can be mounted in two locations, one upstream and one downstream, a total viewing length of 79 cm is obtainable in the streamwise dimension. A fourth fused silica window, mounted in the diffuser section of the facility, provides direct optical access to the plane perpendicular to the flow direction and allows for visualization the entire span of the tunnel (see Figure 3.1).

For the present experimental program, A 1.27-cm-thick strut (held in place by grooves in the tunnel side walls) provided rigid support for the nozzles and had the added benefit of producing a recirculation zone for flame holding in combustion applications. The strut is held in the tunnel by grooves in the tunnel side walls. The 94 cm long strut extended 7 cm into the settling chamber and downstream a distance of approximately 7 cm into the test section. This strut is similar to a typical splitter plate used in shear layer studies [Bogdanoff 1983, Papamoschou and Roshko 1988, Elliott and Samimy 1990], with the following exceptions: the flow velocity is identical on both sides of the strut and the base of the strut is blunt rather than tapered to a knife edge. By extending the strut upstream through the nozzle into the settling chamber, as shown in Figure 3.2, and using the method of characteristics to design the nominal Mach 2 nozzles, the presence of strong waves in the freestream was avoided. Laser Doppler velocimetry profiles show very symmetric and uniform flow on each side of the strut. The mean velocity and turbulence profiles in the freestream show a repeatable Mach 1.92 flow with turbulence intensities less than 1%.

The injection nozzles were rigidly mounted in the base of the strut at the center-line of the wind tunnel and held in place with a retaining plate. The modular design of the interchangeable nozzles and retaining plate allows quick changeover of the different nozzles and nozzle orientations. A straight flow section of over 24 nozzle equivalent exit diameters preceded the nozzles to insure uniform flow at the nozzle exit. Figure 3.3 shows the retaining plate, the circular nozzle, and the connected extension tube. On each side of the nozzle are counter sunk bolt holes for mounting the base plate and nozzle assembly securely to the strut.

A special piping system was constructed to supply the injectors with helium gas. A series of high pressure regulators controlled the flow of helium to the test section. Tube trailers containing large volumes of high pressure (14 MPa) helium were available

outside the test cell. The helium entered the test section through a port in the side wall of the tunnel, after which it was fed into a channel in the strut leading to the nozzle port. A photograph of the nozzle and test section with the side wall removed is shown in Figure 3.4.

The final component of the downstream supersonic research facility is the diffuser. This device connects the exit of the test section to the exhaust line of the facility. The simple-dump diffuser was designed to slow and cool the incoming airflow to the velocities and temperatures required by the air coolers of the air supply facility. Further details of the supersonic combustion facility are available in other publications [Gruber and Nejad 1994].

Injection from circular, circular-with-tabs, and elliptic nozzles was investigated in this study. Photographs of the nozzle tips are shown in Figure 3.5. The circular nozzle was chosen as the reference nozzle for comparison. The elliptic nozzle was chosen as a sample of a simple asymmetric nozzle geometry known to increase mixing [Hussain and Husain 1989]. The elliptic shape was chosen over other simple geometries, such as triangular or rectangular, because the elliptic geometry is rounded; corners at the nozzle exit induce vortices and produce a more complex flow [Gutmark et al. 1985, Schadow et al. 1988]. In addition, the elliptic jet represents oblong nozzles, which undergo distinct axis-switching, a mechanism shown to be a key factor in increased mixing as compared to circular jets [Hussain and Husain 1989]. The circular-with-tabs nozzle was chosen because of its recognized mixing enhancement capability [Zaman et al. 1994, Samimy et al. 1993, Reeder 1994]. In addition, similar nozzle geometries (a vertical slot injector and a nozzle with vortex generators) were considered to be the most promising candidates for future research in studies of injection through different nozzle geometries from the base of a swept ramp injector [Haimovitch et al. 1994].

The diameter of the circular and circular-with-tabs nozzles was 3.5 mm. The circular-with-tabs nozzle includes two tabs located on opposite sides of the nozzle exit circumference. Details of the tab geometry are shown in Figure 3.6. The tab width was 0.86 mm, 22% of the nozzle exit diameter. The tabs extended into the flow a projected length of 0.38 mm, 11% of the nozzle exit diameter. Ideally, the tabs would be infinitely thin in order to maximize the vortex-inducing pressure gradient across them. A delta tab is the optimal shape [Zaman et al. 1994]. However, machining and strength limitations require thicker tabs, with a square shape. The tabs were angled downstream into the jet flow (i.e., with an angle of 135° from the nozzle wall). This tab configuration has been shown to have the greatest mixing effect [Reeder and Zaman 1994].

The elliptic nozzle had a semimajor diameter of 6.15 mm and a semi-minor diameter 2.05 mm, resulting in an equivalent diameter of 3.5 mm and an aspect ratio of 3:1. The 3:1 aspect ratio was chosen as a substantial intermediate value as compared to previous research by other groups [Ho and Gutmark 1987, Hussain and Husain 1989, Quinn 1989, Lee and Baek 1993].

All three nozzles were machined by Electric Discharge Machining, or EDM, to converge to a minimum cross-sectional area of 9.9 mm^2 at the nozzle exit. A cubic curve fit was used to generate the internal contour of the circular and circular-with-tabs nozzles. The prohibitive cost of fabricating a cubic curve fit for the inside contour of the elliptic nozzle dictated that instead, wire EDM be used to generate a constant taper for the inside contour. A small straight length, 0.8 mm, at the exit of the all three nozzles helps to assure that the flow exits the nozzle parallel to the nozzle axis. Table 3.1 lists the dimensions of the injector nozzles used in the present study.

The elliptic and circular-with-tabs nozzles were rotated to test different orientations with respect to the base of the extended strut (see Figure 3.2 for the reference coordinate system). The nozzles with the orientations shown in Figure 3.7 will be hereafter referred

to by the following symbols: C for circular nozzle, T1 for circular-with-tabs nozzle oriented with the tabs along the transverse (Y) axis, T2 for circular-with-tabs nozzle oriented with the tabs rotated counterclockwise to a negative 45° angle with respect to the transverse (Y) axis, T3 for the circular-with-tabs nozzle oriented with the tabs along the spanwise (Z) axis, E1 for the elliptic nozzle oriented with its major axis along the transverse (Y) axis, E2 for the elliptic nozzle oriented with the major axis rotated counterclockwise to a negative 45° angle with respect to the transverse (Y) axis, and E3 for the elliptic nozzle oriented with its major axis along the spanwise (Z) axis. N represents the baseline flow without injection. Nozzle icons representing the different nozzle orientations and no injection case are placed alongside the flow visualization images for clarity.

Helium, was used as the injectant to simulate hydrogen fuel. The helium mass flow rate was varied so that the ratio of the static pressure of the helium jet at the nozzle exit to the static pressure of the freestream air was approximately $\Psi = P_{\text{nozzle}} / P_{\text{freestream}} = 1, 2, \text{ and } 4$. Injectant velocity at the exit of the converging nozzles was sonic in all cases. A pressure transducer mounted in the helium piping just outside the tunnel wall recorded the instantaneous stagnation pressure. The stagnation temperature was equal ambient temperature. The static pressure of the helium jet at the exit of the nozzle was calculated from the stagnation pressure and temperature, assuming isentropic flow between the helium pressure transducer and the nozzle exit. Likewise, the static pressure of the freestream air was computed from stagnation pressure and temperature measured in the settling chamber of the tunnel. The resulting operating conditions are listed in Table 3.2 and the associated calculations are contained in Appendices A and B.

The $\Psi = 4$ static pressure ratio was chosen to obtain a highly underexpanded jet. The $\Psi = 4$ case was the focus of this study because they most accurately mimic the most likely operational fuel injection conditions in scramjet propulsion systems.

The following chapter describes the various diagnostic tools and experimental methods that were used in the present experimental study of parallel injection from an extended strut in a supersonic freestream flow.

Table 1. Nozzle Dimensions.

<u>Circular nozzle</u> exit diameter $d_e = 3.55$ mm exit area = 9.9 mm^2
<u>Circular-with-tabs nozzle</u> exit diameter $d_e = 3.55$ mm exit area = 9.9 mm^2 tab width = 0.86 mm tab length projected into jet flow = 0.38 mm area of tab projected into jet flow = 0.33 mm^2 ratio of projected tab area to nozzle exit area = 3%
<u>Elliptic nozzle</u> equivalent diameter $d_e = 3.55$ mm exit major diameter = 6.15 mm exit minor diameter = 2.05 mm exit area = 9.9 mm^2

Table 2. Operating conditions for helium injection into Mach 1.92 air freestream.

	Po	To	M	P_∞ (P_e)	T_∞ (T_e)	ρ_∞ (ρ_e)	U_∞ (U_e)	\ddot{P}_∞ (\ddot{P}_e)
	KPa	K		KPa	K	kg/m ³	m/s	kg·m ² /s ²
Freestream	345	300	1.92	50	172	1.01	506	1.29×10^5
Helium ($\Psi = 1$)	97	300	1	47	225	0.10	871	0.39×10^5
Helium ($\Psi = 2$)	207	300	1	101	225	0.22	871	0.86×10^5
Helium ($\Psi = 4$)	414	300	1	201	225	0.44	871	1.72×10^5

* See Appendices A and B for calculations.

** Subscript " ∞ " indicates freestream and subscript "e" indicates nozzle exit value.

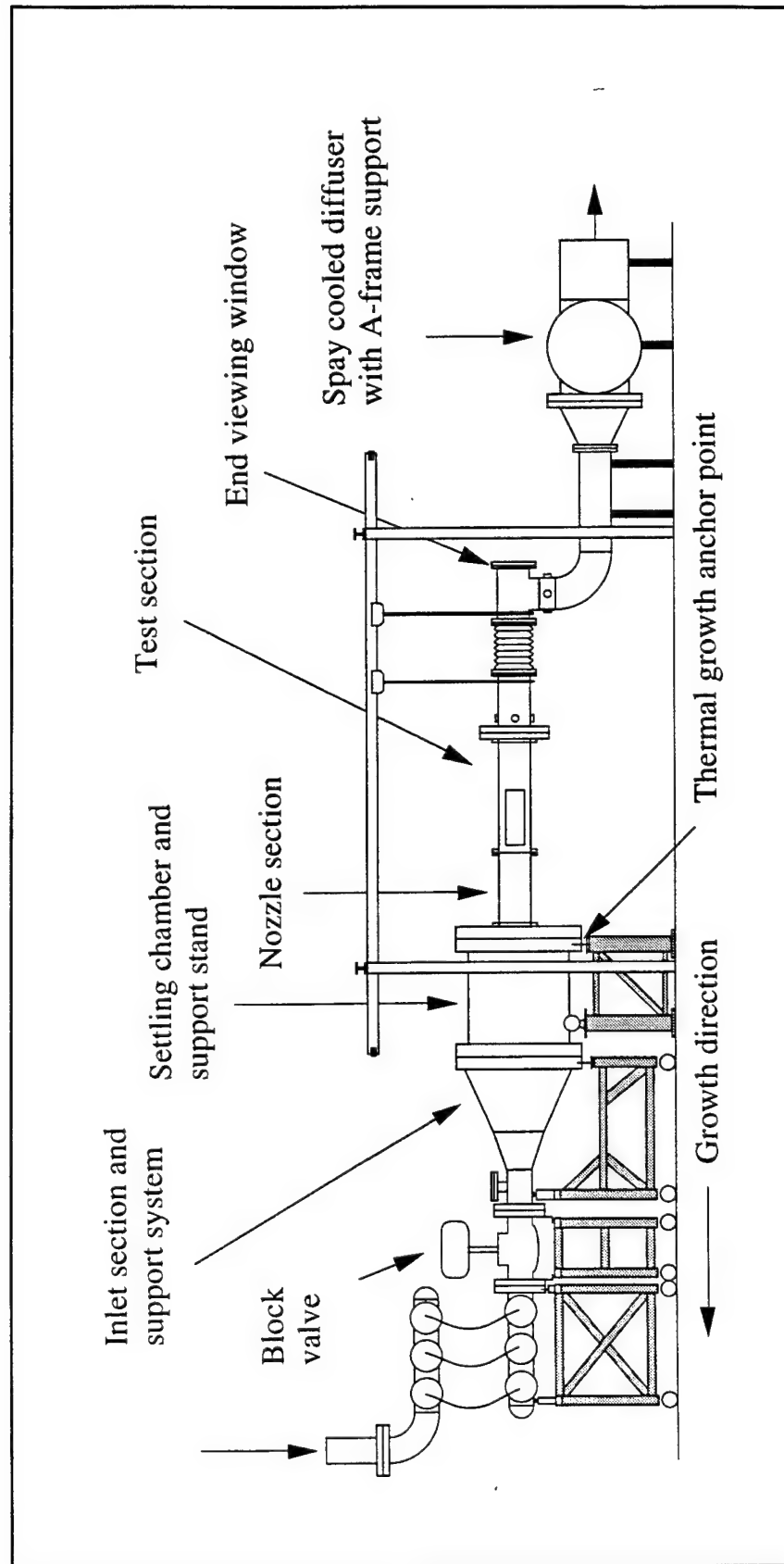


Figure 3.1. Schematic of supersonic combustion facility.

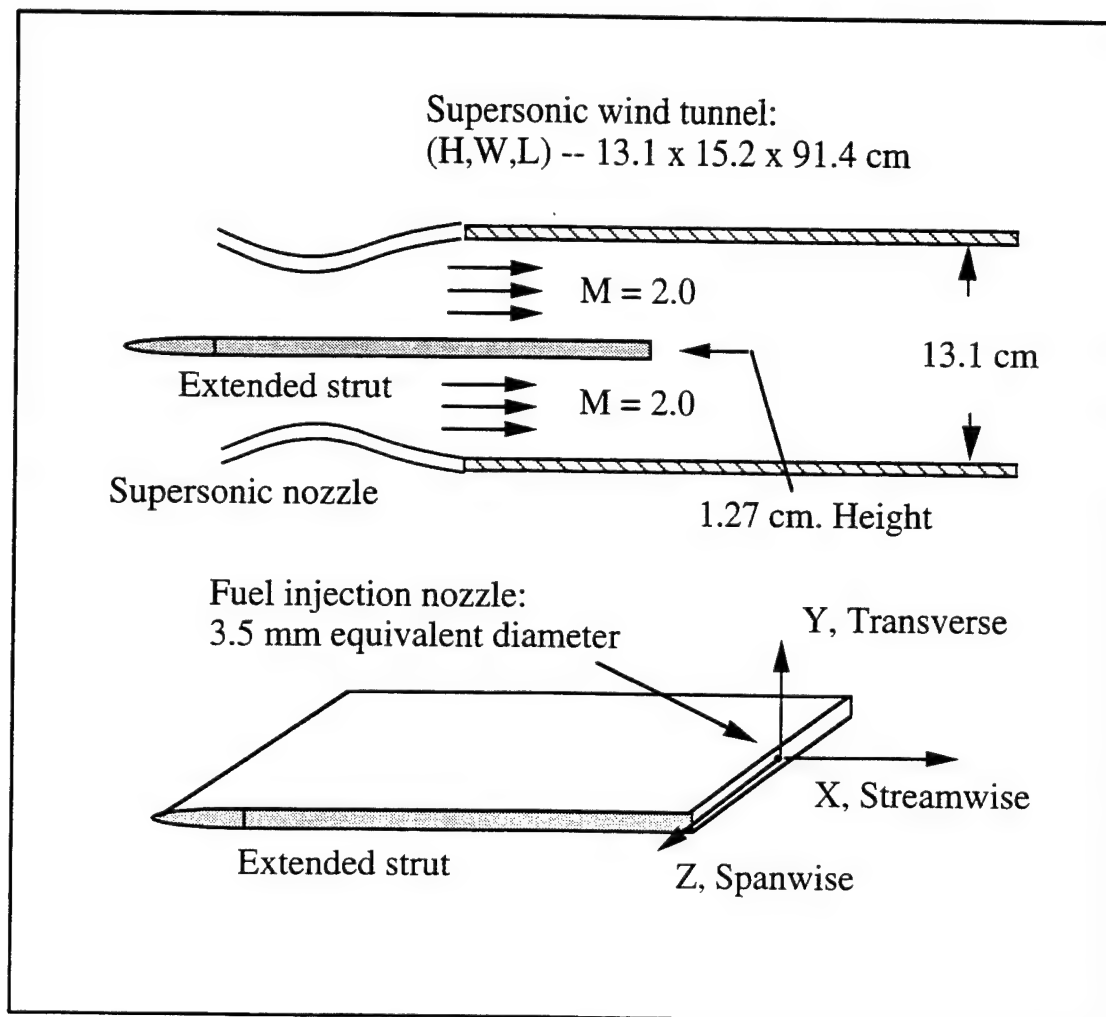


Figure 3.2. Schematic of extended strut and reference coordinate system.

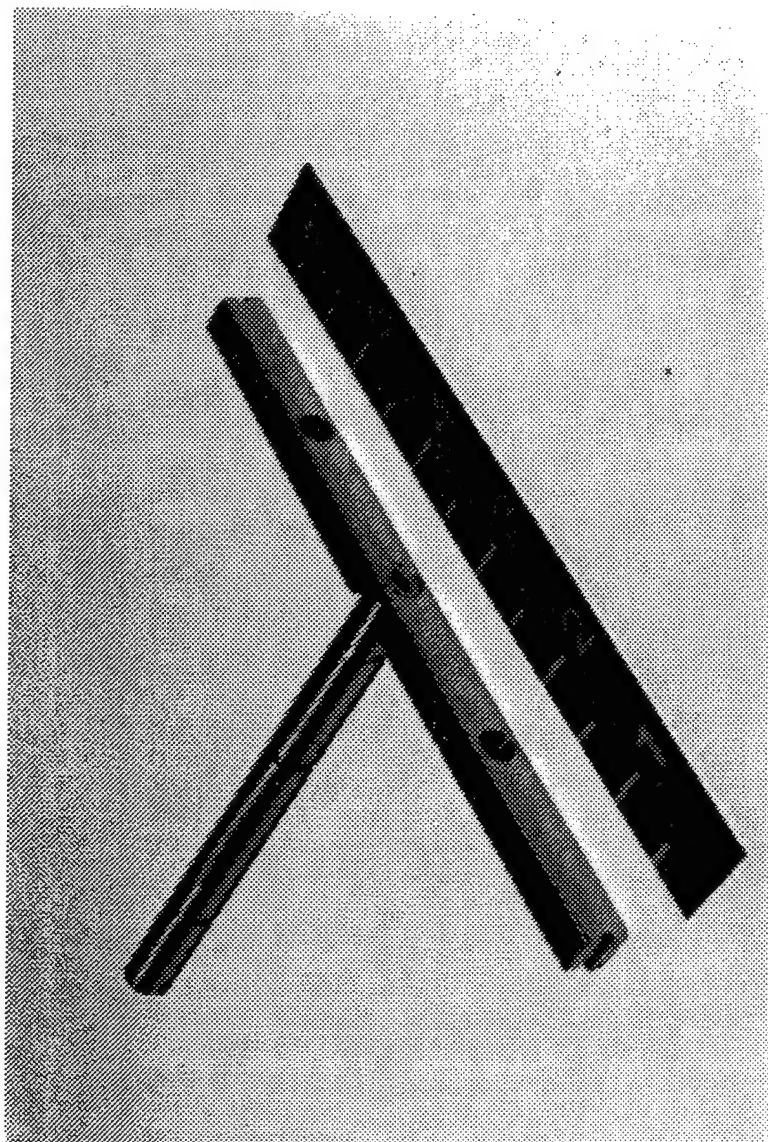


Figure 3.3. Nozzle and nozzle extension tube mounted in base retainer plate.

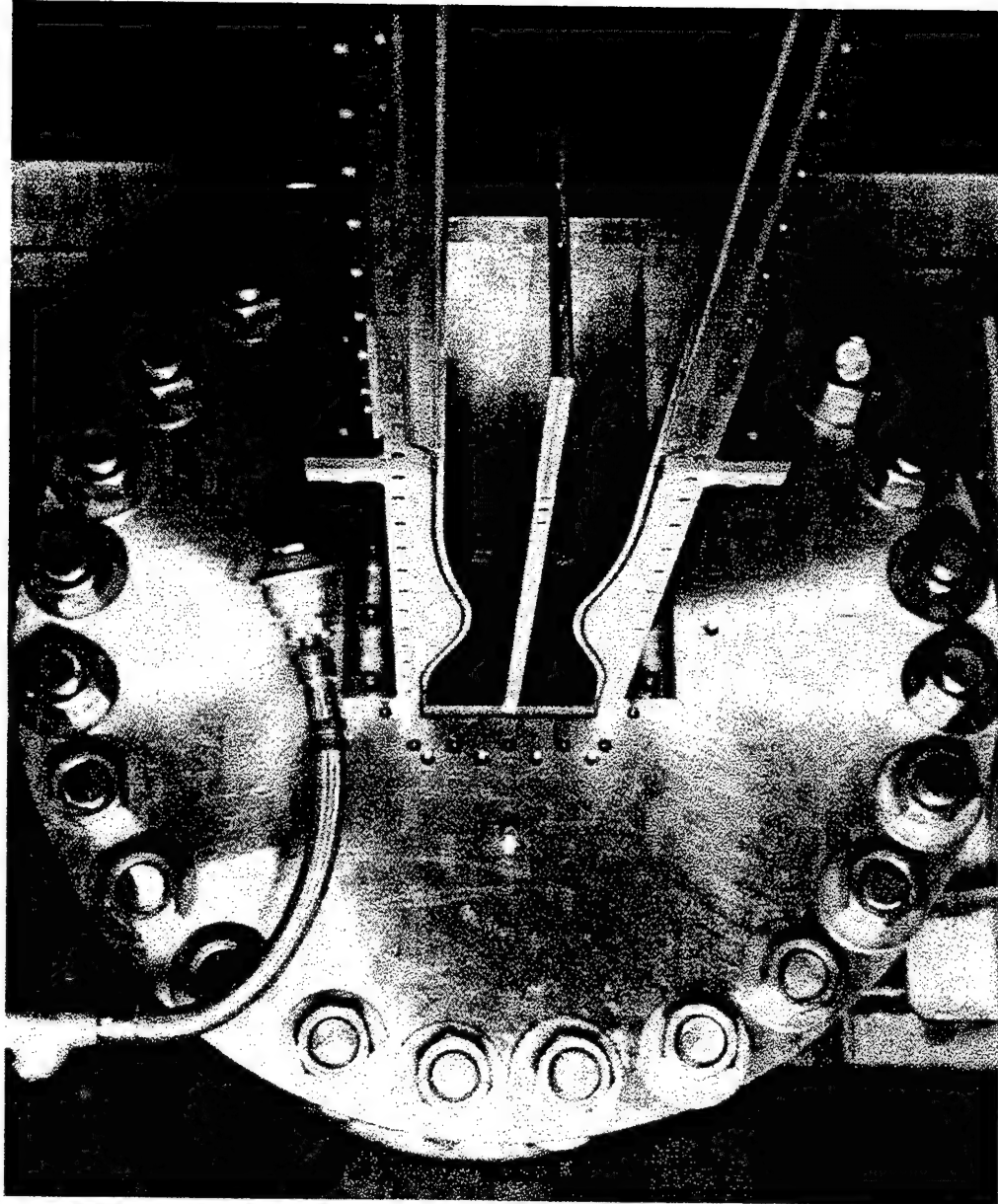


Figure 3.4 Windtunnel with side wall removed showing the nominal Mach 2 nozzle, extended strut, and beginning of the test section.

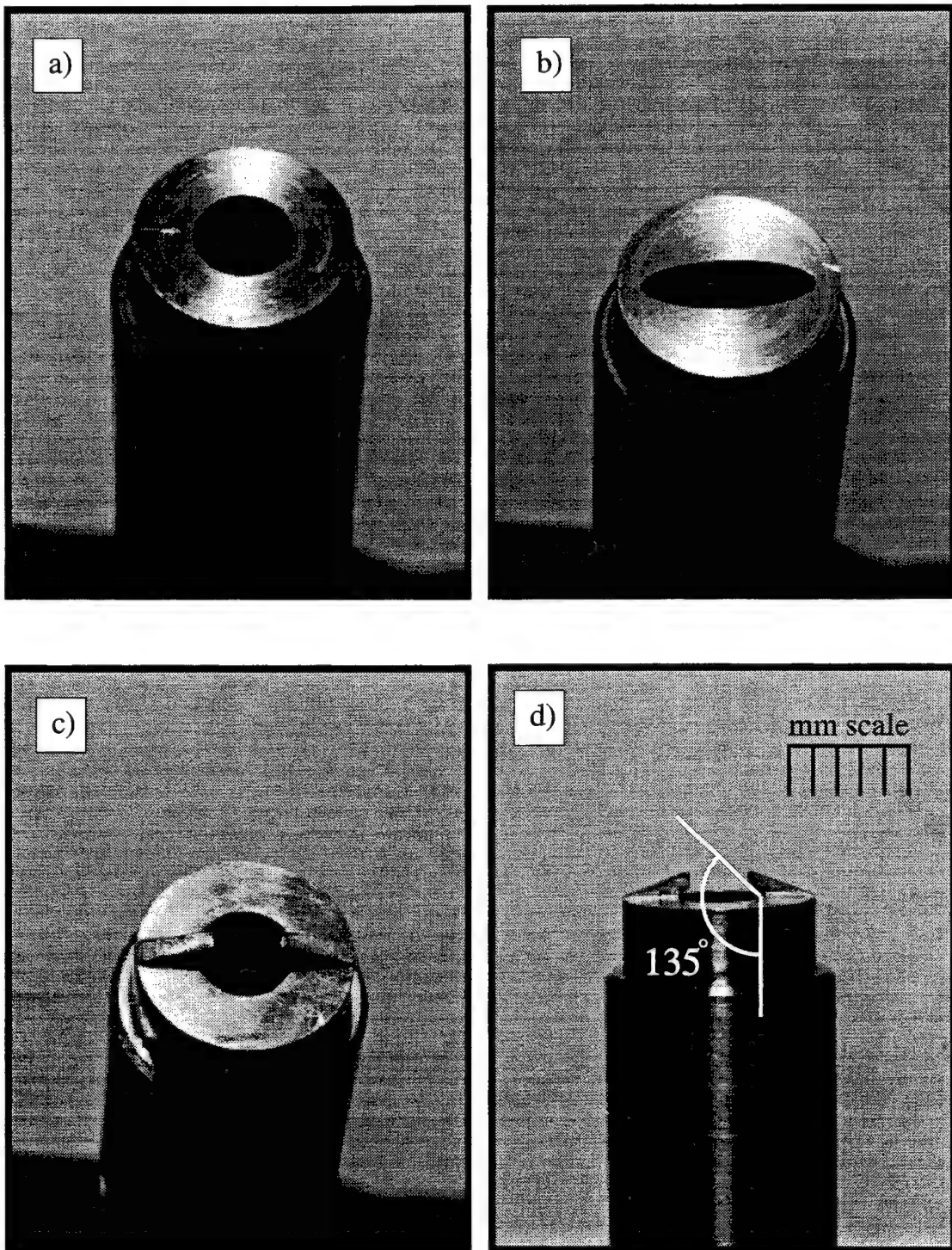


Figure 3.5. Photographs of the tips of the injector nozzles: a) circular, b) elliptical, and c) and d) circular-with-tabs.

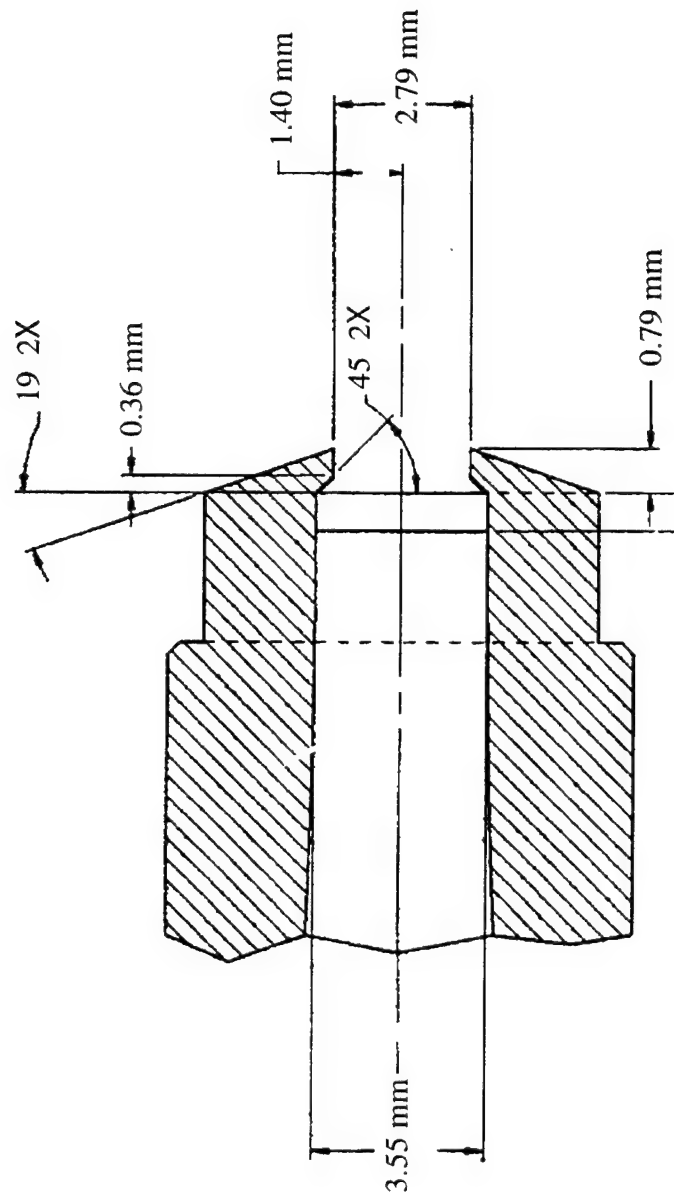


Figure 3.6. Design specifications for circular-with-tabs nozzle.

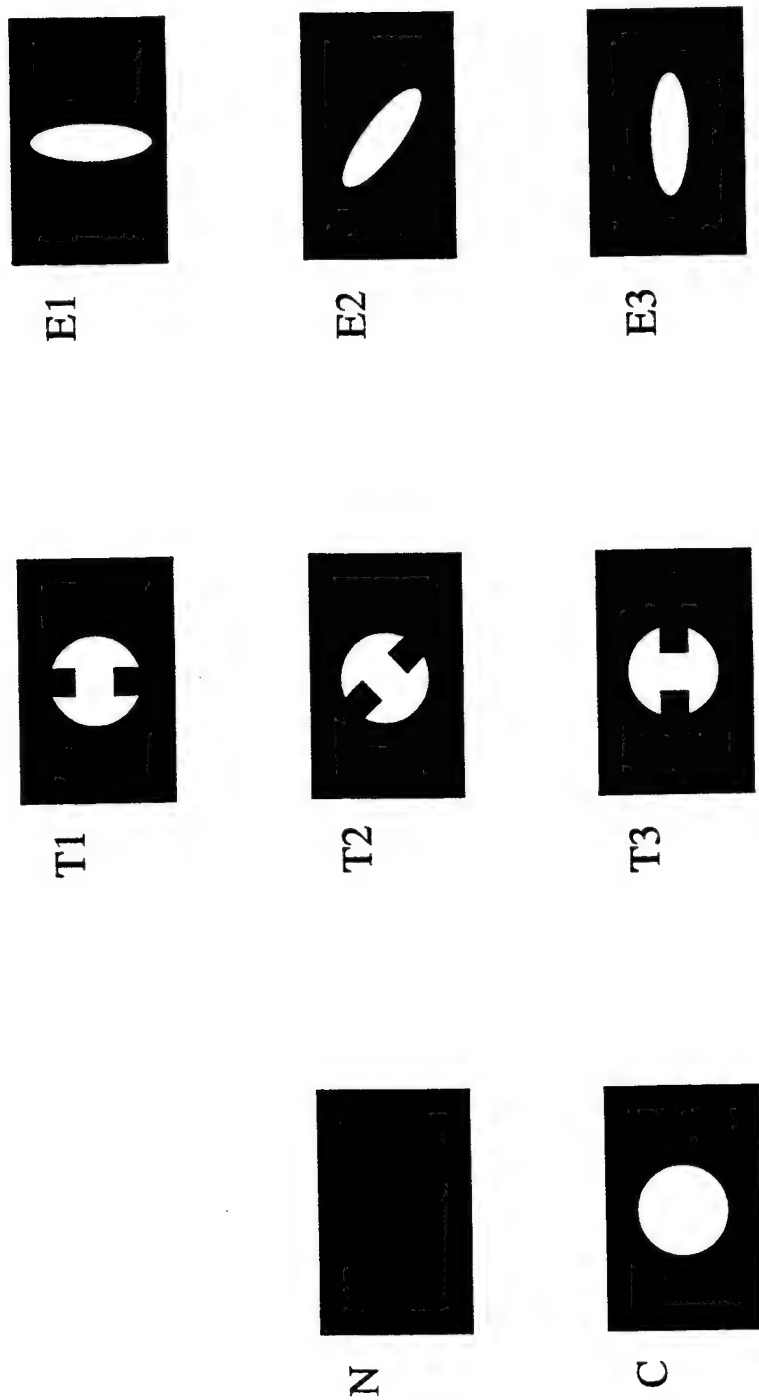


Figure 3.7. Schematic of nozzle mounting orientations. No injection (N) case and injection cases: circular (C), circular-with-tabs (T1, T2, T3), elliptic (E1, E2, E3).

CHAPTER 4

EXPERIMENTAL TECHNIQUES AND INSTRUMENTATION

Various complementary methods were used to obtain a description of the flow field around the strut both without and with helium injection. Schlieren photography, planar Rayleigh/Mie scattering, acetone Planar Laser-Induced Fluorescence (PLIF), and flow visualization using titanium tetrachloride were used to visualize the flow field, while Laser Doppler Velocimetry (LDV) was used to measure flow velocities. Schlieren photography provided preliminary views of the flow field which were used to check for unexpected flow disturbances and to identify the domain of interest in the flow field. Planar Rayleigh/Mie scattering in three orthogonal planes of view, with the primary flow seeded, provided a visual image of the helium jet shape and mixing structures. LDV was used to obtain quantitative velocity data to provide a statistical description of the flow field. LDV velocity profiles were recorded at the same streamwise locations as the face-on view Rayleigh/Mie images in order to allow direct comparison between the velocity contours and the visible flow structures. Acetone PLIF, with the helium jet seeded, revealed the structure of the jet at the exit of the injector nozzle, where the Rayleigh/Mie images provided insufficient information. Light scattered from products of the chemical reaction between titanium tetrachloride and water highlighted the jet and the recirculation zone in a manner visible to the naked eye. The titanium tetrachloride seeding provided a three-dimensional view of the flow field with helium injection. The basic experimental

concepts and data analyses involved in each of these techniques will be discussed in this chapter.

4.1 Schlieren photography

Schlieren images indicate the density gradients present in a flow field [Holman 1994]. The images are created by projecting a beam of collimated light through the test section of the wind tunnel, focusing the light on a knife edge, and collecting the refracted light on a screen or optical recording device. This is a line-of-sight technique, and thus the density gradient indicated at any point in the image is integrated along a line through the test section perpendicular to the plane of view. As a result, some detailed features of the flow may not be captured. Furthermore, because of this integrating effect, schlieren photography is better suited to the study of two-dimensional flow fields than to three-dimensional flow fields.

Figure 4.1 shows a schematic of the schlieren photography system used in these studies. A mercury arc lamp was positioned at the 122-cm focal length of a 20-cm-diameter plano-concave mirror. The light was focused on a slit and then reflected from the surface of this mirror (mirror 1), ideally collimated, through the tunnel test section to a second mirror (mirror 2) positioned directly across from the first. A knife edge was positioned at the 122-cm focal point of a second plano-concave mirror (mirror 2). Finally, a 10.2-by-12.7-cm Graphlex camera (consisting of a 127-mm lens, extended bellows, and film holder) was positioned so that an image of the test section filled the entire frame of the film holder. The knife edge was adjusted to maximize sensitivity to density gradients as observed in an image projected on a piece of ground glass which was placed in the film holder for visualization purposes. The aperture was set at $f/4.5$ with a shutter speed of $1/400$ second and a series of Polaroid images were taken on type 52 Polaroid 10-cm-by-12-cm film (1000 ASA), one photograph for each injection nozzle at

various operating conditions. The schlieren photographs are time averaged visualizations of the flow and shock system.

The schlieren images provided preliminary views of the flow field for two purposes: 1) to check the flow field for any density gradients resulting from unexpected flow disturbances, and 2) to identify the domains of interest for further flow visualization and velocity measurements. The schlieren photographs were scanned, digitized, and superimposed on a calibration scale for reference. The photographs were examined for the locations of the expansion fans, shock waves, the extent of the jet and wake regions, and the presence of unexpected density gradients.

4.2 Rayleigh and Mie scattering

4.2.1 Rayleigh and Mie scattering technique

There are two basic regimes of elastic scattering (scattering processes which leave the internal energy of the scatterer unchanged), and the type that occurs in a given situation is dependent on the relative magnitudes of the characteristic dimensions of the scattering particles and the wavelength of the incident light [McCartney 1976]. If the size of a particle is greater than or equal to the wave length of the illuminating light (i.e., $r_p \geq \lambda$; r_p being the radius of the particle and λ the wavelength of light), then the particle is referred to as a "Mie" scatterer and the scattering is described by Mie theory. If a particle is sufficiently small (i.e., $r_p \ll \lambda$), it is referred to as a "Rayleigh" scatterer; that is, the scattering is adequately described by the much simpler Rayleigh theory. Rayleigh and Mie scattering have distinct scattering intensity profiles as a function of observation direction

(ϕ). Rayleigh scattered intensity $I_s(\phi_x)$, given in units of watts per steradian, is proportional to the sixth power of the particle radius (i.e., $I_s(\phi_x) \propto r_p^6$) and inversely

proportional to the fourth power of the incident wavelength (i.e., $I_s(\phi_X) \propto \lambda^{-4}$). Mie scattering shows an almost exponential dependence on the ratio of particle radius to light wavelength (r_p/λ). For the present study, however, as long as the particles follow the flow, their size and whether the particles are within the Rayleigh regime are not of critical importance. Since the particle size was not specifically measured in these experiments, the term Rayleigh/Mie scattering will be used in subsequent discussion.

The scattering images were created by illuminating the flow with a sheet of laser light, capturing the scattered light with a photosensitive recording device, and converting the signal into a digitized planar image. In recent years, two methods of flow visualization through light scattering, referred to as "product formation" and "scalar transport" techniques, have been used to study the mixing of two fluids in high speed flows [Clemens and Mungal 1991]. In the "product formation" technique, vapor is added to one fluid that is warm enough to sustain the vapor. The vapor remains in vapor state until it comes in contact with the cooler fluid of the second stream. The vapor then condenses at the interface of the two fluids, forming small particles, therefore, effectively marking the mixing region.

In the "scalar transport" technique, one fluid is seeded with a vapor that condenses and freezes as it expands to the desired velocity. Thus, only one stream is marked and the interface between the two streams is seen as the transition from marked to unmarked fluid. Both techniques highlight the flow structures at the interface of the two fluids. The transitional area provides information on the mixing dynamics between the two fluids which is of utmost interest in the present study. A detailed description of these two techniques is presented by Clemens and Mungal [1991].

4.2.2 Scattering particles

The present study utilized the scalar transport technique to highlight the mixing interface between the helium jet and the primary freestream air. The scattering particles were the ice crystals which condensed from the small amount of moisture naturally present in the wind tunnel supply air. As air passed through the supersonic nozzle, the moisture condensed to form an ice "fog" that effectively scattered radiation at the incident wavelength ($\lambda = 248 \text{ nm}$) in the present experiment. This visualization method using naturally present moisture has previously been used in supersonic boundary layers [Miles and Lempert 1990, Arnette et al. 1993a], mixing layers, [Elliott et al. 1992 and 1995], and a transverse sonic jet [Gruber et al. 1995]. Likewise, condensation of ethanol vapor added to the supersonic stream has previously been used in visualizing supersonic mixing layers [Clemens and Mungal 1991, Messersmith et al. 1991] and in a study of a transverse sonic jet [Hermanson and Winter 1993].

Studies of condensation inside supersonic nozzles have shown that the ice crystals are nearly mono-dispersed with diameters between $0.003 \text{ }\mu\text{m}$ and $0.014 \text{ }\mu\text{m}$, depending on the moisture content of the inlet air [Wegener and Pouring 1964, Wegener and Parlange 1967]. During operation of the wind tunnel at thermodynamic conditions similar to those used in the present study, the signal scattered from the ice crystals in the tunnel disappeared when the polarization of the 532 nm wavelength illuminating laser sheet was changed [Gruber 1995]. Since Mie scattering would be insensitive to this change in polarization, according to the aforementioned Rayleigh theory, the diameter of the particle must be an order of magnitude smaller than $0.532 \text{ }\mu\text{m}$.

As stated previously, the primary concern about particle size is whether the particle is small enough to accurately follow the turbulent fluctuations of the flow in the present study. For particles to accurately respond to flow fluctuations, the Stokes number (St)

must be less than about 0.05 [Samimy and Lele 1991]. The Stokes number is a nondimensional parameter defined as a time scale ratio relating the magnitude of a characteristic flow time scale (τ_f) and a particle response time scale (τ_p),

$$St = \frac{\tau_p}{\tau_f}. \quad 4.1$$

For a free shear layer, τ_f reflects the motion of the large-scale structures, which are known to dominate turbulent mixing layers [Brown and Roshko 1974].

An estimate of τ_f for the extended strut configuration used in this study is the ratio of half the strut width ($h/2$) and the velocity difference between the freestream air and the recirculating fluid behind the base of the strut (ΔU):

$$\tau_f = \frac{h/2}{\Delta U}. \quad 4.2$$

The particle response time scale (τ_p) is defined as the time required for a particle to accelerate from rest to 63% of a constant free stream velocity, assuming a spherical particle and Stokes drag. The particle response time is given by Melling [1986]

$$\tau_p = (1 + 2.76 \cdot K_n) \frac{\rho_p d_p^2}{18\mu}, \quad 4.3$$

where ρ_p (kg/m³) is particle density, d_p (m) is particle diameter, μ (kg/m·s) is absolute fluid viscosity and K_n is the non dimensional Knudsen number,

$$K_n = \frac{3}{2} \frac{\mu}{\rho a d_p}, \quad 4.4$$

where ρ (kg/m³) is fluid density and a (m/s) is the speed of sound in the freestream fluid. Using a conservative estimate of the ice crystal diameter (d_p) of 0.03 μm (compared to that determined by Wegener and Pouring [1964] and Wegener and Parlang [1967]), a half strut width ($h/2$) of 6.35 mm, and a velocity difference (Δu) of 520 m/s, the Stokes number is calculated to be 0.003 for the operating conditions of this experiment. This Stokes number is well below the upper limit of 0.05 as calculated by Samimy and Lele [1991]. Therefore, the ice crystals found in the subject flow are predicted to be small enough to follow the large-scale turbulent fluctuations within this flow field.

However, the ice particles in the flow evaporate when subjected to the elevated temperatures in the recirculation zone behind the strut and then recondense downstream. Further, the ice crystal size is likely to change in the boundary layer and through the expansion waves. Given these observations, the particles are not considered a conserved scalar, and the Rayleigh/Mie images cannot be used to compute quantitative mole fraction of air to helium. However, since scattering intensity is proportional to the number density of the scattering particles outside regions of significant temperature or pressure gradients, the intensity of scattered light can be considered a qualitative indicator of air concentration. As a result, intensity range mapping could be used to examine propagation of the jet core and the dynamics of the mixing between the helium jet and freestream air.

4.2.3 Rayleigh/Mie scattering instrumentation

A Lambda Physik EMG 150 Excimer pulsed laser produced the 248 nm wavelength ultraviolet radiation used for these Rayleigh/Mie scattering experiments. The laser beam was focused into a sheet and projected through the test section by a series of lenses and prisms. The sheet thickness was estimated to be 300 μm .

As shown in Figures 4.2, 4.3, and 4.4, the optical components were arranged in three separate configurations to produce laser sheets in three orthogonal planes: streamwise, face-on, and plan views. The images shown on the "monitor" in these figures provides a general sketch of the flow field resulting from helium injection from a circular nozzle as seen using the planar Rayleigh/Mie scattering technique from each of the three different perspectives. The streamwise view shows the image created by passing a sheet of laser light oriented in an (X,Y) plane through the test section of the wind tunnel. The face-on views show images created by passing a sheet of laser light oriented in the (Y,Z) plane through the test section. It should be noted that the face-on view is recorded with the camera located 30° off of the streamwise tunnel axis resulting in an 8% compression in the spanwise coordinate (which is later corrected). For the streamwise and plan views, the camera is perpendicular to the sheet. The plan view shows the image created by passing a sheet of laser light oriented in an (X,Z) plane through the test section of the wind tunnel.

The focusing optics used to produce the laser sheet for the streamwise views included a 200-mm-focal-length plano-convex cylindrical lens followed by a 500-mm-focal-length plano-convex spherical lens. The plano-convex 200-mm-focal-length cylindrical lens was replaced by a plano-concave 250-mm-focal-length cylindrical lens to form the laser sheet for both the plan and face-on images. This change was made to accommodate space limitations on the optical table.

The scattered light signal was collected through a Nikon UV-Nikkor 105-mm $f/4.5$ telephoto lens and was imaged onto the 578-by-384-pixel array of a Princeton Instrument Intensified Charge Coupled Device (ICCD) camera having a 14-bit resolution. Accordingly, each of the 221,952 pixels was assigned an intensity or "gray level" value between 0 and 16,384 based on the amount of light collected by that pixel in the array. The gain of the camera was adjusted to maximize its dynamic range while avoiding

saturation at any one pixel. The camera aperture gate width was set at 2 μ s. However, the effective gate width is set by the laser temporal pulse width of approximately 20 ns. Therefore, the effective gate width is sufficiently short in duration to consider the images instantaneous. Various thickness (3.2 mm, 6.4 mm and 12.7 mm) extension spacer disks were fabricated and mounted between the ICCD camera body and lens for greater magnification (higher spatial resolution) in each plane of view. The ICCD camera and sheet-forming optics were mounted onto the same table so that the camera and laser sheet could be moved in unison. This allowed the camera's focus on the laser sheet to be easily maintained. Software was developed to capture and label a series of images and store them on a personal computer. The data were then transferred to optical disks for permanent storage and subsequent analysis.

4.2.4 Planar Rayleigh/Mie scattering images

A series of 20 instantaneous images was recorded for selected locations and operating conditions. Both the streamwise and the spanwise images represent a 4.32-by-2.79-cm field of view, with the flow from left to right while the face-on view has a 3.30-by-2.03-cm field of view with the flow direction out of the plane of the page. These dimensions were imaged onto the 578-by-384-pixel array of the camera, giving a planar pixel resolution of about 75 μ m per pixel for the streamwise and spanwise planes as opposed to 53 μ m per pixel for the face-on view plane. The images are not intended to show microscopic mixing. Rather, the images, being spatially integrated over the 300 μ m laser sheet thickness, yield a view of the large scale flow structures.

4.3 Acetone Planar Laser-Induced Fluorescence (PLIF)

4.3.1 Acetone PLIF technique

Planar Laser-Induced Fluorescence (PLIF) provides a planar image of the number density of fluorescing medium suspended in a fluid [Lozano et al. 1992]. Although results obtained with PLIF are nominally similar to those obtained with Rayleigh/Mie scattering, in that a planar image of the flow field is obtained, there are some important differences. Most importantly, in the high temperature region at the base of the strut, fluorescence from acetone vapor effectively marks the helium jet whereas the moisture, forced into the vapor state by the elevated temperature, contained in the air does not effectively scatter light to mark the presence of air. Thus, acetone PLIF was used to depict the shape of the barrel shock and the location of the Mach disk in the jet, issuing from a circular nozzle, at the nozzle exit where no information is derived from Rayleigh/Mie images. PLIF is also attractive because wavelength of the fluorescence is different from the wavelength used for excitation, and thus by proper choice of optical filters, scattering from surfaces in the tunnel can be eliminated.

Acetone has proven to be an excellent molecular tracer for experimental use because of the high signal-to-noise ratio of the derived PLIF images, acetone's non-toxic nature, and an excitation frequency that is easily accessible by different lasers [Lozano et al. 1992]. Acetone ($\text{CH}_3\text{-CO-CH}_3$) has a molecular weight of 58.08, a specific gravity of 0.79, and a vapor pressure of 24 KPa (3.48 psia) at 293 K (527 R). It absorbs radiation and is excited from a ground singlet state to a first excited singlet state in the 225 to 320 nm region. Most of the excited acetone molecules in the singlet state are transferred to the triplet state, and almost all of the remaining excited singlet molecules fluoresce at a wavelength of 350 - 600 nm with a lifetime of a few nanoseconds [Lazano et al. 1992].

The triplet state molecules undergo phosphorescence which is shifted toward the red with respect to the singlet-state fluorescence, with a natural lifetime of approximately 200 ms [Greenblatt et al. 1984, Copeland and Crosley 1985]. However, the triplet state is effectively quenched by O₂. In addition, the phosphorescence can be discriminated against by using a very short camera gate width.

In order to determine whether acetone vapor is a conserved scalar under the present test conditions, it is necessary to determine the dependence of the intensity of acetone fluorescence on temperature and pressure in the ranges present. Lozano et al. [1992] suggest that acetone fluorescence is independent of temperature and local gas composition and assume so for their experiments. However, experiments by Tait and Greenhalgh [1992] show acetone to be temperature dependent at least in the 200-900 K range, whereas a comparative vapor of acetaldehyde was not. Tait and Greenhalgh [1992] suggest that this temperature dependence is due to two separate nearly degenerative fluorescing states and quenching. Therefore, it appears that in highly underexpanded supersonic flows, an acetone PLIF image is a qualitative "picture" of the number density field. In this study, acetone PLIF was used solely to visualize the internal structure of the helium jet, including the Mach disk, and to observe the presence of helium in the recirculation zone.

4.3.2 Acetone PLIF instrumentation

A frequency-doubled Spectra-Physics Quanta-Ray DCR-4 Nd:YAG laser ($\lambda = 532$ nm) in conjunction with a Quanta-Ray wavelength extender (WEX-1) produced the ultraviolet radiation (266 nm) for acetone PLIF. The laser overall power was maintained at approximately 400 mJ. The acetone added to the helium jet was regulated along with the helium gas flow rate. The experimental configuration for acetone PLIF is shown in Figure 4.5. It is nearly the same configuration used for the Rayleigh/Mie scattering

technique for the streamwise plane of view (Figure 4.2), except that the Excimer laser was replaced by the YAG/WEX laser system. Likewise, nearly the same imaging system was used as in the Rayleigh/Mie setup, except that a Nikon Nikkor 60-mm f/2.8 Micro lens replaced the UV telephoto lens. Because the acetone fluorescence is visible ($\lambda = 350 - 600$ nm), a standard camera lens can be used; an added advantage of using a standard lens is that it effectively filters out the strong scattering and reflections from wind tunnel wall surfaces (windows) at the wavelength of the incident radiation ($\lambda = 266$ nm).

4.4 Titanium tetrachloride based visualization

A titanium tetrachloride based flow visualization technique was used to investigate the development of the jet as it moved further downstream. Since this technique depends on a reaction between titanium tetrachloride and moisture in the flow, moist air was used as the injectant fluid instead of helium (which is essentially moisture-free). Air was passed through a reservoir containing titanium tetrachloride powder several meters upstream of the injection point. Titanium tetrachloride (TiCl_4) seeded into moist air reacts with the vapor-phase H_2O to produce titanium dioxide (TiO_2) and hydrochloric acid (HCl). The balanced chemical equation for this reaction is



The titanium dioxide and hydrochloric acid molecules remained suspended in the air as the jet passed through the nozzle into the primary flow. A tungsten lamp strobe light was projected in the spanwise direction through the tunnel. The flow was illuminated at a pulse rate of 10 Hz. The scattered light from the TiO_2 molecules was substantial enough to be seen by the naked eye with even a modest number density of titanium tetrachloride seed.

Since the illuminating light was passed across the entire tunnel instead of in a sheet like the Rayleigh-Mie and acetone PLIF technique, the view is spatially integrated as in the schlieren technique. Therefore, the fine detail seen in the planar images is absent. This technique showed the structure of the jet and the shape of the recirculation zone (which contained some of the titanium tetrachloride escaping the jet). Due to the corrosive nature of the hydrochloric acid byproduct, experiments in this study involving titanium tetrachloride were limited to two nozzle geometries (elliptic and circular-with-tabs) and run time was limited to a few minutes.

4.5 Laser Doppler velocimetry

4.5.1 Laser Doppler velocimetry technique and instrumentation

Laser Doppler velocimetry (LDV) provides point velocity measurements in a flow by detecting the Doppler shift of light scattered by particles moving with the flow [Drain 1980]. LDV has been used extensively to map the velocities of subsonic and supersonic flow fields and to provide quantitative mean velocity and turbulence data [Samimy 1984, Raffoul 1995].

A finite measurement volume for one-component LDV measurements is created by focusing two coherent laser beams of known wavelength at a point in space. Figure 4.6 shows the one-component LDV measurement volume created by the intersection of two laser beams. Two- or three-component LDV, in general, is obtained by superimposing two or three one-component LDV measurement volumes created with beams at different wavelengths. Both one- and two-component LDV were used in these experiments.

An interference fringe pattern is formed where each two beams of a pair cross (Figure 4.6). The fringe spacing (d_f) is calculated by the equation

$$d_f = \frac{\lambda}{2 \sin \kappa}, \quad 4.6$$

where λ is the wavelength of the laser light and κ is the lens half angle. The number of fringes (N_{fr}) in the measurement volume is calculated by the equation

$$N_{fr} = \frac{1.27 d_b}{D_{e^{-2}}}, \quad 4.7$$

where $D_{e^{-2}}$ is the diameter (at which the intensity is equal to e^{-2} of the centerline intensity) of the laser beam and d_b is the distance between the beams entering the lens system of the LDV.

Particle velocity is calculated from the time rate at which the particle passes through the fringes. The laser beam wavelength in combination with the measurement volume fringe spacing and orientation dictates the range of velocities measurable with the LDV system.

In the one-component LDV setup the laser beam from an argon-ion laser was passed through a collimator and then separated into its blue ($\lambda = 488$ nm) and green ($\lambda = 514.5$ nm) components using a prism. Figure 4.7 shows a schematic of the LDV system. The blue beam was passed through a polarizing filter and then a beam splitter where two, parallel blue beams emerged 15.6 mm apart. The blue beams ($D_{e^{-2}} = 1.22$ mm) were then passed through a 250-mm-focal-length spherical lens to form the measurement volume at the desired point of interrogation. The fringe spacing (d_f) was determined to be $7.82 \mu\text{m}$ ($\kappa = 1.787^\circ$) for the blue component of the LDV system; while the number of fringes (N_{fr}) in the measurement volume was calculated to be 16. The green beam was likewise polarized and split into two parallel beams ($D_{e^{-2}} = 1.25$ mm), 16.28 mm apart, and focused in a plane orthogonal to the plane of the blue beams. The resulting

measurement volume also contains 16 fringes with a $7.9 \mu\text{m}$ fringe spacing created by the $\kappa = 1.865$ degree half angle.

The blue and green beams were adjusted to cross at the same location (Figure 4.7). The planes of the two fringe patterns were oriented perpendicular to one another and at $\pm 45^\circ$ to the mean streamwise flow velocity vector. The combined velocity components were then used to compute the streamwise velocity u along the X-axis and the transverse velocity v along the Y-axis.

The length (l_m) and width (d_m) of the measurement volume in this experiment were calculated to be approximately $130 \mu\text{m}$ and 4 mm , respectively (Figure 4.6). These dimensions were calculated from the equations

$$l_m = \frac{d_m}{\tan \kappa}, \quad 4.8$$

and

$$d_m = \frac{4\lambda f}{\pi D_{e^{-2}}}, \quad 4.9$$

where f is frequency of the laser beam light. However, A $100\mu\text{m}$ aperture placed in front of the collecting optics created an effective measurement volume length of $l_m = 100 \mu\text{m}$.

The measurement volume was systematically moved to obtain a series of velocity profiles along the X, Y and Z axes in the same planes of view as the Rayleigh/Mie face-on images. This allowed direct comparison of the velocity parameters acquired by LDV measurements and the flow structures captured in the Rayleigh/Mie images.

Light scattered from particles in the flow was collected and focused onto photo multiplier tubes (PMTs) positioned outside the tunnel windows. Since light transmitted and refracted through the tunnel windows is most intense in the forward scattering direction, collecting light off-axis reduces the intensity of spurious light entering the

PMTs. The PMTs were positioned at 21° to the direction of propagation of the incident laser light to optimize the signal-to-noise ratio of the light scattered by the particles. Viewing the measurement volume at 21° off the forward scattering direction reduced the length of the measurement volume by 7%. But as previously mentioned, the 100- μm aperture placed in front of the PMTs blocked light outside the 100 μm dimension and thus determined the effective measurement volume size.

LDV requires particles that are small enough to follow turbulent fluctuations in the flow but large enough to scatter an amount of light adequate for detection above background noise. As discussed in Section 4.2.2, particle motion is governed by the Stokes number [Samimy and Lele 1991]. For this experiment, the ice crystals formed from the moisture present in the supply air were small enough to adequately follow the flow but generated only a low rate of data collection. This suggests that the LDV signal processor was accepting only the particles on the high end of the particle size distribution. To increase the data rate, additional water was added through a spray atomizer connected to seed port of the settling chamber section of the wind tunnel (see Figure 3.1 for the tunnel schematic). This increased the data rate substantially but did not significantly affect the resulting mean velocity and turbulence intensity measurements. The deviations between data collected with and without the additional spray atomized water were 1% for the mean streamwise velocity, 6% for the streamwise turbulence intensity, and less than 1% for the transverse turbulence intensity in a region behind the strut known to incur high turbulence. Since this is within reasonable agreement, a minimal amount of water was spray atomized into the settling chamber to increase the data rate.

A 40 MHz frequency shift of one of the blue and one of the green beams was used to shift the range of measurable velocities u and v from 0 to 1060 m/s to -461 to 600 m/s (for the two-component system). This range allowed measurement in both the freestream

(where U is approximately 520 m/s, V nominally zero m/s) and in the recirculation zone (where U reaches approximately -40m/s, V small positive and negative values). A TSI Intelligent Flow Analyzer (IFA) 750 auto correlation signal processor evaluated the signals and eliminated those that were generated by the presence of more than one particle in the measurement volume, the signals that were too weak, or those that passed through less than 4 of the 16 fringes. The signal processor was operated in coincident mode in order to accept data from only those particles that scattered adequate light to generate acceptable signals from each of the two fringe patterns within the coincidence time window of 20 μ s.

The most upstream streamwise LDV measurement that could be acquired downstream of the base of the strut without the strut blocking one of the beams was $X/h = 0.80$. However, a film repeatedly developed on the window in the region of the recirculation zone just behind the strut base making measurements closer than $X/h = 1$ problematic. Thus, $X/h = 1$ is the streamwise location of the first measurement location downstream of the base of the strut. One or more of the beams forming the two-component measurement volume, centered spanwise in the tunnel, were blocked by the strut or top/bottom tunnel walls when the measurement volume was within 1.9 mm of the strut and tunnel surfaces. Therefore, a one-component LDV system was used for near-wall boundary layer measurements.

The one-component LDV system set-up was similar to that of the two-component system, except that a single fringe pattern was oriented to obtain the streamwise velocity component U alone. The data collected using the one-component LDV system stretched from 0.25 mm to 1.65 mm off the surface of the strut. Measurements further from the surface were prohibited by the frequency limitations of the signal processor (corresponding to a maximum velocity of 424 m/s). The data taken with the one-

component LDV system combined with the data taken with the two-component system covered the entire transverse span of the tunnel.

4.5.2 Laser Doppler velocimetry measurements

The TSI software included in the LDV system computes the streamwise and transverse velocities and associated statistical parameters for the one- and two-component LDV configurations [TSI Incorporated 1992]. A FORTRAN program was written to extract the velocities from the data file generated by the TSI system and to compute mean velocities, turbulence intensities, correlation coefficients, and turbulent shear stresses. The equations defining the aforementioned parameters are discussed in Section 5.3. and listed in Appendix C.

The LDV system recorded approximately 5,120 measurements per location. The time between bursts varied with an overall time limit of 90 seconds per location (this limited the number of bursts for some locations to lower than 5,120). A typical coincident data rate was between 50 and 500 data points per second. This is too low for temporal based analysis such as standard spectral analysis or auto correlation analysis; however this information was considered as random data and valid for mean and standard deviation calculations. Higher data rates could be obtained by increasing the number density of the seed particles, though, increasing the amount of water added to the tunnel could result in excessively large particles (through agglomeration). Thus, it was decided to limit the amount of spray atomized water and accept the low data rate to assure a reasonable particle size for the LDV measurements.

Comparison of the LDV data with expected velocity values and the turbulence level in the freestream and incoming boundary layers (discussed in Section 5.3.1) indicates that the velocity data accurately represents the flow field. Nonetheless, several possible biasing factors must be acknowledged. First, the primary flow alone was seeded

with particles capable of scattering light to be recorded by the LDV system. Therefore, no velocity data was acquired in the helium jet prior to the location at which air with condensed moisture is entrained into the jet (the moisture in the air of the recirculation zone is in vapor form and does not produce appreciable scattering). Second, since the helium in the jet has a different index of refraction than the primary flow air, any measurement taken when one or more laser beams has passed through the jet is liable to experience some beam steering, although slight, due to a change in the fringe spacing. Likewise, the index of refraction changes across a shock wave and measurements taken when one or more laser beams pass through the shock may also be biased due to a change in fringe spacing. Other possible sources of error include: spatial averaging over the entire measurement volume, bias toward higher velocities, counter resolution, particle lag, fringe biasing, and signal biasing. Precautions were taken to reduce the potential for fringe biasing error by using the optimal fringe orientation of $\pm 45^\circ$ to the mean flow velocity for the two-component system, a 40 MHz frequency shift of one of the beams forming the measurement volume to distinguish directionality, using seed particles small enough to follow the turbulent fluctuations, and taking an adequate sample size to minimize statistical uncertainty. Nonetheless, as discussed above, the experimental LDV data closely matches the calculated and predicted values, so that the cited sources of error appear to have had minimal effects.

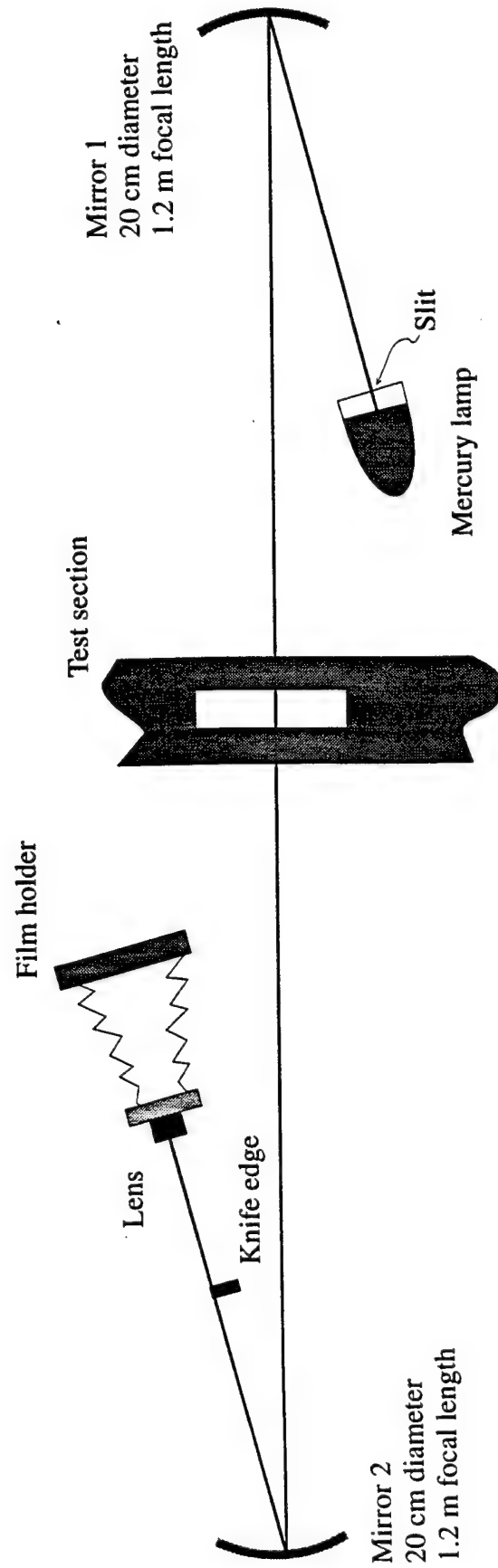


Figure 4.1. Schematic of schlieren photography system.

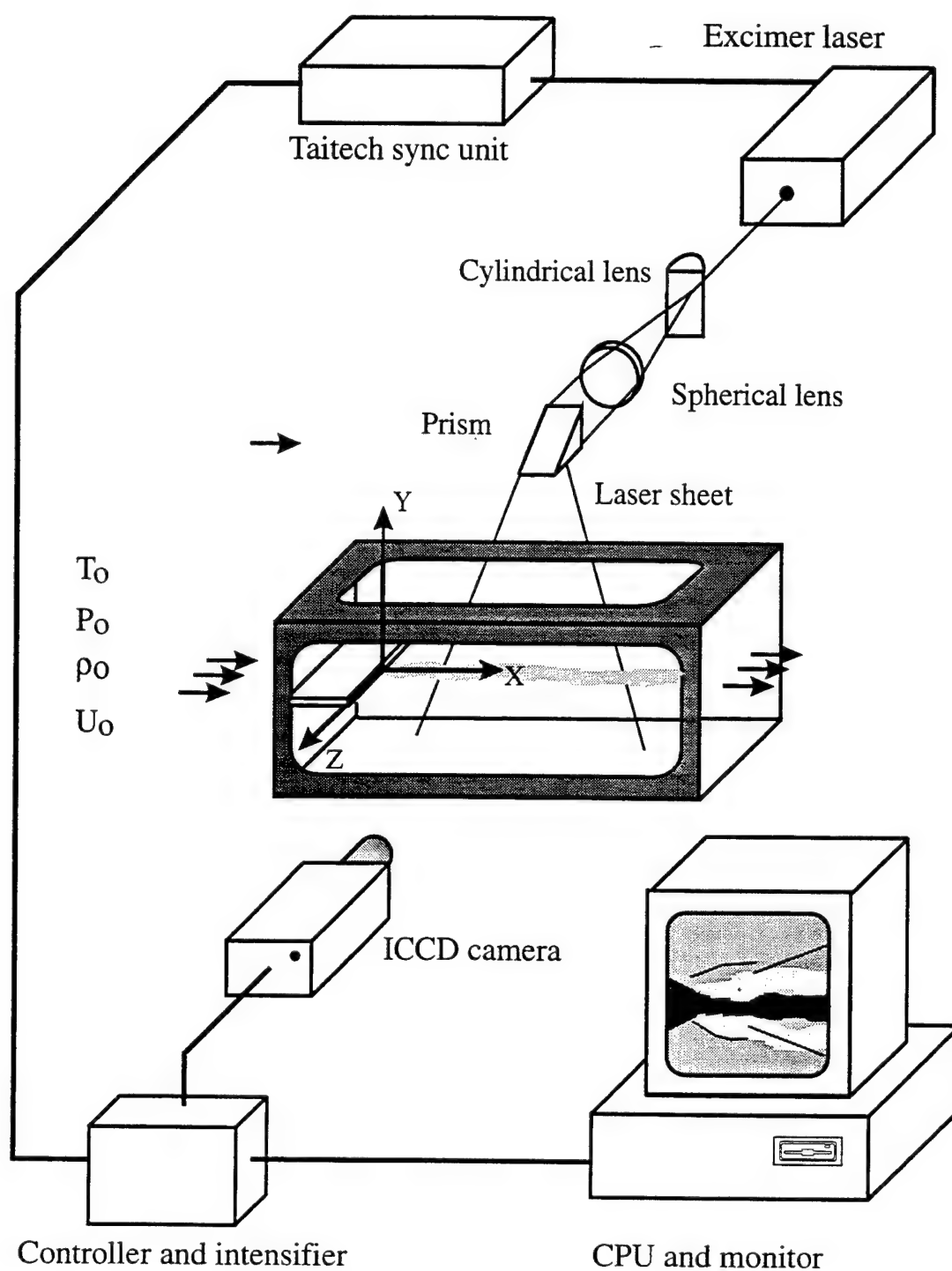


Figure 4.2. Schematic of flow visualization system to obtain Rayleigh/Mie scattering images of the streamwise (X,Y) plane of view.

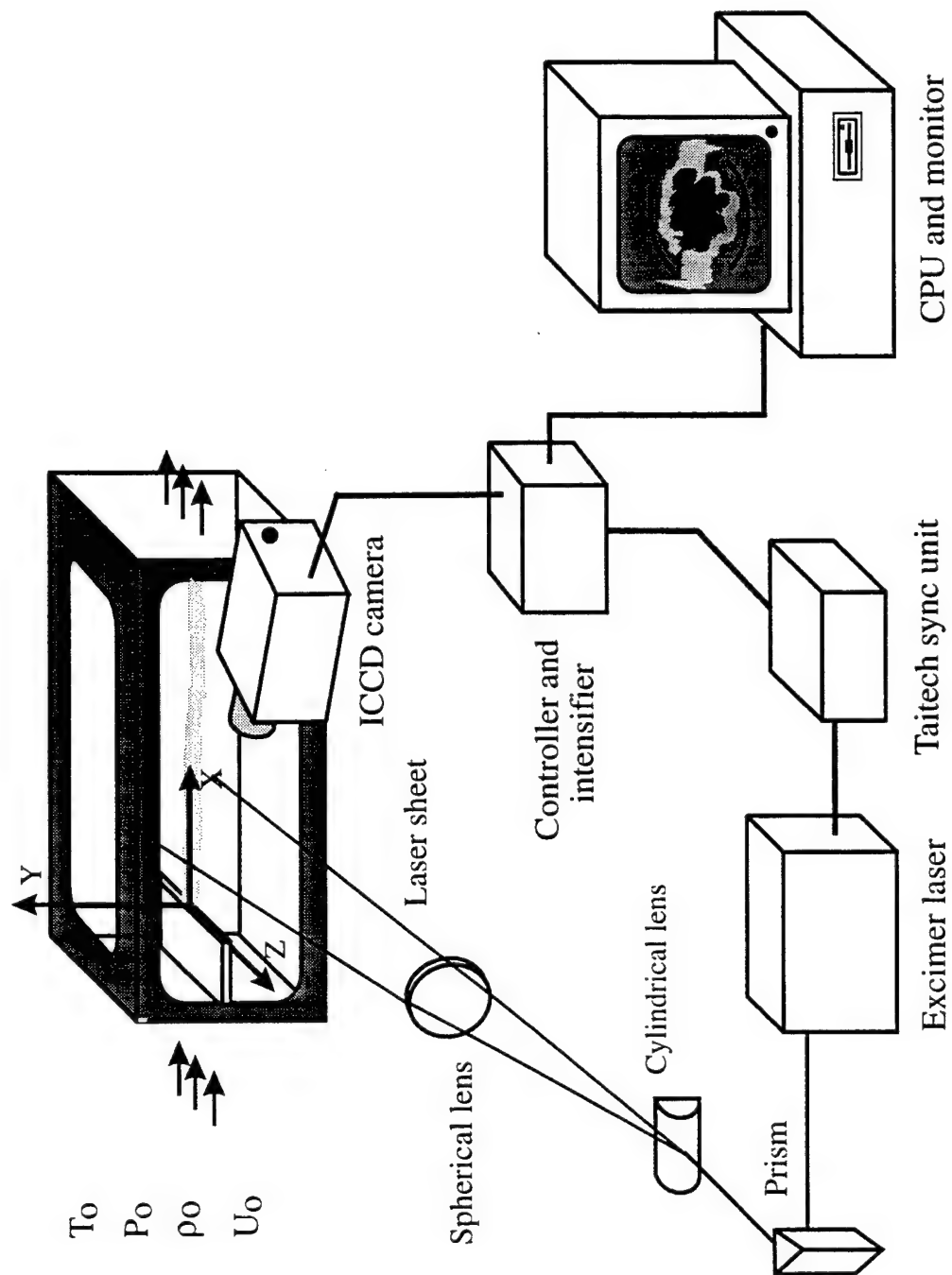


Figure 4.3. Schematic of flow visualization system to obtain Rayleigh/Mie scattering images of the face-on (Y,Z) plane of view.

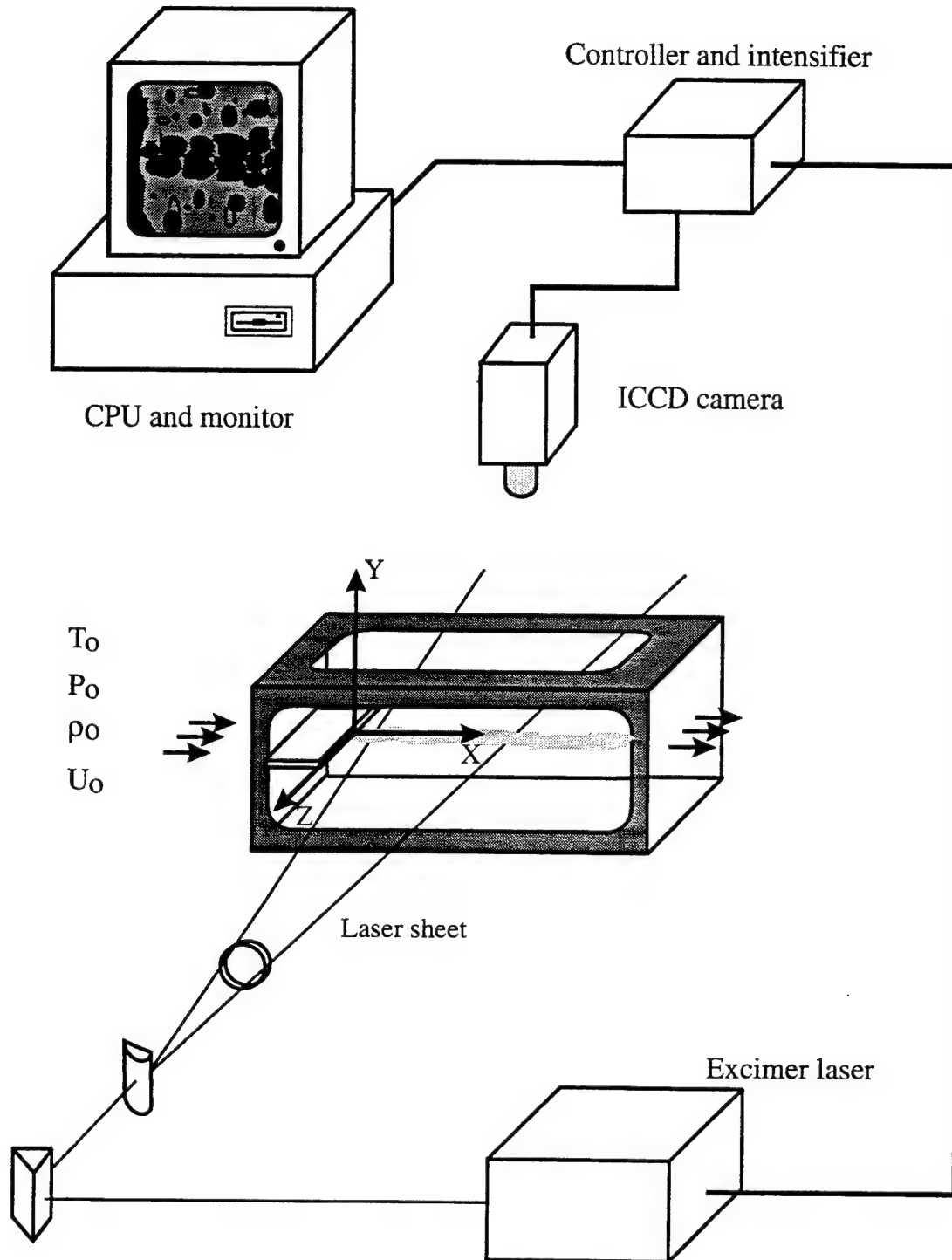


Figure 4.4. Schematic of flow visualization system to obtain Rayleigh/Mie scattering images of the plan (X,Z) plane of view.

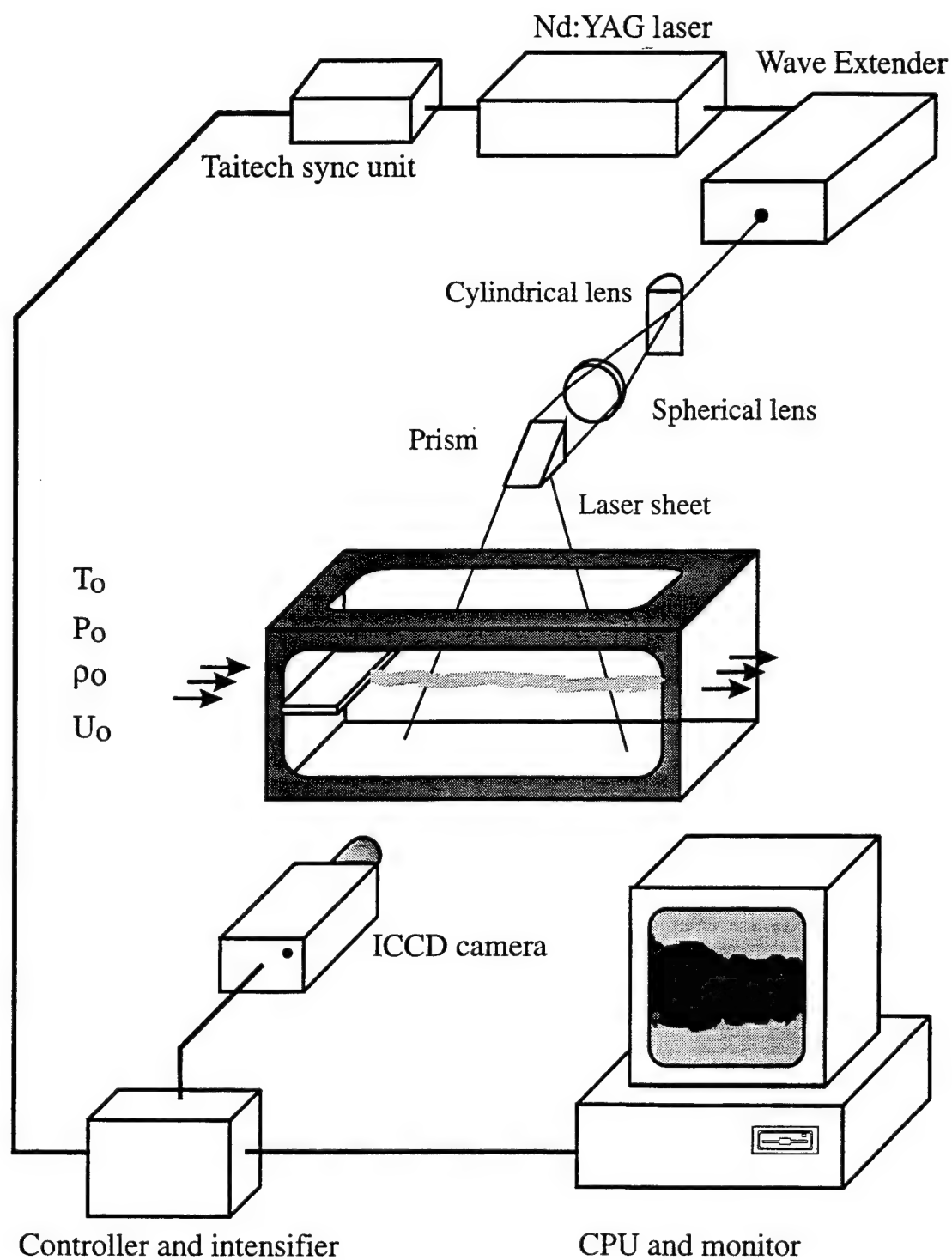


Figure 4.5. Schematic of acetone Planar Laser Induced Fluorescence (PLIF) imaging system to obtain PLIF images of the streamwise (X,Y) plane of view.

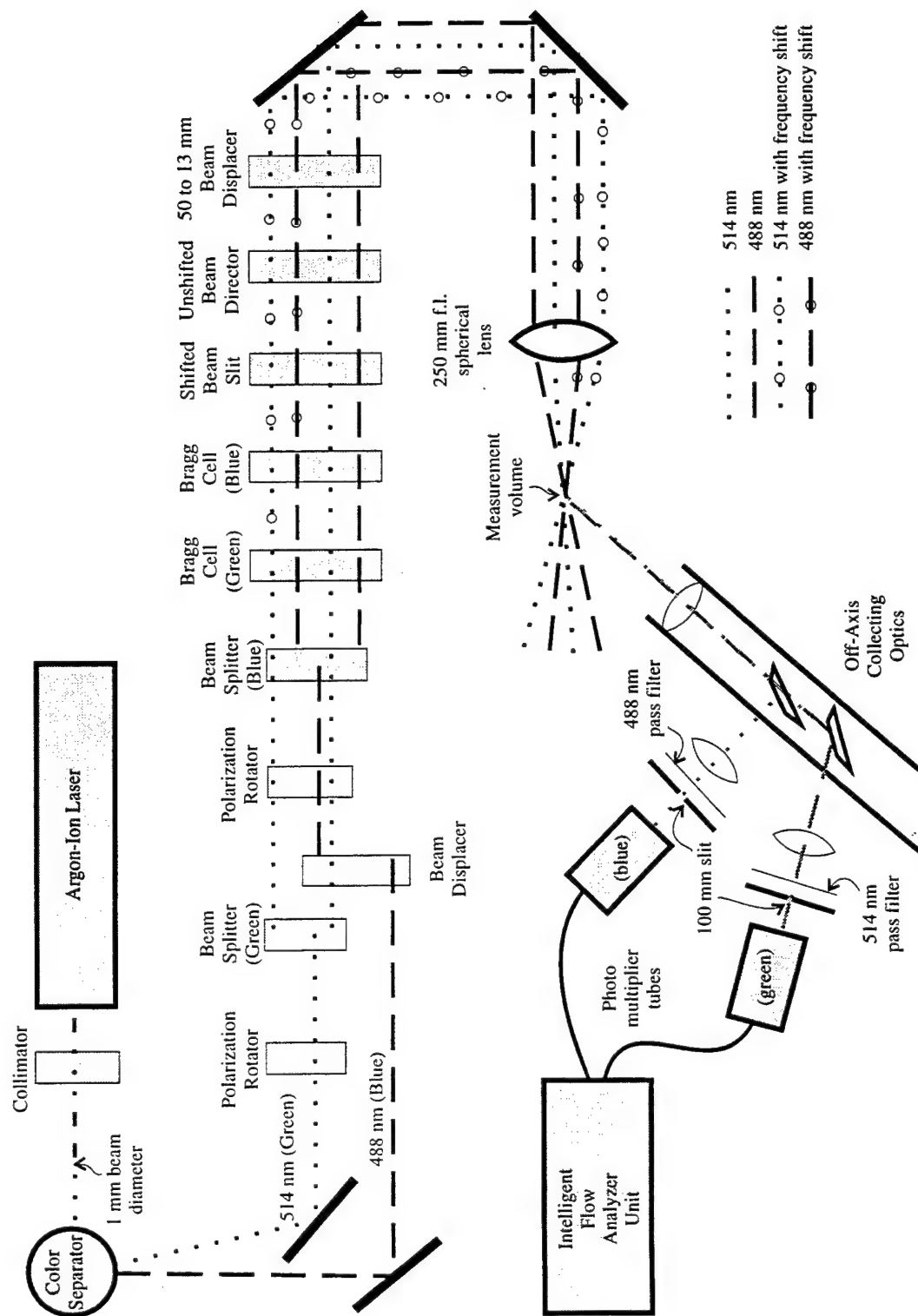


Figure 4.7. Schematic of experimental instrumentation for two-component Laser Doppler Velocimetry (LDV) measurements.

CHAPTER 5

EXPERIMENTAL RESULTS AND DISCUSSION

In the flow under investigation, the injected jet of helium and the mixing layers formed between the primary flow and the recirculating flow at the base of the strut undergo complex interactions. Modern computational techniques and advanced experimental methods can be used to explore details of turbulent phenomena in simple flows, but these methods render only limited results when applied to complex three-dimensional flows. It is therefore particularly difficult to gain a solid understanding of the underlying physics of complex three-dimensional flows, such as the one studied here.

Direct applicability of data obtained in basic flows to the present flow is restricted to the boundary layer on the strut before the complex three-dimensional effects are encountered and to the base flow without helium injection. Knowledge obtained in simple flows, such as planar shear layers and free jets, is of some limited use in the present investigation. The dynamics of planar shear layers apply to the dynamics of the two mixing layers formed between the primary freestream expanding around the base of the strut and the recirculation zone before the mixing layers encounter the severe pressure gradient in the recompression region. The jet dynamics involved in free jet injection are used to explain the basic characteristics of the different nozzle geometries and as a comparison to demonstrate the modification of jet dynamics caused by the mixing layers from the strut. Since traditional measurements of the jet spread for axisymmetric jets does permit a full description (and can even be deceiving) when applied to asymmetric

jets, new (novel) techniques were developed to compare jet spread and mixing resulting from injection through the different nozzle configurations in this study.

This chapter is presented in three sections. The first section discusses the features of the flow without injection. The second section presents visualization of the flow field resulting from helium injection using the circular (C), circular-with-tabs (T1, T2, T3), and elliptic (E1, E2, E3) nozzles in all the different orientations considered in the present study, (refer to Figure 3.7). The third section presents quantitative velocity-based data of the flow field without helium injection and with helium injection from the circular (C), circular-with-tabs (T1), and elliptic (E1) nozzles. This second and third sections highlight the jet dynamics and mixing performance resulting from helium injection using the different nozzle configurations.

5.1 Flow field components without injection

The flow field without injection was examined to establish a reference case against which the flow field with helium injection from the various nozzle geometries could be evaluated. Schlieren photography provided preliminary views of the flow field which were used to check for unexpected flow disturbances and to identify the domain of interest in the flow field. Figure 5.1 shows a schlieren photograph of the flow field without injection (see Table 2 and Appendix A for operating conditions). The flow is from left to right with $X/h = 0$ corresponding to the end of the strut; h is the thickness of the strut. This image covers the 12.7 cm streamwise length of flow considered in this study. The vertical lines located at $X/h = 1, 2, 4, 6.8$ and 10 indicate the locations of the cross-sectional face-on views for the Rayleigh/Mie scattering images to be presented in Section 5.2.

The black to white color gradients on the schlieren photograph in Figure 5.1 represent the density gradients in the flow field without injection. The knife edge at the

focal point of the second mirror is in a horizontal position, so the system is sensitive to density gradients in the transverse (Y) direction. The density gradients highlight the main features of the flow field: boundary layers on the top and bottom surface of the strut, expansion waves originating at the base of the strut, recompression shock waves, and mixing layers formed at the base of the strut between the primary flow and the recirculating flow. Since the time exposure of the schlieren photograph (1/400 s) is long as compared to the time scale of motion of the flow, the density gradient effects are integrated over time and over line of sight.

The boundary layer appears as a region of high density gradient on the surface of the strut and is more visible on the top surface (bright region) than on the bottom surface. It should be noted that the density gradient toward the edge of the boundary layer is very small, so that the edge is difficult to locate.

The Mach 2 freestream, including the boundary layers, expands around the base of the strut and encircles a recirculation zone. In Figure 5.1, the expansion fans appear as a bright band (top) and a dark band (bottom) emanating from the base of the strut and angled away from the centerline of the strut (X-axis). The photograph shows an upstream angle ($m1$) of 30° and a downstream angle ($m2$) of 24° for the top and bottom expansion fans (see Figure 5.2 for an illustration of terminology). These angles were measured from Figure 5.1 at about $X/h = 4.2$, outside the influence of the mixing layers formed at the base of the strut. They agree, to within a few degrees, with the value calculated from a simple Prandtl-Meyer expansion wave model, assuming an 18° slipline between the primary flow and the recirculation flow at the base of the strut. The assumed slipline angle of 18° was approximated from a Rayleigh/Mie scattering image of the flowfield without injection (discussed in Section 5.2.1) and computed from LDV data (discussed in Section 5.3.2.1).

The recirculation zone at the base of the strut is not well defined on the schlieren photograph. Rayleigh/Mie images capturing the recirculation zone will be presented in Section 5.2.

Two mixing layers, one on each side of the strut, are formed between the primary flow and the recirculating flow. These two mixing layers merge downstream at a location which is referred to as the recompression region. The region occupied by the mixing layers is referred to as the wake of the strut. It is evident in Figure 5.1 that the wake shows virtually no spread downstream.

Recompression shock waves are formed from the coalescing of compression waves in the region where the two mixing layers meet. The density increases through the recompression shock waves while it decreases in the expansion waves, causing the shock wave to appear of opposite intensity (i.e., dark vs. bright) to the adjacent expansion fan on the schlieren photograph. Two weak shock waves appear to be generated in the top air stream upstream of the base of the strut, while one appears in the bottom stream. These shock waves are reflected from the top and bottom walls of the tunnel and intersect the mixing region at the very end of the test domain in this study ($X/h = 10$).

The following two sections describe quantitative and qualitative characteristics of these components in the flow field with emphasis on the mixing region behind the base of the strut with and without helium injection.

5.2 Flow visualization

Each flow visualization image provides qualitative information about an entire plane of the flow. The Rayleigh/Mie scattering images are created by passing a laser sheet light through the test section and capturing the scattered light using an ICCD camera (see Section 4.3.2, Figure 4.5). The light is scattered off ice crystals in the primary freestream air flow. Moisture, naturally present in the supply air, condenses and

freezes as the air expands to Mach 1.92 in the supersonic nozzle. The resulting ice crystals, suspended in the freestream air, effectively scatter laser light. Thus, the free stream appears as bright regions on the Rayleigh/Mie image. On the contrary, the helium jet is unseeded and thus the mixing interface between the jet and the primary freestream flow appears on the Rayleigh/Mie images as a transition from marked fluid (bright regions) to unmarked fluid (dark regions). This technique of seeding only one of the two mixing fluids is referred to as the "scalar transport" technique [Clemens and Mungal 1991]. In addition to highlighting the mixing interface, the variation in number density of ice crystals in the boundary layer and across the shock waves in the freestream air highlights the boundary layer and shock waves.

Rayleigh/Mie scattering images were taken in three orthogonal planes of view: the streamwise (X,Y) plane, the face-on (Y,Z) plane, and the plan (X,Z) plane. The combination of these three planes of view provide a three-dimensional representation of the flow field. This is important in the injection cases since injecting helium from the base of the strut creates a highly three-dimensional flow field. The face-on (Y,Z) plane of view is located at the same streamwise (X/h) stations as the LDV profiles. This allows for direct comparison between velocity based profiles and structures appearing in the flow field.

A series of 20 instantaneous images was recorded for each selected plane of view. Both the streamwise and the spanwise images represent a 4.32-by-2.79-cm field of view, with the flow from left to right while the face-on view has a 3.30-by-2.03-cm field of view with the flow direction out of the plane of the page. These dimensions were imaged onto the 578-by-384-pixel array of the camera, giving a planar scale of about 75 μm per pixel for the streamwise and spanwise planes as opposed to 53 μm per pixel for the face-on view plane. However, the overall resolution of the image is limited by the laser sheet thickness of about 300 μm .

Rayleigh/Mie images in the Figures between 5.3 to 5.23 highlight the flow features with and without helium injection. The images of the flow field without injection serve as a reference case, to which the helium injection cases can be compared to. The images of the flow field with injection provide information on the dynamics and mixing characteristics of the jets issued from each of the nozzle geometries investigated in the present study (refer to Figure 3.7).

A circular (C) nozzle is considered as the baseline case for helium injection from the base of the strut. A circular-with-tabs nozzle in various orientations (T1, T2, T3) and an elliptic nozzle in similar orientations (E1, E2, E3) are the asymmetric geometries used to explore the effect of the nozzle geometry on mixing of the helium jet with the freestream air. The primary freestream Mach number for the no injection and the injection cases is 1.92. For the injection cases, the helium exits the converging nozzles at sonic velocity, and static pressure equal to four times the static pressure of the freestream air. This static pressure ratio is denoted by (Ψ). Thus $\Psi = 4$ for all the Rayleigh/Mie images presented in the present work (see Table 2 and Appendices A and B for operating conditions). The $\Psi = 4$ ratio was chosen to obtain a highly underexpanded jet. This closely mimics operational fuel injection in scramjets.

5.2.1 Flow field components

Figure 5.3 shows instantaneous Rayleigh/Mie images in the streamwise (X,Y) plane for the no injection (N) case and the helium injection case using a circular (C) nozzle. The plane of view for these figures is located on the centerline of the tunnel (coincident with the centerline of the jet for the injection case) with $X/h = 0$ corresponding to the end of the strut; the flow direction is from left to right. As seen by the dark regions on the right and left sides of the images, the laser sheet of light did not span the entire width of the image field of view. Also, since the sheet of light propagates

from top to bottom, the strut (which appears as the dark rectangular shape at the left side of the image) blocks the laser light from reaching the flow field under the strut. This is the reason for the absence of light under the strut.

Boundary Layer

The boundary layer appears as a slightly brighter region on the top surface of the strut. Since these images are instantaneous, they capture the rough, wavy structures of the turbulent boundary layer. Although it is possible that the addition of enough helium at high pressure could transform the favorable pressure gradient between the freestream primary flow and the region behind the base of the strut into an adverse pressure gradient large enough to cause separation upstream of the shoulder of the strut base. The presence of the helium jet in this study does not appear to have caused the boundary layer to separate from the surface of the strut upstream of the shoulder (Figure 5.3).

The boundary layer on the surface of the strut, by definition, stops at the end of the strut. However, the structures in the boundary layer propagate downstream and are labeled as "boundary layer remnants" in Figure 5.3. These structures grow as they pass through the expansion waves at the base of the strut. It is possible that this growth is proportional to the amount of expansion through the expansion waves over the edge of the strut in a manner similar to that discussed by Arnette et al. [1993a] in his analysis of the effects of expansion on compressible boundary layers. Arnette et al. observed the presence of well-defined turbulent structures of a very large streamwise, and limited spanwise, extent in the boundary layer of a Mach 3 flow. The large structures increased in scale across a 7° and 14° central expansion and a 7° and 14° gradual expansion while the small scales appeared to be quenched during expansion.

Recirculation Zone

As the incoming flow expands over the edge of the base, fluid is "trapped" in the recirculating region behind the base of the strut. Fresh fluid feeds into this region from

the recompression region, while part of the recirculating flow provides entrainment of the mixing layer. The region behind the base of the strut is referred to as the recirculation zone and contains regions both positive and negative streamwise velocities.

The recirculation zone in the Rayleigh/Mie images appears as the dark triangular region behind the base of the strut in the flowfield without helium injection, as illustrated by the no injection (N) case in Figure 5.3. The static temperature of the recirculation zone is approximately equal to the stagnation temperature (300 K). This elevated temperature (300 K compared to the freestream static temperature of 167 K) drives the ice crystals formed in the freestream back into the vapor state. This destruction of the scattering sites is why the recirculation zone appears dark in the Rayleigh/Mie image of the no injection (N) case.

For the injection cases, the dark region at the base of the strut in the Rayleigh/Mie image is largely a result of the presence of helium. However, as cited previously in Section 4.2.2, the ice particles present in air captured in the recirculation zone are vaporized, thus the air in the recirculation zone also appears dark in the Rayleigh/Mie scattering images. Because of the similar appearance of air and helium in the recirculation zone, the Rayleigh/Mie scattering technique cannot be used to study the detailed evolution of the helium jet in the recirculation zone. This ambiguity is confined to the recirculation zone. Further downstream, the evaporated water in the recirculating air recondenses as it mixes with freestream air downstream.

Jet Structure

To see the helium jet structure in the recirculation zone, two separate techniques were employed in which effectiveness of the flow marker was not destroyed by the elevated temperature behind the base of the strut. The first technique was acetone planar laser-induced fluorescence (PLIF). Acetone was added to the helium reservoir that fed the jet flow. A Nd:YAG laser, operated at $\lambda = 266 \text{ nm}$, was used with a series of lenses

and prisms to form a sheet of laser light (Figure 4.5). The laser sheet was passed through the test section to illuminate a streamwise "slice" of the flow field. Figure 5.4 shows the resulting PLIF images for the helium jet injected from a circular (C) nozzle mounted in the base of the strut into a Mach 1.92 freestream flow at jet-to-freestream static pressure ratios (Ψ) of one, two and four. Although the $\Psi = 4$ pressure ratio is the focus of this study, $\Psi = 1$ and 2 are shown here to demonstrate the effects of varying the static pressure ratio. The high intensity (bright) regions show acetone fluorescence, and reveal the presence of acetone vapor suspended in the helium jet. The acetone PLIF images provide a qualitative "picture" of the number density field. The images of the underexpanded jets ($\Psi = 2, 4$) shows the presence of a barrel shock and a Mach disk. The Mach disks for $\Psi = 2$ and 4 appear to be located at about 5 and 8 mm downstream of the nozzle exit (i.e., $X/d_e = 1.4$ and 2.2 respectively). The acetone PLIF images also show the presence of helium in the recirculation zone.

As the $\Psi = 4$ underexpanded jet exits the nozzle at sonic speed, it expands within the bounds of the barrel shock to a calculated peak Mach number of about 4 [Chen et al. 1995] before passing through the Mach disk and becoming subsonic once again after which the jet accelerates to a high subsonic or supersonic velocity as it mixes with the supersonic freestream air (Figure 2.18). The underexpanded jets show a higher initial jet radius, but the jets appear to remain more collimated than the $\Psi = 1$ case. The $\Psi = 1$ jet appears to be much more intermittent, suggesting the presence of higher-order modes of large-scale structures. Such structures would likely appear further downstream for the $\Psi = 2$ and 4 cases when the higher pressure effects diminish. This implies quicker mixing for the $\Psi = 1$ case. However, less fuel would be injected (i.e., $\dot{m}_{He, \Psi=1} = 1/2 \dot{m}_{He, \Psi=2} = 1/4 \dot{m}_{He, \Psi=4}$) in this case. Thus, injecting fuel at $\Psi = 1$ would require more injection ports at the base of the strut than the $\Psi = 4$ case; this would not be a problem if space permitted.

In addition to acetone PLIF, titanium dioxide (another medium that retains its effectiveness as a marker at elevated temperature) was suspended in an air jet in order to observe the behavior of the recirculation zone with a jet emanating from the elliptic (E1) and the circular-with-tabs (T1) nozzles. To generate a flow of titanium tetrachloride suspended in air, air was passed through a swirl chamber filled with titanium tetrachloride. The swirl chamber consists of a spiral inlet tube extending into a canister containing titanium tetrachloride and then an exit port. The amount of titanium tetrachloride added to the jet was increased by increasing the pressure (mass flow rate) of the air entering the swirl chamber. When a low mass flow rate of air was passed through the swirl chamber and the injection nozzle, a light mist of titanium dioxide appeared in the recirculation zone. When a higher mass flow rate of air was passed through the swirl chamber and injection nozzle, a dense opaque fog appeared in the recirculation zone, clearly marking its boundary. Both mass flow rates were high enough to maintain choked conditions at the nozzle exit and thus maintain an underexpanded sonic jet.

When the tunnel was disassembled, it was discovered that the base plate of the strut was coated with residual titanium tetrachloride. The residue extended from the nozzle exit halfway to the side wall on both spanwise sides of the nozzle. This suggests the presence of counter-rotating recirculation cells on each spanwise side of the nozzle, as seen in supersonic flow over a rearward facing step [Petrie et al. 1986], and in subsonic flow over a finite strut [Raffoul 1995]. Multiple recirculation cells in the spanwise direction behind the base of the strut would support organized spanwise motion of the recirculating fluid between the tunnel side walls. The sense of rotation of the circulating fluid in these cells would be such that velocity vectors adjacent to the helium jet would point downstream to match the velocity vector of the helium exiting the nozzle.

Expansion Fans

As the freestream flow expands around the base of the strut, two-dimensional expansion fans emanate from the top and bottom edge of the base of the strut. For the no injection (N) case, a slipline exists at the boundary between the primary flow and the recirculating flow. The slipline appears as the separating line between the bright region marking the freestream and the dark region marking the recirculation zone in the instantaneous Rayleigh/Mie scattering images of the no injection (N) case (refer to Figure 5.3). The sliplines enclosing the recirculating flow appear to be at an angle of approximately 18° to the X-axis for the no injection (N) case.

The streamwise Rayleigh/Mie image on the centerline of the injector nozzle for helium injected from the circular (C) nozzle (Figure 5.3) illustrates that the presence of the helium jet acts to separate the mixing layers formed at the base as compared to the flow field without injection. This suggests that the mass of the jet fluid acts as a bluff body extension of the strut as discussed by Sullins et al. [1982].

Up until this point, the discussion of the flow visualization results has focused on the differences between the no injection (N) and the baseline helium injection cases using the circular (C) nozzle. The following discussion focuses on the differences created by using different nozzle geometries for the helium injector. Figure 5.5 shows schematics of the flow components present with helium injection, appearing in the instantaneous Rayleigh/Mie images of the three orthogonal planes of view. The instantaneous images shown in this publication are representative of the group of 20 instantaneous images taken at each station. These schematics are intended as a reference to facilitate discussion of the Rayleigh/Mie scattering images.

The illustration in Figure 5.5a depicts an instantaneous Rayleigh/Mie scattering image in the streamwise (X,Y) plane of view located on the centerline of the injector nozzle. The flow is from left to right with the origin of the (X, Y) coordinate system

located at the center of the nozzle exit. This Rayleigh/Mie scattering image highlights the shock waves and the fluid previously in the boundary layer (remnants of boundary layer) surrounding the jet and recirculation zone.

The illustration in Figure 5.5b depicts an instantaneous Rayleigh/Mie scattering image in the plan (X,Z) plane of view located on centerline of the injector nozzle. The flow is left to right with the origin of the (X, Z) coordinate system at the center of the nozzle exit. Helium and air from the recirculation zone sputters downstream alongside the jet and appears on the images as dark blobs (pictured as open spirals on the illustration). As previously discussed, warm air from the recirculation zone appears dark because it contains moisture in a vapor state, which doesn't scatter appreciable light until it mixes with cooler air and condenses downstream. This view doesn't show the shock waves as they are above and below this spanwise plane located on the centerline of the tunnel.

The illustration in Figure 5.5c depicts the instantaneous Rayleigh/Mie images taken in the face-on (Y,Z) plane of view, specifically at $X/h = 1$. The face-on (Y,Z) planes of view are perpendicular to the jet flow, with the flow direction being out of the plane of the page. The face-on plane of view is actually skewed slightly and creates an image that is compressed by approximately 8% in the spanwise direction as described in Section 4.2.3. This was corrected by stretching the spanwise dimension of the original image by 8%. The face-on views shows the three dimensionality of the "conical shock waves," in that they are curved around the jet. These "conical shock waves" will be discussed in this section. The face-on images at $X/h = 1$ are upstream of the location where the nominal two-dimensional recompression shock waves originate. Thus, the two-dimensional shock waves are not present in this schematic of the face-on view at $X/h = 1$.

Average images are also presented in this section. The average images represent the mean intensity values at each pixel location as calculated from each group of 20 instantaneous images. Average images were generated for the group of 20 images taken at each station by computing the average intensity values for each pixel in the 578 by 384 pixel array representing the image field of view. The governing equation for average intensity is

$$\bar{I}_{i,j} = \frac{1}{n} \sum_{k=1}^n (I_{i,j})_k, \quad 5.1$$

where $I_{i,j}$ is the instantaneous intensity of the pixel located in row i and column j of the image pixel array, and n is the total number of samples in the summation set ($n = 20$ in this study).

Figures 5.6 and 5.7 show the instantaneous and average Rayleigh/Mie images of the streamwise (X,Y) plane for the no injection (N) case and the seven different helium injection cases ($\Psi = 4$) with various nozzle configurations (C, T1, T2, T3, E1, E2, E3). The plane of view for these figures is located on the centerline of the tunnel (coincident with the axis of the nozzles) with $X/h = 0$ corresponding to the end of the strut and the flow direction being from left to right. The field of view is 4.32 cm wide and 2.79 cm high. As mentioned previously, the dark triangle at the base of the no injection (N) case shows warm air in the recirculation zone where the scattering particles are vaporized, and the dark regions at the base of the strut for the helium injection case show predominantly helium, void of scattering particles, and also contain warm air from the freestream.

Purple plasma

A ghostly looking white smudge at the nozzle exit seen most clearly in the instantaneous and average streamwise Rayleigh/Mie scattering images of the T2, T3 and

E3 cases was caused by a purple plasma formed at the nozzle exit (Figures 5.6 and 5.7). The plasma appeared several times throughout the experiments for all jet-to-freestream static pressure ratios ($\Psi = 1, 2$, and 4) and nozzle configurations. The short plume of purple plasma intermittently moved from one side of the jet to the other. Since the plasma acted as a continuous light source, it illuminated the ICCD camera pixel array during the entire time the camera aperture was open (the gated time), whereas the Rayleigh/Mie scattering only illuminated the pixel array during the shorter duration of the laser pulse. Thus, the longer exposure time of the relatively weak plasma illumination, as compared to the strong Rayleigh/Mie scattering, was enough to produce the ghostly looking white smudge extending from the exit of the nozzle to about $X/h = 1$. Since the plasma occurred on some nights and not others, it was thought to be related to atmospheric conditions. Two theories of causality are: 1) stripping of electrons between the air and the helium, and 2) a build up of static charge between the windows mounted in the side walls of the tunnel, which was carried to the helium jet via the strut spanning the tunnel.

Recompression shock waves

The recompression shock waves appear in instantaneous (Figures 5.6) and average (5.7) Rayleigh/Mie scattering images in the streamwise (X, Y) plane of view as the dark lines in the freestream flow which diverge downstream. For the no injection (N) case, a two-dimensional recompression shock wave is generated at the location where the mixing layers formed between the primary flow and the recirculating flow merge (Figure 5.6). The mixing layers appear to merge at a streamwise distance of approximately $X/h = 1.3$; where $h = 1.27$ cm is the strut thickness. This distance is the streamwise length of the recirculation zone outlined in Figure 5.3. This value is in close agreement with the work of Amatucci et al. [1992], in which the recompression region occurred at approximately $X/h = 1.4$ for a configuration similar to this study. The main difference between

Amatucci's work and the present study is that Amatucci had a Mach 2.0 flow on top of the strut and a Mach 2.5 flow below, whereas the present work employs a Mach 2.0 flow on both sides of the strut.

The recompression shock waves that emanated from the interaction of the mixing layers are modified when helium is injected from the base of the strut. Therefore, the aforementioned recompression shock wave will be referred to as the two-dimensional recompression shock wave in the no injection (N) case, and as the nominally two-dimensional recompression shock wave in the injection cases (C, T1, T2, T3, E1, E2, E3). When helium is injected from the base of the strut, additional shock waves appear upstream of the nominally two-dimensional recompression shocks waves. These shock waves are also recompression shock waves. They result from the intersection of the mixing layers formed between the primary flow and the recirculating flow, and the helium jet mixing layer.

Since the helium jet is highly underexpanded, the rapid expansion of the jet at the exit of the nozzle causes the mixing layers encompassing the jet to diverge outward from the nozzle exit, which results in the interaction with the nominally two-dimensional mixing layers. Given that the injector nozzle exit is circular or elliptic, it is not surprising that the recompression shock wave formed by the interaction of the jet with the nominally two-dimensional mixing layers is itself not two-dimensional. They appear very much like longitudinal segments of a cone. For this reason and for the sake of clarity, these initial recompression shock waves resulting from the jet/mixing layer interaction will hereafter be referred to as "conical shock waves."

The three-dimensional conical shock waves coalesced with the nominally two-dimensional recompression shock waves between $X/h = 1.5$ and 3.0 , depending on which injection nozzle configuration was used. The resulting recompression shock is reflected off the top and bottom walls of the tunnel and was calculated to intersect the jet

at approximately $X/h = 21$. This is well downstream of the region examined in this study, which ends at $X/h = 10$.

The fact that the recompression shock waves in the average Rayleigh/Mie images (Figure 5.7) appear to be the same thickness as in the instantaneous images (Figure 5.6) indicates that these shock waves are stationary. If the shock waves fluctuated significantly, they would appear blurred in the average image as compared to the instantaneous images; this is not the case. The increase in pressure and corresponding increase in number density across the shock waves causes the flow to appear brighter downstream of the shock waves. Evidently, the increase in temperature across the shock waves is not enough to destroy the ice particles and to counteract the increase in number density due to the pressure rise.

Figure 5.8 shows the instantaneous Rayleigh/Mie images of the streamwise (X,Y) plane of view for the no injection (N) case and the injection cases. The plane of view is located on the centerline of the tunnel ($Z=0$) and just downstream of those images shown in Figure 5.6. The flow direction is from left to right. The recompression shock wave formed from the coalescing of the nominally two-dimensional and conical shock waves appears in the upper and/or lower left corner of these images. These planar images do not provide a complete representation of the three-dimensional jets, especially since they have different cross-sectional shapes. However, the transverse span of relatively unmixed helium shown in Figure 5.8 suggests that the helium jets in the C, T3 and E3 cases mix the least with the freestream air.

Since the camera was at a 30° angle to (rather than aligned with) the X-axis for the face-on plane of view, the horizontal scale is foreshortened relative to the vertical scale by about 8% in the original images. Figure 5.9 shows the original and corrected scale and Figure 5.10 shows an example of an original and corrected image. All subsequent face-on images shown in the figures are corrected face-on images.

Figures 5.11 and 5.12 show the instantaneous and average Rayleigh/Mie images of the face-on plane of view located at $X/h = 1$. The field of view is 3.30 cm wide and 2.03 cm high. All face-on images presented have been corrected for the 8% spanwise compression due to the view angle of the camera. The flow direction is out of the plane of the page. The dark horizontal stripe spanning the base of the strut is warm air present in the recirculation zone. For the injection cases, the darkest region in the center of the image that extends slightly above and below the recirculation zone (Figure 5.11) is the helium jet. The distinctly different shapes of the jets emanating from the various nozzle geometries are clearly seen in the face-on Rayleigh/Mie scattering images. The evaporation of the ice particles (used to mark the primary air flow) in the recirculation zone makes identifying the interface between the helium and the air in the recirculation zone difficult. The conical shock waves appear as the arc above and below the strut, enclosing a bright region, best seen on the average Rayleigh/Mie images of the face-on plane of view located at $X/h = 1$ (Figure 5.12). As discussed for the streamwise images, the fact that the conical shock waves are most distinct on the average images signifies that they are stationary shock waves. They are most pronounced (largest curvature) for the T3 and E3 cases and barely noticeable for the T1 and E1 cases. The strength of the shock wave indicates the extent to which jet spread in the transverse direction disturbs the nominally two-dimensional mixing layers.

The conical shock waves are present, but less distinct on the instantaneous and average images at $X/h = 2$ shown in Figures 5.13 and 5.14. These images capture the developing region of the nominally two-dimensional recompression shock as well as the conical shock waves. A series of weak nominally two-dimensional shock waves appear as series of horizontal dark lines spanning the image slightly above and below the jet (best seen in the E2 case of Figure 5.13); these waves coalesce to form a single stronger recompression shock wave. The dark region in the center of the image represents the

helium jet and the dark strip spanwise across the image represents the fluid from the recirculation zone propagating downstream. In comparing the jet cross-sectional view in the Rayleigh/Mie face-on images at $X/h = 1$ and 2, it is evident that the jets have spread slightly and the evaporated water in the warm air from the recirculating flow has begun to recondense as it mixes with the cooler air in the freestream. The bright region sandwiching the jet is a consequence of the primary flow having experienced a pressure increase (and corresponding number density increase) as it passed through the nominally two-dimensional recompression shock waves. This intensity increase was likewise shown in the streamwise images (Figures 5.6 and 5.7). The conical shock waves merge with the nominally two-dimensional shock waves and travel outside the field of view before the next streamwise station at $X/h = 4$. The instantaneous and average Rayleigh/Mie images of the face-on (Y,Z) plane of view for this station are given in Figures 5.15 and 5.16. The instantaneous and average face-on Rayleigh/Mie images for stations $X/h = 6.8$ and 10 are given in Figures 5.17 to 5.20. The face-on Rayleigh/Mie images clearly show that the jet shape, most distinct in at $X/h = 2$ and 4, and the mixing of the jet with the freestream air, most noticeable further downstream at $X/h = 6.8$ and 10, are different for the different nozzle geometries. The Rayleigh/Mie scattering face-on plane of view is most descriptive of the cross-sectional shape of the jet and will be used extensively in analysis of the jet development.

5.2.2 Jet dynamics governing jet shape

For the most part, the regions of influence of the mixing layer surrounding the jet and the mixing layers from the base of the strut overlap. Therefore, the data in these regions cannot be directly compared to data acquired in simple free jet flows or shear layer flows, but can be evaluated for similar trends. Identifying the similarities and differences between the results of the present study (concerning base injection with

different nozzle geometries) and the results from other studies (concerning free jets with different nozzle geometries) should give insight into the mechanisms at work in the present flow field and their relative importance. The flow dynamics for each of the nozzle configurations (C, T1, T2, T3, E1, E2, E3) will be discussed in this section using instantaneous and average Rayleigh/Mie scattering images. The instantaneous images show an array of structures of different sizes at the interface between the jet and the primary flow. The average images exemplify the stationary structures since the nonstationary structures are "filtered-out" in the image averaging process.

The face-on images show the jet shape most clearly as it develops downstream. The jet shapes are distinct for the face-on images at $X/h = 1, 2$ and 4 , but lose their form as they travel downstream to the point that they are amorphous at $X/h = 10$. Therefore, the jet shapes will be described primarily with reference to the face-on instantaneous and average images at $X/h = 1, 2$ and 4 .

5.2.2.1 Circular nozzle configuration (C)

Since the air in the recirculation zone behind the strut is of relatively low velocity and at a lower pressure as compared to the helium at the injector nozzle exit, the injected jet is expected to behave much like an underexpanded free jet until it interacts with the mixing layers formed between the primary flow and the recirculating flow at the base of the strut. Upon exiting the nozzle, the underexpanded helium jet forms a barrel shock and a Mach disk. The barrel shocks for a circular jet at jet-to-freestream static pressure ratios of $\Psi = 2$ and 4 are shown in the acetone PLIF images of Figure 5.4. The high intensity (bright) regions show acetone fluorescence and thus mark the presence of acetone vapor suspended in the helium exiting the injector nozzle. Acetone PLIF images were taken only for the circular nozzle and not for the jets emanating from the circular-with-tabs or elliptic nozzles. The geometry of the shock structure would most certainly

be different. Once the jet interacts with the mixing layers the flow dynamics become very complex.

It is obvious from the face-on images of the jet in Figures 5.11 to 5.20 that the mixing layers formed between the primary flow and the recirculating flow at the base of the strut restrict jet spread in the transverse direction compared to free jet behavior. This is most evident for the case of the circular (C) injector, the circular-with-horizontal-tabs injector (T3), and the elliptic injector nozzle with a horizontal major-axis (E3) as discussed in the following paragraphs.

For helium injection from the circular (C) nozzle, an oblong jet is produced where a circular jet would be expected in a free jet case (see Figures 5.11 to 5.16). Using terminology for an ellipse, the major-axis of the oblong jet cross-section is a little over twice the minor-axis dimension at $X/h = 2$. The structures seen at the circumference of the jet in the instantaneous images are "averaged out," for the most part, on the average images of the circular (C) nozzle except for the "lobe" protruding from the upper right corner of the jet cross-section on the images at $X/h = 1, 2$, and 4 (Figures 5.11 to 5.16). The fact that the lobe appears on these average images indicates that it is spatially stationary and propagates downstream without significant changes until between $X/h = 4$ and 6.8 . This stationary anomaly in the jet shape is likely a result of a perturbation and Taylor-Görtler type instability, inherent in underexpanded jets, which creates a pair of counter rotating vortices with the sense of rotation to eject jet fluid into the primary flow [Arnette et al. 1993b]. The source of perturbation could be as minute as a scratch inside the nozzle as discussed by Novopashin and Perepelkin [1989] and King et al. [1994]. By $X/h = 6.8$ the well defined large-scale structures have disappeared and the jet achieves a circular-type cross-section on average (Figure 5.18). By $X/h = 10$ only a small amount of core fluid is left unmixed (Figure 5.19)

For the injector with horizontal tabs (T3) and the elliptic nozzle (E3), based on the dynamics of similar free jets, growth in the transverse direction is expected to be more pronounced than the growth in the spanwise direction. Figures 5.14 and 5.16 show that this is not the case. The differences between jet dynamics of injection into a base flow as opposed to injection into ambient air or a coaxial flow for circular-with-tabs and elliptic nozzles will be discussed in the following two sections.

5.2.2.2 Circular-with-tabs nozzle configurations (T1, T2, T3)

Previous studies have shown that tabs in subsonic and supersonic free jets generate a pair of counter-rotating vortices which engulf ambient fluid [Samimy et al. 1993, Reeder 1994, Reeder and Zaman 1994, and Zaman et al. 1994]. The generation of these vortices has been attributed to a pressure "hill" upstream of the tab and a lower pressure downstream of the tab. The strength of the pressure gradient was seen to increase with an increase in jet-to-freestream pressure ratio [Zaman et al. 1994]. As a result, one would expect that the circular-with-tabs nozzle cases (T1, T2, T3) would generate counter-rotating vortices like those shown in Figure 2.16. A more detailed discussion of the evolution of jets emanating from nozzles with tabs is contained in background Section 2.6.2.

Indeed, it does appear that these vortices are initiated at the exit of the circular-with-tab nozzles. The mixing layers formed between the primary flow and the recirculating flow at the base of the strut appear to either reinforce or degrade these vortices depending on the orientation of the nozzle with respect to the base flow. The interaction between the mixing layers and the counter-rotating vortices in the jet can be understood by considering the free jet dynamics for injection from a circular nozzle with two tabs, combined with the dynamics of the flow around the base of the strut without injection. For a free jet emanating from a circular (C) nozzle with two tabs, the jet fluid is expected

to flow predominantly in the streamwise direction along the axis of the nozzle. However, a strong secondary flow is present in the direction radially outward along a line perpendicular to the nozzle diameter which connects the two tabs, as illustrated in Figure 2.15. This motion relative to the strut for the three different orientations of the circular-with-tabs nozzle (T1, T2, T3) is shown in Figure 5.21. For the T1 case, this motion is directed along the spanwise axis of the tunnel, tangent to the mixing layers. This same secondary motion of jet fluid for the T2 case is directed at an angle into the mixing layers on the top and bottom of the strut. For the T3 case, the motion is directly into the mixing layers, i.e., normal to the mixing layers. The expected flow dynamics and vortices generated by each tab are shown in Figures 2.15 and 2.16, that is, until interaction with the mixing layers occurs at the base of the strut.

The presence of the mixing layers in the T1 case appears to reinforce the effect of the counter-rotating vortices at each tab to engulf freestream air and quickly bifurcates the jet into two adjacent cores. Bifurcation, in the T1 case is clearly shown in the face-on views at $X/h = 1, 2$ and 4 (Figures 5.11 to 5.16). The bifurcation is so pronounced that enough freestream fluid is allowed to flow between the cores that it appears, on the Rayleigh/Mie images, almost as if there were no jet on the ejector nozzle centerline. This can be seen by consulting the streamwise view of the injector nozzle centerline for the T1 case presented earlier, which looks nearly identical to the no injection (N) case (Figure 5.6 and 5.7). The development of this bifurcated jet can be seen on the plan (X,Z) view image as well. Figures 5.22 and 5.23 show the instantaneous and average plan (X,Z) views on the nozzle centerline (X-axis); the flow is from left to right and $X/h = 0$ corresponds to the origin at the base of the strut. The field of view is 4.32 cm wide and 2.79 cm high. Refer to Figures 4.2, 4.3, and 4.4 for laser sheet and camera orientations for the three planes of view. The two core centers become distinct at about $X/h = 1$ and travel in relatively parallel paths downstream.

For the T2 case, it is evident that the pair of streamwise vortices created by the tabs is distorted by the mixing layer to form the "S" like jet contour shown in Figure 5.13 and 5.14. Since the strength of the conical shock depends on the force of the interaction between the jet and the mixing layers, the conical shock wave can be used to identify where the most significant jet-wake flow impingement occurs around the jet perimeter, and the relative strengths of the interactions. The conical shock for the T2 case is lopsided (Figure 5.12) with the strongest interaction (largest curvature) being at the point where the jet secondary motion is directed as illustrated in Figure 5.21. Also, fluid from the primary flow appears to be engulfed in the same orientation as the tab locations. This is shown by the bright wisps of freestream fluid penetrating the T2 jet region and appearing on the instantaneous and average images at $X/h = 1$ and 2. (Figures 5.11 to 5.14). This is presumably a result of counter-rotating pair of streamwise vortices generated by each tab.

A noticeably larger conical recompression shock wave is generated for the T3 case. The conical shock wave is the strongest for the T3 case since the strongest radial component of jet flow generated by the tabs in this orientation was expected to be directly toward, i.e., normal to, the mixing layers rather than at an angle to them as in the T2 case or tangent to them as in the T1 case. [Refer to Figure 5.21 for the expected direction of the secondary (radial flow) component.] The two-dimensional mixing layers appeared to drastically suppress the action of the vortices generated by the tabs in the T3 case (Figures 5.11 to 5.20). No concrete evidence of stationary streamwise vortices is seen in the face-on Rayleigh/Mie images located at $X/h = 1, 2$, and 4. The jet remains compact in a cross-sectional area similar to that of the circular jet until $X/h = 6.8$ where it appears that the primary fluid is ingested at the sides of the jet as indicated by the indents in the jet (Figure 5.18). This is evidence of the presence of counter rotating vortices at these downstream locations.

5.2.2.3 Elliptic nozzle configurations (E1, E2, E3)

Jets emanating from elliptic nozzles evolve significantly different from those emanating from circular (and circular-with-tabs) nozzles. The elliptic jets begin with different dynamics. The large azimuthal variation in curvature of the elliptic vortical structures causes nonuniform self-induction and subsequent complex three-dimensional deformation. The most notable phenomenon of an oblong jet is axis-switching, in which the jet cross-section contracts in the direction of the major-axis and expands along the minor-axis, so that the two axes are eventually interchanged [Hussain and Husain 1989]. This phenomenon is believed to be intimately related to momentum thickness around the jet perimeter [Koshigoe et. al 1989].

The instantaneous and average face-on Rayleigh/Mie scattering images for injection from the elliptic nozzles (E1, E2, E3) are shown in Figures 5.11 to 5.20. It is evident from these images that motion of the jet fluid emanating from the elliptic nozzle configurations (E1, E2, E3) is modified by the mixing layers when compared to jets emanating from circular-with-tabs nozzles in a free jet situation. This is most obvious when comparing the evolution of the jets emanating from E1 and E3 nozzles. The jet emanating from the E1 nozzle configuration appears to have switched axes once immediately upon exiting the nozzle while the jet emanating from the E3 configuration appears to switch axes much further downstream. It appears from Figure 5.11 that the elliptic jet in the E1 orientation has gone through one axis switching by $X/h = 1$ and achieves an aspect ratio greater than three by $X/h = 4$ (Figure 5.15). Face-on images further downstream show that the E1 jet continues to spread along its new major axis and does not incur another axis-switching. On the other hand, the jet emanating from the E3 nozzle maintains a rather square shape from $X/h = 1$ to 4 (Figures 5.10 to 5.15) and then elongates slightly in the transverse direction $X/h = 6.8$ (Figure 5.16) to achieve one axis-

switch. The aspect ratio of the E3 jet at $X/h = 6.8$ is approximately half that of the E1 jet $X/h = 4$, showing the retarding effect of the mixing layers on the E3 jet dynamics relative to the E1 jet. The mixing layers do not appear to hinder the observed axis-switching in the E1 case, and perhaps even induced the axis switch and subsequent jet spread in the spanwise direction. However, the mixing layers could have been a prohibitive factor for subsequent axis-switching.

The instantaneous and average plan view images (Figures 5.22 and 5.23) of the E1 jet show that the jet core bifurcated (albeit less completely than in the T1 case) and that each core appears to be traveling away from the centerline as opposed to the T1 case in which the separated cores travel in relatively parallel paths. Bifurcation of a subsonic jet emanating from an elliptic nozzle is explained by a connecting type action of adjacent sides of the elliptic vortical structure [Hussain and Husain 1989]. If the "connection" becomes complete, the elliptic jet separates into two adjacent, almost circular, jets.

A distorted axis-switch is seen for the E2 case. The ends of the major axis of the elliptic E2 jet was distorted by the wake flow in a manner similar to the T2 case and also formed an "S" shaped jet cross-sectional area (Figure 5.13 and 5.14). The E3 jet remains rather compact until station $X/h = 6.8$ where an axis switch is apparent. Noticeable "curls" are present on the sides of the jet in the instantaneous face-on Rayleigh/Mie images at $X/h = 2, 4$, and 6.8 (Figures 5.13, 5.15, and 5.17). These curls are presumably caused by streamwise vortices. They appear to be spatially stationary in an average sense, judging from the indents in the sides of the jet. These indents indicate the presence of engulfed air between the location of the curls seen on the average images at $X/h = 2, 4$, and 6.8 (Figures 5.14, 5.16, and 5.18).

The mixing layers formed between the primary flow and the recirculating flow definitely impact the dynamics of the jets. One interesting observation shows that the wake flow is reciprocally distorted by the jet. The turbulent flow in the region behind the

jet creates a sinuous cross-sectional shape of the wake flow, seen as an undulating pattern across middle of the instantaneous figure of the no injection (N) case at $X/h = 2$ (Figure 5.13). This is characteristic of an instability and perturbation in the developing region of a shear or mixing layer. It is also present in the injection cases. The sinusoidal pattern appears in the average images of the T2 and E2 cases (Figure 5.14), signifying that the undulation is random in the other cases and becomes stationary during interaction with the T2 and E2 case flow dynamics. The other jets may have an equally effective stationary pattern, but its not obvious because the likely direction is either normal or parallel to the mixing layers and is masked by the other dynamics.

5.2.3 Comparison of jet mixing performance

The different nozzle geometries and orientations indeed create different jet dynamics and resulting shapes. This leads one to consider which nozzle configuration promotes the best mixing. The evaluation of mixing is a challenging task; researchers and engineers have taken many approaches to examine and compare mixing using a plethora of measurement techniques.

In order to judge mixing performance, it is essential to understand the meaning of the term "mixing" and its significance in combustion applications. Fuel and air molecules react and combust in a specific stoichiometric ratio described by a balanced chemical reaction combustion equation. Therefore, complete mixing for combustion applications is achieved when the fuel and oxidizer are homogeneously mixed at the molecular level. When fuel molecules are not adjacent to oxygen molecules, due to either incomplete mixing or to a shortage of oxidizer, the hydrogen and carbon components of the fuel molecules are not burned to their most oxidized state and the full potential energy of the fuel is not realized [Glassman 1987].

Mixing is initiated by large-scale structures that entrain large quantities of fluid into the mixing region. As the large scale structures are stretched by fluid motion, they impart energy to smaller scale turbulent structures, which in turn impart energy to yet smaller structures; thus forming an energy cascade. This process has been shown to be primarily inviscid down to the finest scale, where viscous diffusion occurs [Tennekes and Lumley 1972].

The initial driving force that generates the large-scale structures, in this case the velocity gradient between fluids, decreases and eventually disappears as the two fluids mix and acquire similar properties. At this point, the cascading process prevails and generates progressively smaller eddies, acting to relaminarize the flow. Although the progress from large-scale to small-scale mixing forms a kind of continuum, the large scale structures that initiate the mixing process and the smaller scale structures that dominate the turbulent mixing downstream typically require different analysis techniques or at least different methods or considerations when interpreting the results. This is especially crucial in combustion applications, where small-scale and even micro-scale turbulence is necessary to achieve efficient combustion. Therefore, in considering mixing, it is important to differentiate between large- and small-scale structures and to identify the regions of the flow where large- and small-scale effects dominate.

In practice, mixing can be evaluated by its status in the process from the initially segregated fuel and air streams toward a micro-mixed molecularly homogenous mixture. Mole fraction measurements are an attractive analysis tool since mole fraction is an ultimate measure of the status of micro-mixing between two fluids. Mole fraction measurements have been achieved using intrusive gas sampling probes [Cox et al. 1994] and nonintrusively with advanced laser techniques [Abbitt et al. 1991]. However, mole fraction measurements are difficult to achieve especially in combustion flows.

Fortunately, other measurement techniques provide useful information to describe mixing.

The traditional line of sight imaging methods using schlieren or shadowgraph systems reveal the area of mixing as in the case of a two-dimensional shear layer flow. As one can imagine, the use of line of sight techniques is limited in three-dimensional axisymmetric and asymmetric flows because of the integrating effect along the line of sight.

Traditional planar flow visualizations, such as Planar Laser Induced Fluorescence (PLIF) or Rayleigh scattering employing laser sheet lighting, provide a two-dimensional plane of information. Strategically positioning the planes of view in series in three orthogonal views provides a complete three-dimensional matrix of information, even for a complex three-dimensional asymmetric flow. The instantaneous planar images can show the overall components of the flow and flow structures at the interface of the mixing fluids.

Digitized planar images offer opportunity for a wide variety of mathematical analyses. Two such as methods of analysis to highlight organized structures in the flow field are fractal analysis [Barnsley 1988], in which turbulent mixing is evaluated based on geometric patterns seen in a cross sectional view of the flowfield [Sreenivasan 1991], and Fast Fourier Transforms (FFTs) to identify spatially repeated structures in the flowfield [Messersmith and Dutton 1991]. In addition, pointwise statistical analysis using mean, and standard deviation values can be used to characterize the flow.

The above methodologies can be applied in parallel to account for the large- and small-scale mixing. In these studies, the large-scale mixing is relayed by the jet spread, the mixing potential as given by means of a shape factor and the quality of small-scale mixing by a mixedness index.

The progress of large-scale mixing in entraining air into the helium jet and expelling helium from the jet into the surrounding air is demonstrated in terms of jet spread. This type of measurement yields large-scale, global mixing patterns, but fails to provide a complete description of mixing. For example, two streams of fluid can merge into a large vortex (appearing as a large mixing region on a schlieren or shadowgraph image), yet the area of chemical reaction which promotes combustion and relies upon micro-mixing may be very small. The "bridge" between the large- and small- scale structures can be visually seen as the stretching and contorting of the large-scale structures down through the smaller scales. This can be quantitatively described on the large-scale level by a shape factor that exemplifies the mixing potential of the large-scale structures capable of imparting energy in a cascading process down to the smaller scales. In addition to providing a parameter for inviscid mixing potential, the shape factor also indicates the relative amount of surface area available for micro-mixing through viscous diffusion between the two fluids. Finally, a measure of the quality of mixing in the mixing region is desirable to completely describe the mixing. The quality of mixing in this study is portrayed by a pointwise statistical parameter referred to as mixedness.

Digitized planar Rayleigh/Mie scattering images provided the two-dimensional array of point measurements used to compute statistical mixing parameters. The ICCD camera used to capture the Rayleigh/Mie images provided a 578 by 384 pixel array of intensity values representing each planar field of view. The pixel intensity values represent the amount of light scattered from the ice particles suspended in the primary air flow. When viewing the Rayleigh/Mie scattering images, it must be kept in mind that the ice particles evaporate in the recirculation zone and recondense downstream.

Since large-scale inviscid mixing dominates the initial development of the jet and small-scale mixing dominates the downstream evolution of the jet, it is reasonable to apply large-scale analysis near the nozzle exit and small-scale analysis further

downstream. It is obvious from the face-on Rayleigh/Mie scattering images in Figures 5.11 to 5.19 that distinct large-scale structures dominate the flow at $X/h = 1$ and 2, and that these large scales are not apparent at $X/h = 10$. However, the growth and decay of the large scale structures is progressive, so that attempting to choose a specific transition *point* where the large-scale and small-scale effects are equal is futile. Rather, an intermediate region of transition can reasonably be identified. It appears that characteristics of the initial large-scale structures, such as the lobe appearing at the upper right corner of the circular (C) jet at $X/h = 1, 2$, and 4, or the ends of the "S" shape in the T2 and E2 jet at $X/h = 2$ and 4, appear to disseminate significantly between $X/h = 4$ and 6.8 (Figures 5.15 to 5.18). Therefore, the large-scale analysis via jet spread and shape factor was executed using the face-on views at $X/h = 1, 2$, and 4 while the mixedness analysis was performed for the face-on images at $X/h = 4, 6.8$, and 10.

5.2.3.1 Jet shape factor

Since the jet is asymmetric, the jet spread cannot be discussed in the conventional terms of increase in jet radius as the jet propagates downstream. Rather, an effective radius, R_0 , defined as

$$R_0 = \sqrt{\frac{A}{\pi}}, \quad 5.2$$

where A is the cross-sectional area of the jet.

In order to evaluate the mixing potential of the different injector geometries, one can consider the interfacial surface area between the jet and surrounding fluid per unit volume of jet fluid available for mixing. When considering a cross-sectional plane of the jet, this corresponds to the ratio of the jet perimeter (p) to the cross-sectional area (A) of

the enclosed region. A circle is the shape with the smallest perimeter to area ratio. Thus, dividing the perimeter to area ratio for an asymmetric jet by the perimeter to area ratio of a circular jet with the same cross-sectional area results in a nondimensional geometric parameter referred to as the shape factor. The shape factor is defined as

$$S = \frac{P}{2\pi R_0}. \quad 5.3$$

The shape factor is similar to the compactness parameter used to evaluate jet spread for a Mach 1.63 air jet injected from various noncircular nozzles mounted in the base of a swept ramp in a Mach 2 freestream air flow [Haimitovich 1994]. Obviously a circular jet has a shape factor of 1. Since a circle is the shape with the smallest perimeter to area ratio, shapes factors for anything but a circular cross-section are greater than one. A large shape factor signifies a convoluted interface between the jet and ambient fluid. A convoluted perimeter suggest the presence of large-scale structures, and large-scale structures posses potential energy to fuel the mixing process. These large-scale structures can impart energy through the energy cascade process down to the small-scale structures needed for complete mixing for combustion. In addition, a larger shape factor also signifies more interfacial surface area available for viscid small-scale mixing per volume of enclosed fluid. From either perspective, a large shape factor inevitably promotes the small-scale mixing necessary for efficient fuel and air combustion.

The challenge in deriving the jet cross-sectional area is defining and identifying the boundary of the jet in a meaningful manner. The two primary regions of the jet are the core and the mixing layer. The core is the portion of the jet that remains unmixed, i.e., 100% helium. The jet mixing layer is the portion of the jet that contains helium mixed with air. The mixing region is characterized by high fluctuating values and gradient of

the physical properties that differ between the two mixing fluids such as mean velocity and helium mean mole fraction for the case at hand. Thus, it seems sensible to identify the boundary of the jet based on the location of fluctuations or gradient of values varying between the helium jet core and freestream air.

Since standard deviation calculations are based on the magnitude of fluctuations relative to the local mean value, the highest standard deviation occurs in the same place regardless of the laser sheet irregularities or other variation effecting image intensity values. Thus, using the high standard deviation values to mark a contour in the mixing layer around the perimeter of the jet avoids the dilemma of calibrating the average images to obtain a threshold value, to mark the edge of the jet, that is consistent from one average image to another. High standard deviation of the intensity values among the 20 instantaneous Rayleigh/Mie images taken at each location arise from the helium and air engulfed in the jet mixing layer intermittently passing the plane of view. The maximum standard deviation values around the jet can be loosely compared to the neutral (or saddle) point about which the shear layer structures seem to rotate. The high standard deviation contours mark the most active region of mixing between the helium jet and freestream air.

The contours marking the highest standard deviation values in the mixing region were used to define the jet contours for subsequent analysis of jet spread and shape factor. The first step in obtaining this contour is to compute a standard deviation image from the 20 instantaneous Rayleigh/Mie images taken at each face-on plane of view of interest. The standard deviation in intensity values for each pixel in the 578 by 384 pixel array was computed using the equation:

$$(\sigma_I)_{i,j} = \sqrt{\frac{1}{n} \sum_{k=1}^n (I_{i,j} - \bar{I}_{i,j})^2} \quad 5.4$$

where i and j are the row and column of the pixel in the 578 by 384 pixel array of the ICCD camera, and n is the total number of samples in the summation set ($n = 20$ in this study). Figures 5.24, 5.25 and 5.26 show standard deviation images for the cross-sectional views of each nozzle configuration at $X/h = 1, 2$, and 4 , respectively. Using a computer graphics program, a contour was visually interpolated to approximate the curve of maximum standard deviation surrounding the injected helium jet. An example contour is shown for the T1 injection case at $X/h = 2$ in Figure 5.27. It is obvious from the standard deviation maps at $X/h = 2$ that the fluctuations in the base flow on each side of the jet are of the same magnitude as the fluctuations in the mixing layer of the jet. This is an unfortunate consequence of using ice crystals which evaporate in the recirculation zone and recondense downstream when mixed with freestream air. The average and instantaneous images were referred to in this area to determine the best fit to create a completely connected contour line around the jet. Once the high standard deviation contours were drawn, A , p , R_o and S were calculated. The cross-sectional areas of the resulting curves gave a comparative parameter for jet spread between injection cases with different nozzle configurations while shape factors revealing mixing potential. Table 3 lists A , p , R_o and S for the face-on images located at $X/h = 1, 2$, and 4 for all the nozzle configuration. The area and shape factors are shown graphically in Figures 5.28 and 5.29.

The combination of a large shape factor and a large cross-sectional area, in the region where large-scale structures dominate mixing, are desired for the most favorable mixing situation. The large shape factor indicates the degree of convolution and large area indicates the magnitude of impact. The data in Table 3 clearly indicate that the circular-with-tabs nozzles, especially the T1 case, produce the largest mixing areas and shape factors.

At the $X/h = 2$ location, the T1 case produces an area which is 34% larger than that obtained with the baseline circular (C) injector, with a shape factor only 15% higher than that of the C case. Although the T3 case produces an area which is also 37% larger than that of the C case, the T3 case shape factor (1.22) is smaller than that of the C case (1.28). Based on the data for the $X/h = 2$ location, the T1 case appears to be the favored configuration for mixing. For the case of the elliptic nozzle, configuration the E3 case generates larger area but the E1 case generates larger shape factor. Both the T3 and E3 cases yield very low shape factors.

At the $X/h = 4$ location, the tabbed nozzle again produces greater mixing areas than the other nozzle geometries. The shape factor of the T1 case (1.82) is 58% higher than that of the C case (1.15). The area for the T1 case is 32% larger than for the C case, similar to the results obtained at $X/h = 2$. Thus the T1 case appears to possess the highest mixing potential of the nozzle configurations tested. Interestingly, the shape factor for the C, T3, and E3 cases are very similar (1.15). This outcome suggests that the T3 and E3 configurations do possess the lowest mixing potential of the nozzle configurations tested. As discussed previously in Section 5.2.2, the mixing layers formed between the primary freestream flow and the recirculating flow at the base of the strut appear to most significantly inhibit the jet dynamics for the T3 and E3 cases.

5.2.3.2 Evaluation of Mixing Quality - Mixedness Index

A mixedness index was developed to give a figure of merit for the small-scale mixing at the downstream locations of a turbulent, mixing flowfield where small-scale effects are most significant. In earlier studies, mixedness parameters were developed to define mixing quality based on concentration of chemical species [Brodkey 1967, Pratt 1975, Konrad 1976]. One such parameter, referred to as "segregation" or "unmixedness," is described by Pratt [1975] as

$$s = \frac{g(\chi_a)}{(\overline{\chi_a})^2}, \quad 5.5$$

where χ_a is the mole fraction of air in an air/fuel mixture, $g(\chi_a)$ is the variance of χ_a over time and $(\overline{\chi_a})^2$ is the square of the mean value for χ_a . Ideally, a segregation value of $s = 0$ signifies complete mixing (molecular homogeneity) and a value of $s = 1$ suggests no mixing has occurred. The segregation is undefined for $\overline{\chi_a} = 0$, that is, for regions where only pure fuel is present.

Unfortunately, the segregation parameter does not detect stream-separated flows in which mixing does not occur. For example, consider the hypothetical case shown in Figure 5.30 of the time-varying concentration of air recorded by a concentration probe located at a fixed point in a two-stream flow. Assume that the two streams are air and gaseous fuel, as in combustion applications, and that concentration is measured in terms of the mole fraction of air, such that $\chi_a = 0$ in pure gaseous fuel and $\chi_a = 1$ in pure air. The square wave represents a completely stream-segregated flow of pure fuel and pure air in which neither large- nor small-scale mixing occurs and only alternate patches of fuel or air intermittently pass the probe volume. This situation results in a variance value of $g(\chi_a) = 0.25$ and a segregation value of $s = 1$. Figure 5.31 shows a similar situation except that one stream is a mixture of 40% fuel in air and the second stream is a mixture of 60% fuel in air. In this case, the resulting variance and segregation values measured at the probe volume are $g(\chi_a) = 0.01$ and $s = 0.04$. If the two cases shown in Figures 5.30 and 5.31 are compared in terms of variance or segregation values alone, the first case exhibits higher fluctuations in the flow and thus suggests better mixing than the second case. In fact, neither case mixes at all since they are both stream-segregated flows.

Konrad [1976] developed an equation that recognizes and identifies stream-segregated flows as unmixed and does not incur mathematical singularities when $\overline{\chi_a}$ equals 1 or 0. This measure of unmixedness is defined as

$$um = \frac{\int_{t_1}^{t_2} (\chi_a - \overline{\chi_a}) dt_1 + \int_{t_2}^{t_2} (\overline{\chi_a} - \chi_a) dt_2}{\int_{t_1}^{t_2} (1 - \overline{\chi_a}) dt_1 + \int_{t_2}^{t_2} (\overline{\chi_a}) dt_2}, \quad 5.6$$

where t_1 is the time during which $\chi_a > \overline{\chi_a}$ and t_2 is time during which $\chi_a < \overline{\chi_a}$. This integral definition is graphically described by the concentration trace shown in Figure 5.32, where um is equal to the sum of the shaded areas divided by the sum of the areas of the rectangles enclosing the shaded areas. It is obvious that for a perfectly mixed flow, $\overline{\chi_a}$ is equal to a constant value and $um = 0$. Likewise, if the two fluids in the flow are perfectly unmixed, as in the case of the two stream segregated flows shown in Figures 5.30 and 5.31, then $\overline{\chi_a} = 1$ or 0 at all times and $um = 1$. Thus the intermittency of the two-stream segregated flow is not mistaken for small-scale mixing and Konrad's equation is a more informative/inclusive measure of mixing than the segregation parameter defined above.

An unmixedness parameter and related mixedness index, introduced by Glawe et al. [1995], was developed for the current study. The unmixedness parameter (um_e) is defined as:

$$um_e = \frac{\sqrt{\frac{1}{t} \int (\chi_a - \overline{\chi_a})^2 dt}}{\left[(\chi_{a_1} - \overline{\chi_a})(\overline{\chi_a} - \chi_{a_2}) \right]^{\frac{1}{2}}}. \quad 5.7$$

where χ_{a_1} and χ_{a_2} are the values of χ_a in the two pure fluids in the flow, with $\chi_{a_1} > \chi_{a_2}$. This equation is similar in theory to Konrad's equation 5.6, in that it represents the actual fluctuation relative to the fluctuation of a corresponding stream-segregated flow. However, equation 5.6 is expressed in terms of a difference and equation 5.7 is expressed in terms of a difference squared (i.e., a standard deviation). In addition, the product in the denominator of equation 5.7 acts to normalize the fluctuations relative to a fully mixed mean value assumed to be equal to $\bar{\chi}_a = (\chi_{a_1} + \chi_{a_2})/2$.

It can be shown for a stream-segregated flow, with one stream of concentration χ_1 and the other of concentration χ_2 , where $\chi_1 > \chi_2$, that

$$\bar{\chi} = \alpha\chi_1 + \beta\chi_2, \quad 5.8$$

where α is the fraction of time during which mole fraction χ_1 is present, β is the fraction of time during which mole fraction χ_2 is present in the measurement volume, and $\alpha + \beta = 1$ [Gouldin and Dandekar 1984]. The standard deviation is then given by

$$\sigma_x = \left[\alpha(\chi_1 - \bar{\chi})^2 + \beta(\chi_2 - \bar{\chi})^2 \right]^{\frac{1}{2}}. \quad 5.9$$

In combination with equation 5.8 and the fact that $\alpha + \beta = 1$ it can be shown that,

$$\sigma_x = \left[(\chi_1 - \bar{\chi})(\bar{\chi} - \chi_2) \right]^{\frac{1}{2}}, \quad 5.10$$

which is exactly the denominator of equation 5.7 (see Appendix E for derivation). The expression in equation 5.10 yields a maximum value of 0.25 when $\bar{\chi}$ is equal to the value for a fully mixed condition, $\bar{\chi} = (\chi_1 + \chi_2)/2$. For all other values of $\bar{\chi} \neq (\chi_1 + \chi_2)/2$ where $0 < \bar{\chi} < 1$, equation 5.10 yields a value smaller than 0.25. A

smaller value in the denominator of equation 5.7 results in a larger value of unmixedness. Thus, in addition to yielding the values of $um_e = 1$ for stream-segregated flows and $um_e = 0$ for fully mixed flows, the unmixedness equation 5.7 also quantifies how closely the mixing approaches the fully mixed equilibrium state of $\bar{\chi} = (\chi_1 + \chi_2)/2$.

To demonstrate the influence of the denominator on the unmixedness value, Figures 5.33 and 5.34 show two concentration traces of identical fluctuation about mean values of $\bar{\chi}_a = 0.5$ and 0.3 , respectively. Since the standard deviation is the same for both traces, the mean value $\bar{\chi}_a$ dictates the value of mixedness for the two different traces. The case with $\bar{\chi}_a = 0.5$ yields the maximum possible value of 0.25 for the denominator, while the case with $\bar{\chi}_a = 0.3$ yields a value of 0.21 . This results in an unmixedness parameter 20% larger for the $\bar{\chi}_a = 0.3$ case as compared to the $\bar{\chi}_a = 0.5$ case.

It should be noted that equation 5.7 contains mathematical singularities for values of $\bar{\chi}_a = 1$ or 0 , which occur outside of the mixing region in either pure air or fuel. Since pure fuel and air are homogeneous, with constant values of $\bar{\chi}_a = 0$ and 1 , the standard deviation of mole fraction in pure fluid is necessarily zero. Therefore, the condition of $\sigma_{x_a} = 0$ can be used to identify and mark regions of pure fuel ($\sigma_{x_a} = 0$ and $\bar{\chi}_a = 0$) and pure air ($\sigma_{x_a} = 0$ and $\bar{\chi}_a = 1$) before application of equation 5.7. Predetermining regions of pure fluid avoids incurring mathematical singularity points during computations. Since $\sigma_{x_a} = 0$ for fully mixed flows as well, regions where $\sigma_{x_a} = 0$ and $\bar{\chi}_a$ equals a value between 0 and 1 can likewise be identified and marked before application of equation 5.7. Since unmixedness values fall in a range between 0 and 1 , a complimentary mixedness index (m) can be defined as

$$m = 1 - um_e, \quad 5.11$$

where $m = 1$ for fully mixed and $m = 0$ for fully unmixed conditions, as expected. The integral mixedness parameter developed for the current study is defined as

$$m = 1 - um_e = 1 - \frac{\sqrt{\frac{1}{t} \int (\chi_a - \overline{\chi_a})^2 dt}}{\left[(\chi_{a_1} - \overline{\chi_a})(\overline{\chi_a} - \chi_{a_2}) \right]^{\frac{1}{2}}}. \quad 5.12$$

This mixedness parameter can be written in a statistical rather than a time-integral format for use with digitized data. For the current study, Rayleigh/Mie images provide digitized pseudo-concentration information for the helium jet mixing with the primary flow of freestream air. Since laser light is scattered from ice particles in the air, the scattering intensity (I) represents the relative amount of air present at each location in the flowfield. In an image including regions of pure helium and air, the maximum pixel intensity (I_1) corresponds to regions of pure air and the minimum pixel intensity value (I_2) corresponds to regions of pure helium. I_1 and I_2 are the upper and lower bounds of the pseudo-concentration range, just as 1 and 0 are the upper and lower bounds of the mole fraction traces used in the previous examples. The mixedness index used to evaluate the quality of mixing based on digitized Rayleigh/Mie scattering images is defined as

$$(m_I)_{i,j} = 1 - \frac{\sqrt{\frac{1}{n} \sum_{k=1}^n (I_{i,j} - \overline{I_{i,j}})^2}}{\left[(I_1 - \overline{I_{i,j}})(\overline{I_{i,j}} - I_2) \right]^{\frac{1}{2}}}, \quad 5.13$$

where n is the total number of samples in a summation set, i and j are the row and column of the pixel in the 578 by 384 pixel array of the ICCD camera, I_1 is maximum intensity

of scattering in air and I_2 is minimum scattering in helium. The mixedness index, m_I , is undefined for $\overline{I_{ij}} = I_1$ and $\overline{I_{ij}} = I_2$, which theoretically occurs in pure air and pure helium, while fully mixed conditions result in a mixedness value of $m_I = 1$.

It should be noted that the resolution of the intensity measurements are limited to the size of the measurement volume recorded by each pixel of the 578 by 384 array of the ICCD camera. For the face-on images, the measurement volume based on the laser sheet thickness dimensions and the ratio of pixels to field of view dimensions is approximately $0.3 \text{ mm} \times 57 \text{ } \mu\text{m} \times 53 \text{ } \mu\text{m}$. This is much larger than the smallest scale of turbulence described by the Kolmogorov microscale of length (η) defined by

$$\eta = \frac{\delta_w}{Re^{3/4}}, \quad 5.14$$

where δ_w represents the size of the largest eddies or the width of the shear layer and Re represents the Reynolds number based on δ_w and the velocity difference across the shear layer. Thus the resolution of the measurement volume is a limiting factor on the precision of the mixedness index and its description of the quality of mixing.

Mixedness plots were generated for the circular (C) nozzle case from Rayleigh/Mie images of the face-on view located at the last four streamwise stations in the test range at $X/h = 2, 4, 6.8$, and 10 . This series of mixedness plots along with the corresponding intensity probability distribution functions shows the trend in mixedness of the jet as it travels downstream. Mixedness plots were also calculated for each of the nozzle configurations (N, C, T1, T2, T3, E1, E2, E3) from images of the face-on view located at the furthest downstream location $X/h = 10$. Small-scale mixing between the different nozzle geometries was evaluated using these maps along with intensity profiles of a horizontal and vertical line across each of the mixedness maps.

In theory, the process of generating a mixedness map consists of identifying the minimum and maximum intensity values corresponding to scattering intensity in helium and air respectively, computing the average and standard deviation of intensity at each pixel in the image array and finally inserting these values into equation 5.13.

In practice however, several experimental realities must first be addressed. First, the values of pixel intensity in the regions of the image corresponding to regions of pure air are not entirely uniform. The variation in scattering intensity in the air is due to slight variations in scattering particle number density and size distribution. The effects of particle size are clearly demonstrated by considering the effects of a large particle passing through the plane of view and scattering far more light than any other particle in the field of view of the image. Setting I_I equal to the pixel intensity corresponding to the scatter from such a large particle would result in a value of I_I which is not indicative of the freestream air as a whole. In the current study, a probability distribution function (PDF) of pixel intensity was used to identify a reasonable upper bound of the freestream pixel intensity (I_I). The scatter from the large particles and higher than average number density of particles in the air appeared as a relatively small number of pixels with intensity values

$I > I_I$. Any pixel location which incurred an intensity value larger than the selected value of I_I for any of the instantaneous images in the set was considered undefined and automatically assigned a mixedness value of $m_I = 1.0$. This value of $m_I = 1.0$ stands out in regions of partial to low mixing. This same problem of nonuniform scatter is also encountered in regions of pure helium, although to a much smaller extent. The intensity values less than the judiciously chosen value of I_2 were also considered undefined and assigned a value of $m_I = 1.0$ for the mixedness images.

The second experimental factor is that a region of pure helium only appears in face-on images at $X/h = 1$. Downstream, the helium has mixed with the air; thus

determining a value for the minimum scattering occurring in pure helium (I_2) must be either approximated based on images at $X/h = 1$ or assigned according to the intensity PDF for the image.

The mixedness maps of the face-on images located at $X/h = 2, 4, 6.8$, and 10 for the circular (C) nozzle case (Figure 5.35) show the progression of mixing downstream. The contrast has been increased in the images, using a computer graphics program, to highlight the mixedness trends so that the gray scale represents the relative mixedness values with black and white both falling between $0 < m_I < 1$ with black indicating low mixing and white indicating a higher degree of mixing. Initially, the mixing around the circumference of the jet is contained in a small layer and the helium at the center of the jet remains unaffected by the mixing layers. The helium at the center of the jet is relatively undisturbed at $X/h = 2$. The mixing layer grows in thickness downstream. The standard deviation values in the mixing layer increase, and the mixedness values decrease, as energy is transferred from large- to small-scale eddies. This continues until a transition point is reached where the mixedness and standard deviation reach a minimum and a maximum value, respectively. Then the standard deviation decreases asymptotically to zero downstream and m_I reaches a value of 1 as the flow undergoes relaminarization. Judging from the mixedness images in Figure 5.35 this transition has occurred by $X/h = 10$ because the mixedness values have increased and the region of mixing has stopped growing, i.e., the spread rate has decreased.

The mixedness maps of all the nozzle configurations from the face-on images at $X/h = 10$ clearly show that the helium jets emanating from the T1 and E1 nozzle configurations have mixed most with the freestream air by this location downstream (Figure 5.36). The low values of mixedness in the C, T3 and E3 cases indicate that there is still significant mixing activity occurring in these jets at $X/h = 10$. Profiles along a

vertical and horizontal line through the center of each image show the relative values of mixedness in each case.

The mottled appearance of the mixedness maps and the nonuniformity of the intensity profiles along a line in a region of uniform mixing, such as in the freestream, is primarily due to the small number of sample images (20) in each set. Subsequent experiments involving normal injection were performed in the same tunnel with 100 sample images at each location [Gruber 1995]. The mixedness maps generated from these 100 images show a more uniform distribution in the freestream mixedness values. Furthermore, analysis of these images showed that the estimated standard deviation computed from 20 images were much higher than those estimated using 50 and 100 images from the same set, with the standard deviation values for 50 and 100 being nearly identical. This suggests that under sampling effects may be present in the ensembles of 20 images used in the current study.

These higher standard deviation values result in lower mixedness values as dictated by equation 5.13. A conservative choice of I_1 and I_2 (i.e., not the absolute maximum and minimum pixel intensities of the image) also acts to limit the mixedness range to a lower bound greater than zero and an upper bound less than the theoretical value of one. The small number of samples, which gives elevated standard deviation values, and the conservative choice of I_1 and I_2 explain why the mixedness values in the freestream, seen in the vertical line profiles (Figure 5.37) are less than 0.6 rather than spanning the range from 0 to 1. Comparison of the horizontal profiles for the different nozzle geometries shows the T1 and E1 case to have the largest values of mixedness in the jet region indicating these jets are further along in the progression towards full mixing. On the other hand, the contours for the other cases (C, T2, T3, E2, E3) show low mixedness values in the regions cutting across the mixing layers of the jet suggesting these jets are not as far along in the process toward the fully mixed condition. The peak

values at the center of the jet, as seen in the horizontal line profiles in Figure 5.38, suggest that this region is just entering into the mixing process and is on the downward portion of the mixedness curve before the transition point. Since the transition point for the jet as a whole is believed to be located upstream of $X/h = 10$, lower levels of mixedness at $X/h = 10$ suggest poorer mixing. The mixedness profiles along a vertical line across the center of the images show mixedness for the T1 and E1 case to be the greatest at $X/h = 10$ and less for the other cases.

A detailed set of experiments in a simple free shear layer would prove useful in further characterizing equation 5.12 and establishing practical limits of application using flow visualization and possibly other measurement techniques.

5.3 Laser Doppler Velocimetry Results

Each flow visualization image provides qualitative information about an entire plane of the flow whereas each LDV measurement provides quantitative data at a single point. Thus, the regions of the flow field represented by the total group of Rayleigh/Mie images is much more inclusive than the total group of LDV profiles. However, since images and LDV measurement provide different information, their combination is complimentary.

Laser Doppler velocimetry (LDV) is a nonintrusive velocity measurement technique which provides a quantitative, statistical velocity and turbulence information in the flow. In this chapter, the base flow, no injection (N) case, is addressed first followed by the baseline helium injection case using the circular (C) nozzle. A comparison is then made between the baseline injection case (C) and two other injection cases using the circular-with-tabs nozzle (T1) and the elliptic nozzle (E1) (see Figure 3.7).

Approximately 5,120 instantaneous velocity realizations were recorded at each measurement point (fewer in the low seed regions). This is a substantial sample for mean flow and second order statistics and appears to be a large enough sample to also compute

meaningful third order and perhaps fourth order statistics. The mean velocity, turbulence intensity, shear stresses, and turbulent triple products were calculated using the equations presented in this section. Complete derivations are included in Appendix C for reference.

The mean streamwise and transverse velocities, \bar{U} and \bar{V} , are defined as

$$\bar{U} = \frac{1}{n} \sum_{k=1}^n U_k, \quad 5.15$$

and

$$\bar{V} = \frac{1}{n} \sum_{k=1}^n V_k \quad 5.16$$

where U_k and V_k are the instantaneous velocities. Then, the fluctuating streamwise and transverse components of velocity are defined as

$$u = U - \bar{U}, \quad 5.17$$

and

$$v = V - \bar{V}. \quad 5.18$$

Each of the calculated values are normalized by the reference velocity (U_{ref}), which is equal to the ideal Mach 2 tunnel velocity (freestream velocity before flow separation at the end of the strut) at the measured stagnation temperature. The velocity standard deviation values for u and v are denoted as σ_u and σ_v respectively and are defined as

$$\sigma_u = \sqrt{\frac{1}{n} \sum_{k=1}^n (u_k)^2}, \quad 5.19$$

and

$$\sigma_v = \sqrt{\frac{1}{n} \sum_{k=1}^n (v_k)^2}. \quad 5.20$$

The streamwise and transverse turbulence intensities are defined as

$$\frac{\sigma_u}{U_{ref}}, \quad 5.21$$

and

$$\frac{\sigma_v}{U_{ref}}. \quad 5.22$$

The streamwise (X), transverse (Y), and spanwise (Z) distances measured from the origin of the reference coordinate system at the base of the strut (Figure 3.2) are normalized by the strut thickness ($h = 1.27$ cm) on all the LDV results.

LDV profiles were taken in the (X,Y) plane passing through the centerline of the strut ($Z = 0$) at stations $X/h = -2, -1, 0, 1, 2, 4, 6.8$ and 10 . In addition, LDV profiles were taken in the (X,Z) plane passing through the centerline of the strut ($Y = 0$) at stations $X/h = 2$ and 6.8 . The LDV profiles in the (X,Y) and (X,Z) planes are presented separately to maintain a clear distinction between the two orientations. Two different formats are presented. First, velocity distributions from consecutive streamwise stations are displayed in series on the same page with the horizontal spacing between the plots proportional to the true streamwise distance between profiles. This overall view emphasizes the progression of the flow characteristics with downstream direction. Second, a composite superimposed view of these same profiles is shown. This view emphasizes the relative shape and magnitude of the velocity and turbulence distributions.

5.3.1 Incoming primary flow conditions

Figure 5.39 shows the LDV profiles of the normalized mean streamwise velocity taken at three streamwise stations above and below the strut just upstream of the base of the strut. These profiles lie within the streamwise (X,Y) plane on the strut centerline ($Z = 0$). The streamwise locations of the stations are referred to in terms of streamwise distance (X) measured from the origin of the reference coordinate system (see Figure 3.2) normalized by the strut thickness ($h = 1.27$ cm). Since these particular LDV profiles are upstream of the base of the strut, their X coordinate is negative, resulting in negative values of X/h . The three stations shown in Figure 5.39 are located at $X/h = -2$, -1 , and 0 .

The solid circles in this figure represent the normalized mean streamwise velocity values obtained from the two-component LDV measurements, while the solid triangles show the mean streamwise velocity values obtained from the one-component LDV measurements. The two-component LDV measurements provide transverse and streamwise velocities up to about 1.9 mm from the strut and the top and bottom wind tunnel wall surfaces. Attempts to move the measurement volume closer to the strut or wall resulted in one of the beams forming the measurement volume being blocked by the tunnel side wall or the strut, thus inhibiting the formation of the measurement volume. The one-component LDV measurements provide streamwise velocities from 0.25 mm to 1.65 mm off the strut and wall surfaces. The velocity scale is located on the bottom axis of each of the three plots and labeled on the plot for station $X/h = -2$. The transverse location of each measurement point, given in terms of Y/h , is marked on the left most axis. The mean streamwise velocity profiles upstream and at the base of the strut show the incoming freestream flow to be uniform and symmetric above and below the strut. The freestream Mach number was calculated to be 1.92 with a unit Reynolds number in the freestream of $4.4 \times 10^7 \text{ m}^{-1}$, see Appendix A.

Figure 5.40 shows the streamwise component of turbulence intensity for the measurements taken in the (X,Y) plane at stations $X/h = -2, -1$, and 0. The empty circles and the empty triangles show the normalized streamwise turbulence intensities from the two-component and one-component LDV measurements, respectively. The scale for the streamwise turbulence intensities is located on the bottom axis of each of the three plots and labeled on the plot at station $X/h = -2$. Turbulence intensities in the freestreams are less than 1% and increase to about 7% in the boundary layer. The low turbulence intensity in the freestream signifies a uniform and disturbance-free flow.

There is a slight deviation between the mean velocity and more noticeably the turbulence intensity values for the one- and two- component measurements. This deviation stems from the differences between the measurement volumes and the associated signal processing for the one- and two- component LDV systems. The general measurement sources of error include: spatial averaging over the entire measurement volume, bias toward higher velocities, statistical uncertainty, counter resolution, particle lag, and fringe biasing. Precautions were taken to reduce the potential for error by using the optimal fringe orientation of $\pm 45^\circ$ to the mean flow velocity for the two-component system, a 40 MHz frequency shift of one of the beams forming the measurement volume to distinguish directionality, using seed particles small enough to follow the turbulent fluctuations to avoid particle lag problems, and taking an adequate sample size to minimize statistical uncertainty. The consistency of the off-set between the one- and two- component streamwise mean velocity and turbulence intensity values suggests a slight difference in the measurement system such as measurement volume location or deviation of the beam orientations incurred during operation of the tunnel.

The boundary layer thickness (δ) determined from velocity profiles is typically defined as the location at which the boundary layer velocity reaches 99% of the freestream velocity. The mean streamwise velocity profile at $X/h = -1$ (the station which

is both closest to the end of the strut and upstream of possible effects from the expansion at the base of the strut) shows the 99% boundary layer thickness to be approximately 5.6 mm.

The extensive data available in the literature and established theoretical laws developed for the boundary layer can be employed to verify the condition of the incoming flow. Figure 5.41 shows the LDV velocity profile at $X/h = -1$ (including the one- and two- component data) superimposed on a turbulent boundary layer curve fit. The curve fit was computed using the Wall and Wake Laws [Sun and Childs 1973] with $\delta = 5.6$ mm, a coefficient of skin friction of $C_f = 0.0016$, and thermodynamic properties of the Mach 1.92 freestream air. Using the Van Driest II equations and theory, Maise and McDonald [1968] have shown the velocity profiles for compressible boundary layers to collapse onto a single line. Figure 5.42 shows that the results derived from the current data are in agreement with the data obtained in previous studies. An explanation of the Van Driest II derivation and the information necessary for the relevant calculations are contained in Schetz [1993].

Figure 5.43 shows turbulence intensities obtained from the LDV data of this study superimposed on the data from previous studies of undisturbed turbulent boundary layers [Kuntz et al. 1987]. Considering that the velocity data from previous studies shows experimental results from a range of flow conditions from Mach 1.72 to 3.88, the data from this study fall within the expected range for a turbulent Mach 1.92 boundary layer.

In summary, comparison of the current data with well established theory and experimental data shows that the incoming flow in the present study is a well behaved, fully developed turbulent boundary layer. Details of the calculations used to determine the boundary layer characteristics are contained in Appendix D.

5.3.2 Baseline no injection (N) flow field

The flow field without injection was examined first to establish a reference baseline case against which the effects of helium injection through different nozzle geometries could be evaluated. LDV velocity profiles were taken downstream of the base of the strut in the (X,Y) plane at streamwise locations $X/h = 0, 1, 2, 4, 6.8,$ and 10 . LDV velocity profiles were also taken in the (X,Z) plane at streamwise locations $X/h = 2$ and 6.8 .

5.3.2.1 LDV profiles in the (X,Y) plane

Mean Velocity

Nondimensional mean streamwise velocity profiles for the base flow without helium injection are shown in Figure 5.44. This figure presents the series of LDV velocity profiles taken in the (X,Y) plane at stations $X/h = 0, 1, 2, 4, 6.8,$ and 10 . All velocity measurements are normalized with the reference velocity (U_{ref}) and all distances are normalized with the strut height ($h = 1.27$ cm). The format of these plots is the same as that described in the preceding section, except that these profiles show only two-component LDV data. These 6 profiles are placed on the page with the horizontal spacing between them being proportional to the streamwise distance between measurement stations at $X/h = 0, 1, 2, 4, 6.8,$ and 10 . The horizontal spacing on the page is 1.5 times the true streamwise spacing between stations, while the vertical scale on the page is nearly the same size as the true transverse scale.

At all stations, the presence of the wake behind the strut can clearly be seen in the center of the flow. The presence of a shear layer at the top and bottom edges of the wake are clearly visible. Immediately downstream of the strut, a recirculation zone is present, with associated reverse mean streamwise velocities. The first station downstream of the base of the strut ($X/h = 1$), shows a maximum normalized reverse velocity equal to 8% of

the reference velocity (U_{ref}). Petrie et al. [1986] recorded reverse velocities up to 26 % of the supersonic freestream velocity in a backfacing step configuration with a Mach 2.07 approach flow. Likewise, Amatucci et al. [1992] reported reverse velocities up to 23% of the supersonic freestream velocity for a strut configuration with a Mach 2.56 stream above and a Mach 2.05 stream below the strut. In the present study, the relatively few measurement stations in the near-field of the strut do not capture the overall maximum reverse velocity behind the step. Measurements at additional stations between $X/h = 0$ and 1 would certainly reveal a peak reverse velocity larger than 8% of the freestream reference velocity.

Since the mean streamwise velocities switch from negative to positive values at the end of the recirculation zone, the length of the recirculation zone is defined as the distance along the centerline to the location of the rear stagnation point where $\bar{U} = 0$. From Figure 5.44, it appears that this transition along the X-axis occurs between the station $X/h = 1$ ($\bar{U}/U_{ref} = -0.08$) and $X/h = 2$ ($\bar{U}/U_{ref} = 0.52$). A curve fit approximation of the centerline mean streamwise velocity values shown in Figure 5.45 gives $\bar{U}/U_{ref} = 0$ at $X/h = 1.1$. This value is lower than the values reported by Samimy and Addy [1986] and Amatucci et al. [1992] for similar configurations. Samimy and Addy reported a rear stagnation point at $X/h = 1.38$ for a Mach 2.07 stream above and a Mach 1.50 stream below a 2.54 cm thick strut. Likewise, Amatucci et al. [1992] reported impingement of the shear layers at approximately $X/h = 1.37$ for a Mach 2.56 stream above and a Mach 2.05 stream below a 2.54 cm thick strut. The rear stagnation point in this study, $X/h = 1.1$, is closer to that observed in a subsonic flow, $X/h = 0.9$, by Raffoul [1995] than in the supersonic flows studied by Amatucci et al. [1992] and Samimy and Addy [1986]. This may be attributed to the fact that the two streams in this study and the subsonic study by Raffoul were equal velocity and pressure matched whereas the two streams in the studies by Amatucci et al. [1992] and Samimy and Addy [1986] were different velocities.

At the end of the recirculation zone, the two streams expanding over either side of the strut merge and the flow is compressed further. The finite region where this occurs, in the vicinity of $X/h = 1.1$ for this study, is referred to as the recompression region. In a backfacing step configuration, instead of two streams merging, the single stream reattaches to the surface of the tunnel wall. The flow over the edge of the backfacing step is indicative of the flow over one side (top or bottom) of the strut. The primary difference occurs downstream, where the reattachment boundary conditions at the wall differ from the merging conditions between the two streams flowing on either side of a strut. Thus, the initial behavior of the flow field at the base of the backfacing step is to some degree similar to the flow field around the strut and can be used for comparison.

Figure 5.46 presents a composite view of the six velocity profiles shown in Figure 5.44. Clearly evident here is the drastic change in velocity deficit in the recompression region between stations $X/h = 1$ and $X/h = 2$. After this marked change, the wake continues to decay gradually downstream with an increasing minimum velocity that reaches a value of $\bar{U}/U_{ref} = 0.78$ by station $X/h = 10$. The initial rapid recovery and the subsequent slow recovery of the mean velocity deficit is consistent with data from Samimy and Addy [1986] and Amatucci et al. [1992] for similar configurations. It appears that the minimum velocity values in the wake region of the present study shift in the negative transverse (Y) direction with each successive downstream location. This suggests that the wake is skewed toward the bottom tunnel wall, which is an important consideration, especially when interpreting turbulent shear stress results. It is likely that the skewness is caused by an asymmetry in the tunnel or flow, downstream of the strut, rather than an inequality between the two streams upstream of the base of the strut. This is because an inequality upstream of the base of the strut would tend to equalize downstream of the strut which it does not.

The width of the wake, which is indicated by the velocity deficit, is a fraction larger than the thickness of the strut. The velocity deficit appears to span a distance of approximately 1.3 strut thicknesses by station $X/h = 4$ and maintains a limited span downstream at $X/h = 6.8$ and 10. This limited span of the wake, formed by the mixing layers, is also shown on the schlieren image in Figure 5.1. Raffoul [1995] found the width of the wake in the near-field behind a bluff body in subsonic flow to be a constant value equal to 1.2 times the base thicknesses ($h = 1.27$ cm). Thus, it appears that the growth of the wake created by flow past a strut (or bluff body) is limited in supersonic and subsonic conditions alike and that this limited width of the wake is only a fraction larger than the strut width.

The maximum values in the velocity profiles are a result of the flow acceleration through the expansion waves emanating from the base of the strut. The maximum velocity occurs just before the flow passes through the recompression shock waves, after which the flow velocity decreases. Thus, the shock location can be identified as the point of transition between the peak velocity and the velocity decrease. The velocity decrease incurred at the shock wave is not to be confused with the velocity deficit in the wake region.

Figure 5.47 presents the mean transverse velocity profiles in the (X,Y) plane at stations $X/h = 0, 1, 2, 4, 6.8$, and 10. This is the second component of the two-component LDV measurements, the streamwise velocity component (Figures 5.44 to 5.46) being the first. As in Figure 5.44, each of these 6 profile plots is placed on the same page with horizontal spacing on the page proportional to the streamwise distance between measurement stations at $X/h = 0, 1, 2, 4, 6.8$, and 10.

The mean transverse profiles are distinctly anti-symmetric at all stations. This is a consequence of the transverse velocity being directed toward the strut centerline to equalize the relatively low pressure region incurred at the base of the strut. Amatucci et

al. [1992] showed a drastic pressure gradient behind the base of a strut in a similar flow field. They recorded the ratio of maximum static pressure in the freestream to the minimum pressure directly behind the strut to be 5.48. Therefore, it follows that as the pressure is equalized, the flow becomes more uniform downstream and the amplitude of the anti-symmetry decreases from peak values of $\bar{V}/U_{ref} = \pm 2.8$ at $X/h = 1$ to $\bar{V}/U_{ref} = \pm 0.1$ at $X/h = 10$, as seen in Figure 5.47.

Figure 5.48 presents a composite view of the six velocity profiles shown in Figure 5.47. This view emphasizes the relative shape and magnitude of the velocity distributions at each station. Like the streamwise mean velocity values, the transverse mean velocity values are highest in the region of the expansion fan (due to flow acceleration) with the peak velocity occurring just before the flow passes through the shock wave. The minimum and maximum values of transverse velocity on both sides match in magnitude within $\pm 0.4\%$ of each other at $X/h = 1$ and within $\pm 9\%$ at $X/h = 10$. The peak velocity values move well outside of the wake region downstream and decrease from $|\bar{V}/U_{ref}| = 0.27$ at station $X/h = 1$ to $|\bar{V}/U_{ref}| = 0.10$ at station $X/h = 10$.

The transition point between the positive transverse velocity values ($\bar{V} > 0$ below the center of the wake) and the negative values ($\bar{V} < 0$ above the center of the wake) is identified by a transverse velocity value of zero $\bar{V} = 0$. In agreement with the streamwise velocity profiles, the center of the wake region (marked by $\bar{V} = 0$) shifts slightly in the negative transverse (Y) direction from $Y/h = 0$ at station $X/h = 1$ to $Y/h = 0.2$ at station $X/h = 10$.

The mean streamwise and transverse velocity components are combined to generate the composite vector representation shown in Figure 5.49. The velocity distribution shows the approach and separation of the two boundary layers from the upper and lower surfaces of the strut, the recompression region around $X/h = 1$ where the velocity vectors show the two shear layers coming together, and the recovery of the

streamwise velocity deficit in the wake of the strut. The turbulent mixing that occurs at the recompression region and in the region immediately following it acts to reduce the velocity deficit, resulting in a relatively uniform velocity distribution in the wake region by $X/h = 10$.

The mean transverse and streamwise velocity profiles presented in Figures 5.41 to 5.49 show that the wake is limited to a width on the order of the strut thickness and that drastic velocity gradients occur in the region between the base of the strut and the recompression region. The maximum turn angle of the flow towards the center of the strut according to the streamwise and transverse velocity components is 18° and occurs at $X/h = 1$. This maximum turn angle corresponds to the fluid that experienced the greatest expansion and thus lies adjacent to the slipline shown in Figure 5.3. The agreement between the angle determined from the LDV data and the Rayleigh/Mie scattering image (discussed in Section 5.2.1) demonstrates how the quantitative velocity data and the qualitative visualizations (which as shown here contains some quantitative information) compliment each other. The extreme velocity gradients, followed by more gradual velocity gradients downstream, can be attributed to the equalization of pressure, which is the driving force of the flow expansion around the base of the strut.

Turbulent normal and shear stresses

Turbulent normal stresses (\overline{uu} and \overline{vv}) and shear stress (\overline{uv}) are defined as the mean rates of momentum transfer per unit area by the fluctuating motion of a fluid. Turbulent stresses are the driving force responsible for fluid mixing in turbulent flows. Turbulent normal stresses (\overline{uu} and \overline{vv}) are discussed here in terms of turbulence intensities which were previously defined. The relationship between these two quantities is:

$$\sigma_u = \sqrt{\frac{1}{n} \sum_{k=1}^n (U_k - \bar{U})^2} = \sqrt{uu}, \quad 5.23$$

and,

$$\sigma_v = \sqrt{\frac{1}{n} \sum_{k=1}^n (V_k - \bar{V})^2} = \sqrt{vv}. \quad 5.24$$

where n is the number of samples in the summation set (20 in the present study).

Figure 5.50 shows the streamwise turbulence intensity profiles taken in the (X,Y) plane at stations $X/h = 0, 1, 2, 4, 6.8$, and 10. As expected, the turbulence intensity distribution shows a double hump behavior in the wake region due to the presence of the mixing layers formed between the primary flow and the recirculating flow at the base of the strut. The local peak turbulence intensity values in the wake region occur at the locations where the mean streamwise velocity gradients are high (see Figure 5.46).

Figure 5.51 shows the superimposition of the streamwise turbulence intensity profiles taken in the (X,Y) plane at streamwise stations $X/h = 0, 1, 2, 4, 6.8$, and 10. The maximum turbulence intensity ($\sigma_u/U_{ref} = 0.23$) occurs in the recompression region at $X/h = 1.0$. This superimposed perspective shows the drastic decrease in the peak values of turbulence intensity immediately downstream of the rear stagnation point and then a more gradual decrease in turbulence intensity to a value of $\sigma_u/U_{ref} = 0.055$ at $X/h = 10$. The maximum value of turbulence intensity at $X/h = 10$ is comparable to the turbulence intensity value in the boundary layer on the tunnel wall along the entire test length. Similar results were reported by Samimy and Addy [1986] and Amatucci et al. [1992]. They recorded high turbulence intensities ($\sigma_u/U_{ref} \approx 0.30$) in the recompression region followed by a rapid decrease downstream, in similar configurations involving supersonic flow past a 1.27 cm thick strut. Amatucci et al. [1992] investigated a Mach 2.05 stream on top of the strut and a Mach 2.56 stream on the bottom, while Samimy and Addy's investigation involved a Mach 2.07 stream on top and a Mach 1.50 stream on bottom of the strut. This trend of high turbulence intensities in the recompression and recovery

region indicates the presence of strong mixing and turbulence in the recompression and recovery region. The local peaks in turbulence intensity between the wake region and the boundary layer seen in the profiles at stations $X/h = 4, 6.8$, and 10 shows the disturbance of the flow passing through the recompression shock waves.

Figure 5.52 shows the transverse turbulence intensity in the (X,Y) plane at stations $X/h = 0, 1, 2, 4, 6.8$, and 10 . The elevated transverse turbulence intensity values shown here span the same region as the elevated streamwise turbulence intensity values in Figure 5.50, although, the transverse turbulence intensity values exhibit a single rather than a double hump behavior. Furthermore, the maximum turbulence intensity value ($\sigma_v/U_{ref} = 0.14$) occurring at $X/h = 1$ (Figure 5.53) is significantly lower than the peak streamwise value ($\sigma_u/U_{ref} = 0.23$) also occurring at $X/h = 1$, and the rate of decay is comparably less in the recompression region between station $X/h = 1$ and 2 .

In an isotropic flow, the turbulence intensities are equal in every direction and therefore the ratio of σ_u/σ_v is everywhere equal to one. This is obviously not the case in the present flow. Figure 5.54 shows the ratio of σ_u/σ_v for the LDV profiles in the (X,Y) plane. The ratio σ_u/σ_v reaches an average value of $\sigma_u/\sigma_v = 0.7$ in the freestream at $X/h = 10$. The ratio σ_u/σ_v deviates most from the ideal isotropic value of one in the wake region at each streamwise station. In the wake region, $\sigma_u/\sigma_v > 1$ and the fluctuations of the streamwise velocity dominate the fluctuation in the transverse velocity. σ_u/σ_v reaches a maximum value of approximately 1.7 at $X/h = 1$ in the vicinity of the recompression region (Figure 5.55). This is opposite to the condition for incompressible flow where the peak transverse turbulence intensity is approximately 2.5 times the value of the peak streamwise turbulent intensity value in the wake [Raffoul 1995].

Turbulent shear stress (\overline{uv}) plays a dominant role in the mean momentum transfer in turbulent flows [Tennekes and Lumley 1972]; shear stress, for example, is the primary

factor in the formation of vortices in a shear flow. The normalized turbulent shear stress is defined as

$$\tau_{uv} = \frac{\frac{1}{n} \sum_{k=1}^n (U_k - \bar{U})(V_k - \bar{V})}{U_{ref}^2} = \frac{\overline{uv}}{U_{ref}^2}. \quad 5.25$$

where n is the number of samples in the summation set (20 in this study) and U_{ref} is the Mach 2 reference velocity.

Figure 5.56 shows the normalized turbulent shear stress for the LDV profiles in the (X,Y) plane. As expected, the shear stress is highest in the two mixing layers, where the streamwise velocity gradients are highest. The maximum value of τ_{uv} exceeds the scale selected to be most effective for all the plots, although the outlying values are included in the superimposed format in Figure 5.57. The shear stress is negative in the top shear layer and positive in the bottom shear layer, as a result of the transverse transport of fluctuation momentum being directed in opposite directions.

Figure 5.57 shows the superimposition of the turbulent shear stress in the (X,Y) plane. This format highlights the drastic decrease in peak shear stress from $\tau_{uv} = 0.22$ at $Y/h = \pm 0.1$ at station $X/h = 1$ to $\tau_{uv} = 0.02$ at $Y/h = -0.4$ and $+0.2$ at station $X/h = 10$. This decrease by a factor of 10 is accompanied by the progression toward a more uniform velocity distribution. A rapid decrease of turbulence intensity in the reattachment region for a flow reattaching onto a surface behind a backfacing step has been attributed to the restriction of the larger eddies [Chandrsuda and Bradshaw 1981] and bifurcation of the turbulent eddies [Eaton and Johnson 1981] resulting in much smaller length scales and lower shear stress. Likewise, interaction of the two merging shear layers behind the strut affects the turbulent structures in a manner to decrease the shear stress in the flow.

The turbulent shear stress correlation coefficient (R_{uv}) indicates the degree of correlation between the two fluctuating velocities (u) and (v), with a value of $R_{uv} = 1$ signifying perfect correlation and $R_{uv} = 0$ signifying no correlation. R_{uv} is defined as

$$R_{uv} = \frac{\frac{1}{n} \sum_{k=1}^n (U_k - \bar{U})(V_k - \bar{V})}{\frac{1}{n} \left(\sum_{k=1}^n (U_k - \bar{U})^2 \right)^{\frac{1}{2}} \left(\sum_{k=1}^n (V_k - \bar{V})^2 \right)^{\frac{1}{2}}} = \frac{\overline{uv}}{\sigma_u \sigma_v} \quad 5.26$$

where n is the number of samples in the summation set (20 in this study).

Figure 5.58 shows the correlation coefficient for the LDV profiles in the (X,Y) plane. A high correlation coefficient indicates that the streamwise and transverse velocities (U and V) are fluctuating in a correlated manner. A high correlation coefficient in the mixing region indicates the presence of coherent structures. The correlation coefficient shown in Figure 5.59 is highest in the vicinity of the recompression region ($R_{uv} = 0.85$ at $Y/h = -0.2$ and 0.1 at station $X/h = 2$) and decreases downstream ($R_{uv} = 0.6$ at $Y/h = -0.6$ and 0.4 at station $X/h = 10$), which suggests that the structures in the mixing layer become less coherent as they travel downstream. As expected, unlike the mean and turbulence intensity profiles, the local peaks in correlation coefficients remain relatively high downstream, decreasing by merely 18% between $X/h = 1$ and 10. The consistency in value suggests the turbulent structures remain organized downstream, and the increased transverse separation between the peak values suggests the slight spread of the mixing layer downstream.

The high correlation coefficients occurring outside, above and below, the wake region appear to be a consequence of division by a small number in the denominator of the governing equation 5.26. The correlation coefficient is only applicable and useful where turbulence intensities are significant. Thus, the correlation coefficient values in

subsequent cases will only be considered in the wake region between $-0.7 < Y/h < 0.7$. Any high values on the edges of the region (near $Y/h = \pm 0.7$) correspond to low turbulence intensity values just outside the wake and are not considered significant, since the absolute magnitude of the effect is minuscule as compared to the effect in the wake region.

5.3.2.2 LDV Profiles in the (X,Z) plane

Mean velocity

Figure 5.60 shows the mean streamwise velocity profiles in the (X,Z) plane at $Y = 0$ at stations $X/h = 2$ and 6.8 . An ideal, two-dimensional flow would have a uniform mean velocity across the entire span of the tunnel. In the present flow, at station $X/h = 2$, the mean streamwise velocity shows a symmetric distribution about the strut centerline ($Z/h = 0$) with a slightly elevated velocity value in the central region of the wake. The mean streamwise velocity distribution at $X/h = 6.8$ is virtually uniform. The variation in the mean streamwise velocity distribution at $X/h = 2$ suggests some three dimensionality of the flow in the recompression region behind the base of the strut.

Previous studies have shown recirculation bubbles, cell-like structures, to exist in the recirculation zone behind the base of backfacing steps and struts. Surface oil flow visualization performed by Petrie et al. [1986] showed the presence of distinct cells behind the base of a backfacing step in a Mach 2.43 freestream. Mean spanwise velocity measurements by Raffoul [1995] suggests the existence of four recirculation bubbles along the spanwise direction and very near the base of a bluff body in a subsonic flow field. Raffoul used a three-component LDV system to obtain velocity measurements behind a bluff body with the same thickness ($h = 1.27$ cm) as the strut used in the present experiment. The normalized mean spanwise velocity (\overline{W}/U_{ref}) distribution appeared anti-symmetric about the strut centerline with a sinusoidal shape. This sinusoidal shape

flipped orientation when the measurement station was moved from $X/h = 0.02$ to 0.2 . This suggests the presence of two pairs of counter rotating vortices with rotational axes, in the Y direction, located between these two stations. The peak mean spanwise velocity reached a substantial value of approximately 16% of the freestream streamwise velocity at the station $X/h = 0.5$ and rapidly decreased to about 8% by $X/h = 1.2$. The sinusoidal shape of the (\bar{W}/U_{ref}) distribution suggests the existence of four counter-rotating vortices in the spanwise direction. The number of cells would scale perhaps with the span of the tunnel among other parameters.

Although surface oil flow visualizations were not obtained at the base of the strut and the spanwise velocity component (W) was not measured in the present supersonic study, it is reasonable to suggest that a highly three-dimensional flow pattern exists behind the base of the strut, similar to those described in the studies of Petrie et al. [1986] and Raffoul [1995].

Figure 5.61 shows the mean transverse velocity in the (X,Z) plane for station $X/h = 2$ and 6.8 . In a symmetric wake, the velocity would be exactly zero on the centerline ($Y/h = 0$), since this is the location where the negative velocity vectors from the expansion over the top edge of the strut base meet the positive velocity vectors originating from the expansion over the bottom edge of the base. However, the mean streamwise velocity profiles (Figure 5.46) show that the wake is skewed towards the negative transverse (Y) direction (towards the bottom wall of the tunnel). Thus, the mean velocity value in the (X,Z) plane on centerline would be expected to be slightly negative. Indeed the mean transverse velocity values are slightly negative ($-0.03 < \bar{V}/U_{ref} < 0$). Since the (X,Y) and the (X,Z) planes intersect at the centerline of the strut, the centerline velocity values measured in each plane are expected to be equal. The centerline mean transverse velocity values obtained in the profiles in the (X,Y) plane are close to the values obtained in the (X,Z) plane. The consistency between these values (as well as \bar{U} ,

σ_u , and σ_v) for profiles in the two orthogonal planes in data taken several days apart demonstrates the repeatability of the tunnel operating conditions and the accuracy and good resolution of the LDV measurements.

Figure 5.62 shows streamwise turbulence intensity in the (X,Z) plane at stations $X/h = 2$ and 6.8. Values vary slightly between $0.13 < \sigma_u / U_{ref} < 0.14$ at $X/h = 2$, and decrease by a factor of nearly two to $0.07 < \sigma_u / U_{ref} < 0.08$ at $X/h = 6.8$. The drastic decrease in turbulent intensity between stations $X/h = 2$ to 6.8, along with the increase in streamwise mean velocity, are changes toward the values of the surrounding air. This illustrates the process of the velocity related values in the wake becoming equal to those in the freestream.

Figure 5.63 shows the transverse turbulence intensity in the (X,Z) plane at stations $X/h = 2$ and 6.8. The values are slightly lower than the streamwise turbulence intensity and decrease by a factor of two between stations $X/h = 2$ and 6.8. Figure 5.64 shows the ratio of σ_u / σ_v for station $X/h = 2$ and 6.8. The flow is relatively isotropic ($\sigma_u / \sigma_v = 1$) at $X/h = 2$ and becomes slightly anisotropic ($\sigma_u / \sigma_v > 1$) downstream at $X/h = 6.8$. This suggests that uniform conditions occur across the span of the wake.

Figure 5.65 shows normalized turbulent shear stress in the (X,Z) plane for profiles at $X/h = 2$ and 6.8. The turbulent shear stress is negative due to the wake shifting toward the negative transverse (Y) direction (toward the bottom wall of the tunnel). The turbulent shear stress distribution varies slightly in a symmetric sinusoidal pattern similar to the mean transverse velocity distribution. The magnitude of the turbulent shear stress decreases downstream.

Figure 5.66 shows the turbulent shear stress correlation coefficient in the (X,Z) plane at stations $X/h = 2$ and 6.8. The magnitude of the correlation coefficient increases slightly downstream except in the central region, where it decreases. Although the shear

stress decreases, the correlation coefficient stays about the same or increases slightly between $2 < X/h < 6.8$.

Summary

The profiles in the (X,Y) plane show that the wake region behind the base of the strut does not spread far beyond the thickness of the strut in the transverse direction. Both the streamwise and transverse turbulence intensities increase from maximum values of about

$\sigma_u/U_{ref} = 7\%$ and $\sigma_v/U_{ref} = 4\%$ in the boundary layer to $\sigma_u/U_{ref} = 23\%$ and $\sigma_v/U_{ref} = 14\%$ in the vicinity of the recompression region and then decrease downstream. The anisotropic nature ($\sigma_u/\sigma_v > 1$) in the wake region is not conducive to turbulent transport in the transverse (Y) direction necessary for effective mixing of the wake with the primary freestream flow.

The profiles in the (X,Z) plane show relatively uniform values across the base of the strut as compared to the profiles in the (X,Y) plane. However, slight fluctuations, especially at $X/h = 2$, show that some three dimensionality exists in the flow behind the base of the strut. Based on previous results, it is hypothesized that spanwise recirculation bubbles exist in the recirculation zone at the base of the strut.

5.3.3 Baseline helium injection case using circular (C) nozzle

A circular nozzle is generally used as a fuel injector. Thus a circular nozzle mounted in the base of the strut is considered as the baseline helium injection case for the present experimental program. In this section, the flow field with helium injected from the circular (C) nozzle injector configuration is investigated and the results are compared with the flow field without injection. The effects of different injector nozzle geometries (circular-with-tabs and elliptic nozzle) on the development and on the mixing of the jet with the primary freestream flow will be discussed in the following sections.

In the injection cases, the initially two-dimensional shear layers emanating from the base of the strut interact with the mixing layers surrounding the jet to form a complex jet mixing region in the center of the volume occupied in the no injection (N) case by the wake flow alone. Figure 5.67 is an illustration of the interaction between the helium jet emanating from the circular (C) nozzle and the mixing layer formed at the base of the strut. The majority of the helium exiting the nozzle travels in the streamwise direction in the form of a plume, which will be referred to as the jet proper. A fraction of the helium exiting the nozzle fills the low pressure region on the spanwise sides of the jet between the mixing layers formed at the base of the strut. This region on each spanwise side of the jet will be referred to as the wake region (this is a modified wake flow and not necessarily two-dimensional).

The primary focus of the present study is on the central region, referred to as the mixing region, where mixing between the helium in the jet proper and the freestream air occurs. Also of concern is the modification of the flow field with the addition of a helium jet.

For this experimental program, LDV measurements were taken in the (X,Y) and (X,Z) planes passing through the centerline of the jet. It should be emphasized that the profiles in the (X,Y) plane of the flow without injection show nominally two-dimensional mixing layers, whereas, in the helium injection cases, the profiles in the (X,Y) plane show a center cross-sectional plane of a very three-dimensional mixing region. Thus, while the profile of the two-dimensional flow (no injection case) in the (X,Y) plane is representative of the flow at any point along the entire span of the strut, every profile of the helium injection cases (three-dimensional flow) in the (X,Y) plane is different, so that the selection of the plane of investigation is critical to the interpretation of the data. Since the helium injection nozzle is mounted in the center of the strut, the centerline of the injection nozzle and the centerline of the strut coincide on the X-axis. The (X,Y) and

(X,Z) planes of investigation also intersect along the X-axis, and the combination of data collected in these two planes provides a three-dimensional matrix of quantitative velocity information throughout the flow field.

In this section, the LDV profiles for the baseline helium injection case using the circular (C) nozzle are presented. Helium, used as the injectant to simulate hydrogen fuel, exits the converging circular (C) nozzle at sonic velocity. The helium jet is unseeded. For all LDV measurements, the static pressure of the helium jet at the exit of the nozzle was four times the static pressure of the freestream air ($\Psi = 4$). The data from the helium injection case using the circular (C) nozzle are compared with the data from the no injection (N) case to identify the characteristics of the jet flow proper and the effects of helium injection on the surrounding wake flow. The flow field generated from helium injection using two other nozzle geometries, circular-with-tabs nozzle in orientation T1 and elliptic nozzle in orientation E1, will be compared with the circular (C) case in the next section (refer to Figure 3.7).

5.3.3.1 LDV profiles in the (X,Y) plane

Mean Velocity

Nondimensional mean streamwise velocity profiles for the helium injection case using the circular (C) nozzle are shown superimposed on the profiles for the no injection (N) case in Figure 5.68. This figure presents the series of LDV velocity profiles taken in the (X,Y) plane at stations $X/h = 0, 1, 2, 4, 6.8$, and 10 . As in the preceding profiles, all velocity measurements are normalized with the reference velocity (U_{ref}) and all distances are normalized with the strut height ($h = 1.27$ cm). These 6 profiles are placed on the page with the horizontal spacing between them being proportional to the streamwise distance between measurement stations at $X/h = 0, 1, 2, 4, 6.8$, and 10 . The horizontal

spacing on the page is 1.5 times the true streamwise spacing between stations while the vertical scale on the page is nearly the same size as the true transverse scale.

A comparison of the LDV measurements at $X/h = 0$ for the injection case versus the no injection case (Figure 5.68) indicates, as it was expected from the flow visualization results presented in Section 5.3.1, that the jet does not induce flow separation upstream of the end of the strut. Although, it is possible that the addition of enough helium at high pressure could transform the favorable pressure gradient between the freestream primary flow and the region behind the base of the strut into an adverse pressure gradient large enough to cause separation upstream of the shoulder of the strut base. This is an important point in combustion applications, where effects upstream of the shoulder could cause problems at the inlet of the combustor. The fact that separation is not apparent for the present cold flow (i.e., flow without combustion), does not preclude the possibility of separation at the shoulder caused by adverse pressure gradients incurred with combustion.

It will be noted that the centerline values for the injection (C) case at $X/h = 1$ and 2 are missing. At these streamwise locations, before station $X/h = 4$, the jet has not yet engulfed enough seed particle material from the primary freestream flow to produce an acceptable sample size for the LDV system. The amount of seed engulfed into the jet is partially a function of the amount of seed material in the freestream flow, and daily changes in atmospheric conditions increase and decrease the seed particle density in the freestream. Therefore, an acceptable number of samples were obtained on centerline at least at station $X/h = 2$ on some occasions (refer to Figure 5.76).

The profiles presented in Figure 5.68 show that the jet spread in the transverse direction is contained in a region corresponding to the area between the mixing layers formed at the base of the strut in the baseline flow without injection. The peak velocity value on the centerline at $X/h = 4$ in the profiles of the C case show the presence of the

helium jet. The helium jet injected from the base of the strut emerges into the complex flow at the base of strut and the jet structures blend with the mixing layer structures, creating an integrated mixing phenomenon.

A composite plot of the centerline values for the helium injection (C) case and the no injection (N) case, shown in Figure 5.69, shows the dramatic rise in centerline velocity just downstream of the base of the strut due to the helium jet. The helium jet exits the nozzle at sonic velocity, then expands to supersonic velocities via an expansion fan, then passes through the Mach disk and becomes subsonic, then accelerates to a high subsonic or supersonic velocity as it mixes with the supersonic freestream air. The mean streamwise velocity values at the centerline of the jet in the C case decrease gradually downstream until about $X/h = 7$, after which the velocity values remain virtually constant downstream, at least within the test range of $X/h = 10$. Thus it appears that a transition occurs somewhere in the range between $X/h = 6$ and 8. This is well beyond the location of the Mach disk at about $X/h = 6$ and could feasibly be the transition from large scale effects of mixing at center of the jet to the smaller scale effects which dominate in the relaminarization process of mixing. This is consistent with the Rayleigh/Mie images that show the disappearance of the large scale structures in the circular jet to occur between $X/h = 4$ and 6.8 (refer to Section 5.2.2.1). The centerline velocity values for the no injection (N) case appear to converge to the helium injection (C) case values downstream.

The static pressure at the base of the strut without injection is several times less than the static pressure in the primary freestream flow [Amatucci et al. 1992]. The helium jet, being of relatively high static pressure, enters the low pressure region at the base of the strut and the jet plume acts as an extension of the strut [Sullins et al. 1982]. If the effect of the jet, acting as a solid mass, is large, the presence of the jet would be expected to weaken the expansion fans emanating from the top and bottom edges of the strut, at least

in the vicinity of the jet. This would be conveyed on the LDV plots as a lower peak transverse velocity and a smaller width of the expansion fan.

Indeed, a weaker expansion fan is suggested by the mean transverse velocity profiles. Figure 5.71 presents the nondimensional mean transverse velocity profiles in the (X,Y) plane at stations $X/h = 0, 1, 2, 4, 6.8$, and 10 for the helium injection (C) and no injection (N) cases. At station $X/h = 1$, the distribution of the mean transverse velocity profile, showing the flow to be directed toward the centerline of the strut, in the helium injection (C) case is more compact around the centerline and has a lower peak value than the no injection (N) case. This suggests that the strength of the expansion fan is slightly reduced in the streamwise (X,Y) plane on centerline of the strut by the addition of the helium jet.

Turbulent normal and shear stresses

Figures 5.71 and 5.72 show the streamwise and transverse turbulence intensity profiles taken in the (X,Y) plane at stations $X/h = 0, 1, 2, 4, 6.8$, and 10 for the helium injection (C) case and the no injection (N) case. The peak streamwise turbulence intensities in the jet mixing region in the injection (C) case are lower than in the wake of the no (N) injection case at every station and form a single peak at $X/h = 4$ and a flat profile at $X/h = 6.8$ and 10 rather than the double peak exhibited by the no injection (N) case (Figure 5.71). Similar to the streamwise turbulence intensity distributions, the transverse turbulence intensity values for the helium injection (C) case are lower than the turbulence intensity values for the no injection (N) case in the jet mixing region, and the double hump behavior marking the two shear layers in the no injection (N) case is replaced by a single hump representing the mixing region of the jet (Figure 5.72). The limited breadth of the streamwise and transverse turbulence intensity distributions is another indication that the turbulent transport in the complex mixing region with injection

is contained in the region marked by the mixing layers formed between the primary flow and the recirculating flow in the flow without injection.

In an isotropic flow, the streamwise and transverse turbulence intensity values are equal in every direction, and therefore the ratio σ_u/σ_v is everywhere equal to one. Figure 5.73 presents the ratio of σ_u/σ_v in the (X,Y) plane for the helium injection (C) case and the no injection (N) case. For the most part, the streamwise turbulence intensity is greater than the transverse turbulence intensity in the mixing region for both the no injection (N) case and the injection (C) case. Since transverse fluctuations are much more significant in the turbulent transport between the helium in the jet and the freestream air than streamwise fluctuations, $\sigma_u/\sigma_v > 1$ is not favorable for mixing between the helium jet and the primary air flow. The anisotropic condition is an important consideration when choosing a turbulence model for Computational Fluid Dynamic (CFD) simulations of a flow field such as the one in the present study. Assuming isotropic conditions would simplify calculations, but lead to erroneous numerical results.

Figure 5.74 shows the turbulent shear stress profiles in the (X,Y) plane at station $X/h = 0, 1, 2, 4, 6.8$, and 10 for the helium injection (C) case and the no injection (N) case. The peak shear stress values for the no injection (N) case at $X/h = 1$ ($\tau_{uv} = 0.024$) are off the scale chosen to be the most effective for all plots. As anticipated from the smaller mean streamwise velocity gradients and smaller turbulence intensity values, the turbulent shear stress is not as large in the mixing region of the injection (C) case as in the wake region of the no injection (N) case. The largest differences in the shear stress distribution occur near the base of the strut and the diminish downstream.

Figure 5.75 shows the turbulent shear stress correlation coefficients in the (X,Y) plane at stations $X/h = 0, 1, 2, 4, 6.8$, and 10 for the helium injection (C) case and the no injection (N) case. The correlation coefficients for the injection (C) case are on the same order of magnitude and show the same general shapes as the no injection case. However,

the peak values are farther from the centerline in the injection case, since the mixing layers are separated on the centerline by the presence of the jet. The peak value is slightly larger for the injection (C) case at the last station $X/h = 10$. This suggests that the mixing structures are more coherent downstream with the jet present.

Summary

Considered as a group, the LDV profiles in the (X,Y) plane show that the helium jet emanating from the circular (C) nozzle mounted in the base of the strut is contained within the region marked by the mixing layers in the no injection (N) case -- that is, the mixing layers formed between the primary flow and the recirculating flow at the base of the strut without injection. The jet acts as an extension of the strut into the low pressure region at the base of the strut at the location of the injector nozzle. This results in dramatic changes in the flow immediately downstream of the strut. Most significant are the decrease in streamwise velocity deficit, the apparent weakening of the expansion fans, and the drastic reduction in shear stress at stations $X/h = 1, 2$, and 4 . It appears that a transition occurs in the injection (C) case somewhere in the range between $X/h = 6.8$ and 8 after which the velocity values on centerline remain virtually constant. This could be related to the transition from large scale mixing which dominates the near base region to small scale mixing which dominates the relaminarization process downstream. The centerline mean streamwise velocity values for the no injection (N) case appear to converge toward the helium injection (C) case values downstream. The anisotropy ($\sigma_u/\sigma_v > 1$) suggests an unfavorable condition for mixing between the jet and the freestream air.

5.3.3.2 LDV profiles in the (X,Z) plane

The LDV profiles in the (X,Z) plane for the helium injection (C) case are drastically different than those for the no injection (N) case. The injection (C) case exhibits distinct

distribution contours in the region occupied by the helium jet, whereas the no injection (N) case shows relatively uniform profiles across the entire span of the tunnel.

Mean velocity

Nondimensional mean streamwise velocity profiles for the helium injection case using the (C) nozzle are shown superimposed on the profiles for the no injection (N) case in Figure 5.76. This figure presents the series of LDV velocity profiles taken in the (X,Z) plane at stations $X/h = 2$ and 6.8. The normalized streamwise velocity distribution for the injection (C) case shows a peak value of $\bar{U}/U_{ref} = 0.89$ on the centerline of the jet at $X/h = 2$. This corresponds to an absolute velocity of 460 m/s.

At first glance this may seem low, since helium exits the sonic nozzle at high velocity ($\bar{U} \equiv 871$ m/s). Furthermore, the helium jet expands and accelerates to supersonic velocities (roughly Mach 4 to 5). However, once the helium jet passes through the Mach disk it becomes subsonic at the center (roughly Mach 0.4 to 0.5) and then accelerates to higher velocities as it mixes with freestream air. The Mach disk in the present experiments for a helium jet ($\Psi = 4$) injected from a circular (C) nozzle appeared in PLIF images (Section 5.2) to be located at approximately $X/h = 0.63$. Computational Fluid Dynamic (CFD) calculations for the same flow predicted a Mach number and mean streamwise velocity of approximately $M = 0.5$ and $\bar{U} = 500$ m/s for the helium jet immediately downstream of the Mach disk [Chen et al. 1995]. The value of 460 m/s measured in the present study at $X/h = 2$ was located 1.37 base thicknesses downstream of the Mach disk and is reasonably subsonic considering the above discussion and the fact that the helium jet is effected by the surrounding air flow by this location. Note that the air surrounding the jet is traveling less than $\bar{U} = 500$ m/s above and below the jet, as a result of the freestream air flow passing through a recompression shock wave, and about 250 m/s in the wake flow on the spanwise sides of the jet.

The mean streamwise velocity distribution in the wake region to each side of the jet proper for the injection (C) case coincides with the distribution for the no injection (N) case at both locations $X/h = 2$ and 6.8 (Figure 5.76). This absence of change in streamwise velocity suggests that the jet is contained predominately in the jet proper. The velocity distribution has become more uniform by $X/h = 6.8$, with the maximum velocity in the jet decreasing and the velocity of the surrounding wake increasing as a result of mixing and flow recovery toward a uniform flow velocity profile.

Figure 5.77 shows the normalized mean transverse velocity profiles in the (X,Z) plane for the injection case using a circular (C) nozzle and the no injection (N) case. An ideally symmetric flow would show a zero value of mean transverse velocity in both the jet proper and the surrounding wake flow. The mean transverse velocity in this figure is nominally zero for the no injection case but deviates to a substantial value of 14% of the freestream reference velocity (U_{ref}) at the center of the jet for the injection (C) case at station $X/h = 2$. The velocity vector at this location, based on the values of \bar{U} and \bar{V} , appears to be at a 10° angle to the X-axis in the negative transverse (Y) direction. Two possible reasons for this are: 1) the measurement volume was not located on the jet centerline and 2) the measurement volume was located on the jet centerline, although the entire jet flow, on the average, is directed downward. The former is most probable because of the large transverse velocity gradients near the jet centerline (Figure 5.70), any slight deviation of the measurement volume from the precise center of the jet would result in a noticeable velocity other than zero. Besides, a 10° skew angle of the jet would have been evident in the flow visualization images. Similar to the streamwise velocity, the transverse velocity distribution becomes more uniform downstream at $X/h = 6.8$.

Turbulent normal and shear stresses

Figure 5.78 shows the streamwise turbulent intensity in the (X,Z) plane for the helium injection (C) and no injection (N) case. The streamwise turbulent intensity is lower in the jet and higher in the surrounding wake flow compared to the value in the wake of the no injection (N) case. The low values of turbulence intensity in the jet proper signify minimal streamwise turbulent transport in the jet proper. Although the mean streamwise velocity in the wake region surrounding the jet was unaffected by the addition of the helium jet, the elevated streamwise turbulence intensity in the region surrounding the jet suggests that the wake is at least disturbed by the jet. The difference in streamwise turbulence intensity between the no injection (N) and helium injection (C) case apparent at $X/h = 2$ decreases significantly by $X/h = 6.8$. However, the same trend in the jet proper and the wake region relative to the no injection (N) case is still apparent.

Figure 5.79 shows transverse turbulence intensity profiles taken in the (X,Z) plane at stations $X/h = 2$ and 6.8 for the helium injection (C) case and the no injection (N) case. The transverse turbulence intensity at $X/h = 2$ shows a wavy contour in the jet proper with local peak values on the edge of the jet proper where the mixing interface between the jet and primary flow is located. This fluctuation becomes a single depression in the profile at $X/h = 6.8$. The transverse turbulence intensity in the wake region on each side of the jet proper is slightly higher than the uniform values in the wake for the no injection (N) case at $X/h = 2$ and nearly equal to the wake values in the no injection (N) case at $X/h = 6.8$. This suggests that the injection of helium from the base of the strut imparts a noticeable streamwise, but not transverse, turbulence intensity to the wake region surrounding the jet. Since transverse turbulent transport is the component significant to the mixing of the fluids into the mixing layers, elevated streamwise turbulence intensity is of little consequence to mixing.

Figure 5.80 shows the streamwise to transverse turbulence intensity ratio (σ_u/σ_v) at stations $X/h = 2$ and 6.8 for the helium injection (C) case and the no injection (N) case. The wake flow, no injection (N) case, shows a streamwise to transverse turbulence intensity ratio between 1 and 1.2 at $X/h = 2$ and 6.8 . The streamwise turbulence intensity ratio in the jet proper region of the injection (C) case at $X/h = 2$ fluctuates above and below the values of the no injection (N) case, but is predominantly below. The distribution is somewhat symmetric about the centerline with a double hump behavior. This shows that along the centerline of the jet, the flow is rather isotropic and towards the edges of the jet, in the mixing layer, the flow becomes anisotropic. The distribution becomes more uniform by $X/h = 6.8$. The overall (σ_u/σ_v) ratio increases downstream for the entire profile of both the no injection (N) and injection (C) cases signifying that fluctuations, and turbulence transport, in the streamwise direction become stronger relative to the transverse direction downstream.

Turbulent normal and shear stresses

Figure 5.81 presents the turbulent shear stress profiles in the (X,Z) plane at stations $X/h = 2$ and 6.8 for the helium injection (C) case and the no injection (N) case. The shear stress for the injection (C) case is nearly zero at the center of the jet and increases to a significant peak value at the spanwise sides of the jet proper. The peak is located at the mixing interface between the jet proper and the wake, and suggest a positive mixing condition here. This peak value is equal to twice the turbulent shear stress value occurring across the span of the strut in the no injection (N) case. The shear stress is also high in the wake region surrounding the jet as compared to the value measured in the wake of the strut for the no injection (N) case at $X/h = 2$. Since the turbulence shear stress is related to mixing potential, it appears that the addition of the helium jet enhances mixing in the wake flow behind the base of the strut. The turbulent shear stress values for the injection (C) case decrease significantly between $X/h = 2$ and 6.8 to reach an

almost uniform distribution very close to the value observed in the no injection (N) case by $X/h = 6.8$.

Figure 5.82 presents the turbulent shear stress correlation coefficient profiles in the (X,Z) plane at stations $X/h = 2$ and 6.8 for the helium injection (C) case and the no injection (N) case. The correlation coefficient distribution in the center of the jet for the injection (C) case is drastically different than the no injection (N) case. This distribution suggests that flow in the jet core near the nozzle exit is uniform, with similar properties to the freestream flow. The correlation coefficients are nearly the same for stations $X/h = 2$ and 6.8 outside the jet region, yet higher than the no injection (N) case at the same stations.

Summary

The distribution of LDV profiles in the (X,Z) plane for the injection (C) case are significantly different than those for the no injection (N) case. The no injection (N) case profiles are relatively uniform across the entire span of the strut, while the helium injection (C) case shows distinct variations inside the jet proper and in the surrounding wake region.

The most surprising effect seen in these profiles is the elevation of streamwise turbulence intensity and shear stress in the wake region on each spanwise side of the jet, showing that the jet disturbs the flow in the wake region. It is probable that the jet adds a substantial spanwise flow component to the recirculation bubbles at the base of the strut (see Section 5.3.2.2). However, transverse turbulence transport is the component significant to mixing of the jet with primary freestream fluid, so that high streamwise turbulence intensity is not as significant to mixing in this study. However, disturbance of the wake region could prove beneficial to age-mixing and flame holding in combustion applications. The jet region itself has lower values of streamwise and transverse

turbulence intensity than the wake flow of the no injection (N) case, signifying relatively uniform flow and low turbulence transport in the jet proper.

Another noteworthy finding is that all the distributions become more uniform downstream at $X/h = 6.8$ as compared to $X/h = 2$, especially the shear stress and the correlation coefficient. This signifies that bulk of the mixing and movement toward equilibrium occurs upstream of $X/h = 6.8$. This is consistent with the concept of a transition occurring between 6 and 8 before which large-scale effects dominate mixing and after which small-scale effects dominate the centerline development of the circular (C) case.

5.3.4 Helium injection cases using circular-with tabs (T1) and elliptic (E1) nozzle.

This section focuses on the similarities and differences between the flow fields created by helium injection using the circular-with-tabs and the elliptic nozzle in their vertical orientations (i.e., T1 and E1) and the baseline injection case using the circular (C) nozzle (refer to Figure 3.9).

In considering helium injection from the base of the strut, it is important to keep in mind that the resulting flow field is the combination of a nominally two-dimensional wake flow behind the strut and a three-dimensional jet flow. Upon exiting the nozzle, the underexpanded helium jet forms a barrel shock and a Mach disk. The barrel shock for injection from the circular (C) nozzle at helium jet-to-freestream air static pressure ratios of $\Psi = 4$ is shown in the acetone PLIF images of Figure 5.4. (The geometry of the shock structure would most certainly be different for the circular-with-tabs and elliptic nozzles.) Since the air in the recirculation zone behind the strut is of relatively low velocity and at a lower pressure than that of the helium at the injector nozzle exit, the injected jet is expected to behave much like an underexpanded free jet until it interacts with the mixing layers formed between the primary flow and the recirculating flow at the base of the strut.

At the point of interaction between the jet and the nominally two-dimensional mixing layers, the top and bottom portions of the shear layer encompassing the jet merge with the mixing layers in the central region behind the base of the strut. This interaction creates a three-dimensional and complex flow field in which the mixing structures of the jet are interwoven with the mixing layers formed at the base of the strut. Figure 5.67 illustrates the interaction between the nominally two-dimensional mixing layers formed at the base of the strut with a helium jet issued from a circular (C) jet.

The vertical orientations of the elliptic and circular-with-tabs nozzles were selected as having the most mixing potential, based on documented subsonic jet dynamics of elliptic nozzles and nozzles with tabs, and their predicted behavior in a wake flow. The Rayleigh/Mie scattering flow visualizations presented in Section 5.2 show these two nozzles to have the best mixing characteristics.

The selection of a circular nozzle with tabs and an elliptic nozzle in a vertical orientation is further supported by the conclusions of Haimovitch et al. [1994], who tested several different nozzles (circular, circular with four tabs, slot, stepped, elliptic, trapezoidal) mounted in the base of a ramp injector. Haimovitch et al. used planar Mie scattering flow visualization, with ethanol as the scatterer, and showed that the circular nozzle with tabs exhibited the best mixing characteristics, although the slot injector in the vertical position showed a good mixing potential. The circular nozzle with tabs and the vertical slot injector were selected as the two emerging candidates for further research. The elliptic nozzle, which did not exhibit favorable mixing, had an aspect ratio of 2:1, as compared to the significantly larger aspect ratio of 2.8:1 for the slot injector. The elongated geometry of the slot injector, which provokes axis switching, appears to be the primary factor in its mixing effectiveness. Thus, the elliptic nozzle for the present experimental program was designed with a substantial aspect ratio of 3:1, similar to that of the slot injector used by Haimovitch et al.

In the present study, LDV profiles for the injection cases using the circular-with-tabs (T1) and elliptic (E1) nozzles were taken in the (X,Y) and (X,Z) planes at $X/h = 2$ and 6.8. LDV profiles in the (X,Y) and (X,Z) planes for the simple wake flow of the no injection (N) case and the injection case using the circular (C) nozzle included measurements at these stations as well. Thus, the profiles of all four cases for which LDV data were obtained [no injection (N) case, and injection cases using: circular (C), circular-with-tabs (T1) and elliptic (E1) nozzles] at the stations $X/h = 2$ and 6.8 are presented in a superimposed fashion in Figures 5.83 to 5.110. The absence of a LDV data on centerline of the injection (C) case at $X/h = 2$ unfortunately limits comparison of results at this location. This superimposed format facilitates direct comparison between the profile distributions for each case.

5.3.4.1 LDV profiles in the (X,Y) plane for the circular-with-tabs (T1) and elliptic (E1) nozzles.

Mean Velocity

Nondimensional mean streamwise velocity profiles in the (X,Y) plane of all four cases for which LDV data was obtained (N, C, T1, E1) are shown in Figures 5.83 and 5.84. These profiles represent a single (X,Y) plane located on the centerline of the jet and therefore represent a single slice of the three-dimensional flow field. It is immediately evident that helium injection from the different nozzle geometries reduces the velocity deficit in the region behind the base of the strut (Figure 5.83). The mean streamwise velocity distribution in the region of the jet is noticeably different for the different nozzle geometries (T1 and E1) at $X/h = 2$. The fact that the distribution for the T1 case is similar in shape to the no injection (N) case shows the absence of strong jet effects on centerline. This is the result of the bifurcation of the jet into two adjacent core flows (see discussion in Section 5.2), allowing primary flow to enter between the core

flows as if the jet were absent. The vast differences in the distribution shape and magnitude at $X/h = 2$ are not as apparent at $X/h = 6.8$ (Figure 5.84).

Figure 5.85 and 5.86 show the mean transverse velocity profiles in the (X,Y) plane for all four cases at stations $X/h = 2$ and 6.8 . These profiles are on the centerline of the jet and represent a single cross-sectional plane. The magnitude of the peak values of the transverse velocity indicate the relative strength of the expansion fan emanating from the top and bottom edges of the base of the strut. The expansion fan, driven by the pressure deficit behind the base of the strut, is the mechanism by which the primary freestream flow is directed toward the centerline of the strut; the figures show that the expansion fan is indeed weakened on centerline by the presence of the jet. At $X/h = 2$, the flow without injection has a slightly higher peak transverse velocity value than the injection cases. At $X/h = 6.8$, the transverse velocity distributions for the T1 and E1 cases show that a larger component of velocity is directed toward the centerline of the jet in the mixing region than the C case, which itself is nearly identical to the no injection (N) case. This suggests the active engulfing of freestream fluid by the jet dynamics of the T1 and E1 cases in the (X,Y) plane located on the centerline of the jet ($Z=0$).

The spanwise velocity and turbulence intensities in this region could prove vital to residence time and flame holding characteristics. Further investigation including spanwise velocity measurements using three-component LDV would be necessary for detailed characterization of the flow.

Turbulent normal and shear stresses

Figures 5.87 and 5.88 show the streamwise turbulence intensities in the (X,Y) plane at stations $X/h = 2$ and 6.8 of all four cases for which LDV data were acquired. At $X/h = 2$, the distributions in the mixing region vary dramatically for the different nozzle geometries (Figure 5.87). The peak turbulence intensities values at for all the injection cases are lower than the peak values for the no injection (N) case. By $X/h = 6.8$, the

shapes of the distributions for the injection cases are not as distinct and the turbulence intensities have decreased dramatically to about 60% of their values at $X/h = 2$.

The most noticeable feature of the streamwise turbulence intensities is the triple hump behavior of the jet emanating from the E1 nozzle at station $X/h = 2$. The central hump reflects the presence of the jet, while the humps on each side show the presence of the mixing layers formed at the base of the strut. The peaks of the two humps corresponding to the mixing layers formed at the base of the strut are farther apart in the E1 case than in the N case. This suggests that the mixing layers are displaced by the jet in the E1 case. Considering the overall configuration of the different nozzles, in different orientations, mounted in the base of the strut, it is evident that the boundary of the jet at the nozzle exit in the E1 case reaches closer to the primary freestream flow passing over the top and bottom edges of the strut than the jet in either the C or T1 cases. Thus, the jet in the E1 case has the strongest effect on the mixing layers at the base of the strut, and vice versa, and acts to deflect the mixing layers so that they travel along a more separated path as compared to the no injection (N) case.

The oblong jet of the E1 case then switches axes immediately downstream of the nozzle exit, so that its major axis is aligned along the span of the strut. This places the smaller dimension (minor axis) of the elliptic jet between the mixing layers and explains why a separation appears between the peak streamwise turbulence intensity values in the jet and those in the mixing layer at $X/h = 2$ shown in Figure 5.87.

Figures 5.89 and 5.90 show the transverse turbulence intensities in the (X,Y) plane at stations $X/h = 2$ and 6.8 of all four cases for which LDV data was obtained. At $X/h = 2$, the distributions for the T1 and E1 cases are similar in shape and are slightly more compact around the jet centerline than the no injection (N) case. The side humps of the transverse turbulence intensity distribution coincide with regions of the expansion fan and thus are related to the dynamics of expansion. At $X/h = 6.8$, the transverse

turbulence intensity for the circular (C) jet is higher than the E1 and T1 cases and is nearly equal to the N case. Since turbulence intensity signifies turbulent transport, which perpetuates mixing, this suggests that the mixing activity progresses more rapidly in the T1 and E1 cases, to achieve more uniform flow by $X/h = 6.8$. Whether the T1 or the E1 nozzle produces more effective mixing is difficult to judge from these profiles.

Figures 5.91 and 5.92 show the ratio of the streamwise to transverse turbulence intensities σ_u/σ_v in the (X,Y) plane at stations $X/h = 2$ and 6.8 of all the cases for which LDV data was obtained. For all the injection cases, as well as for the no injection (N) case, the streamwise turbulence intensity is significantly higher than the transverse turbulence intensity in the mixing layers. The mixing layers in the no injection case are, of course, the nominally two-dimensional mixing layers emanating from the base of the strut, and the mixing layers in the injection cases are the composite mixing layers created from interaction of the jet and the aforementioned mixing layers formed at the base of the strut. The peak streamwise to transverse turbulence intensity ratio ($\sigma_u/\sigma_v = 2.4$) occurs at $X/h = 2$ for the E1 case. At $X/h = 6.8$, the peak streamwise turbulence intensity values are still higher than the transverse values ($1.5 < \sigma_u/\sigma_v < 1.7$). The dominance of the streamwise turbulence intensity over the transverse turbulence intensity is attributed to compressibility effects in the mixing region.

Figures 5.93 and 5.94 show the turbulent shear stress in the (X,Y) plane at stations $X/h = 2$ and 6.8 of all the cases for which LDV data were obtained. At $X/h = 2$, the distribution for all the injection cases (C, T1, E1) are virtually the same and drastically lower (five times) than for the no injection (N) case in the mixing region. Since turbulent shear stress indicates mixing potential, these results suggest that the shear layers between the helium and air is not as active as the shear layers of the wake flow without injection. This maybe due to velocity, density, or compressibility effects. By $X/h = 6.8$ the

turbulent shear stress distribution has dropped drastically for the no injection (N) case and slightly for the injection cases.

Figures 5.95 and 5.96 show the turbulent shear stress correlation coefficient in the (X,Y) plane at stations $X/h = 2$ and 6.8 of all the cases for which LDV data was obtained. A high correlation coefficient indicates the presence of coherent structures. At $X/h = 2$, the correlation coefficient for the C case most closely follows the no injection (N) case. The T1 and E1 cases have a slightly different distribution in the vicinity of the mixing layers. This suggests that structures in the mixing layers of the wake flow prevail, but are modified, with injection of helium from the base of the strut.

Summary

A survey of the LDV data in the (X,Y) plane at $X/h = 2$ and 6.8 suggests that the injected helium jet for all nozzle configurations is contained in the transverse (Y) direction within the region marked by the mixing layers formed at the base of the strut in the flow without injection. The relative magnitudes and shapes of the streamwise velocity and turbulence intensity values are significantly different for the various nozzle geometries tested: circular (C), circular-with-tabs (T1), and elliptic (E1). The similarity in shape between the streamwise velocity profile for the T1 case and the N case at $X/h = 2$ suggests a bifurcation of the jet emanating from the T1 nozzle, as seen in the Rayleigh/Mie images in Section 5.2.2. The shape of the streamwise turbulent shear stress profile for the E1 case indicates that the jet does not expand to fill the entire region between the two mixing layers formed at the base of the strut as the circular jet does. Furthermore, this contour shows that the jet issuing from the E1 nozzle displaces the mixing layers on each side of the jet away from the centerline of the strut relative to the mixing layers of the no injection (N) case.

5.3.4.2 LDV Profiles in the (X,Z) plane

As expected, unlike the profiles in the (X,Y) plane, the LDV profiles in the (X,Z) plane for the helium injection cases (C, T1, E1) are drastically different from the no injection (N) case across the entire span of the strut (Figures 5.97 to 5.110). The majority of the helium exiting the nozzle travels in the streamwise direction in the form of a plume, which will be referred to as the jet proper. However, a fraction of the helium exiting the nozzle fills the low pressure region on the spanwise sides of the jet between the mixing layers formed at the base of the strut. This region on each spanwise side of the jet will be referred to as the wake region (this is a modified wake flow and not necessarily two-dimensional). The flow properties, in both the jet proper and in the wake regions on each spanwise side of the jet, in the (X,Z) plane differ significantly with the various injector geometries.

Mean velocity

Normalized mean streamwise velocity profiles in the (X,Z) plane at stations $X/h = 2$ and 6.8 of all four cases for which LDV data was obtained (N, C, T1, E1) are shown in Figures 5.97 and 5.98, respectively. At $X/h = 2$, the profiles vary in shape, spanwise spread of the jet proper, peak velocity magnitude in the jet proper, and velocity magnitude in the wake region (Figure 5.97). The distribution of the (C) case in the jet proper is Gaussian shape with a peak velocity of $\bar{U}/U_{ref} = 0.89$ being the largest of all the injection cases. This corresponds to an absolute velocity of 460 m/s, as discussed in Section 5.3.3.2). The velocity distribution outside the jet proper coincides with the profile of the no injection (N) case, suggesting that the helium issuing from the circular (C) nozzle remains predominantly in the jet plume. The distribution for the (E1) case exhibits a double hump, reflecting the jet bifurcation commonly occurring in jets emanating from large aspect ratio nozzles, with a peak value of $\bar{U}/U_{ref} = 0.84$. The

relatively high velocity values in the wake region for the E1 case as compared to the no injection case suggests that a significant portion of the helium exiting the E1 nozzle enters the wake region. The dips at the edge of the jet proper suggests that structures in the flow cause velocity deficits at these points. The T1 case exhibits a flat profile with small irregular variations in the jet proper and streamwise velocity values in the wake flow that are lower than the no injection (N) case. The slightly lower velocity in the wake region suggests that perhaps the helium jet exiting the T1 nozzle engulfs a small amount of fluid from the wake region. This seems counter intuitive since the jet fluid in the T1 is expected to flow radially outward on the sides of the nozzle without tabs as discussed in Section 5.2.2.2. Further investigation, including measurements of spanwise velocity, would be useful in analyzing the complete dynamics in the wake flow.

At $X/h = 6.8$, the absolute peak velocity of the circular jet decreases slightly while the peak velocities of the T1 and E1 cases increase as compared to the peak values at $X/h = 2$. The E1 case still shows a double hump, representing the bifurcation of the jet. The T1 case now shows a triple peak, with the center peak being highest. The central peak is related to the engulfing of freestream air, traveling faster than the jet proper, into the center of the helium jet where bifurcation occurs; the side peaks represent the bifurcated cores of the helium jet in the T1 case.

Figures 5.99 and 5.100 show the mean transverse velocity profiles in the (X,Z) plane at stations $X/h = 2$ and 6.8 . In an ideally symmetric flow, the transverse velocity along the base of the strut, both in the jet proper and wake, would be zero. This is the case for the flow without injection. However, at $X/h = 2$, the transverse velocity distribution for the injection cases are nonzero and somewhat symmetric about the jet centerline. For example, the C case exhibits a fluctuating velocity contour with a peak negative velocity equal to 15% of the freestream reference velocity (U_{ref}) at the center of the jet. This is not surprising considering the large transverse velocity gradients on centerline, and the

fact that a slight deviation of the LDV measurement volume from the jet centerline would result in velocity values other than zero. The symmetry of the distributions about the jet centerline suggests the presence of structures in the jets. At $X/h = 6.8$, the transverse velocity is relatively uniform in the jet proper.

Turbulent normal and shear stresses

Figures 5.101 and 5.102 show the streamwise turbulence intensities in the (X,Z) plane at stations $X/h = 2$ and 6.8 of all cases for which LDV data was obtained. At $X/h = 2$, for all injection cases, the streamwise turbulence intensity is smaller in the jet proper than in the wake regions on each side of the jet proper. For example, the turbulence intensity in the E1 case is the most uniform and lowest ($\sigma_u/U_{ref} = 0.06$) in the jet proper, and has a value 3 times smaller than the value in the wake flow to each side of the jet proper

($\sigma_u/U_{ref} = 0.20$). The turbulence intensity values in the wake flow on each side of the jet proper is highest for the E1 case ($\sigma_u/U_{ref} = 0.20$), and only slightly higher for the C case ($\sigma_u/U_{ref} = 0.15$) and about equal for the T1 case, as compared to the value ($\sigma_u/U_{ref} = 0.13$) for the flow without injection. Downstream, at $X/h = 6.8$, the streamwise turbulence intensity is still lower in the jet proper, with E1 being lowest, followed by the T1 and C cases. However, the values in the wake region on each streamwise side of the jet proper are nearly equal to the no injection case values.

Figures 5.103 and 5.104 show the transverse turbulence intensities in the (X,Z) plane at stations $X/h = 2$ and 6.8 of all cases for which LDV data was obtained. At $X/h = 2$, the profiles show the same trend, with all the jets having a lower turbulence intensity in the jet proper as compared to the wake region surrounding the jet proper. Since the streamwise and transverse turbulence intensities are so uniform and low in the jet proper of the E1 case ($\sigma_v/U_{ref} = 0.06$), it seems that the jet proper is most coherent for this

nozzle configuration. Downstream at $X/h = 6.8$, the transverse turbulence intensities in the jet proper are still lower than the wake flow on each spanwise side of the jet.

Figures 5.105 and 5.106 show the ratio of streamwise to transverse turbulence intensity ratios in the (X,Z) plane at stations $X/h = 2$ and 6.8 . The flow is isotropic ($\sigma_u/\sigma_v = 1$) in the wake of the no injection (N) case. The flow is anisotropic for the injection cases, signifying that turbulent transport at each point is biased either in the transverse or streamwise direction. Since turbulent transport in the streamwise direction is insignificant to the mixing of the helium jet with the surrounding air, the locations where $\sigma_u/\sigma_v < 1$, and σ_u and σ_v are large, are favorable for jet mixing. At $X/h = 2$ the circular (C) case exhibits larger transverse than streamwise turbulence intensities in the jet to each spanwise side of the center. The entire σ_u/σ_v distribution for the T1 case is close to one. The streamwise turbulence intensity values in the center of the distribution for the E1 case are one, although, the side values are near $\sigma_u/\sigma_v = 1.5$, which is not favorable for mixing in the wake of the E1 case. The distribution becomes more uniform downstream at $X/h = 6.8$ for all the injection cases.

Figures 5.107 and 5.108 show the turbulent shear stress profiles in the (X,Z) plane at stations $X/h = 2$ and 6.8 of all cases for which LDV data was obtained. The shear stress is relatively low in the jets as compared to the wake flow surrounding the jets. The most noticeable factor is the relatively high shear stress in the wake region to each spanwise side of the jet proper in the E1 case, with virtually zero shear stress in the jet proper. The C case shows nearly zero shear at the jet centerline and relatively high values in the wake region. At $X/h = 6.8$, the turbulent shear stresses have diminished to nearly zero for the injection cases and the no injection case.

Figures 5.109 and 5.110 show the turbulent shear stress correlation coefficient profiles in the (X,Z) plane at stations $X/h = 2$ and 6.8 of all cases for which LDV data was obtained. Similar to the shear stress profiles, the correlation coefficients fluctuate in

the jet proper, with values less than the surrounding wake flow, suggesting that the jet structures are not very coherent. However, the correlation coefficients for the C and (E1) case are higher in the wake region to each spanwise side of the jet, as compared to the wake flow without injection, which suggests that the addition of helium has enhanced the flow pattern in the wake region.

Summary

The profiles in the (X,Z) plane at $X/h = 2$ show significant differences between the injection cases for which LDV data were obtained (N, C, T1, E1). The most noticeable differences are the increase in streamwise velocity, streamwise turbulence intensity, and shear stress in the wake region at $X/h = 2$ for the jet emanating from the elliptic nozzle in the E1 orientation. This suggests that a substantial amount of the helium exiting the E1 nozzle enters the wake region and greatly effects the wake region. The differences diminish downstream to be nearly uniform at $X/h = 6.8$. This suggests that the bulk of the mixing occurs upstream of $X/h = 6.8$. However, the low values of transverse turbulence intensity in the jet proper (which may be largely due to compressibility effects) suggests that the elliptic nozzle shows little promise for jet mixing in the transverse direction. Nonetheless, it appears clear that the different nozzle geometries do have an effect on the overall spanwise flow field behind the base of the strut in the nearfield and that this effect diminishes as the jet fluid travels downstream, becoming negligible by $X/h = 6.8$.

Table 3. Parameters of large-scale mixing.

X/h	Nozzle	Area (square pixels)	Perimeter (pixel units)	Effective Radius	Shape Factor
1	c	26368.00	695.12	91.61	1.208
1	t1	25166.00	807.00	89.50	1.435
1	t2	26373.00	759.80	91.62	1.320
1	t3	30597.00	711.10	98.69	1.147
1	e1	23355.00	685.60	86.22	1.266
1	e2	22945.00	688.30	85.46	1.282
1	e3	27035.00	645.00	92.77	1.107
2	c	25533.00	730.00	90.15	1.289
2	t1	34193.00	974.00	104.33	1.486
2	t2	28209.00	729.00	94.76	1.224
2	t3	34943.00	796.00	105.46	1.201
2	e1	22674.00	786.00	84.96	1.472
2	e2	24613.00	792.00	88.51	1.424
2	e3	28978.00	693.00	96.04	1.148
4	c	26415.00	662.89	91.70	1.151
4	t1	34807.00	1204.50	105.26	1.821
4	t2	32160.00	1039.00	101.18	1.634
4	t3	34414.00	767.75	104.66	1.167
4	e1	29532.00	950.70	96.96	1.561
4	e2	19352.00	752.20	78.49	1.525
4	e3	31456.00	721.70	100.06	1.148

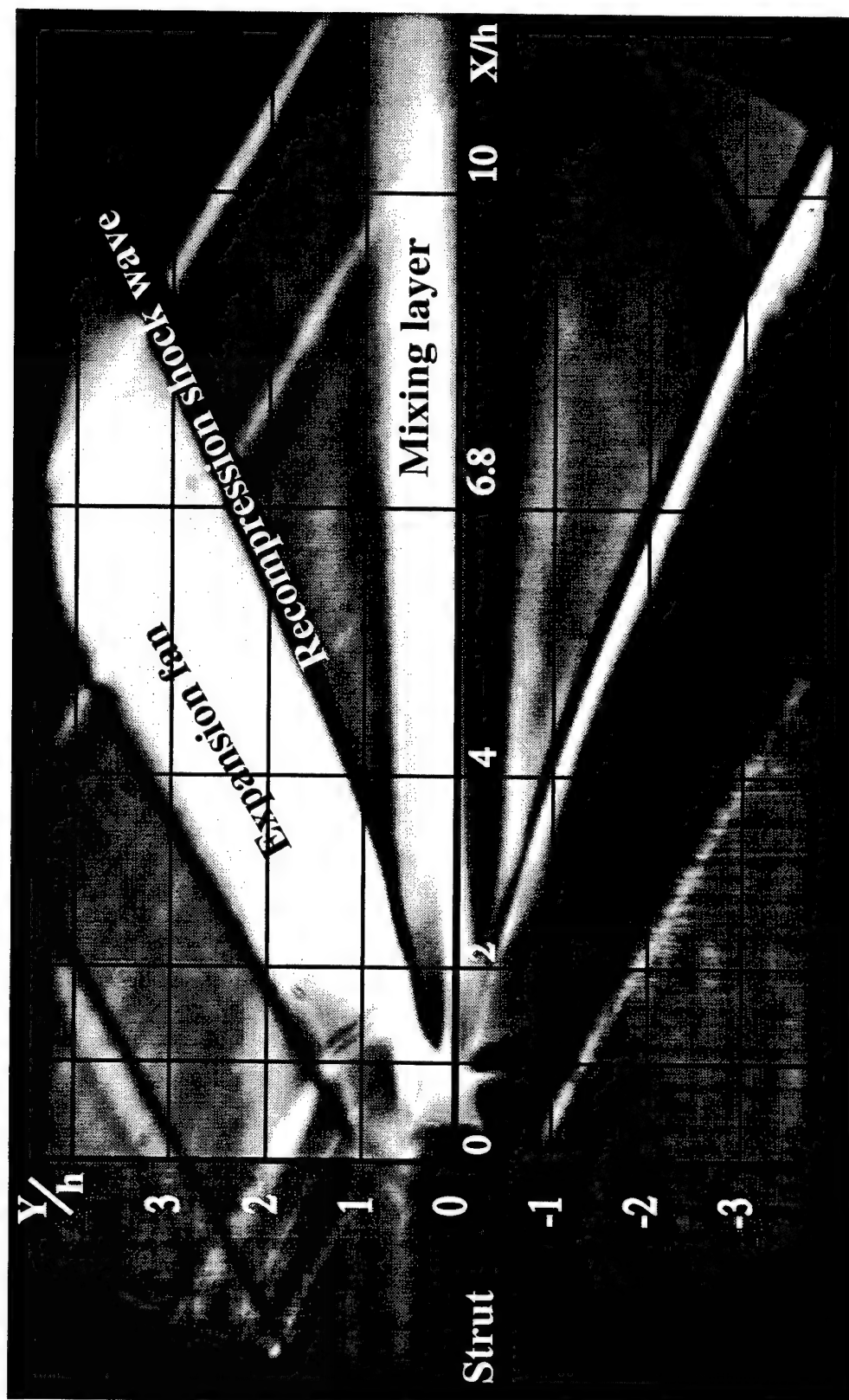


Figure 5.1. Schlieren photograph of streamwise (X,Y) plane of view without injection.

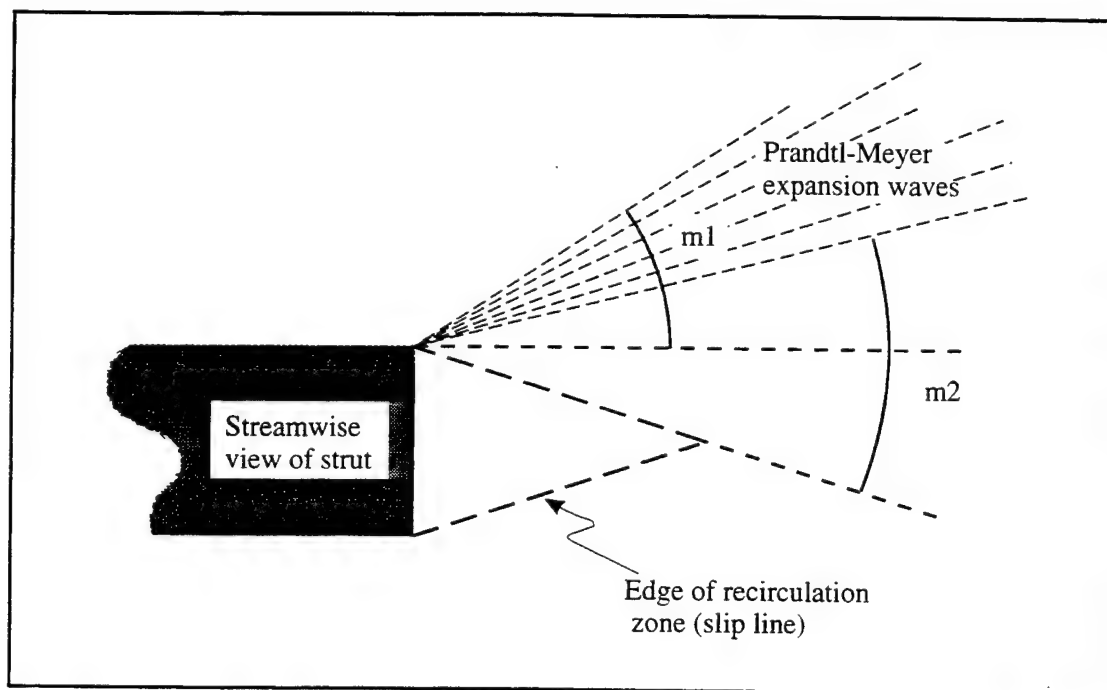


Figure 5.2. Illustration of Prandtl-Meyer expansion wave theory at base of the extended strut without injection.

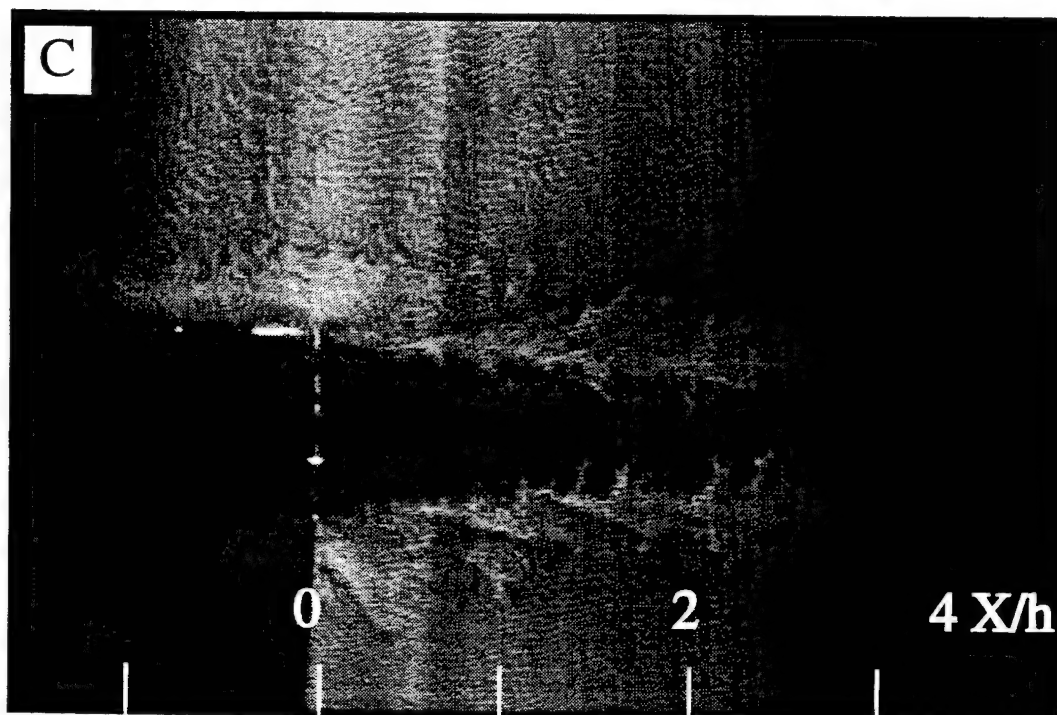
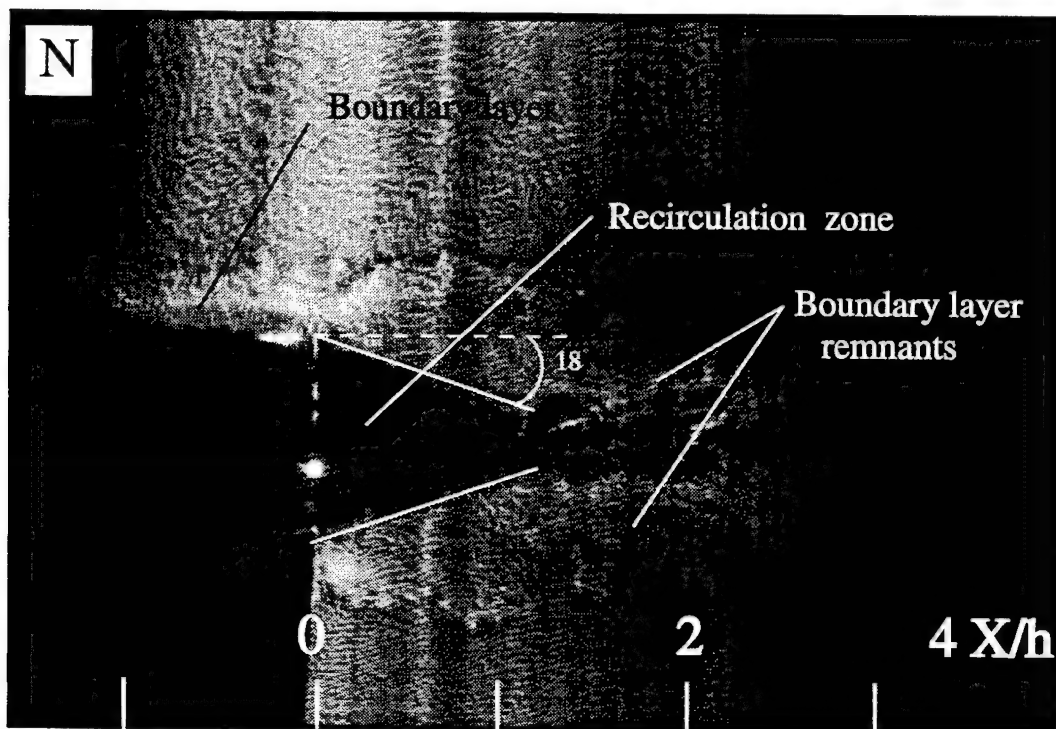


Figure 5.3. Instantaneous Rayleigh/Mie images of boundary layer. Streamwise (X,Y) plane of view located on centerline of the strut ($Z=0$) for the no injection (N), and helium injection ($\Psi=4$) through circular (C) nozzle.

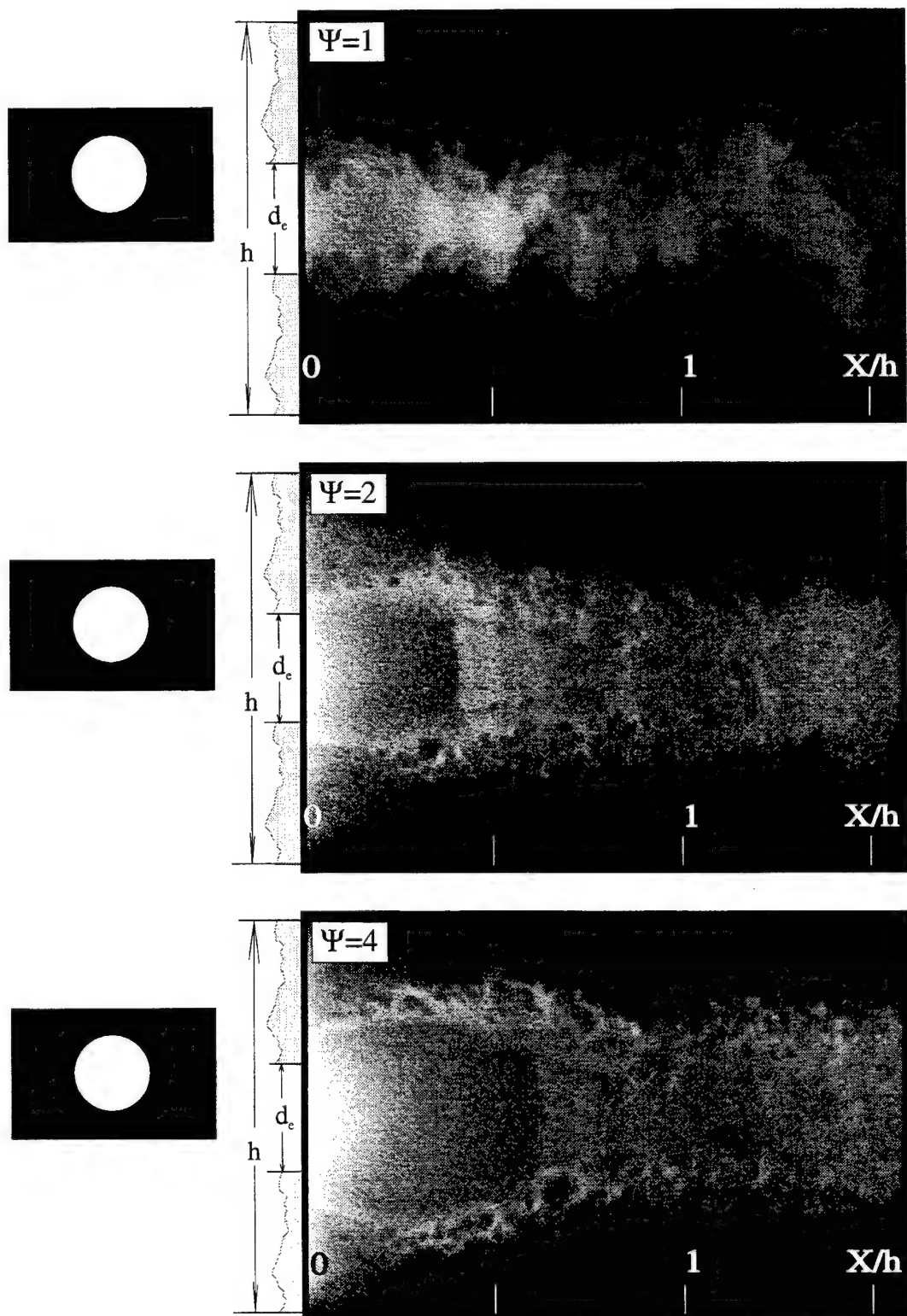


Figure 5.4. Instantaneous acetone PLIF images of helium injection through circular nozzle (C) at static pressure ratios $\Psi=1$, $\Psi=2$, and $\Psi=4$. Streamwise (X,Y) plane of view located on centerline of the jet.

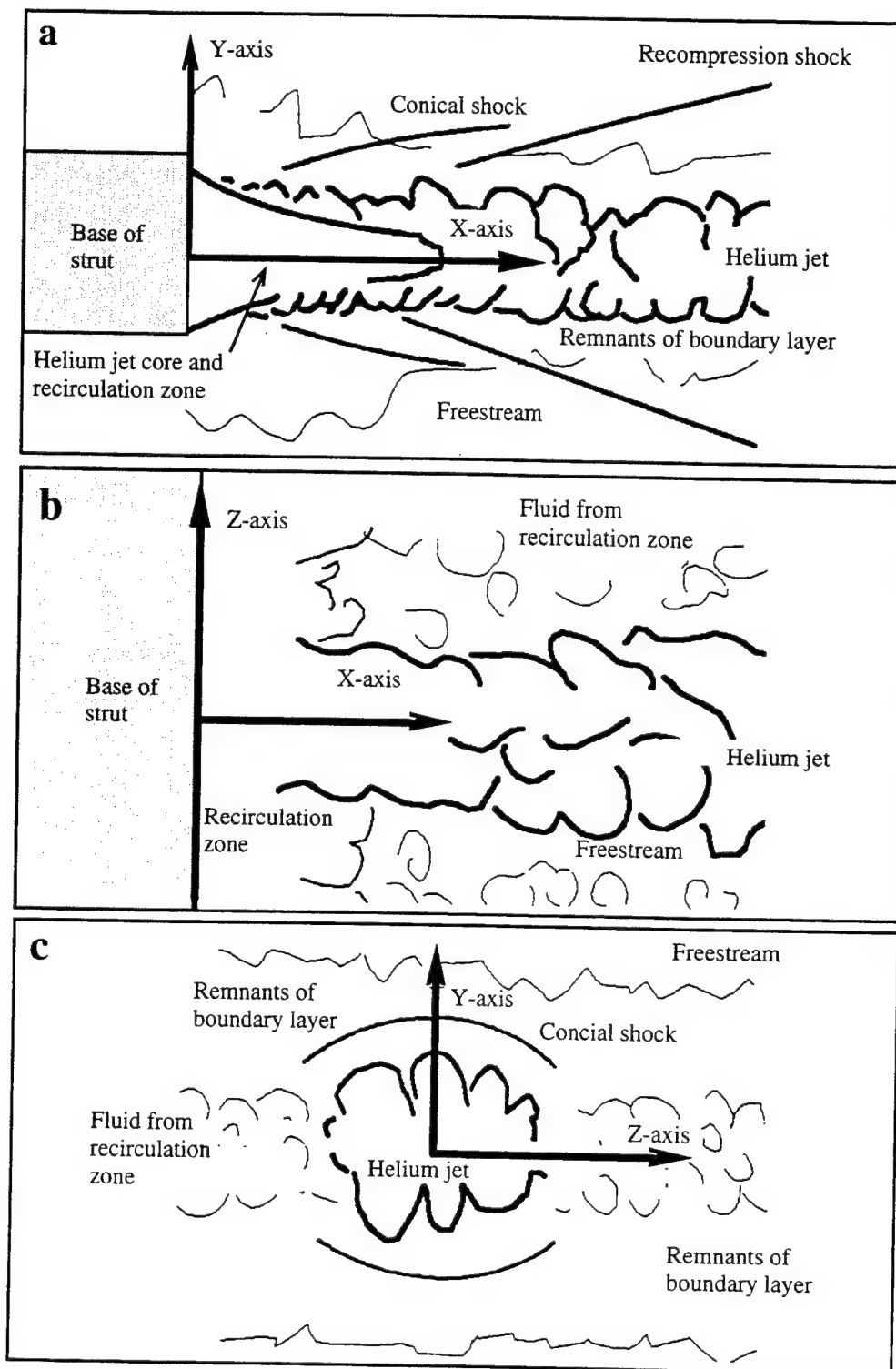
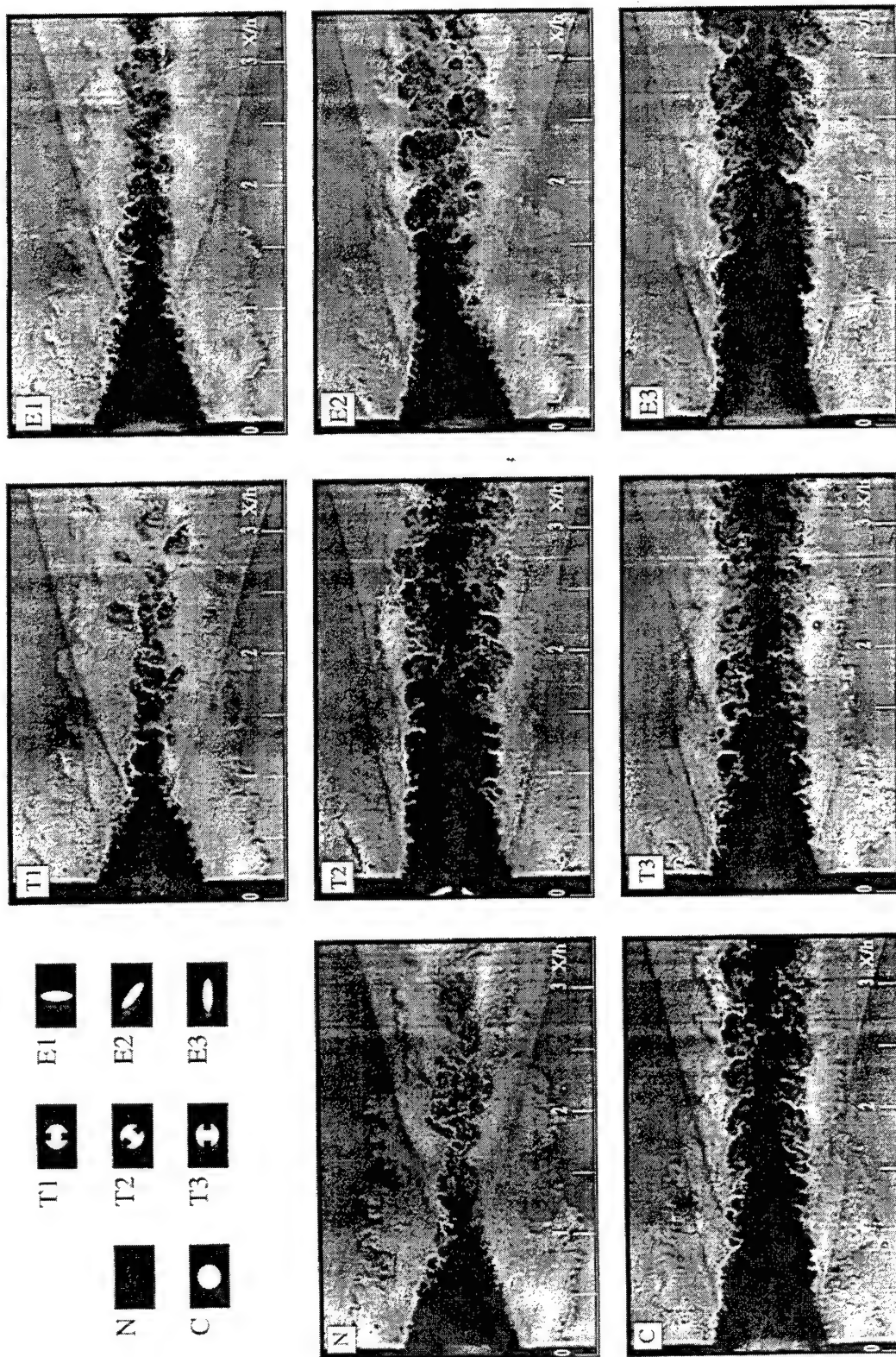
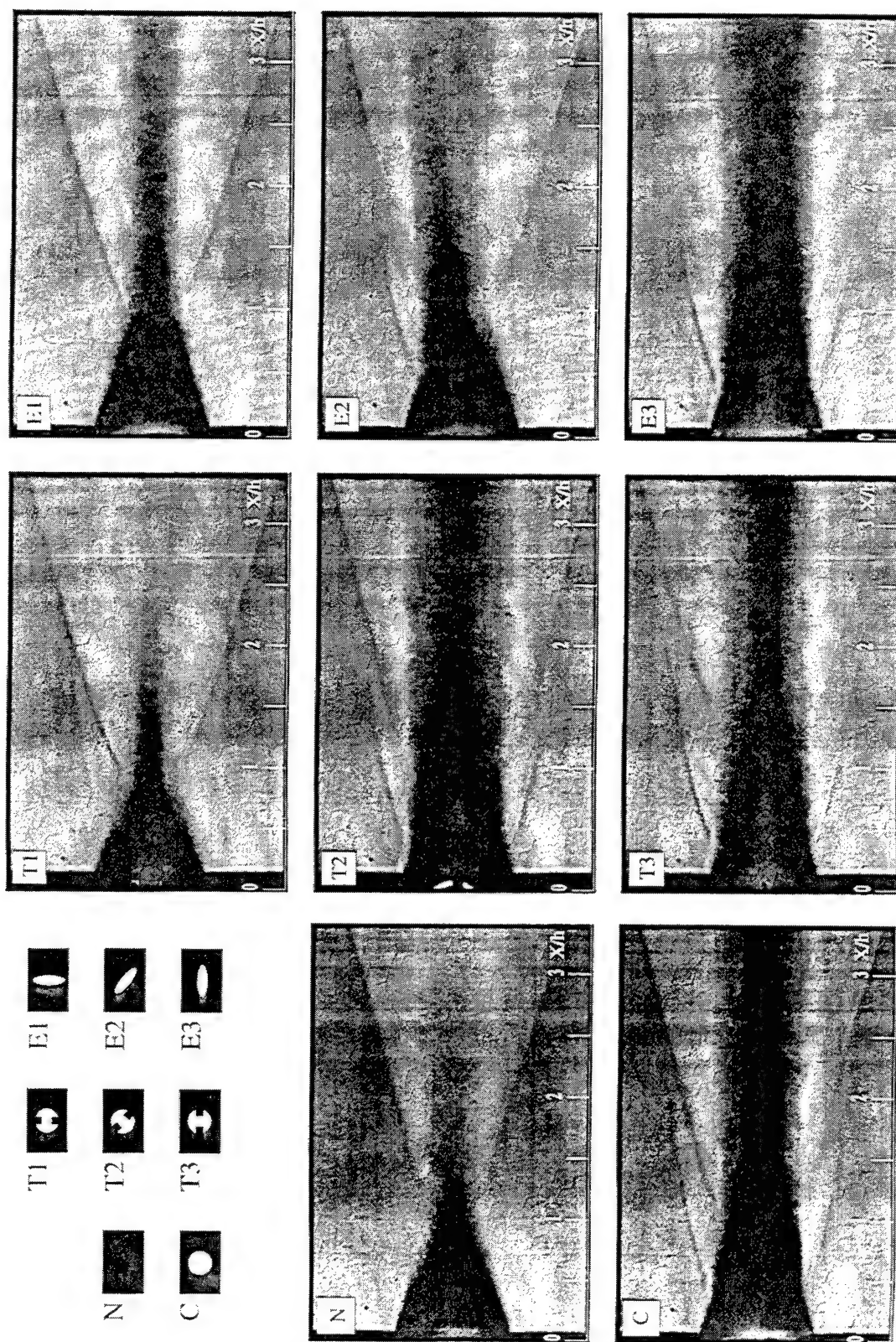


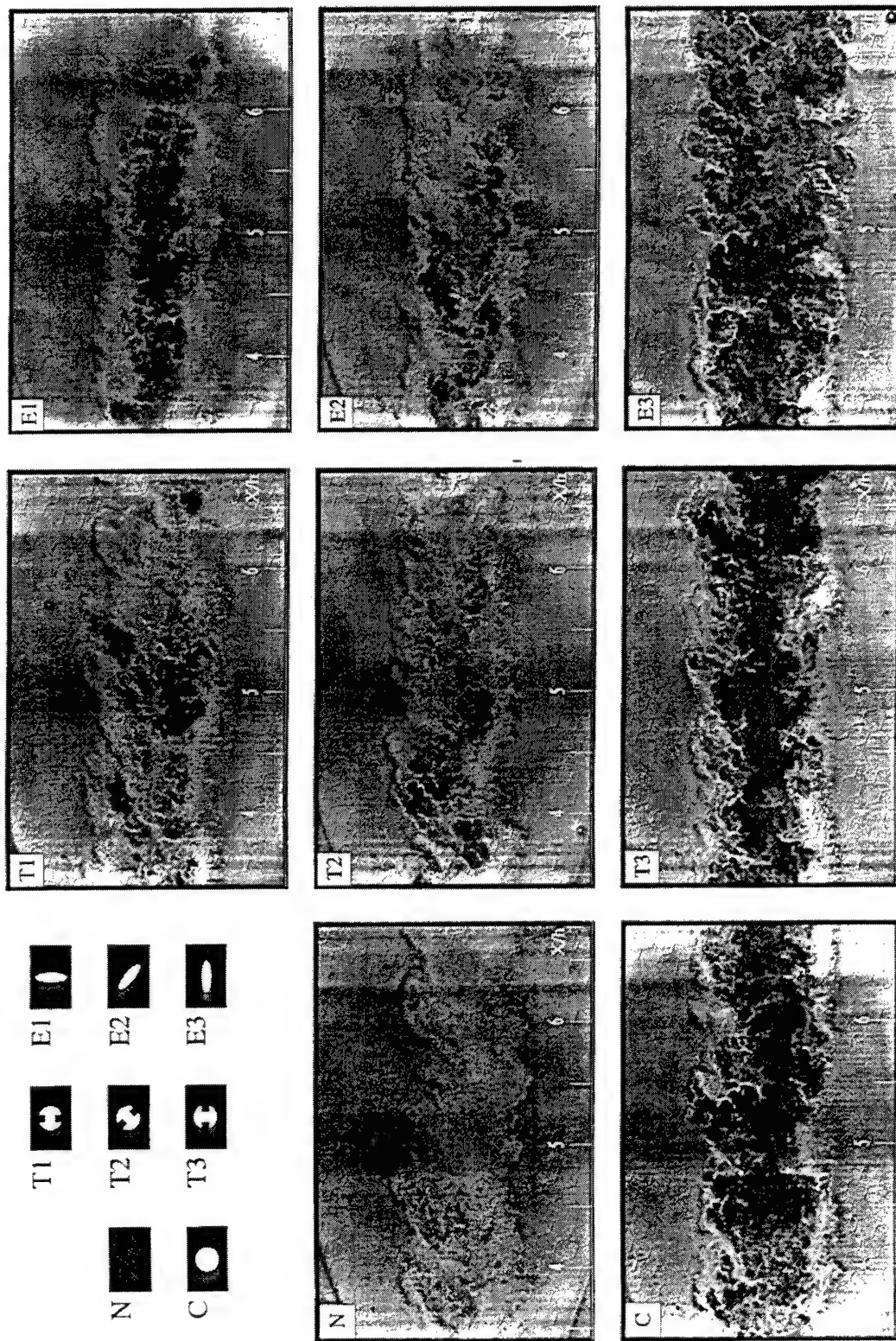
Figure 5.5. Schematic of instantaneous Rayleigh/Mie scattering images for the a) streamwise (X,Y), b) plan (X,Z) and c) face-on (Y,Z) planes of view.



5.6. Instantaneous Rayleigh/Mie images of streamwise (X,Y) plane of view located on the centerline of injector nozzle ($Z=0$) for the no injection (N) case and helium injection ($\Psi = 4$) cases (C, T1, T2, T3, E1, E2, E3). Upstream view.



5.7. Average Rayleigh/Mie images of streamwise (X,Y) plane of view located on the centerline of injector nozzle for no injection (N) case and helium injection ($P = 4$) cases (C, T1, T2, T3, E1, E2, E3). Upstream view.



5.8. Instantaneous Rayleigh/Mic images of streamwise (X,Y) plane of view located on the centerline of injector nozzle ($Z=0$) for the no injection (N) case and helium injection ($\Psi = 4$) cases (C, T1, T2, T3, E1, E2, E3). Downstream view.

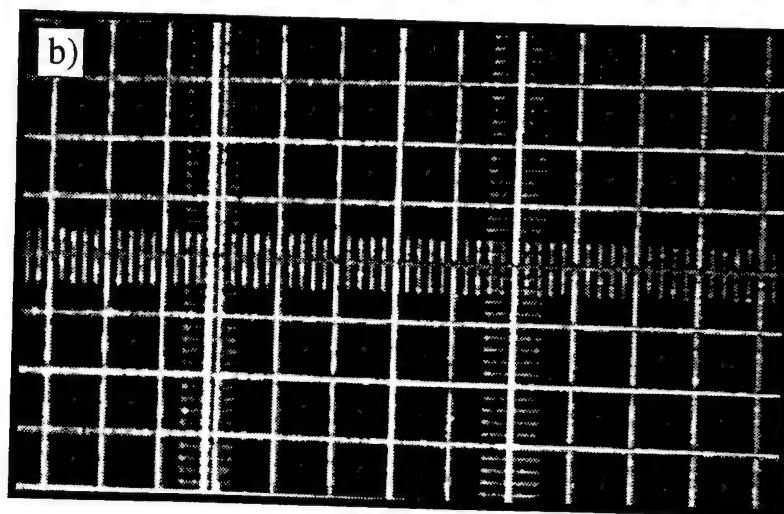
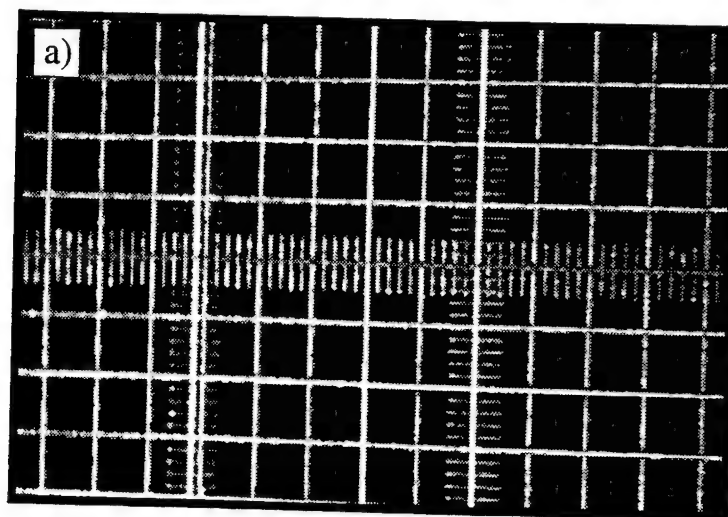


Figure 5.9. a) Original and b) corrected image of scale used for Rayleigh/Mie scattering images of the face-on (Y,Z) plane of view. Grid size is 2.54 by 2.54 mm.

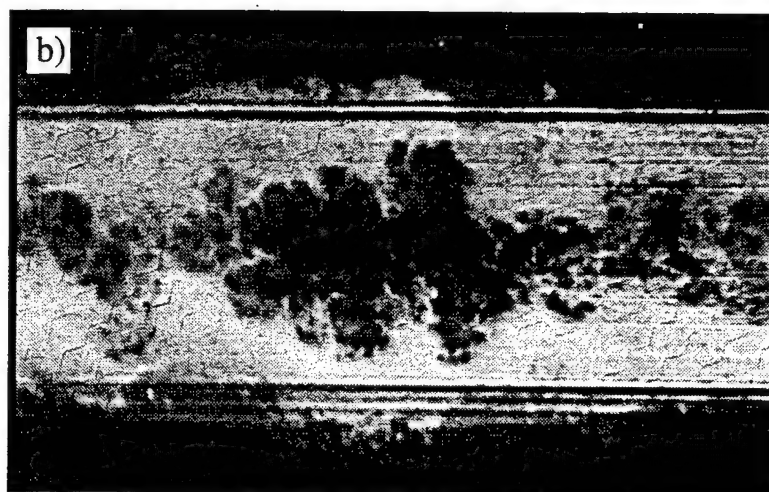
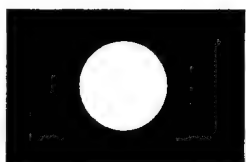
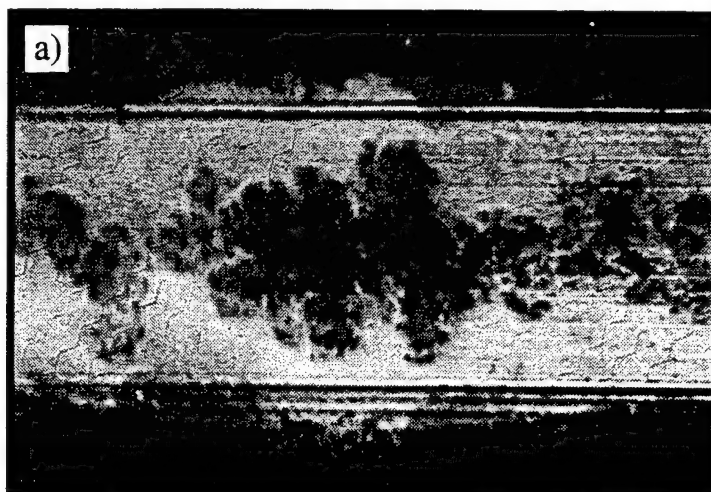
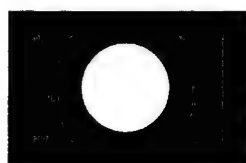
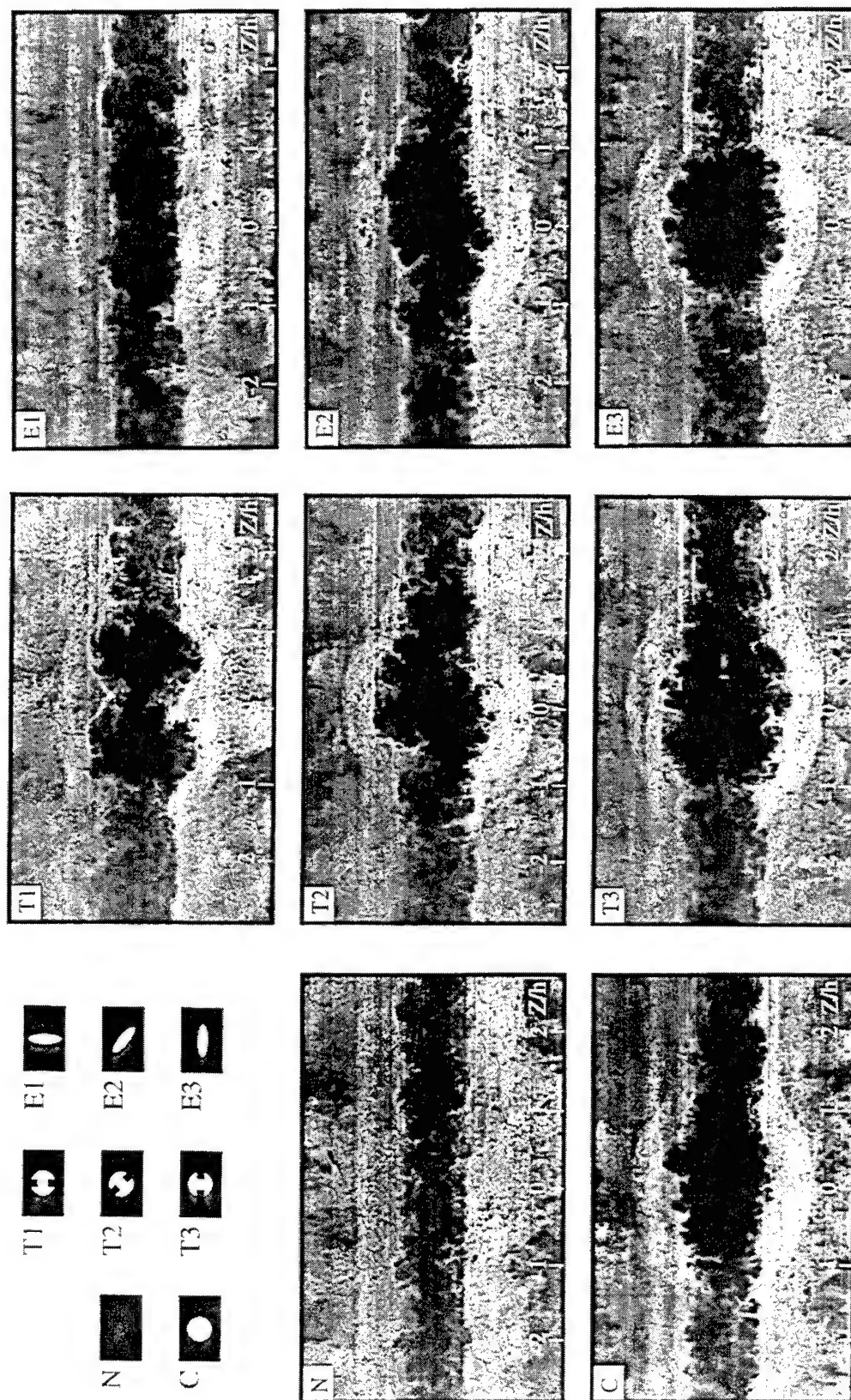
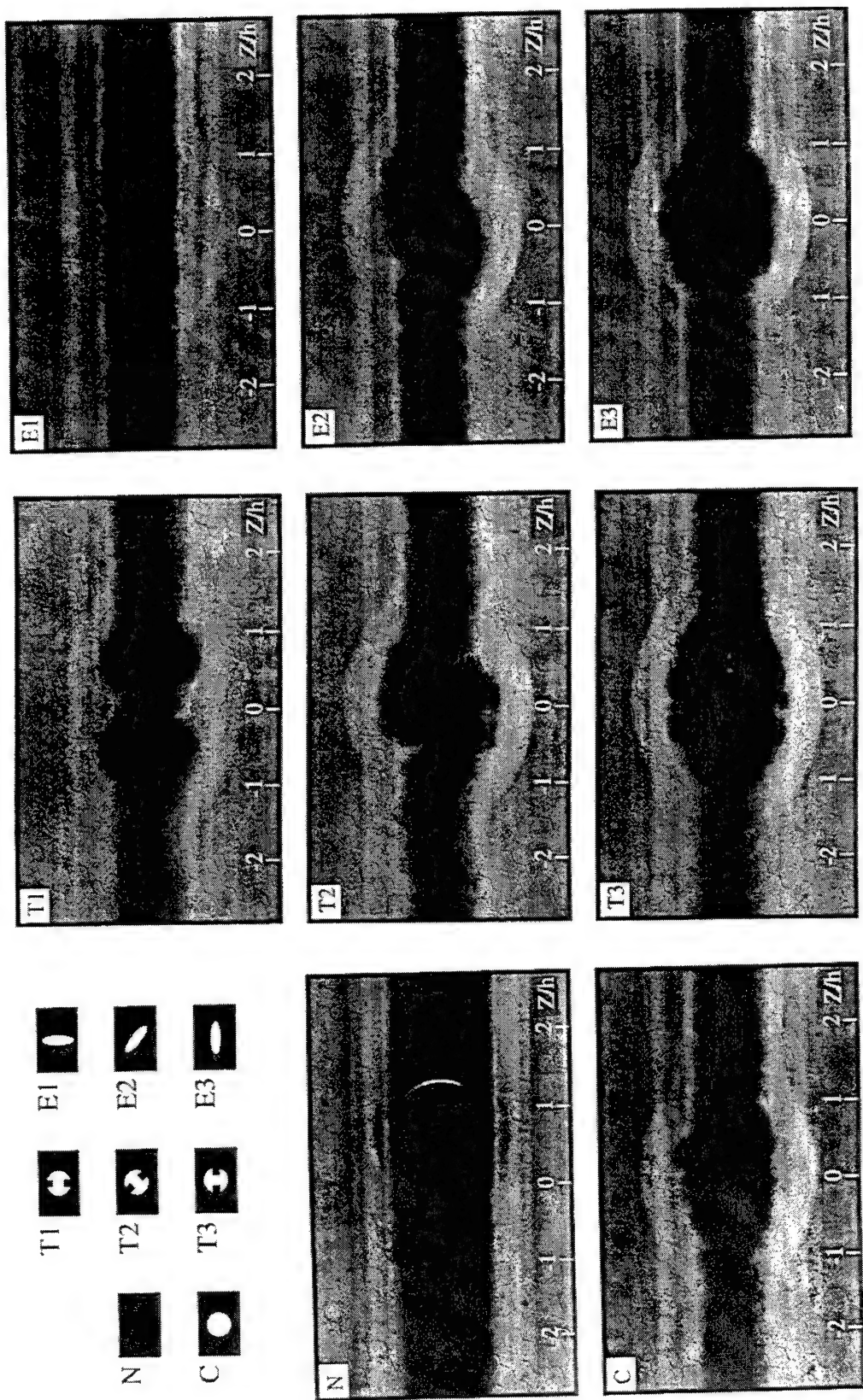


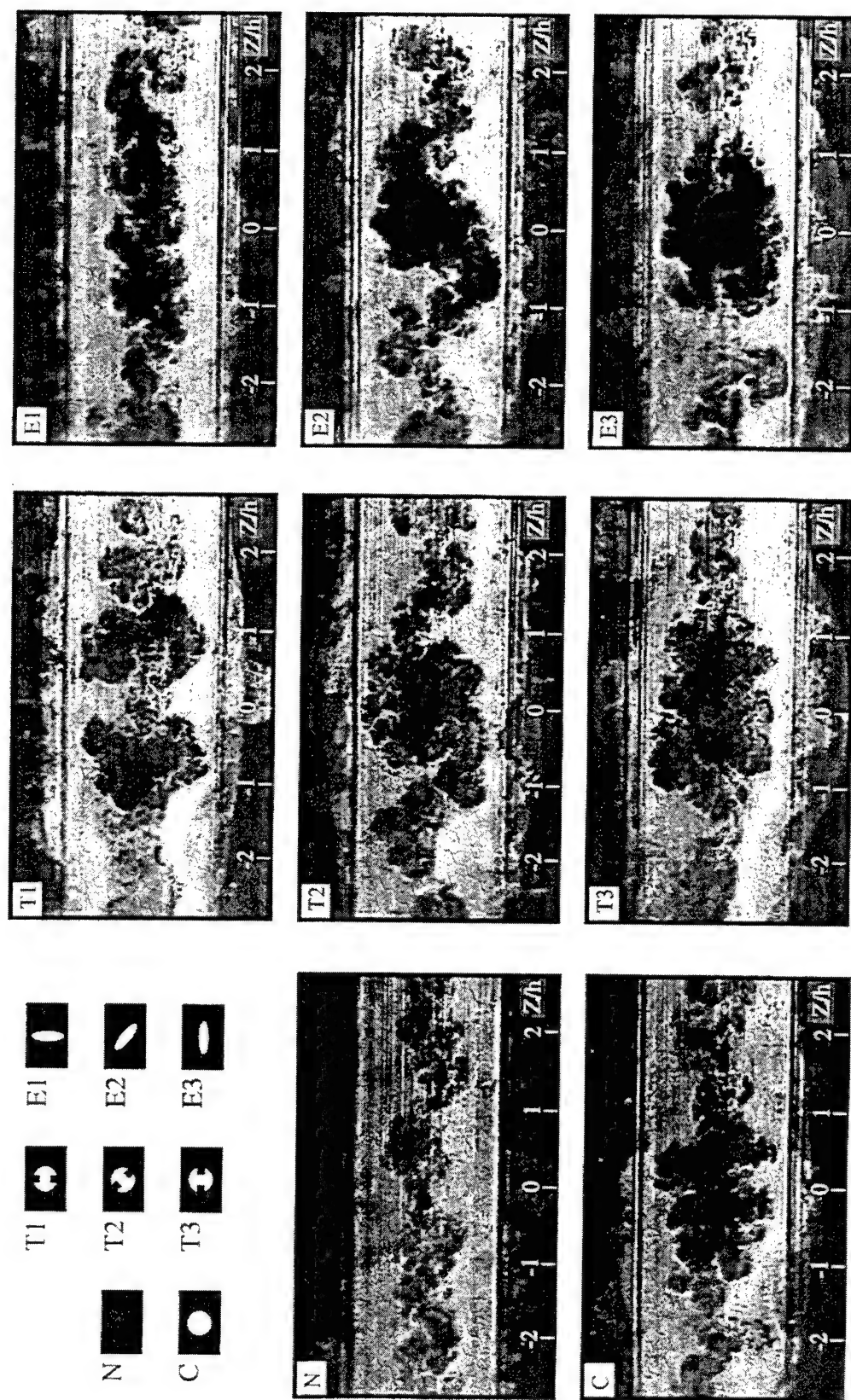
Figure 5.10. a) Original and b) corrected instantaneous Rayleigh/Mie image of the face-on (Y,Z) plane of view located at $X/h=2$ for helium injection ($Y=4$) using circular (C) nozzle.



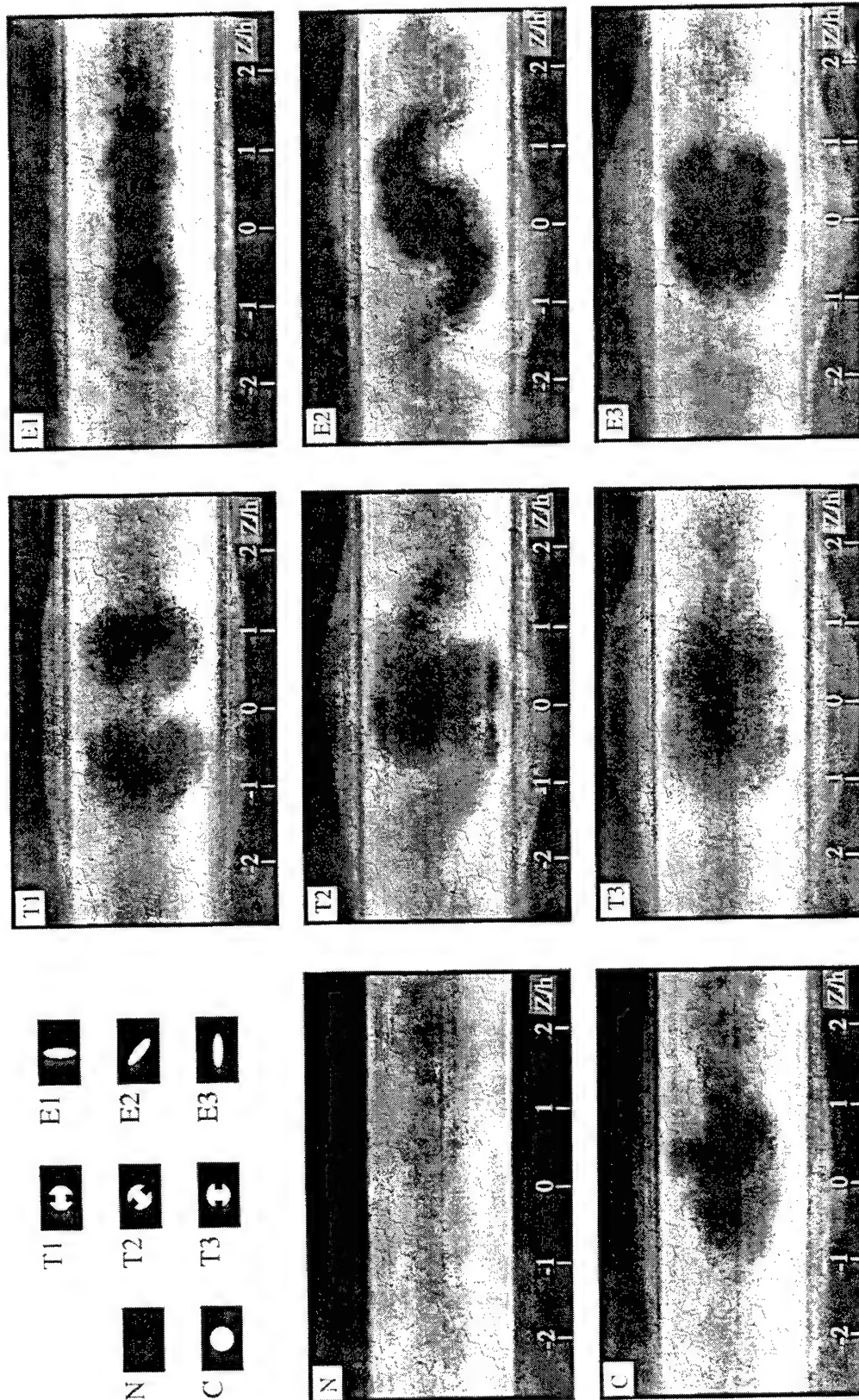
5.11. Instantaneous Rayleigh/Mie images of face-on (Y,Z) plane of view located at $X/h = 1$ for the no injection (N) case and helium injection ($\Psi = 4$) cases (C, T1, T2, T3, E1, E2, E3).



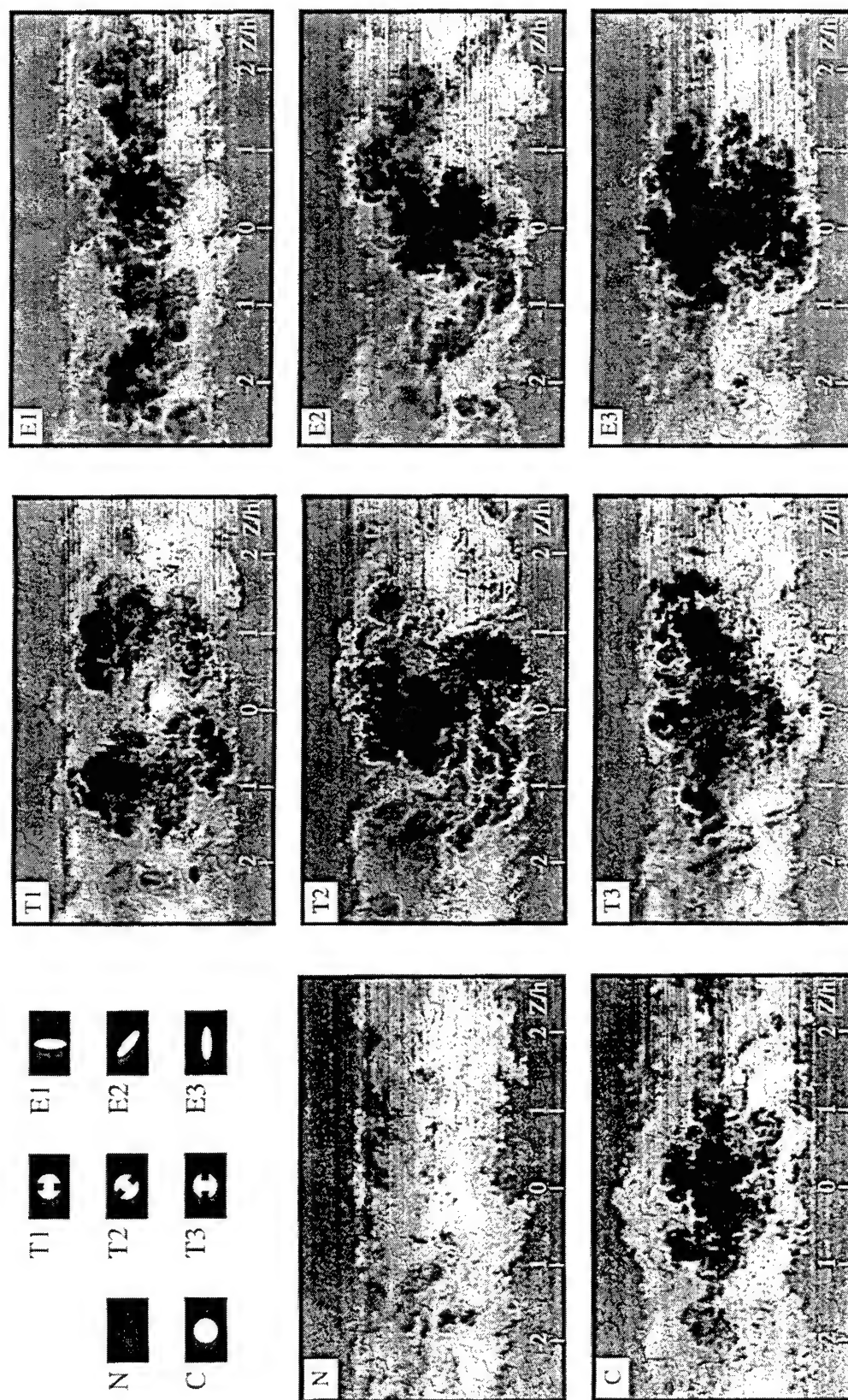
5.12. Average Rayleigh/Mie images of face-on (Y,Z) plane of view located at $X/h = 1$ for the no injection (N) case and helium injection ($\Psi = 4$) cases (C, T1, T2, T3, E1, E2, E3).



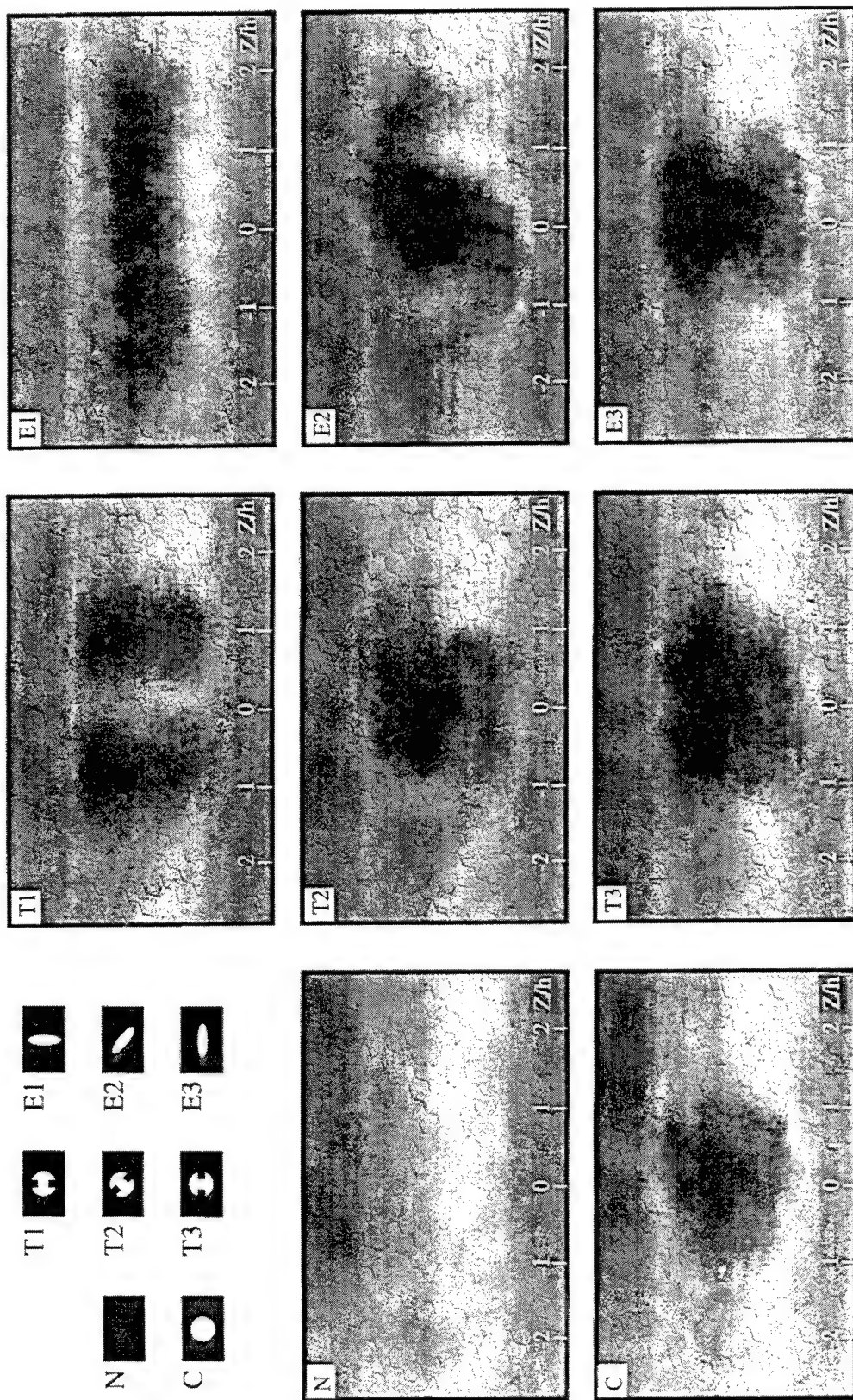
5.13. Instantaneous Rayleigh-Mie images of face-on (Y,Z) plane of view located at $X/h = 2$ for the no injection (N) case and helium injection ($\Psi = 4$) cases (C, T1, T2, T3, E1, E2, E3).



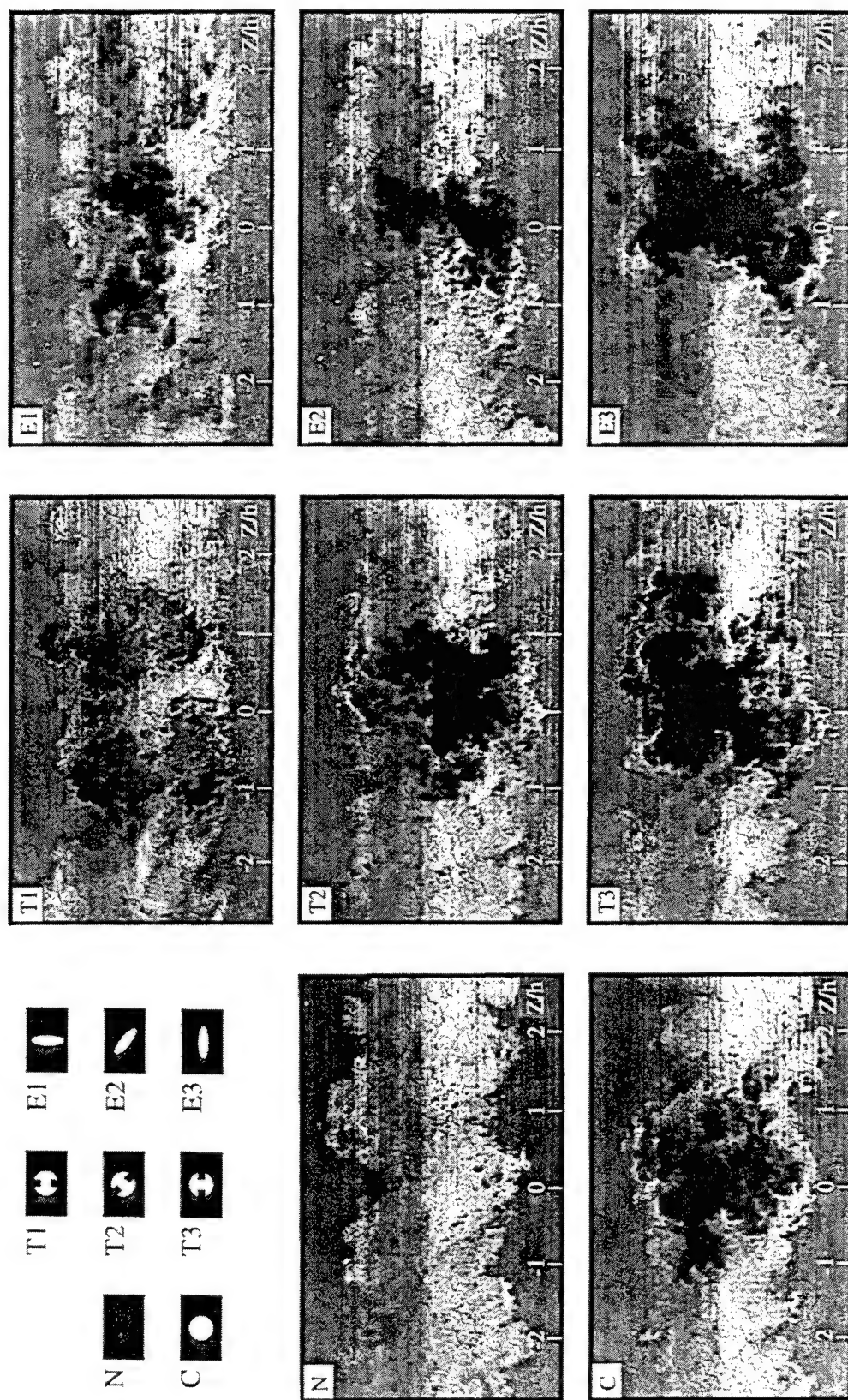
5.14. Average Rayleigh/Mie images of face-on (Y,Z) plane of view located at $X/h = 2$ for the no injection (N) case and helium injection ($\Psi = 4$) cases (C, T1, T2, T3, E1, E2, E3).



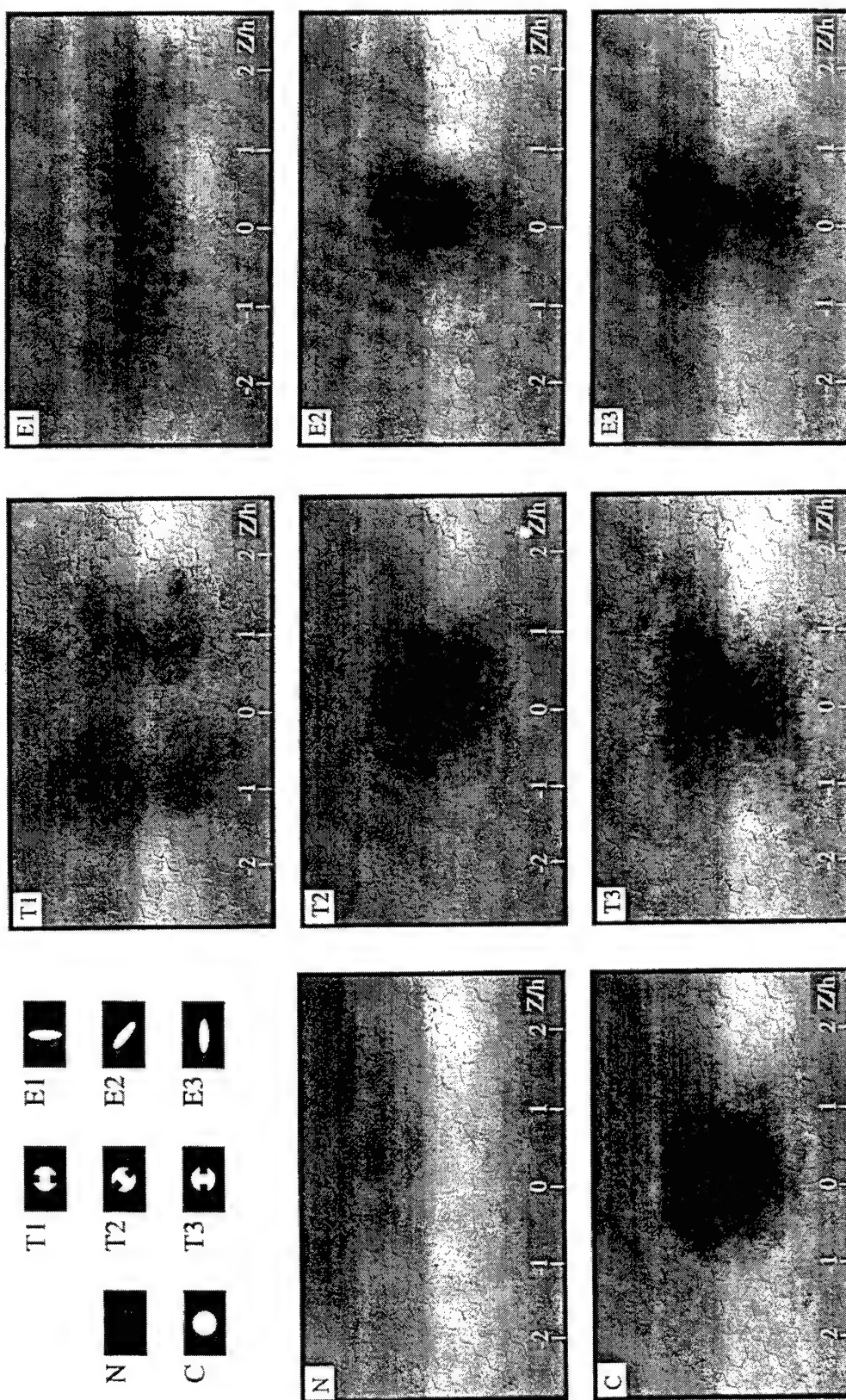
5.15. Instantaneous Rayleigh-Mie images of face-on (Y,Z) plane of view located at $X/h = 4$ for the no injection (N) case and helium injection ($\Psi = 4$) cases (C, T1, T2, T3, E1, E2, E3).



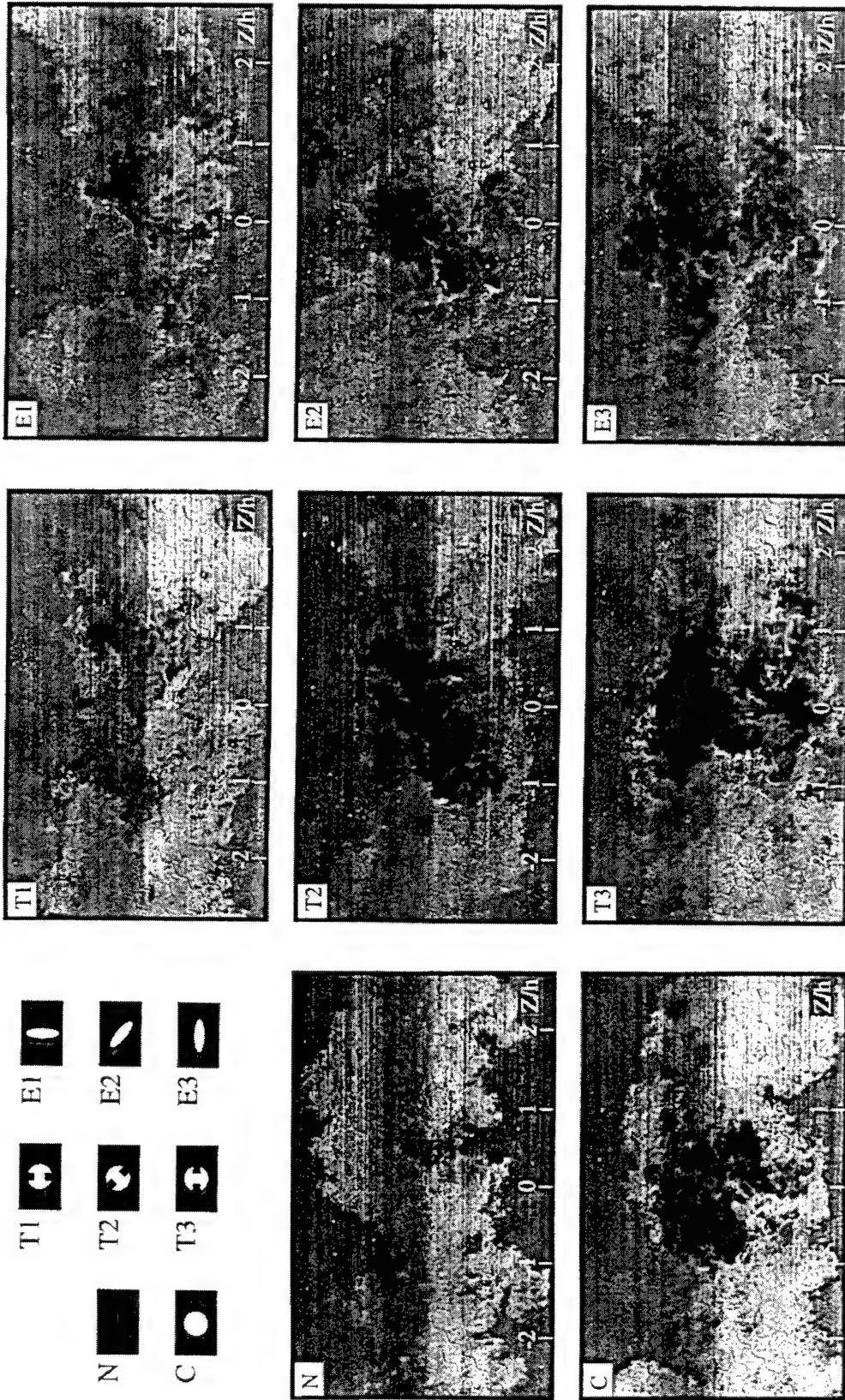
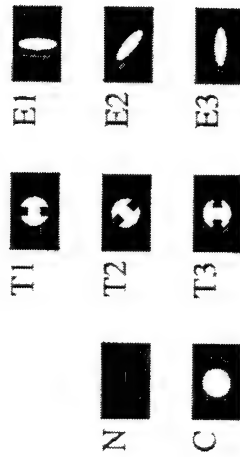
5.16. Average Rayleigh/Mie images of face-on (Y,Z) plane of view located at $X/h = 4$ for the no injection (N) case and helium injection ($\Psi = 4$) cases (C, T1, T2, T3, E1, E2, E3).



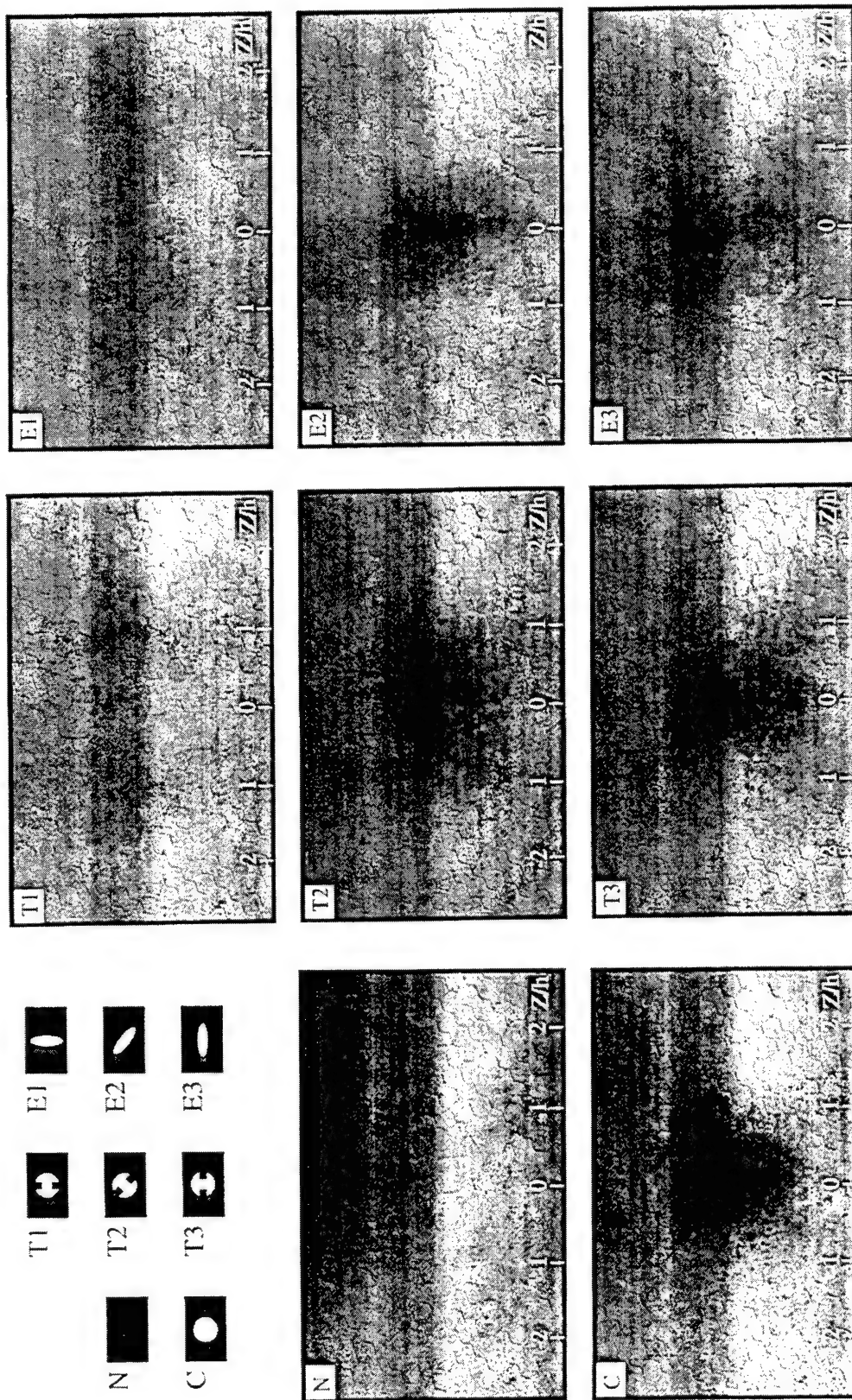
5.17. Instantaneous Rayleigh-Mie images of face-on (Y,Z) plane of view located at $X/h = 6.8$ for the no injection (N) case and helium injection ($\Psi = 4$) cases (C, T1, T2, T3, E1, E2, E3).



5.18. Average Rayleigh/Mie images of face-on (Y,Z) plane of view located at $X/h = 6.8$ for the no injection (N) case and helium injection ($\Psi = 4$) cases (C, T1, T2, T3, E1, E2, E3).



5.19. Instantaneous Rayleigh/Mie images of face-on (Y,Z) plane of view located at $X/h = 10$ for the no injection (N) case and helium injection ($\Psi = 4$) cases (C, T1, T2, T3, E1, E2, E3).



5.20. Average Rayleigh-Mie images of face-on (Y,Z) plane of view located at $X/h = 10$ for the no injection (N) case and helium injection ($\Psi = 4$) cases (C, T1, T2, T3, E1, E2, E3)

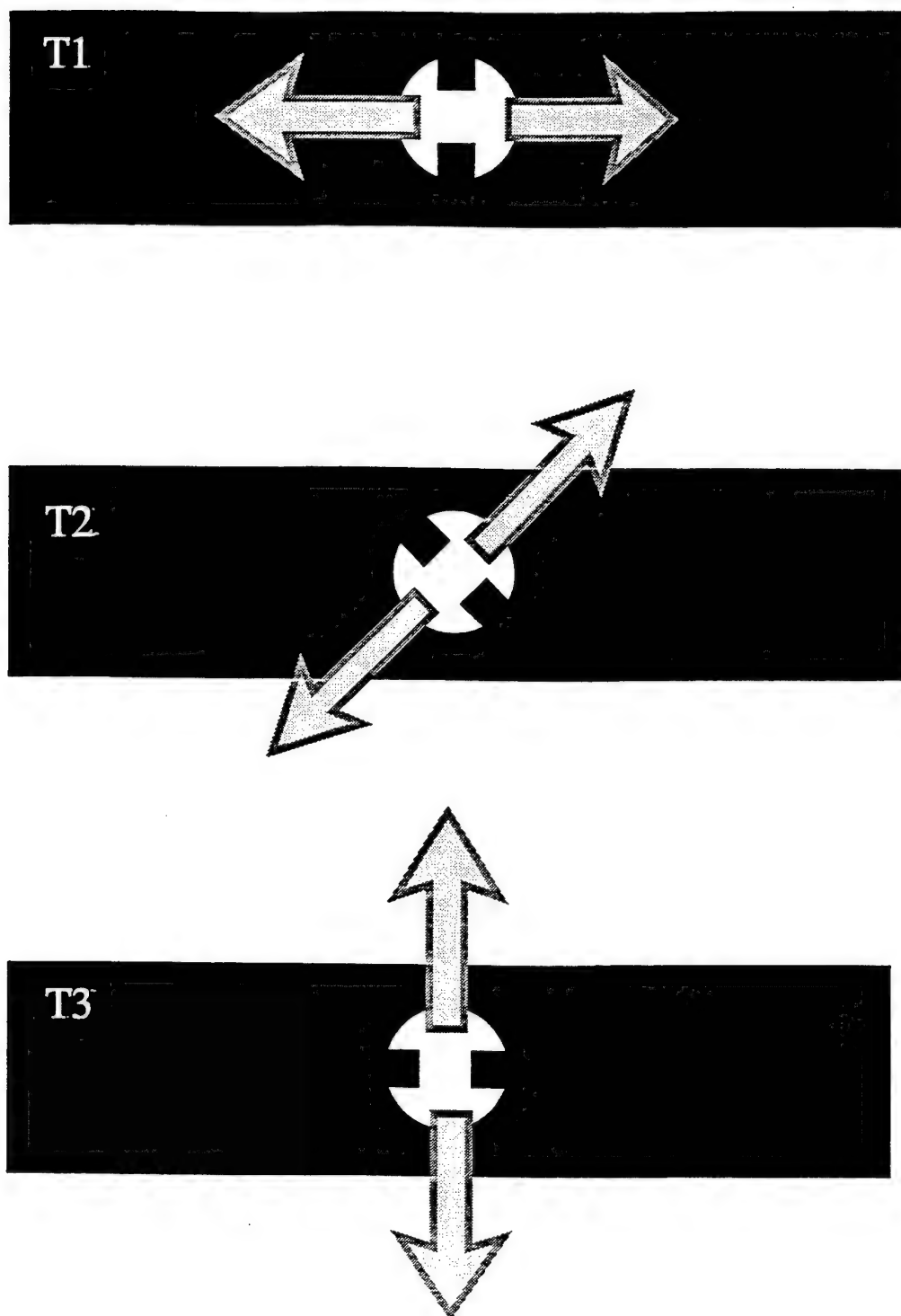
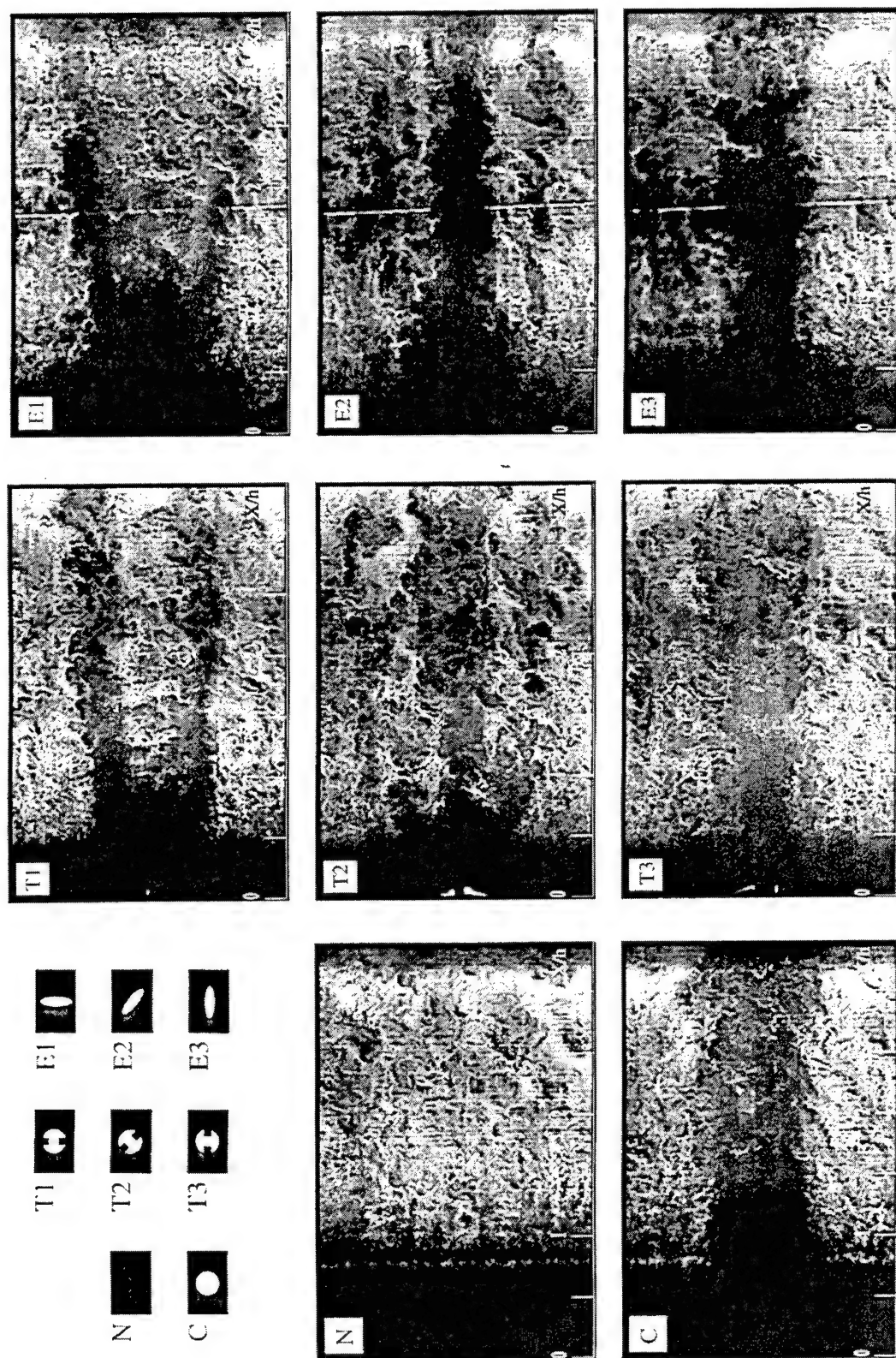
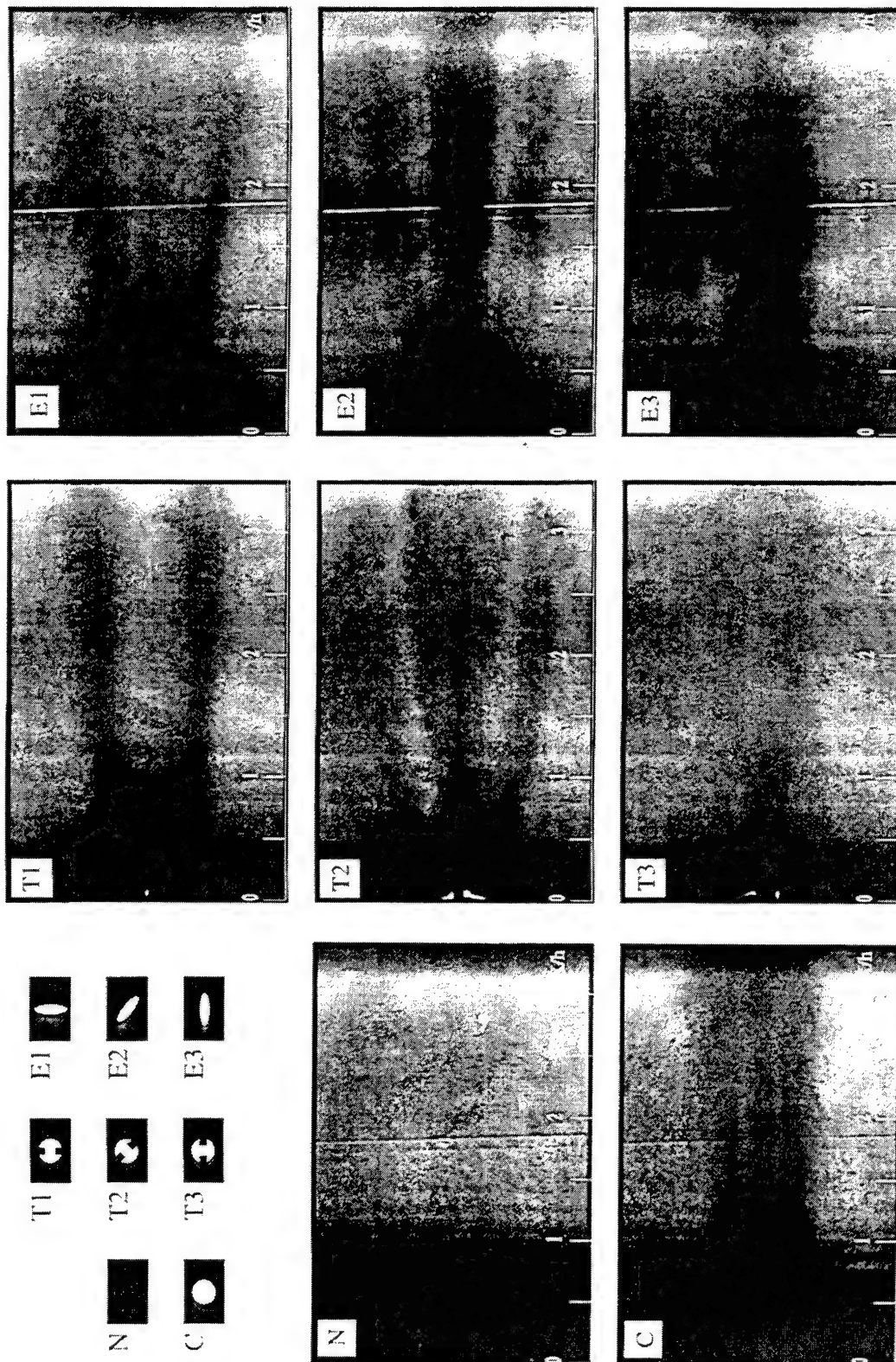


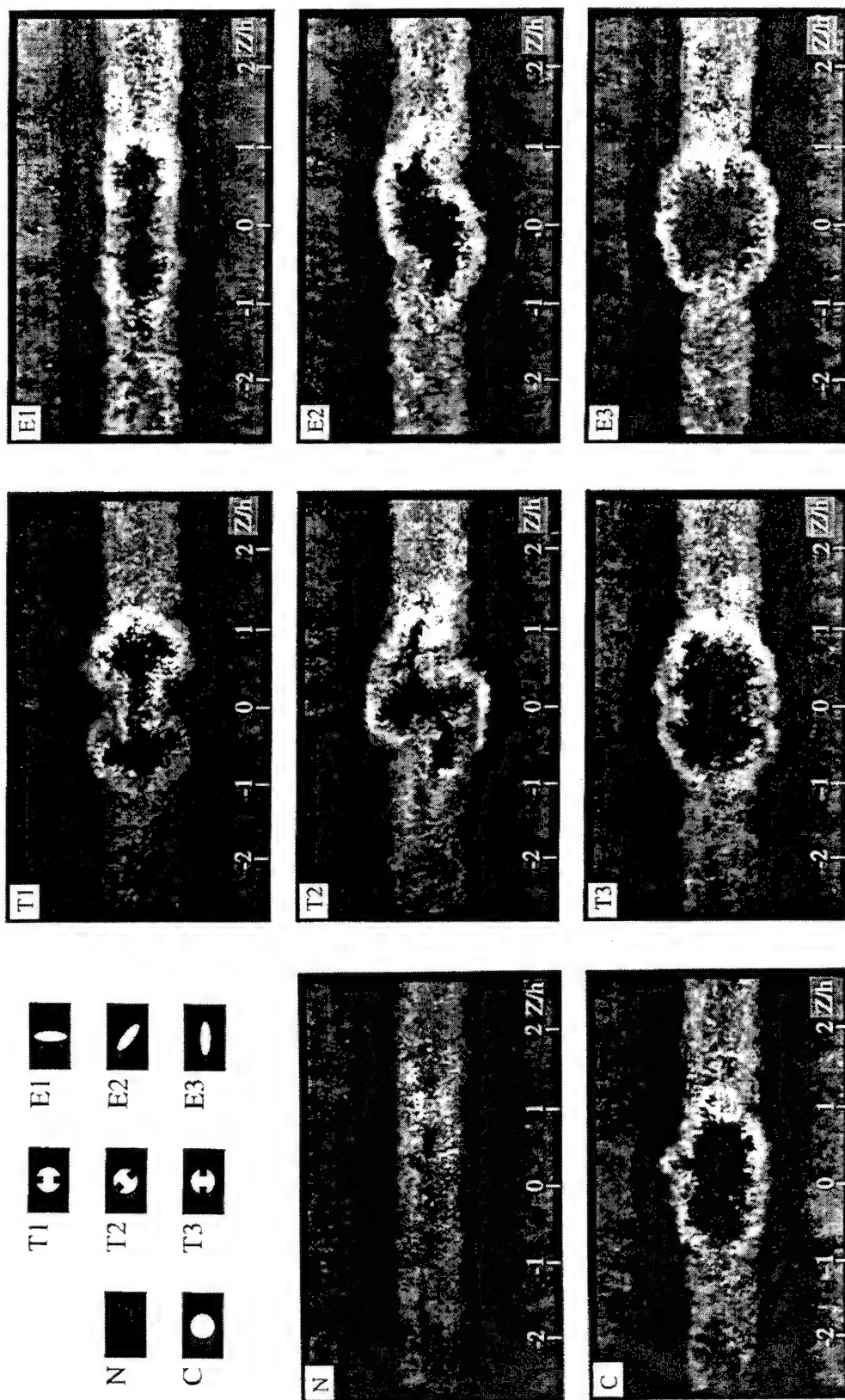
Figure 5.21. Illustration depicting the second most dominant component of mean flow velocity of the jet issuing from the circular-with-tabs nozzle configurations T1, T2, and T3. The most dominant component of the jet mean flow velocity is the streamwise component directed out of the plane of the page.



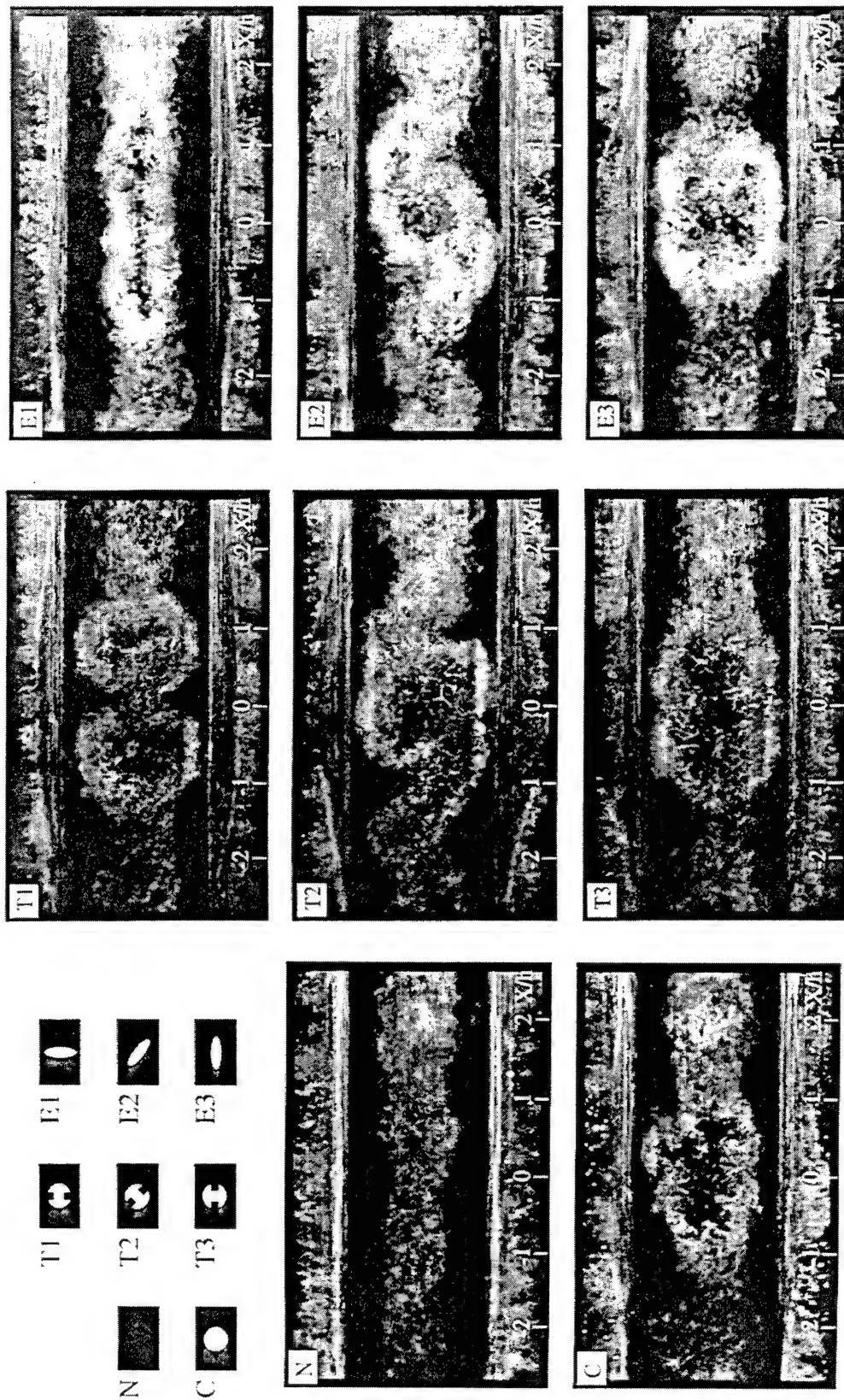
5.2.2. Instantaneous Rayleigh/Mie images of plan (X,Z) plane of view located on the centerline of injector nozzle ($Y=0$) for the no injection (N) case and helium injection ($\Psi = 4$) cases (C, T1, T2, T3, E1, E2, E3).



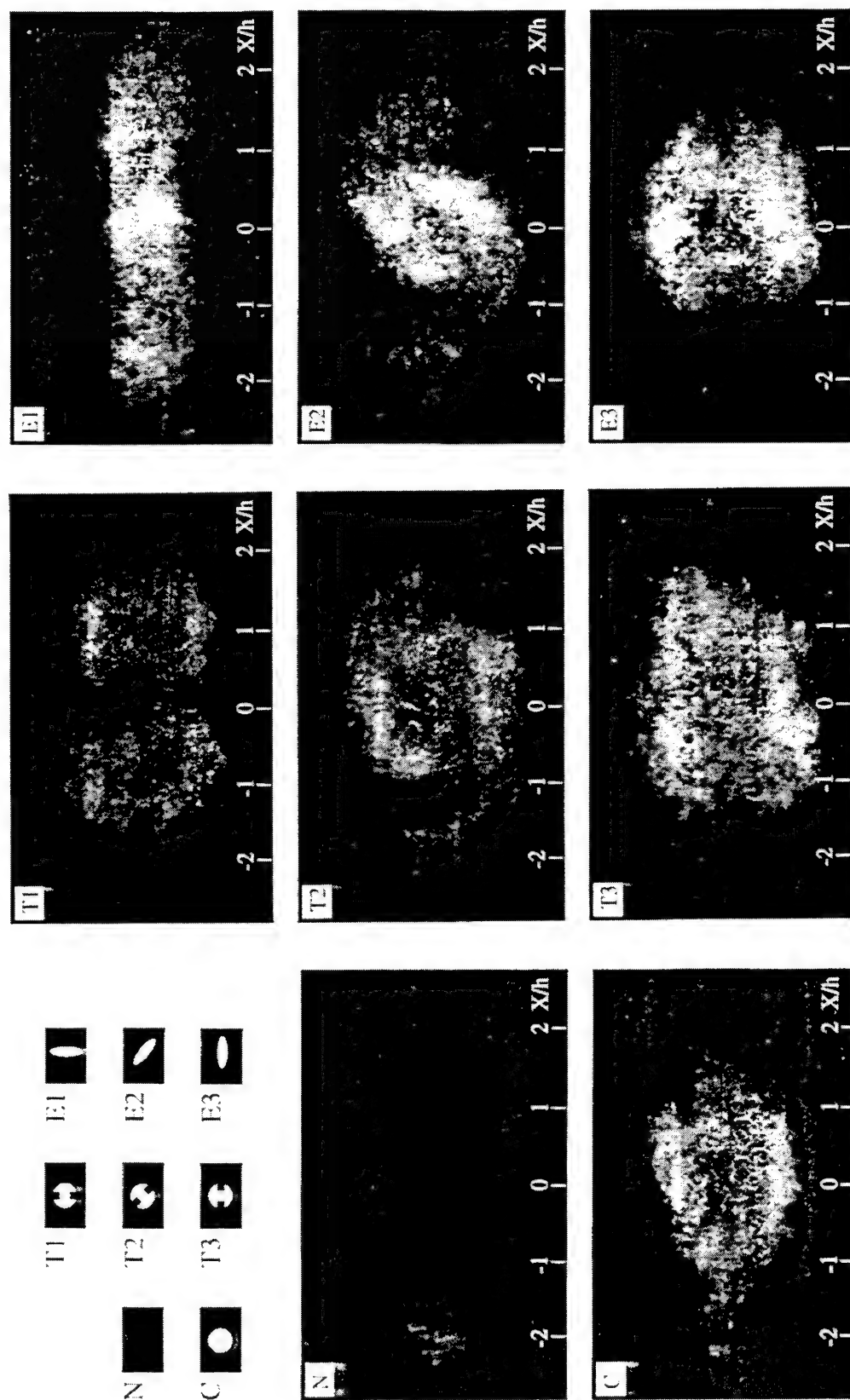
5.23. Average Rayleigh/Mie images of plan (X,Z) plane of view located on centerline of injector nozzle ($Y=0$) for the no injection (N) case and helium injection ($\Psi = 4$) cases (C, T1, T2, T3, E1, E2, E3).



5.24. Standard deviation of Rayleigh/Mie images of face-on (Y,Z) plane of view located at $X/h = 1$ for the no injection (N) case and helium injection ($\Psi = 4$) cases (C, T1, T2, T3, E1, E2, E3).



5.25. Standard deviation of Rayleigh-Mie images of face-on (Y,Z) plane of view located at $X/h = 2$ for the no injection (N) case and helium injection ($Q^* = 4$) cases (C, T1, T2, T3, E1, E2, E3).



5.26. Standard deviation of Rayleigh-Mie images of face-on (Y,Z) plane of view located at $X/h = 4$ for the no injection (N) case and helium injection ($\Psi = 4$) cases (C, T1, T2, T3, E1, E2, E3).

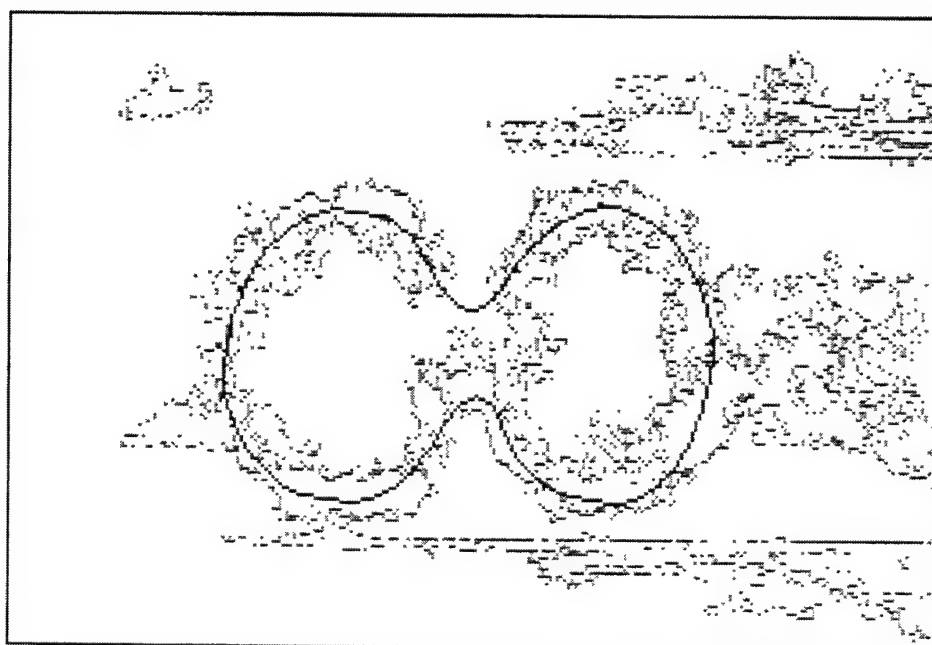
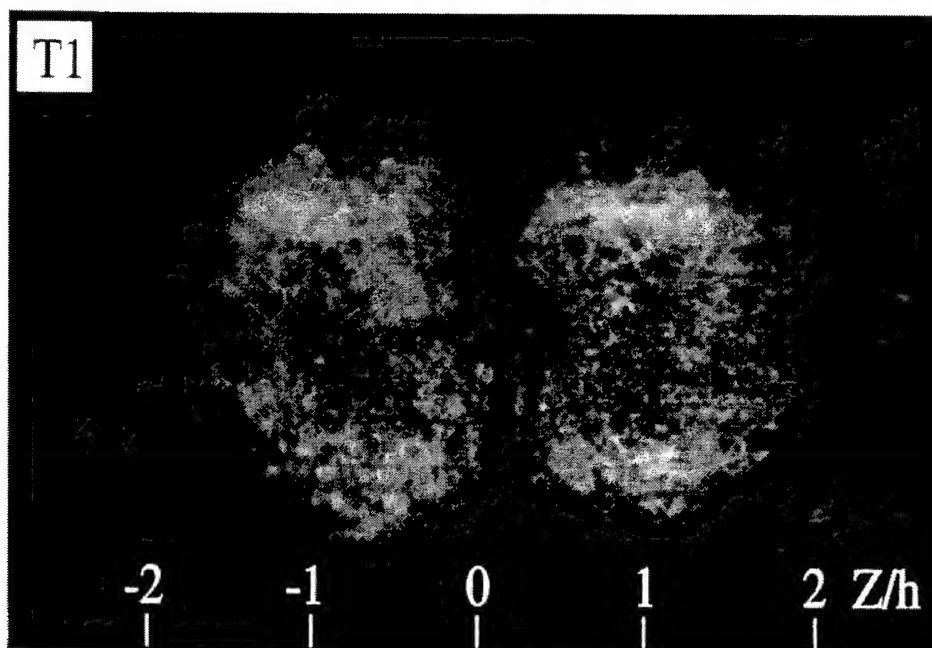


Figure 5.27. Example of a standard deviation of Rayleigh/Mie image of face-on (Y,Z) plane of view with corresponding schematic of visually approximated contour of highest standard deviation values.

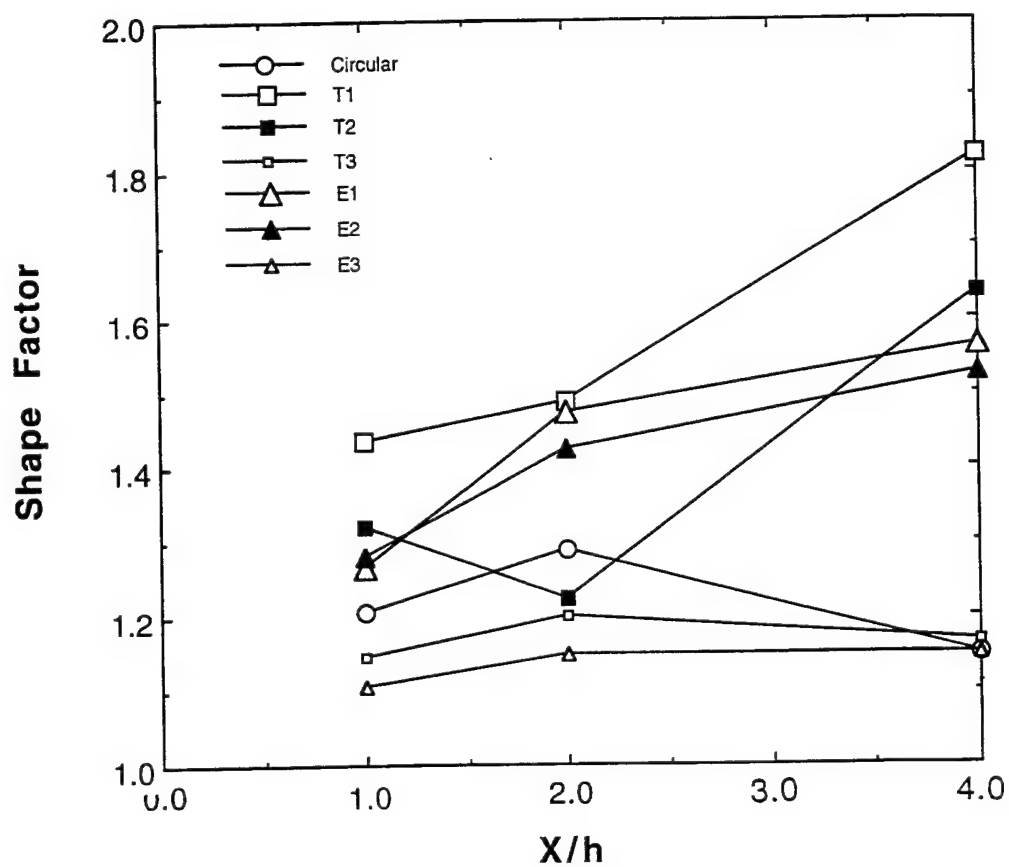


Figure 5.28. Plot of cross-sectional areas of the helium jet ($\Psi=4$) determined from Rayleigh/Mie scattering images of face-on (Y,Z) planes of view located at $X/h = 1, 2,$ and 4 .

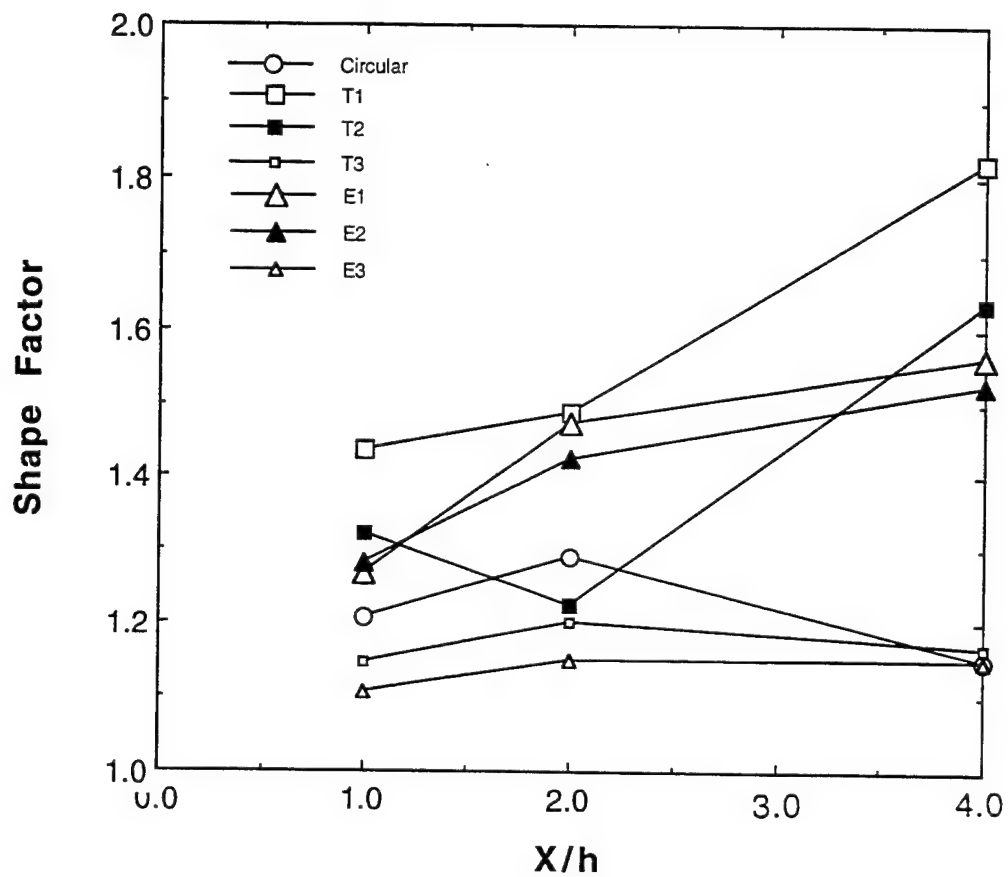


Figure 5.29. Plot of shape factors for helium jet ($\Psi=4$) calculated from cross-sectional area and perimeter calculations.

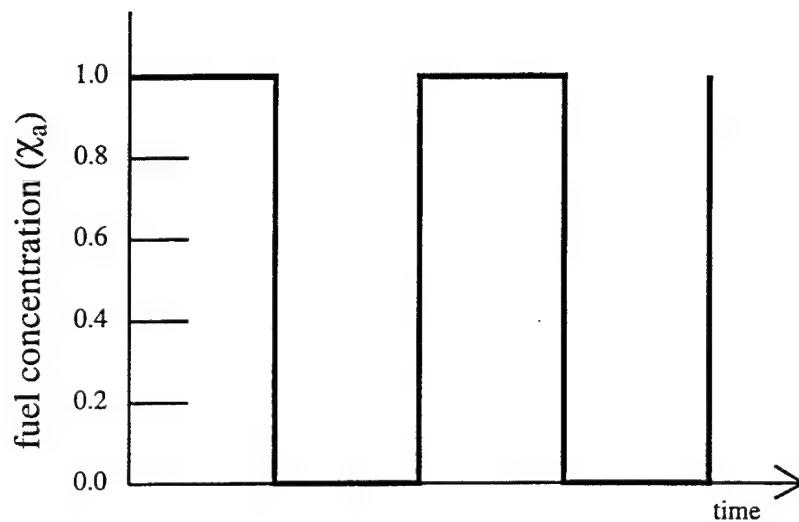


Figure 5.30. Hypothetical fuel concentration measurements at a point in a two segregated-stream flow of pure air and pure fuel.

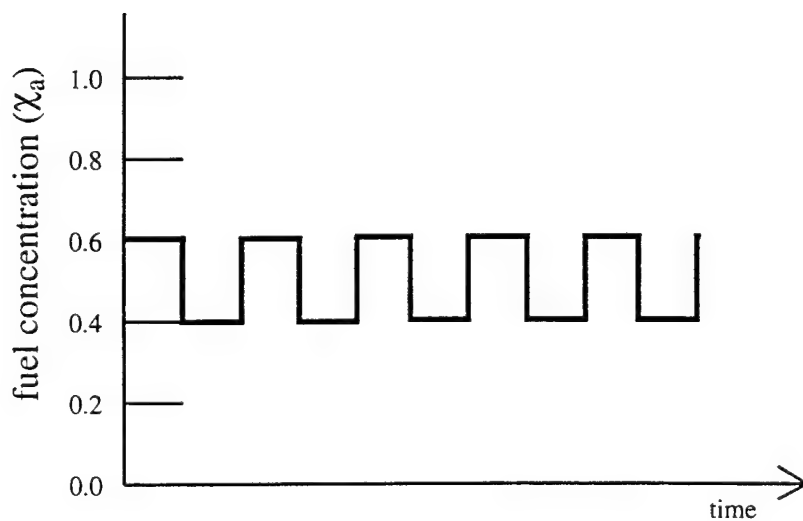


Figure 5.31. Hypothetical fuel concentration measurements at a point in a two segregated-stream flow of 60% and 40% fuel to air ratio mixtures.

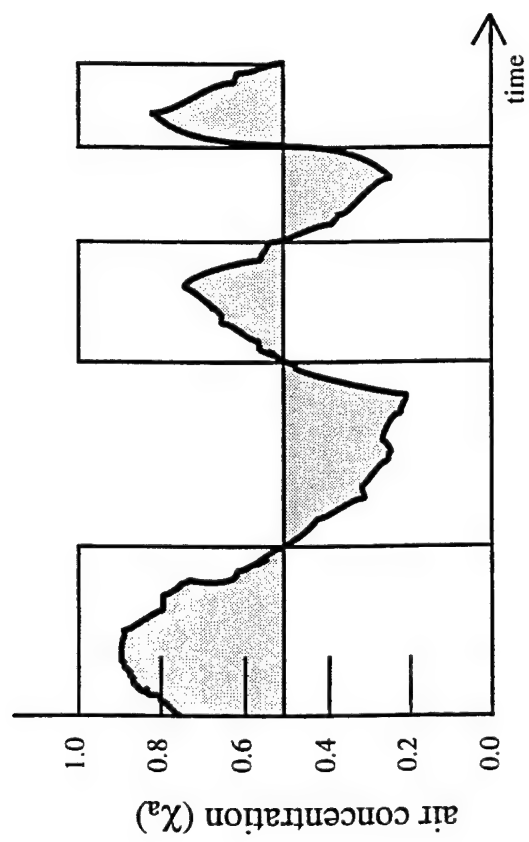


Figure 5.32. Graphical representation of Konrad's unmixedness parameter

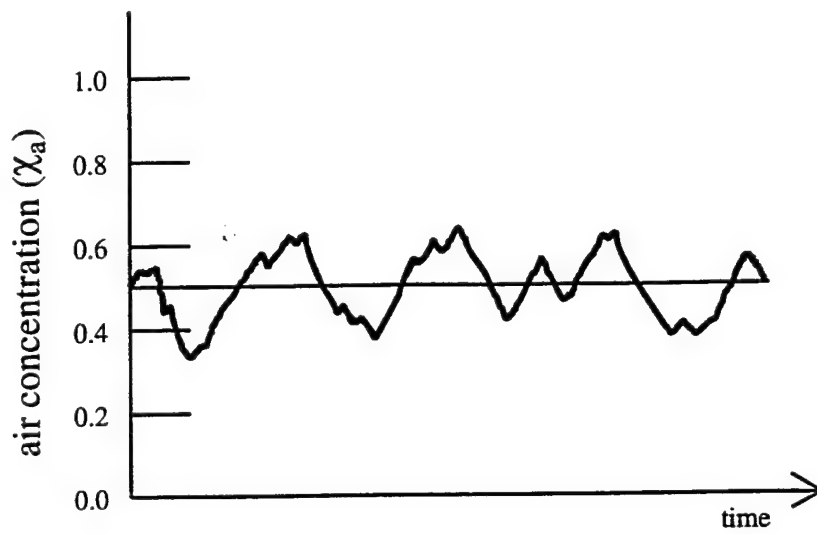


Figure 5.33. Example of concentration trace about local mean value $\chi_a = 0.5$.

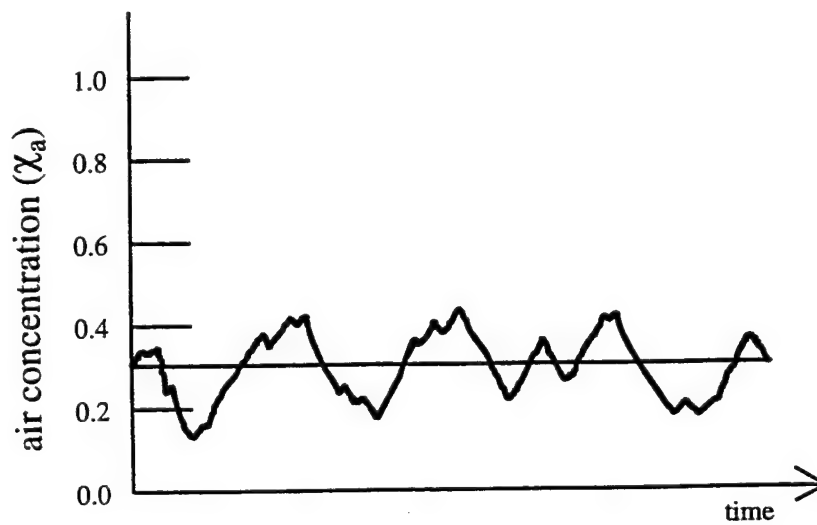


Figure 5.34. Example of concentration trace about local mean value $\chi_a = 0.3$.

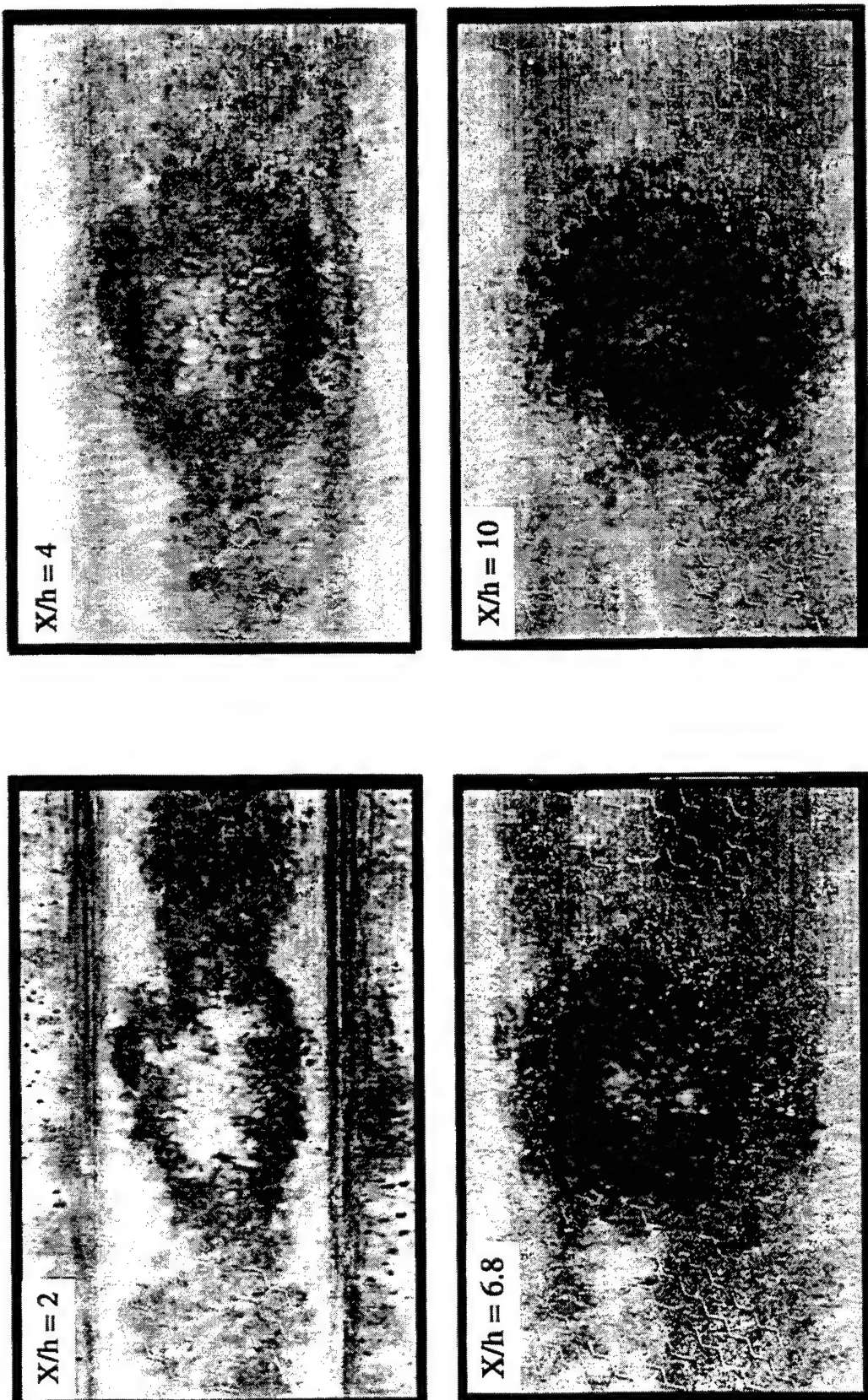
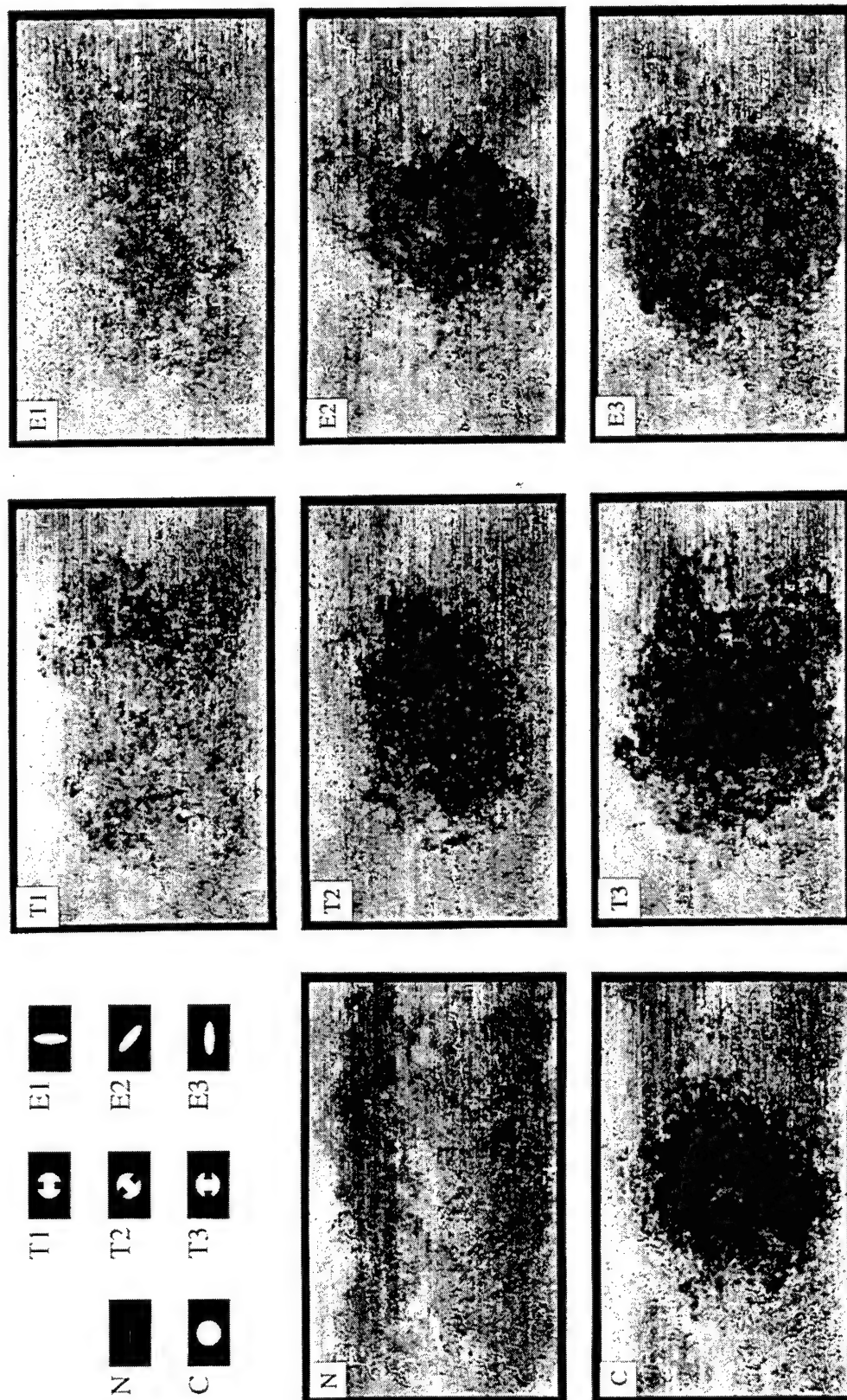


Figure 5.35. Mixedness maps of face-on (Y,Z) plane of view located at $X/h = 2, 4, 6.8$, and 10 for the helium injection ($\Psi=4$) case using circular (C) nozzle.



5.36. Mixedness maps of face-on (Y,Z) plane of view located at $X/h = 10$ for the no injection (N) case and the helium injection ($\Psi = 4$) cases (C, T1, T2, T3, E1, E2, E3).

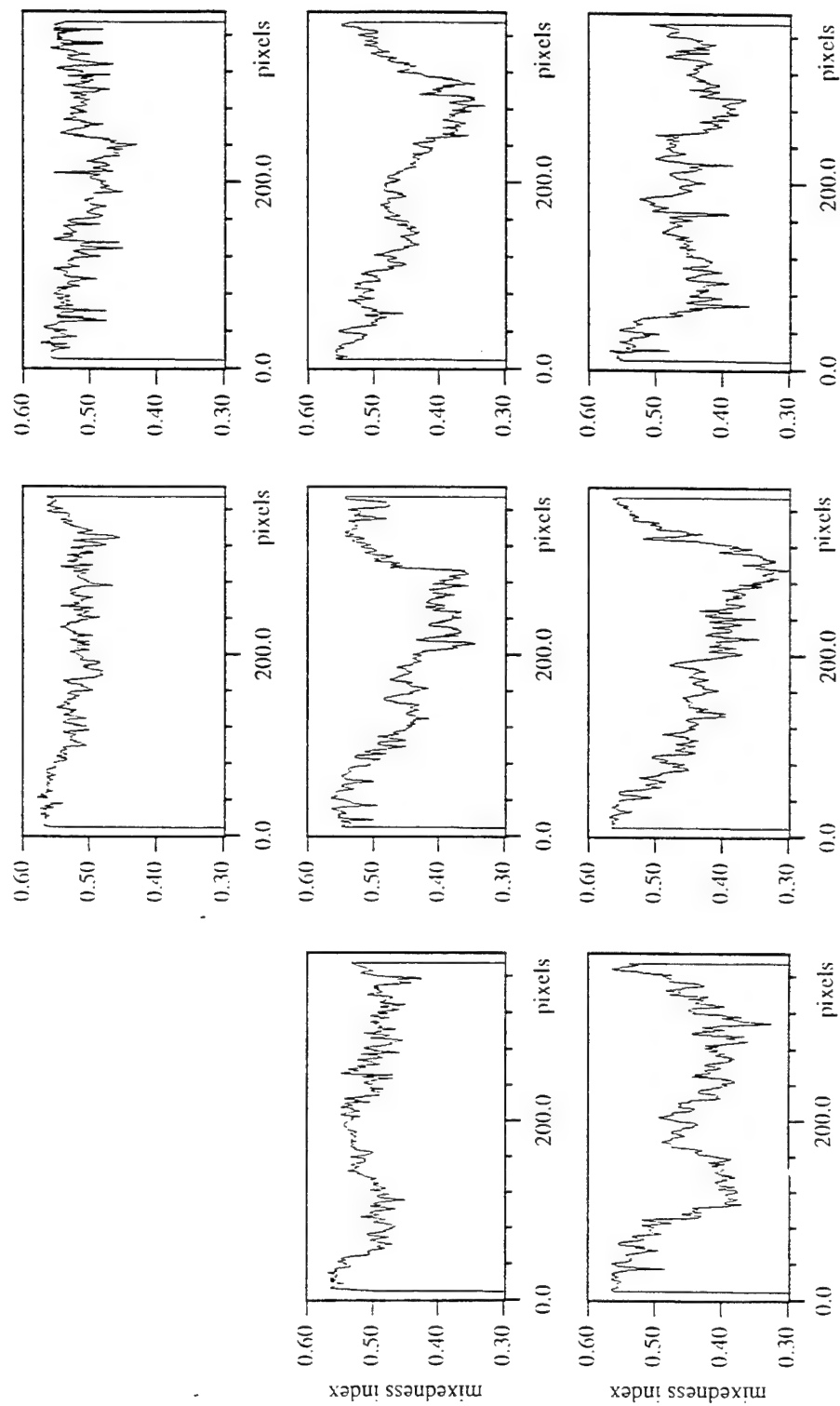


Figure 5.37. Mixedness contours along a vertical line passing through the center pixel of the mixedness maps shown in Figure 5.36.

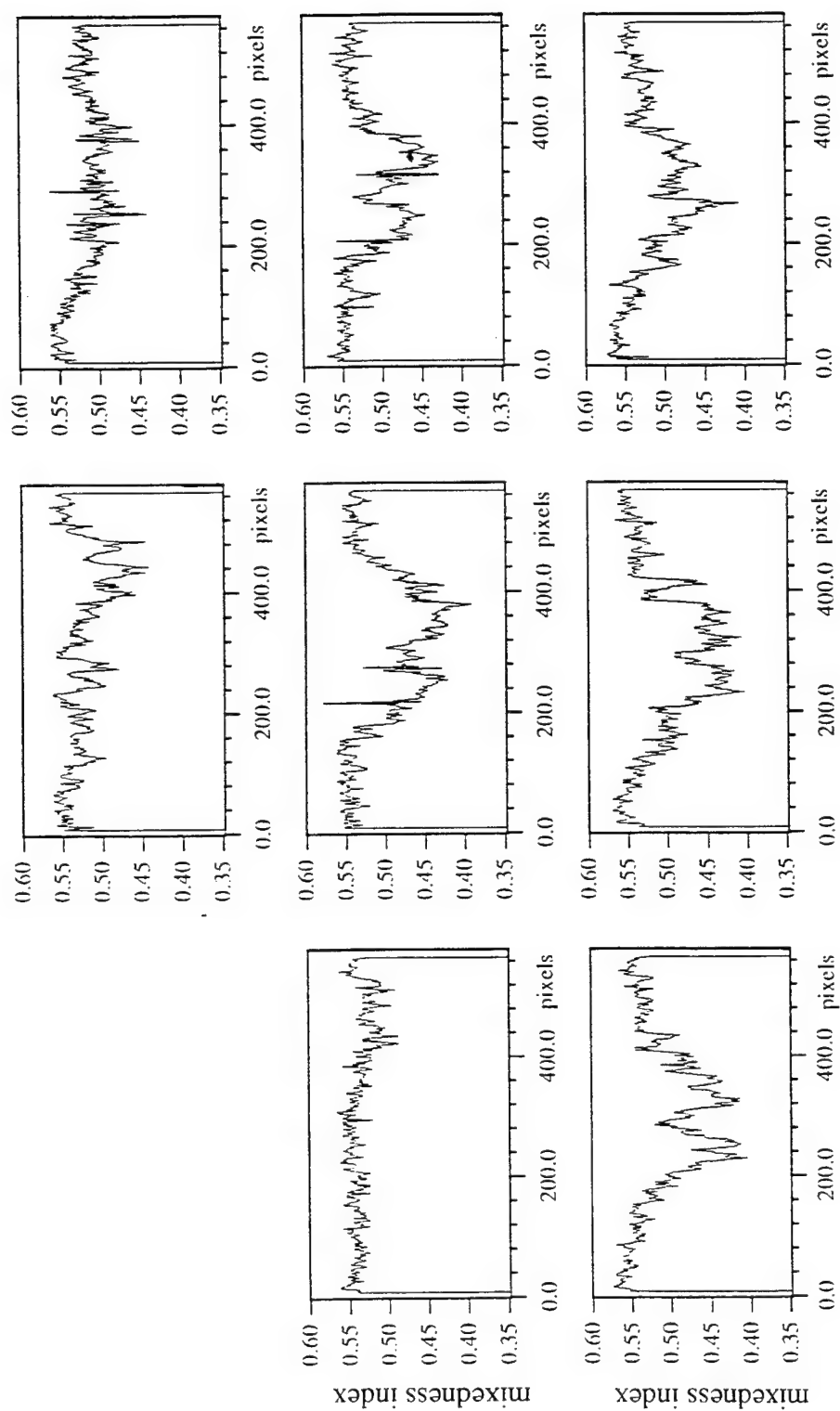


Figure 5.38. Mixedness contours along a horizontal line passing through the center pixel of the mixedness maps shown in Figure 5.36.

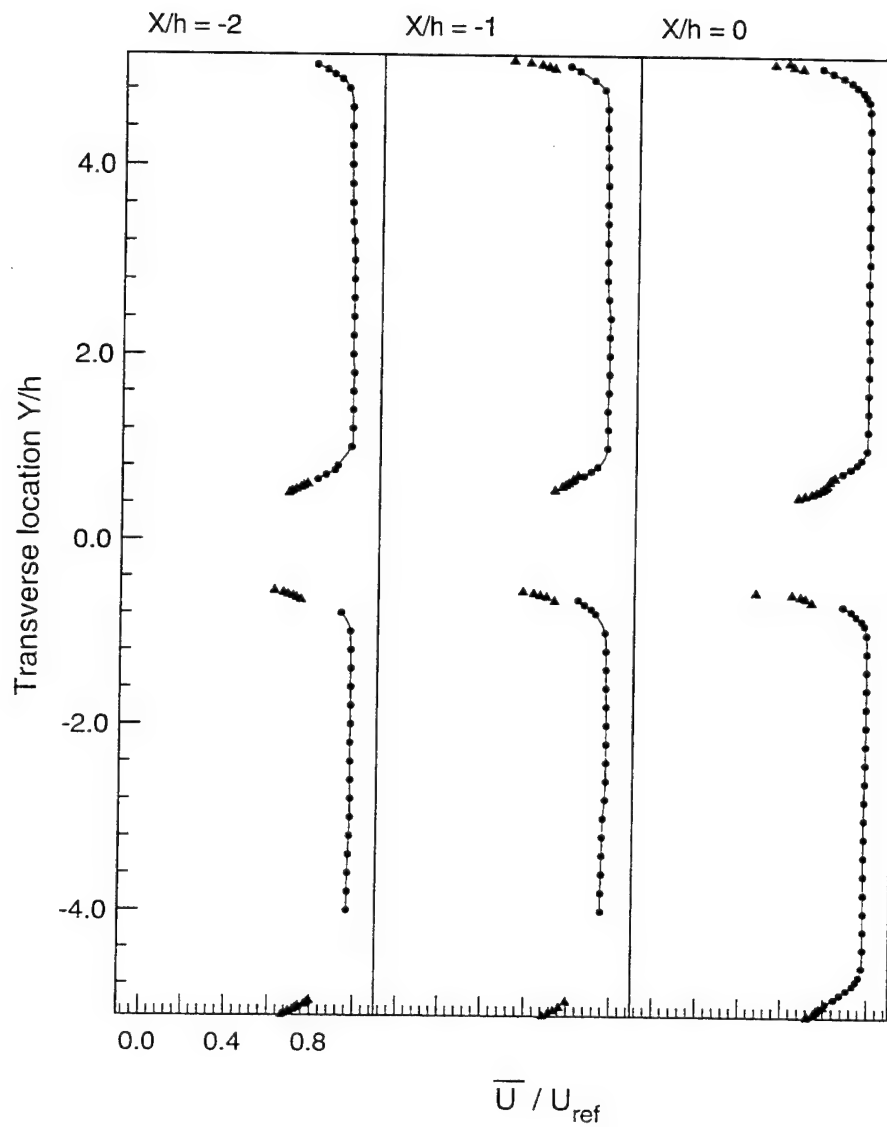


Figure 5.39. Normalized mean streamwise velocity in (X, Y) plane at $X/h = -2, -1, 0$. One-component ($\blacktriangle \bar{U} / U_{\text{ref}}$) and two-component ($\bullet \bar{U} / U_{\text{ref}}$) measurements.

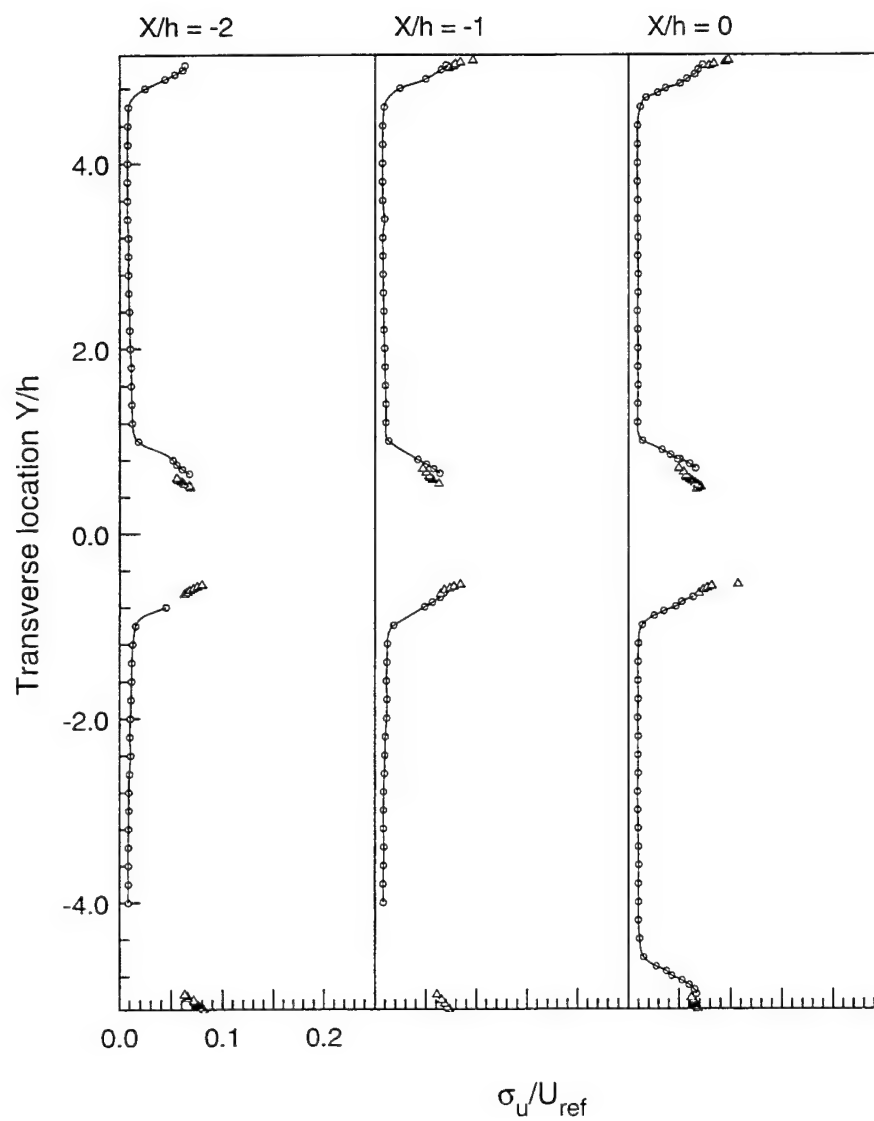


Figure 5.40. Normalized mean streamwise turbulence intensity in (X,Y) plane at $X/h = -2, -1, 0$. One-component ($\triangle \sigma_u/U_{ref}$) and two-component ($\circ \sigma_u/U_{ref}$) measurements.

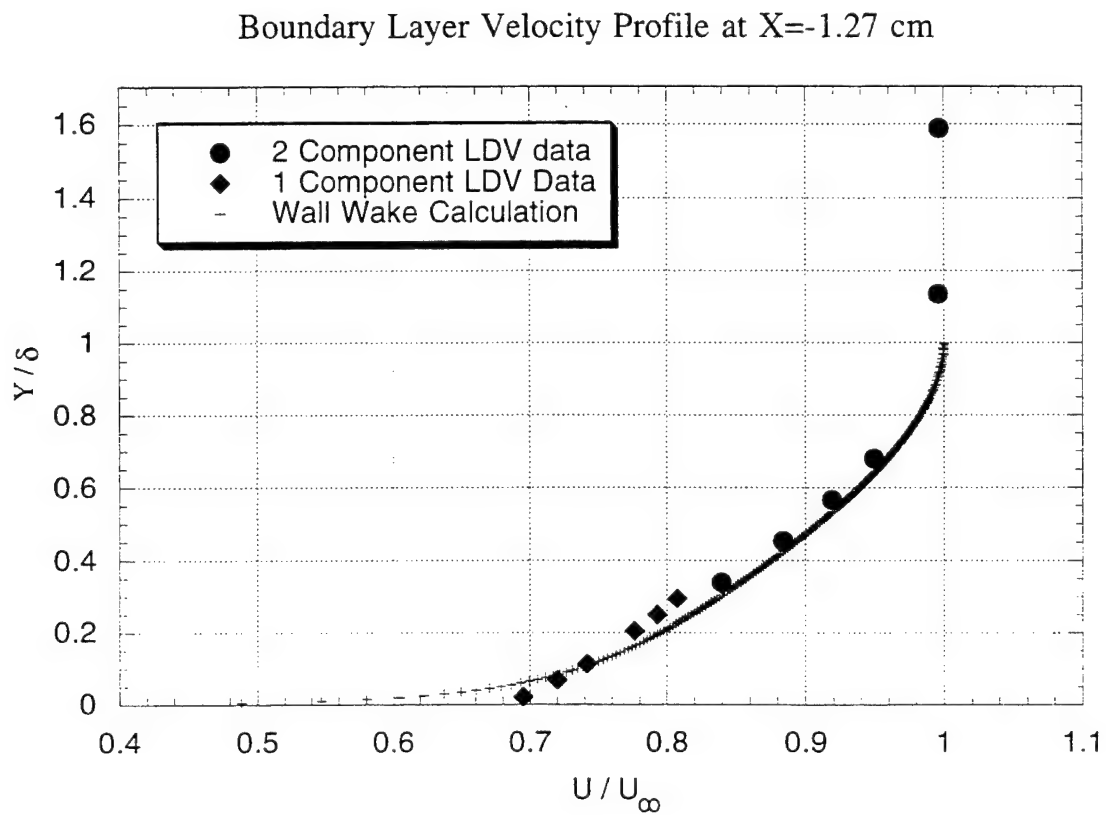


Figure 5.41. Boundary layer velocity profiles from one- and two-component Laser Doppler Velocimetry (LDV) measurements at $X/h=1$ superimposed on Wall-Wake Law calculated boundary layer profile assuming $\delta=5.6$ mm and $C_f=0.0016$.

	M_e	Re_θ	
∇	1.47	4.56×10^3	Seddon
\triangle	2.669	7.02×10^5	Moore and Harkness
\square	2.91	5.4×10^4	Moore and Harkness
\circ	4.93	5.53×10^3	Lobb et al.
\blacksquare	1.85	3.09×10^3	Michel
\blacktriangledown	2.10	2.78×10^3	Michel
\blacktriangle	2.57	3.24×10^3	Michel
\bullet	2.96	2.64×10^3	Michel
\bullet	1.966	2.98×10^3	Coles
\blacksquare	4.512	3.47×10^3	Coles
$*$	1.92	1.7×10^3	Present results

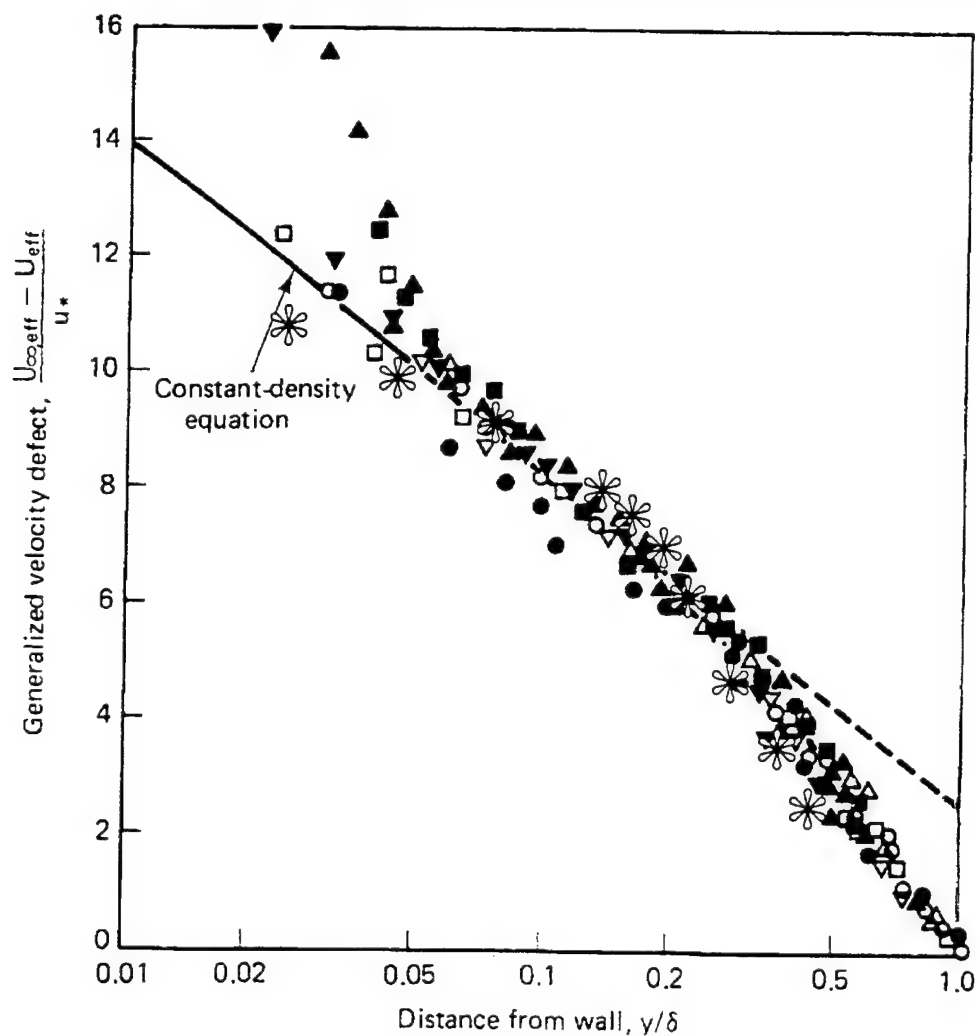


Figure 5.42. Generalized velocity defect in boundary layer for present study superimposed on profiles for compressible, adiabatic flat-plate boundary layers (from Maise and McDonald [Copyright © 1968 AIAA - Reprinted with permission]).

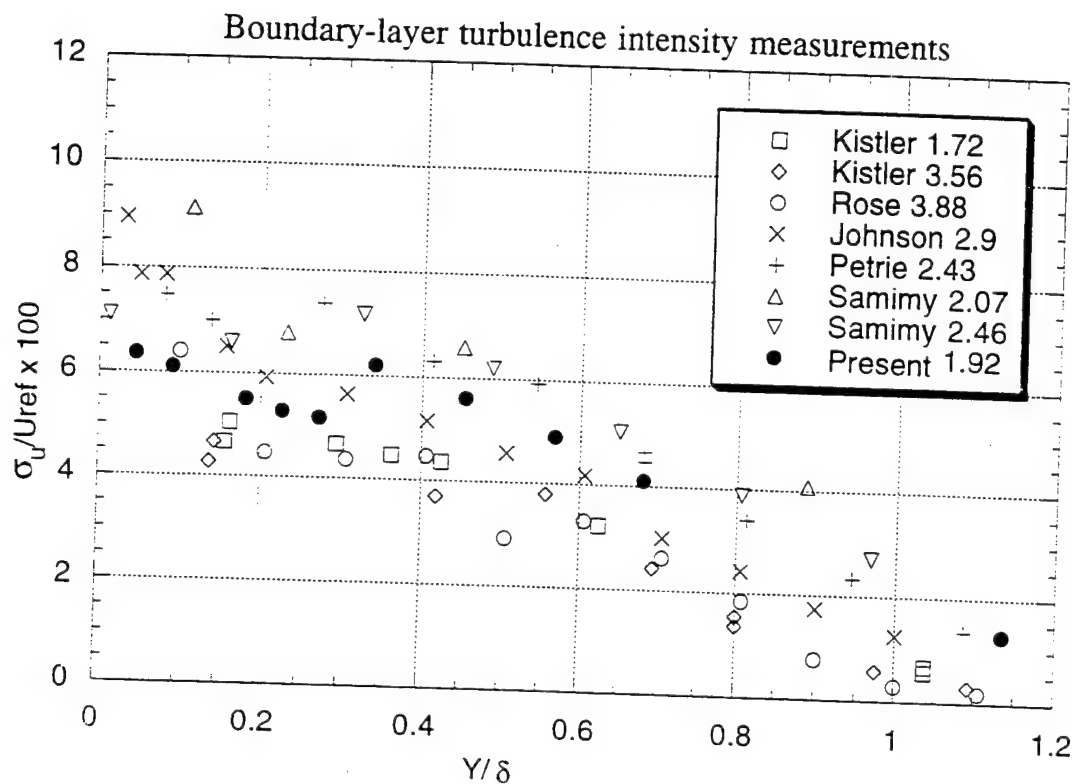


Figure 5.43. Turbulence intensity measurements in the boundary layer of the present study superimposed on measurements from previous studies for various Mach numbers from Kuntz et al. [Copyright © 1973 AIAA - Reprinted with permission].

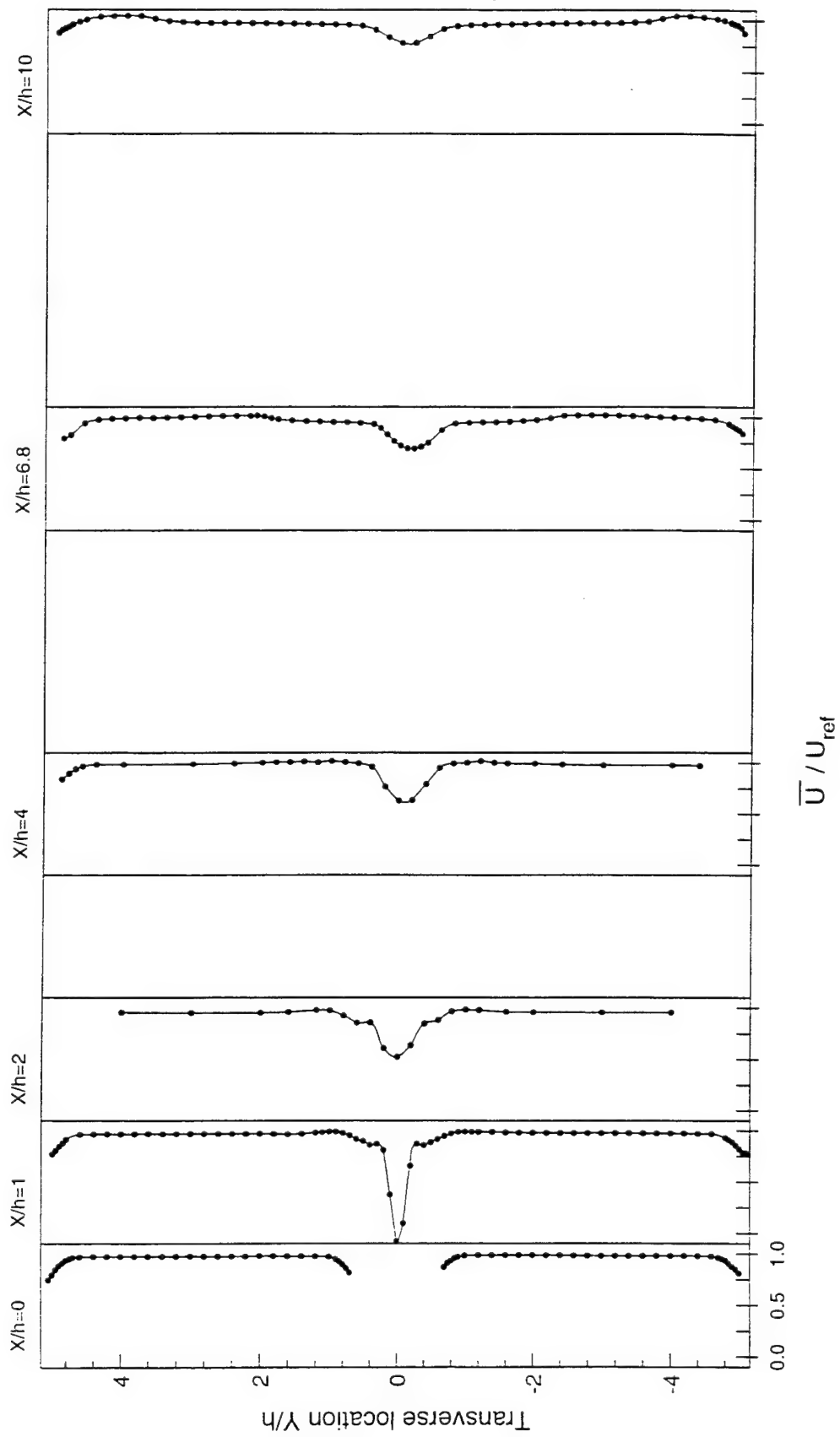


Figure 5.44 Normalized mean streamwise velocity in (X,Y) plane for the no injection (N) case.

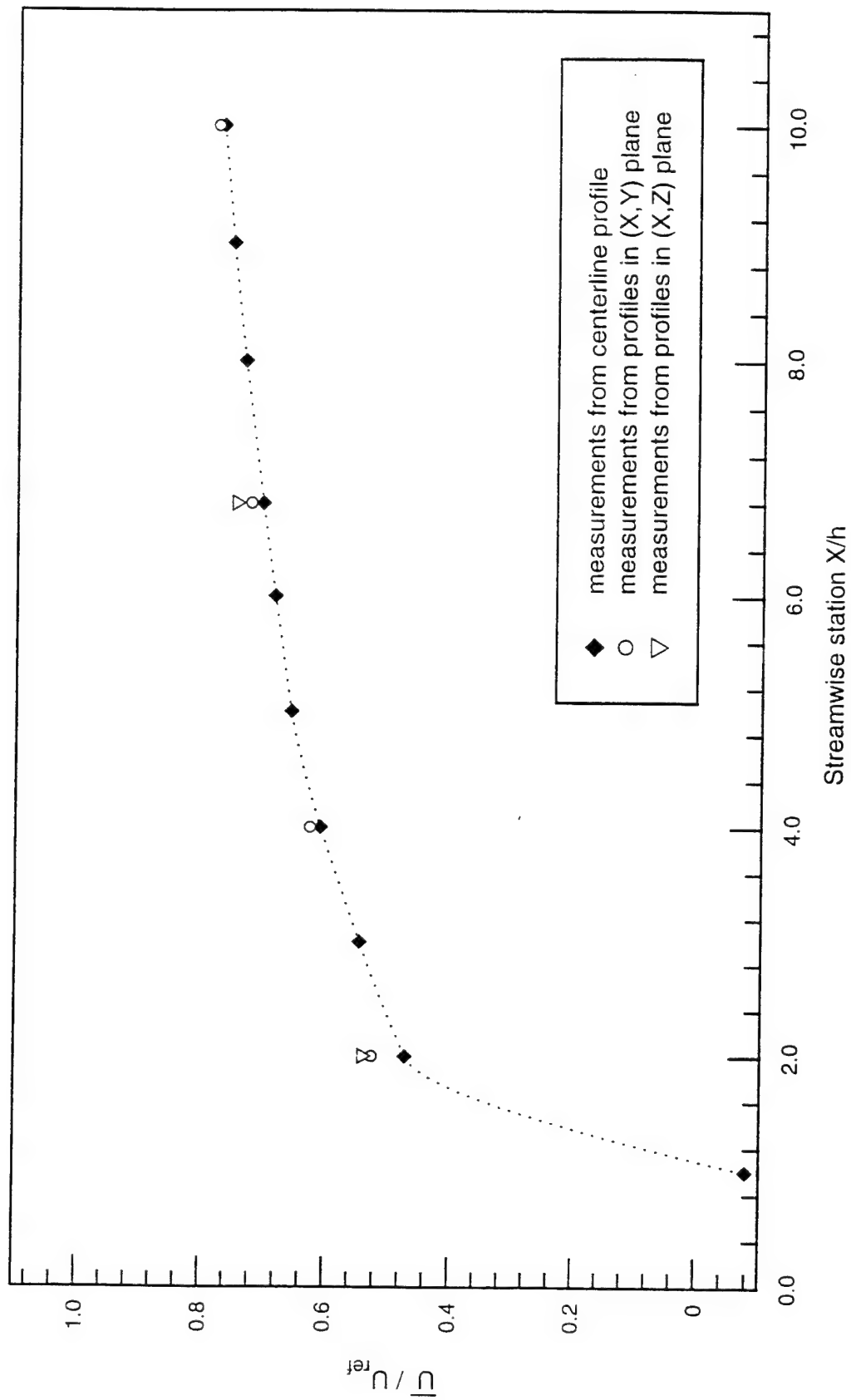


Figure 5.45 Normalized mean streamwise velocity on centerline of strut (X-axis) for the no injection (N) case.

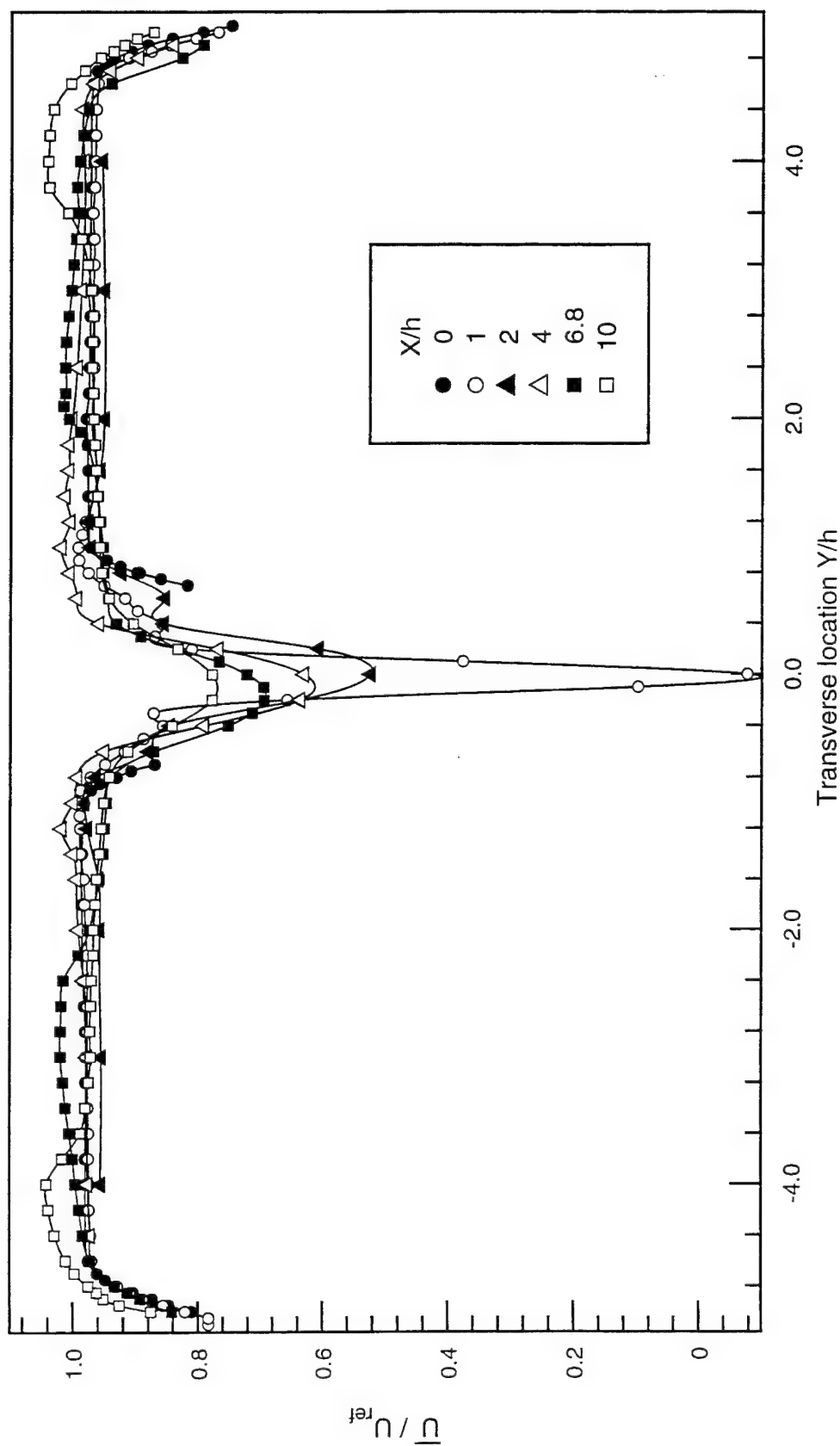


Figure 5.46. Normalized mean streamwise velocity in (X, Y) plane for the no injection (N) case. Composite plot.

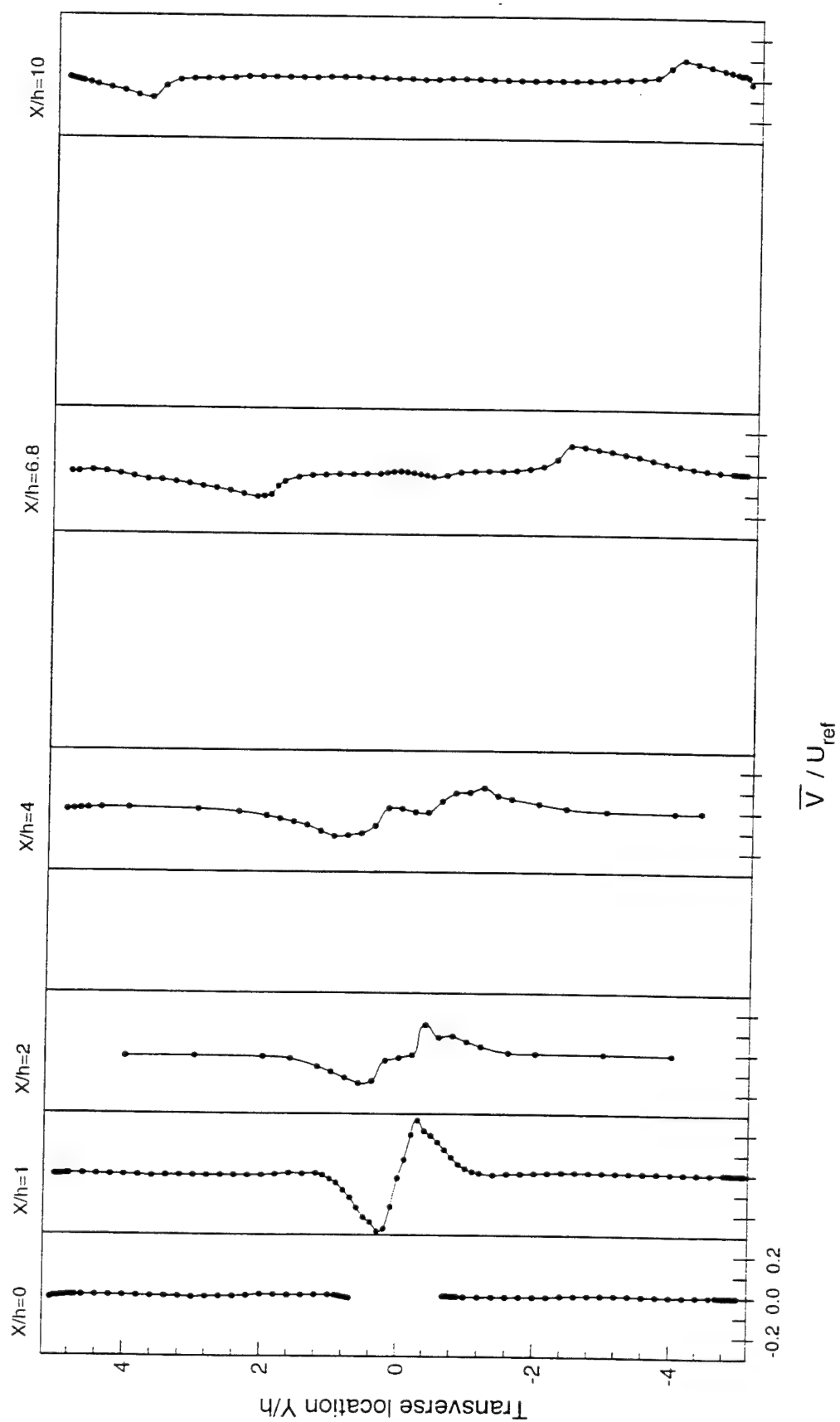


Figure 5.47 Normalized mean transverse velocity in (X, Y) plane for the no injection (N) case.

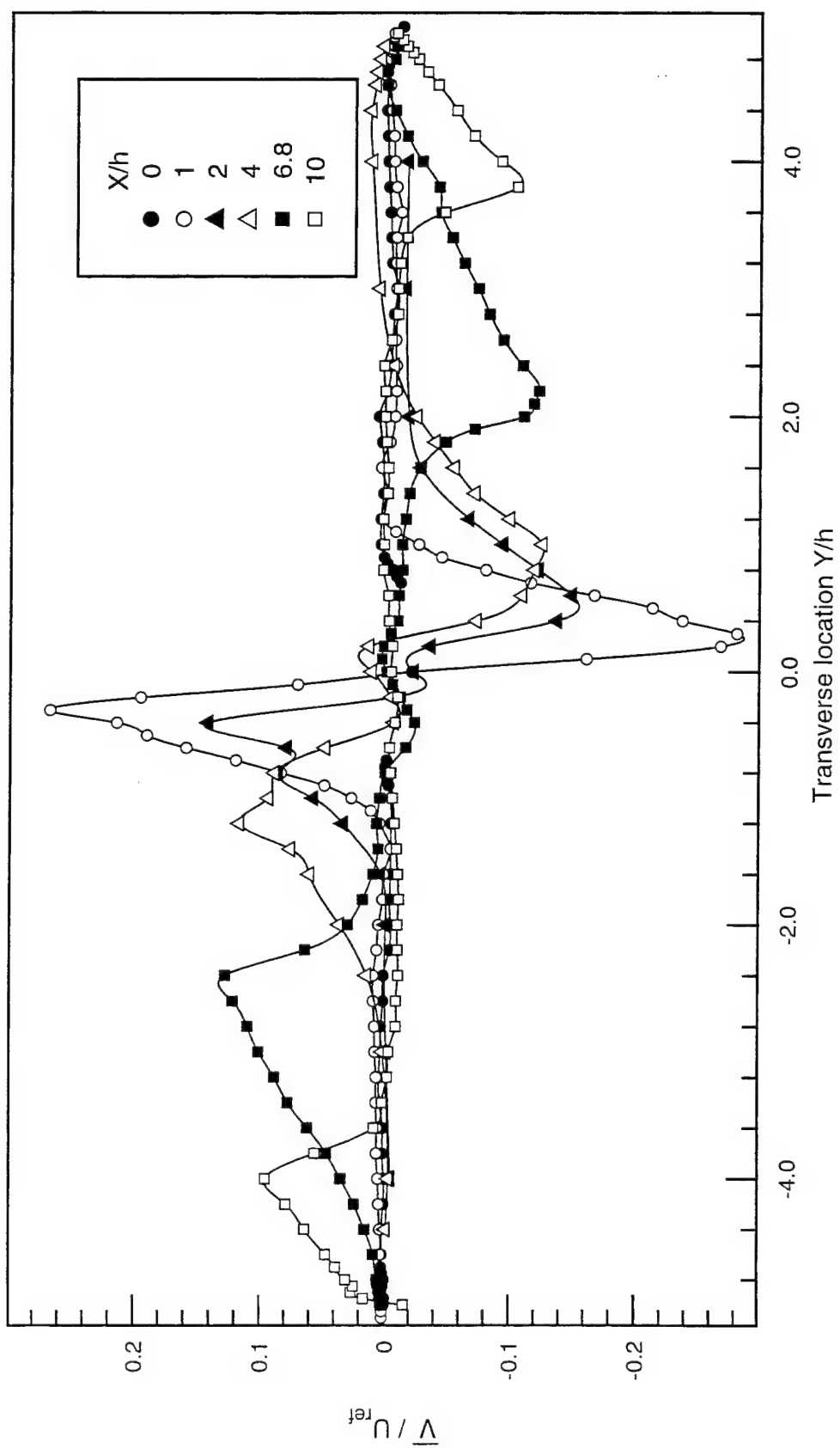


Figure 5.48. Normalized mean transverse velocity in (X, Y) plane for the no injection (N) case. Composite plot.

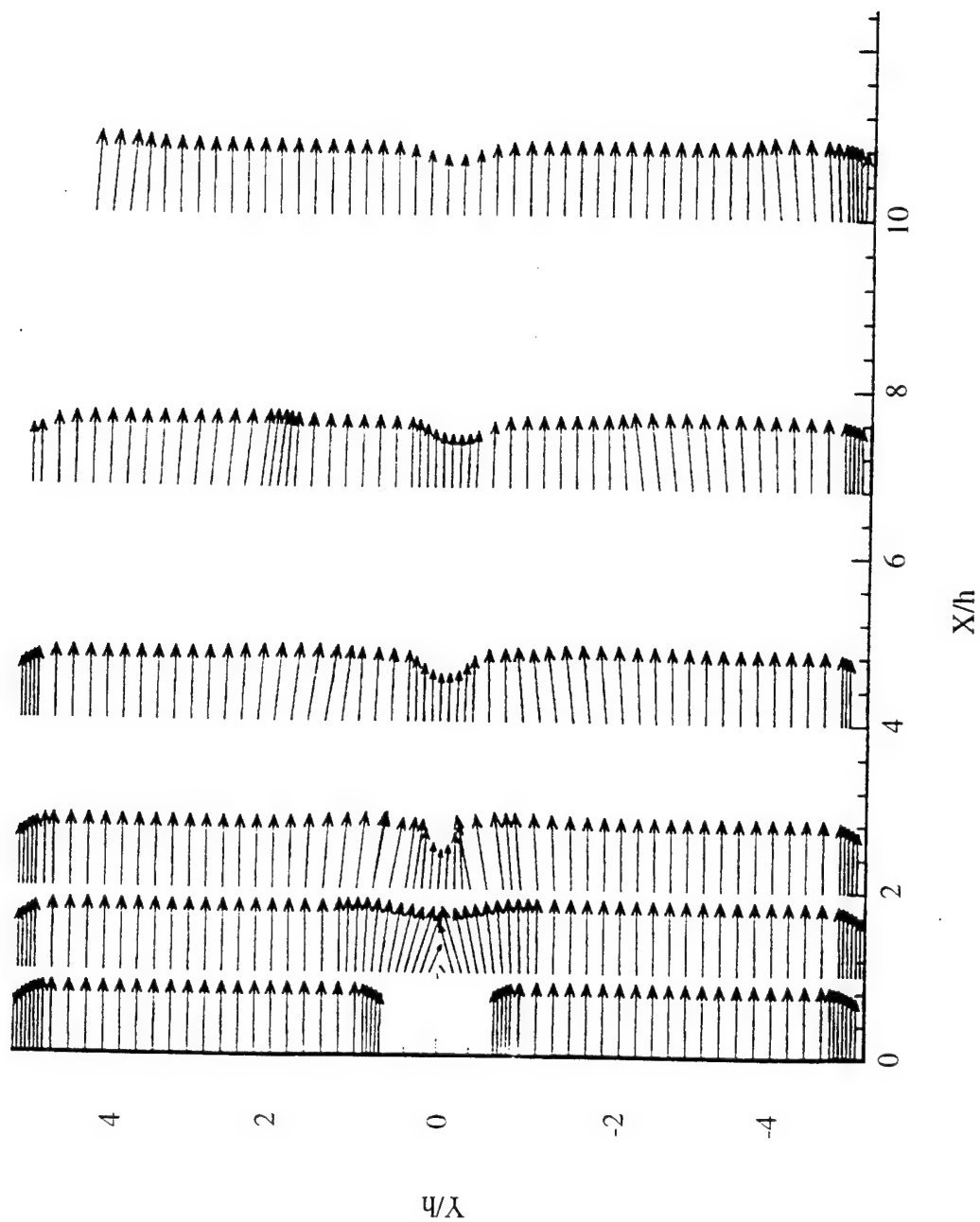


Figure 5.49. Velocity map of two-component LDV data in (X, Y) plane on centerline of strut without injection.

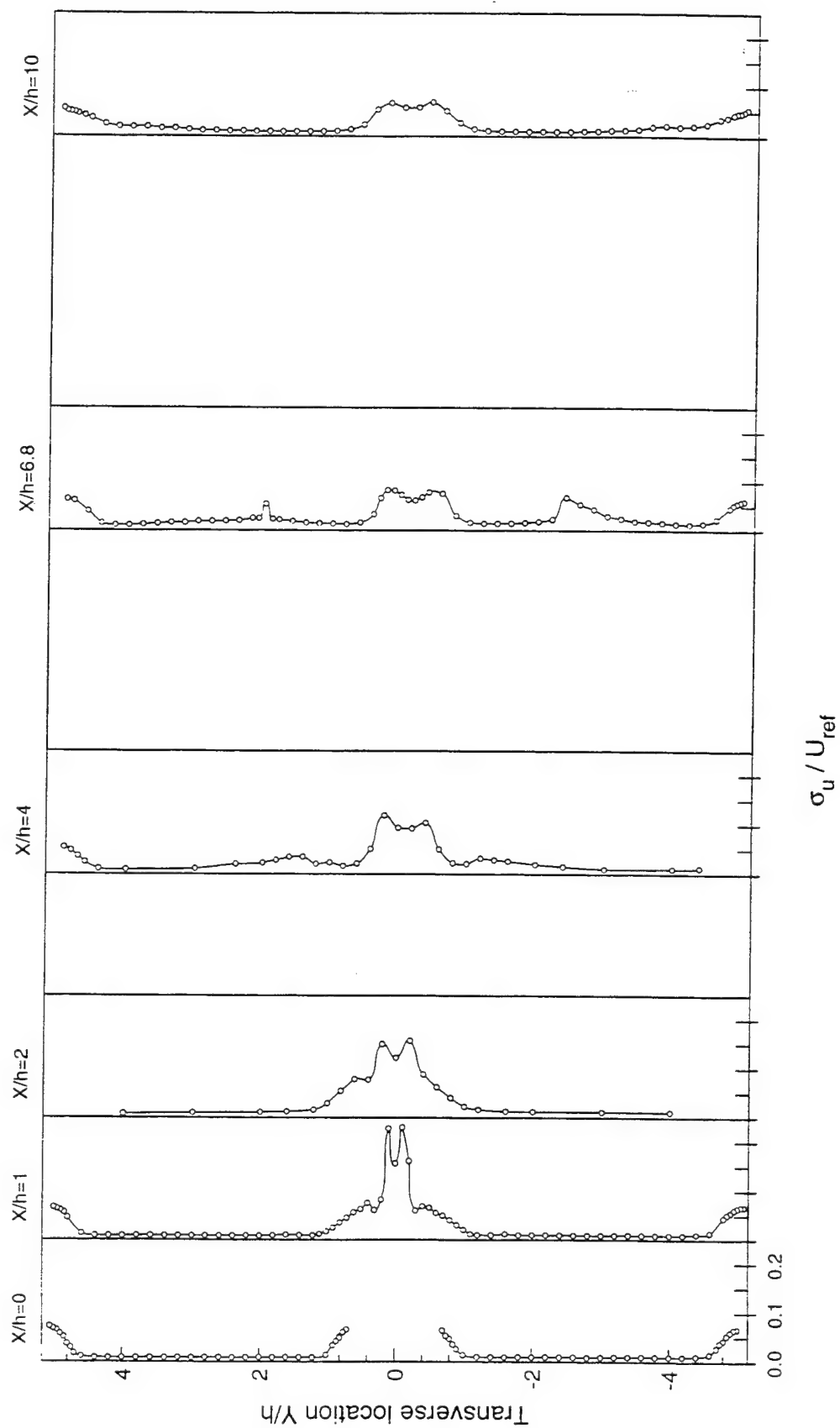


Figure 5.50 Streamwise turbulence intensity in (X,Y) plane for the no injection (N) case.

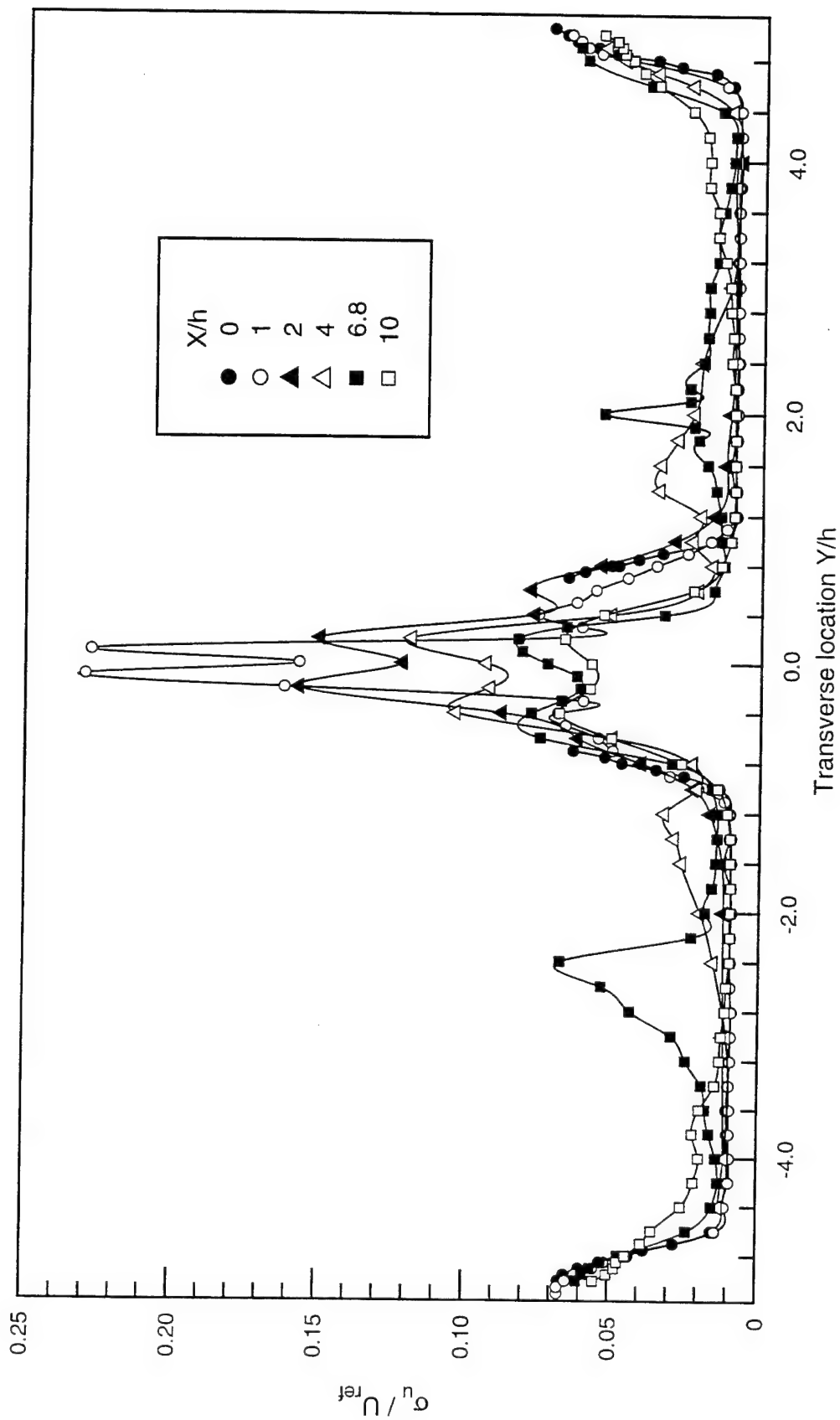


Figure 5.51. Streamwise turbulence intensity in (X, Y) plane for the no injection (N) case. Composite plot.

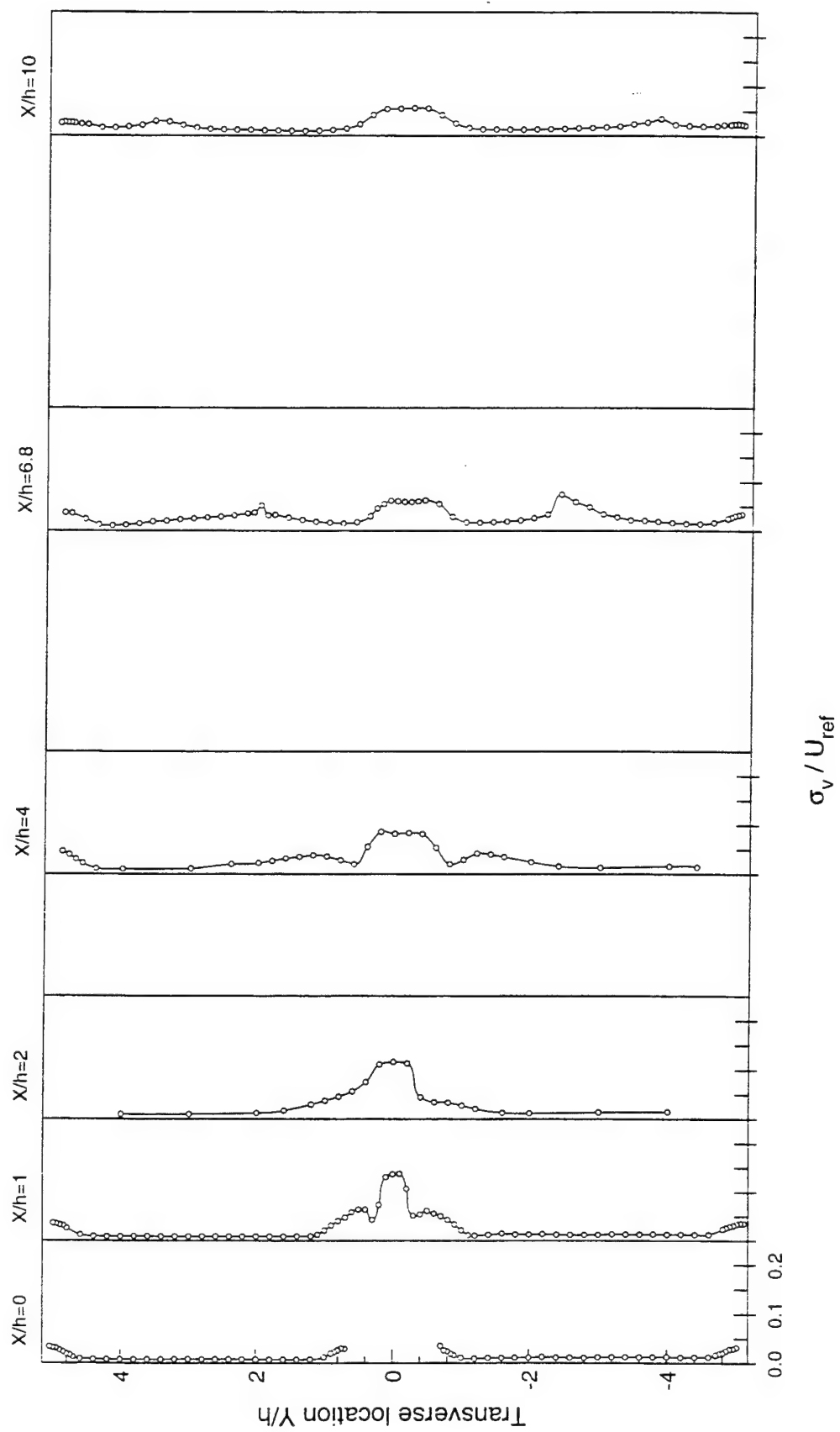


Figure 5.52 Transverse turbulence intensity in (X, Y) plane for the no injection (N) case.

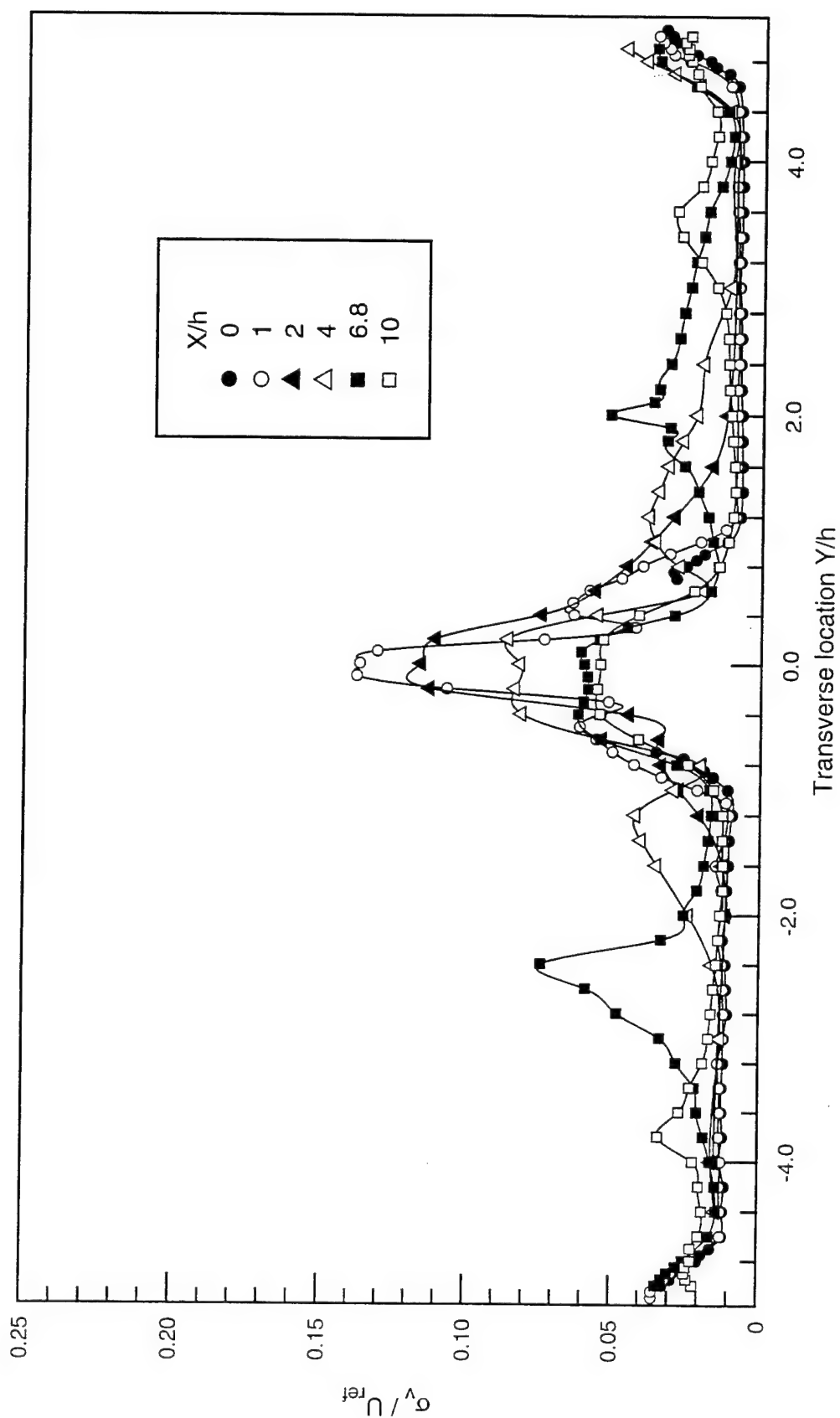


Figure 5.53. Transverse turbulence intensity in (X,Y) plane for the no injection (N) case. Composite plot.

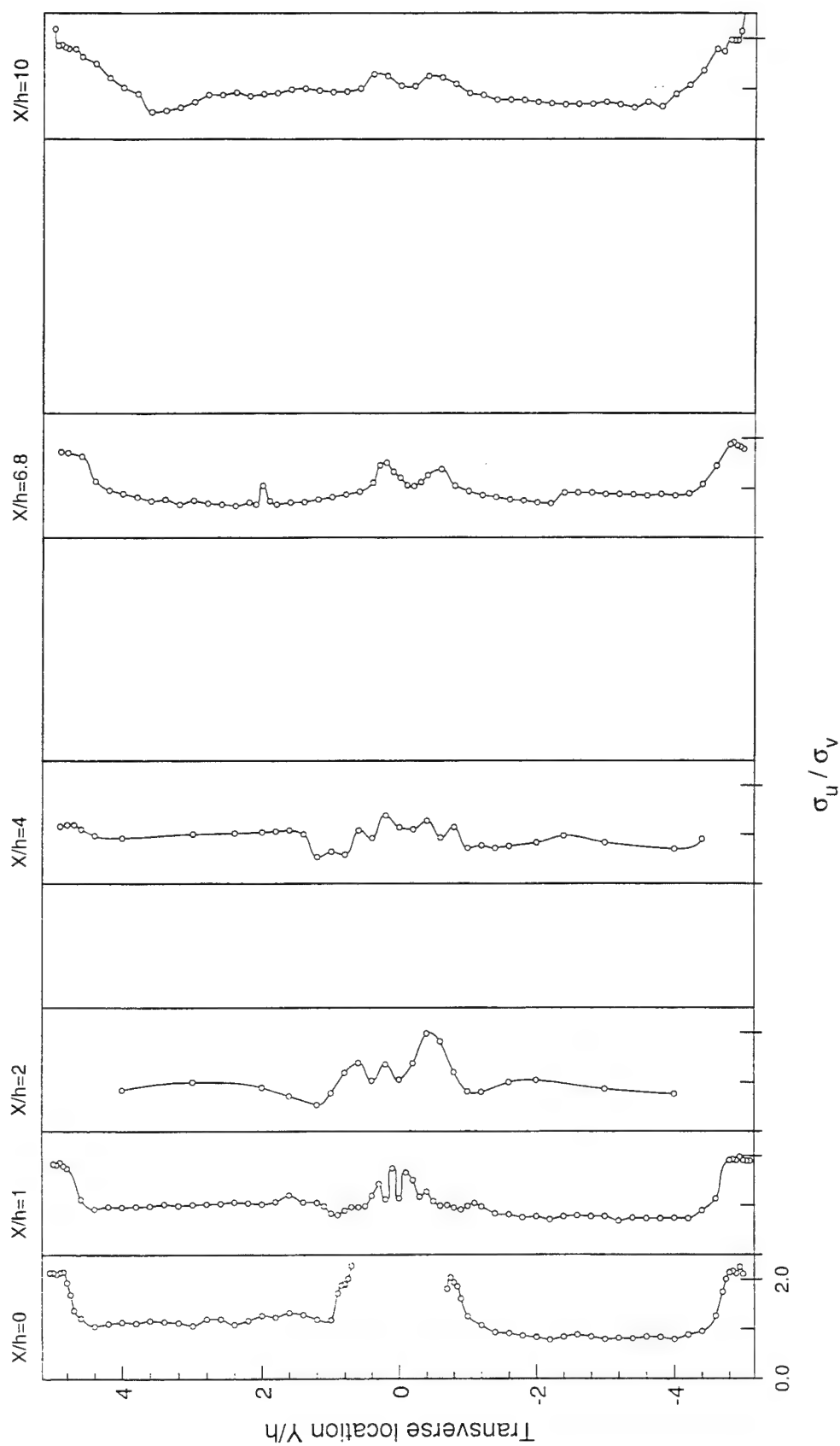


Figure 5.54. Ratio of streamwise to transverse turbulence intensities in (X,Y) plane for the no injection (N) case.

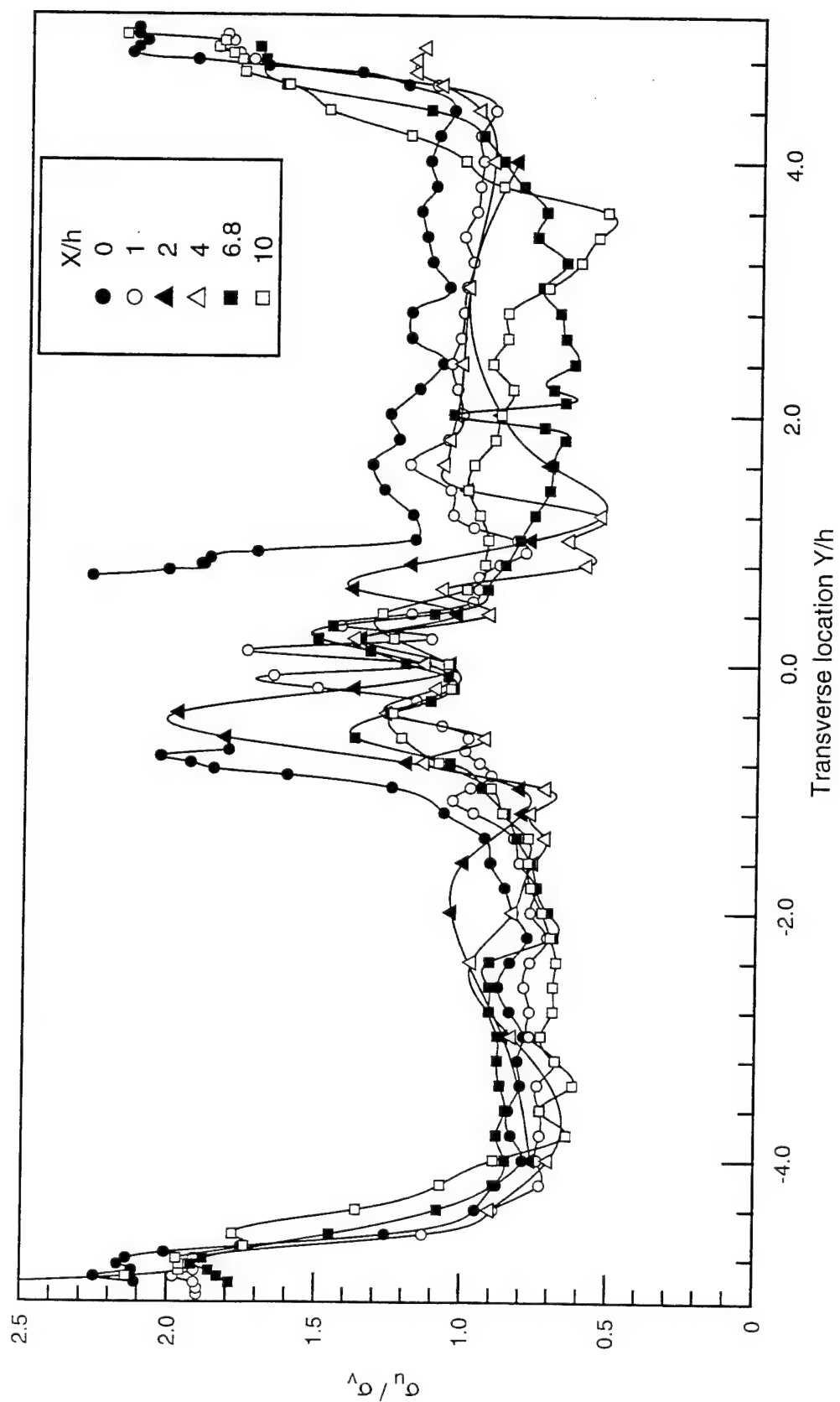


Figure 5.55. Ratio of streamwise to transverse turbulence intensities in (X,Y) plane for the no injection (N) case. Composite plot.

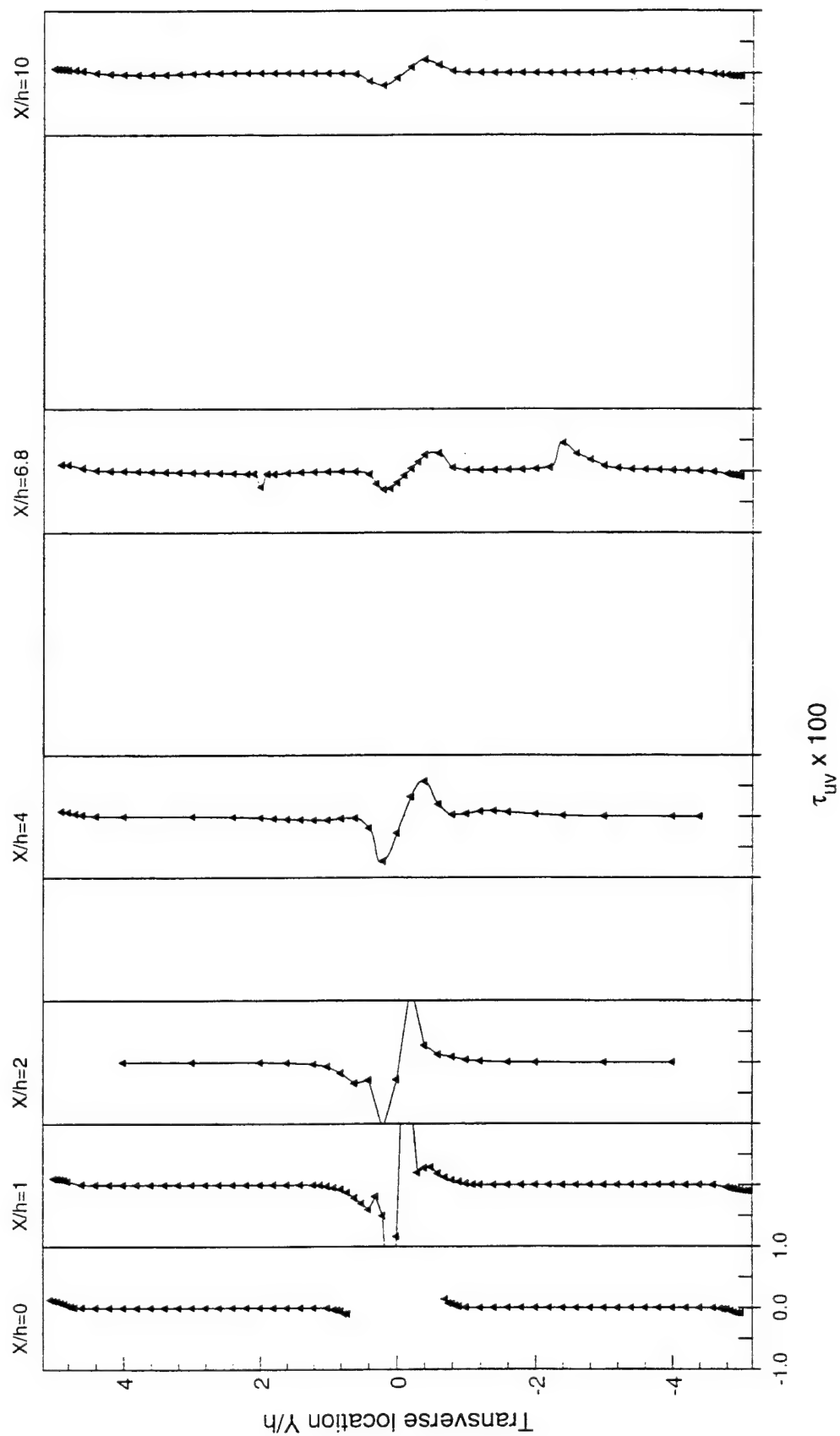


Figure 5.56 Turbulent shear stress in (X, Y) plane for the no injection (N) case.

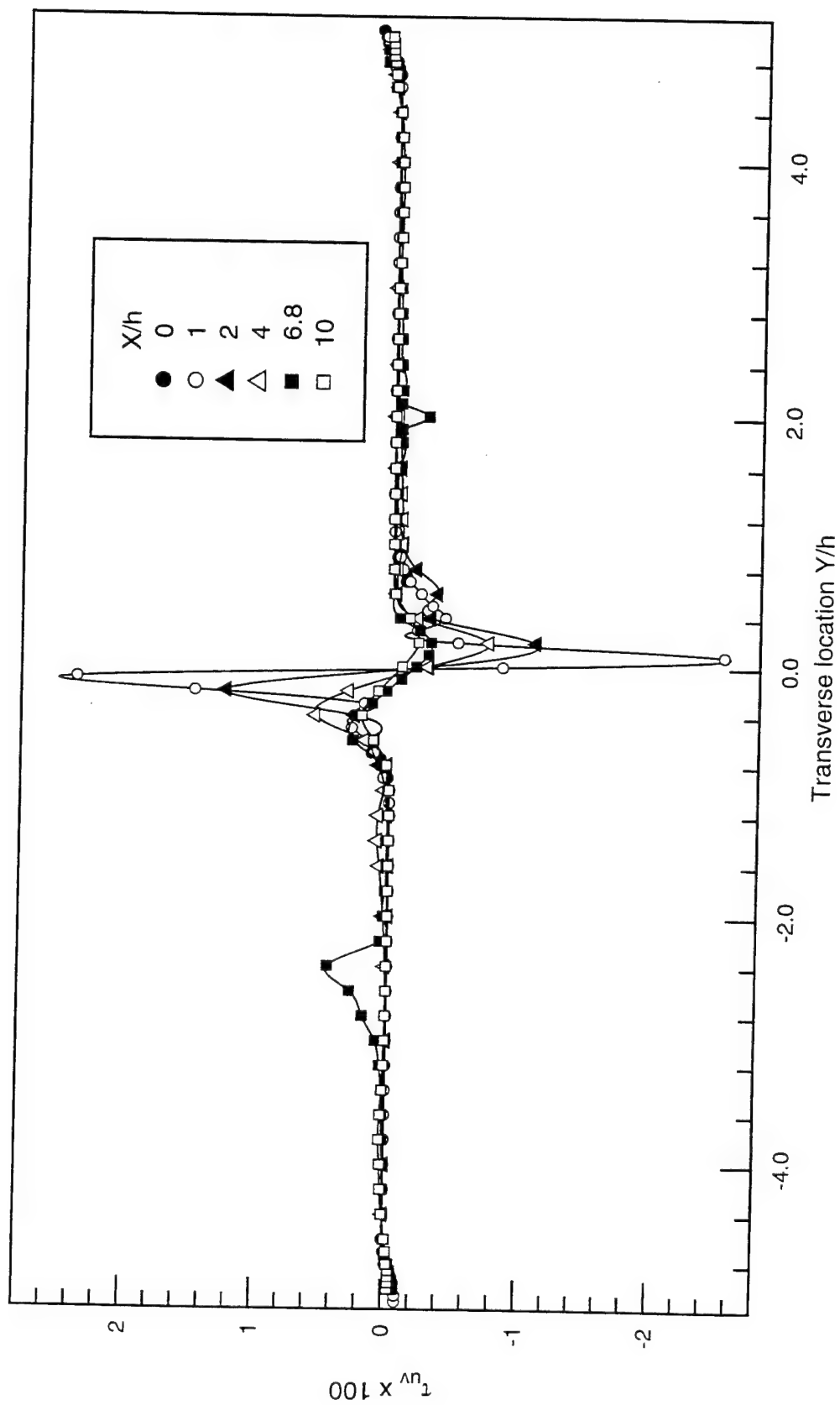


Figure 5.57. Turbulent shear stress in (X, Y) plane for the no injection (N) case. Composite plot.

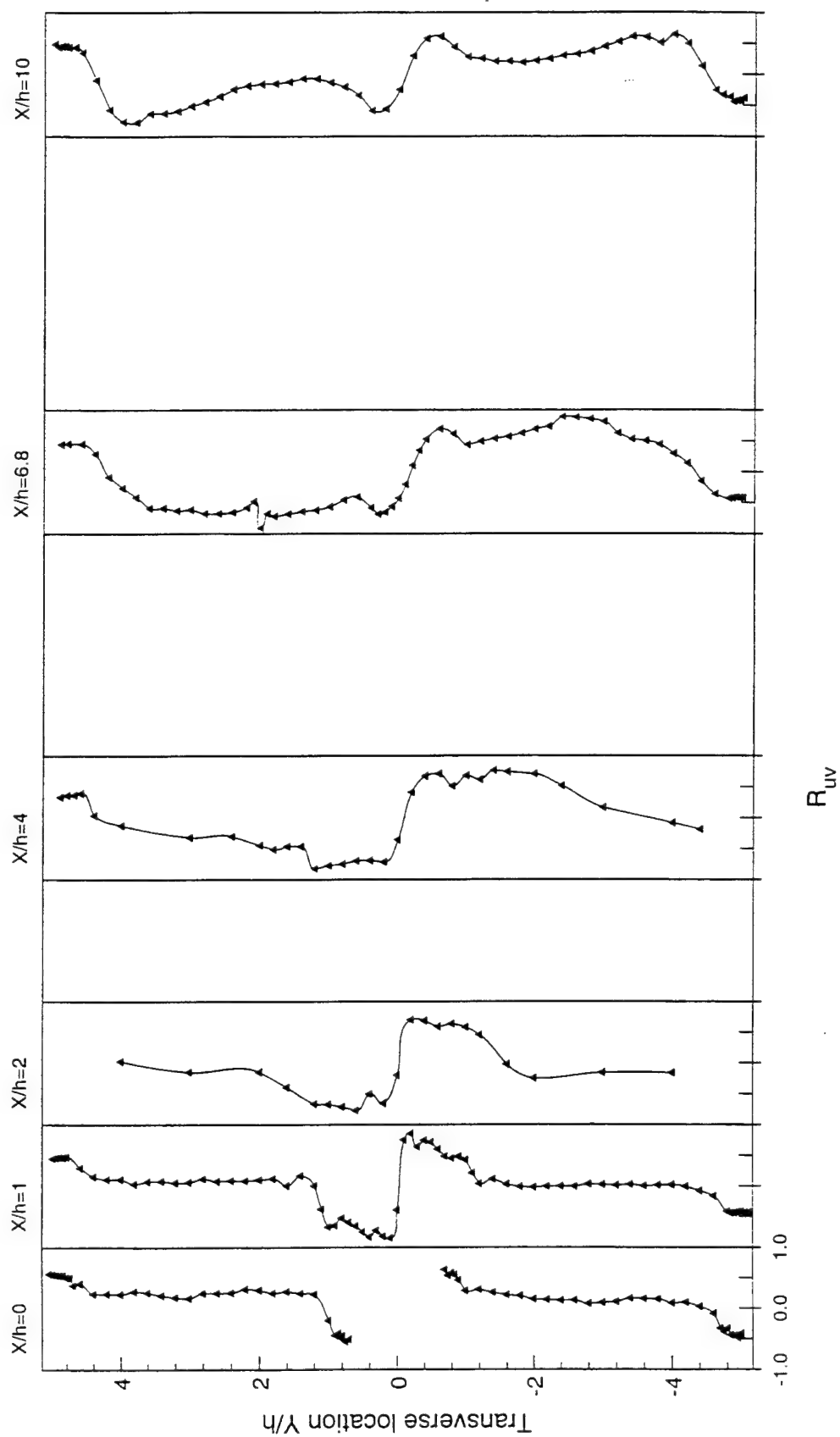


Figure 5.58 Turbulent shear stress correlation coefficient in (X, Y) plane for the no injection (N) case.

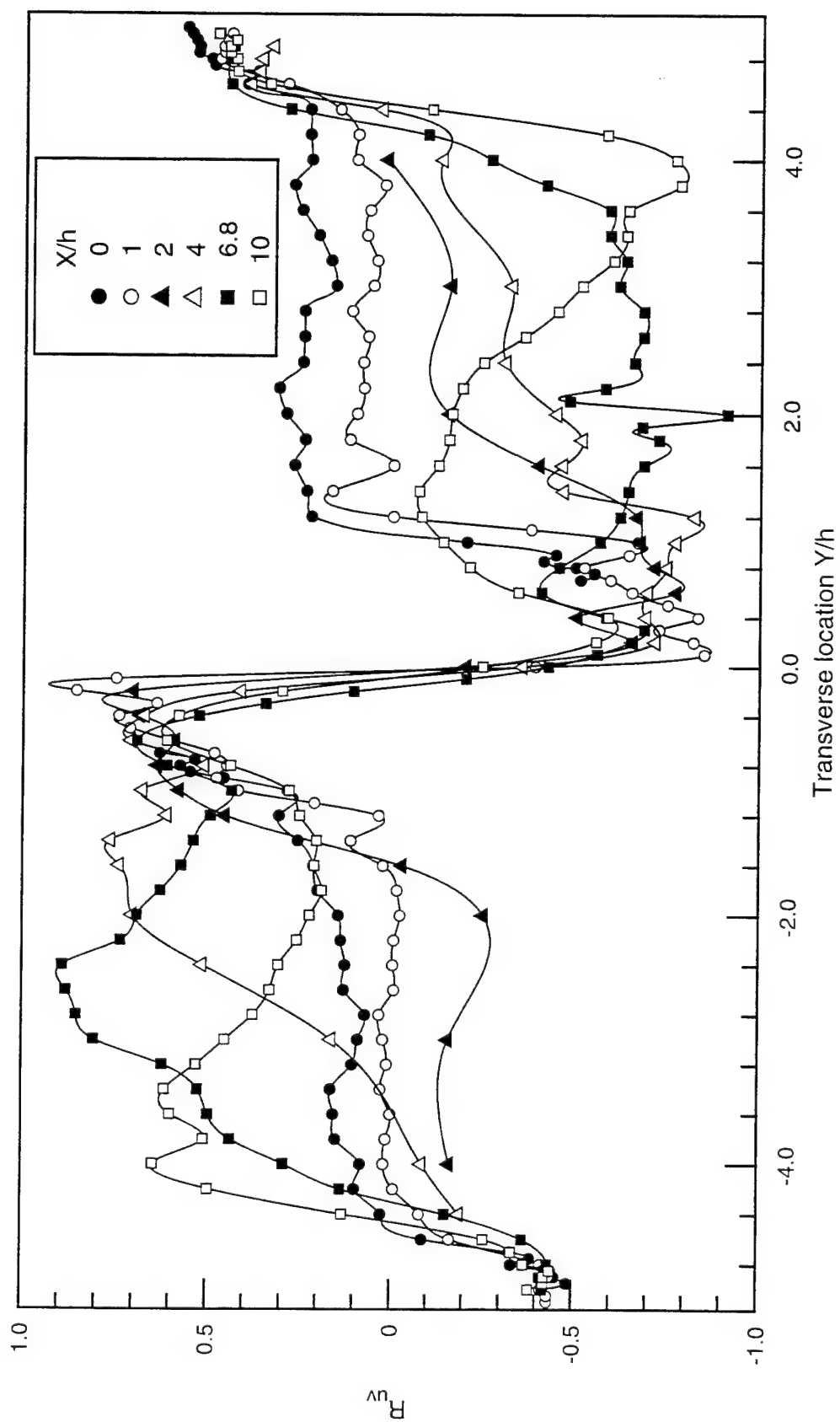


Figure 5.59. Turbulent shear stress correlation coefficient in (X,Y) plane for the no injection (N) case. Composite plot.

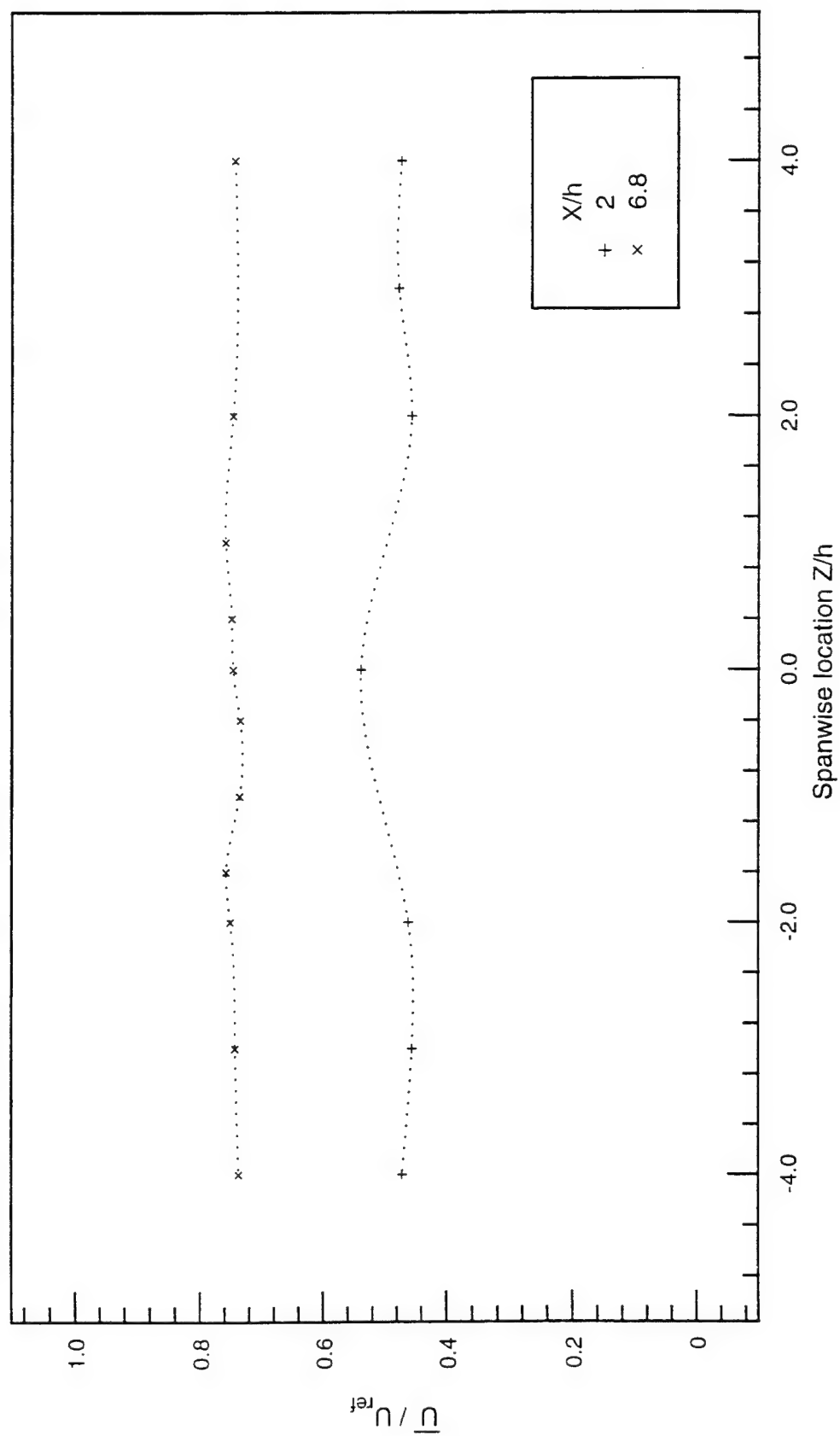


Figure 5.60 Normalized mean streamwise velocity in (X,Z) plane for the no injection (N) case.

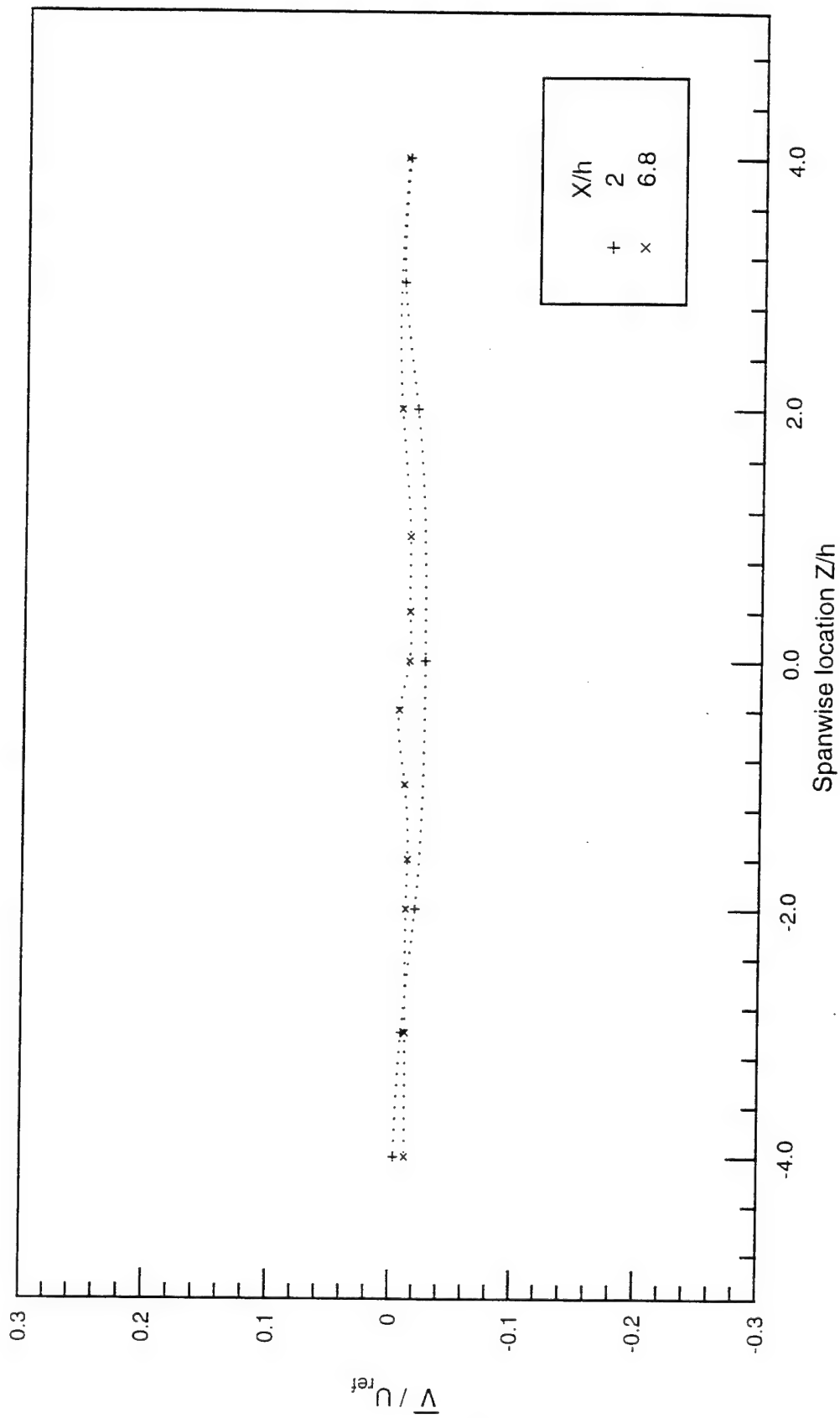


Figure 5.61 Normalized mean transverse velocity in (X,Z) plane for the no injection (N) case.

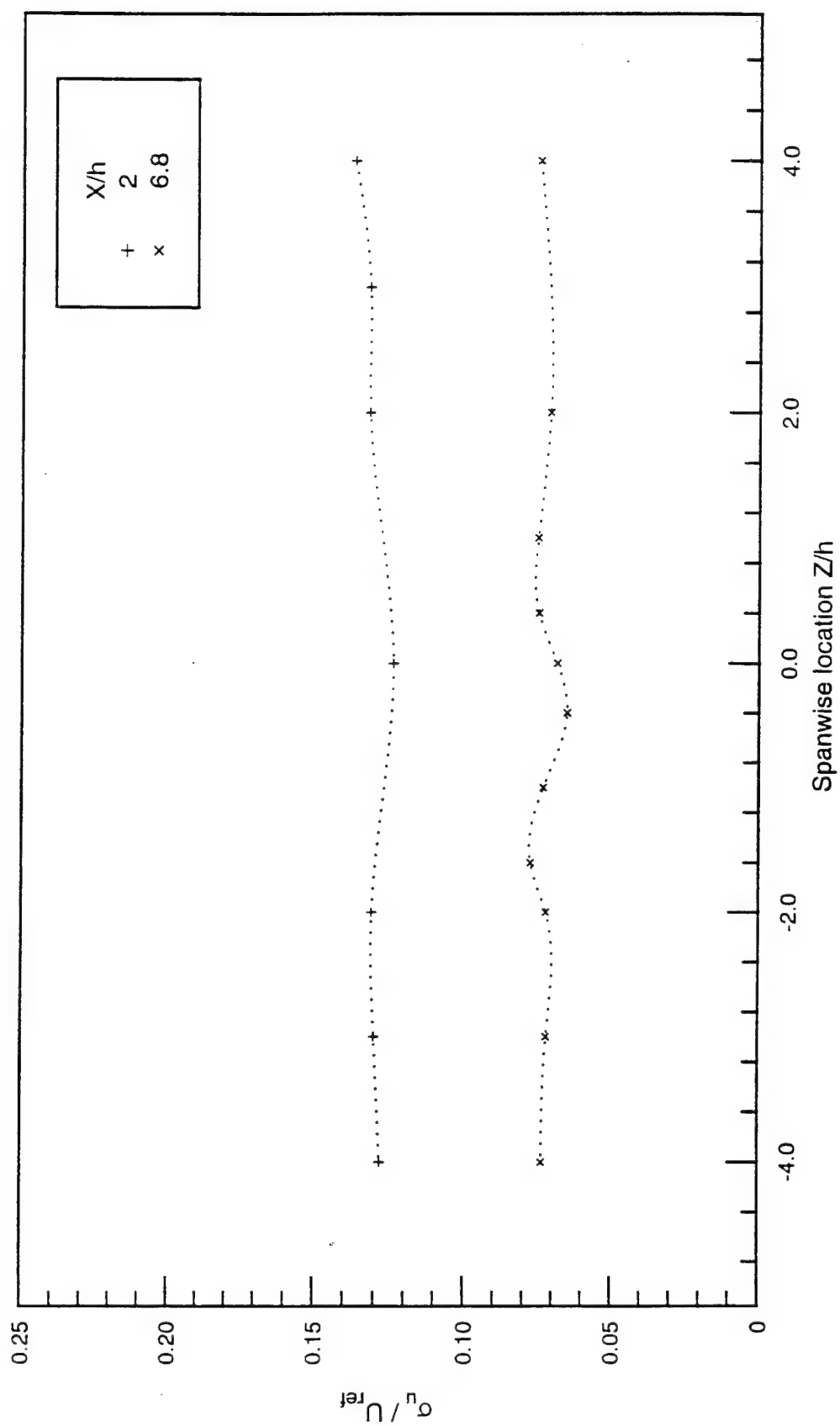


Figure 5.62 Streamwise turbulence intensity in (X,Z) plane for the no injection (N) case.

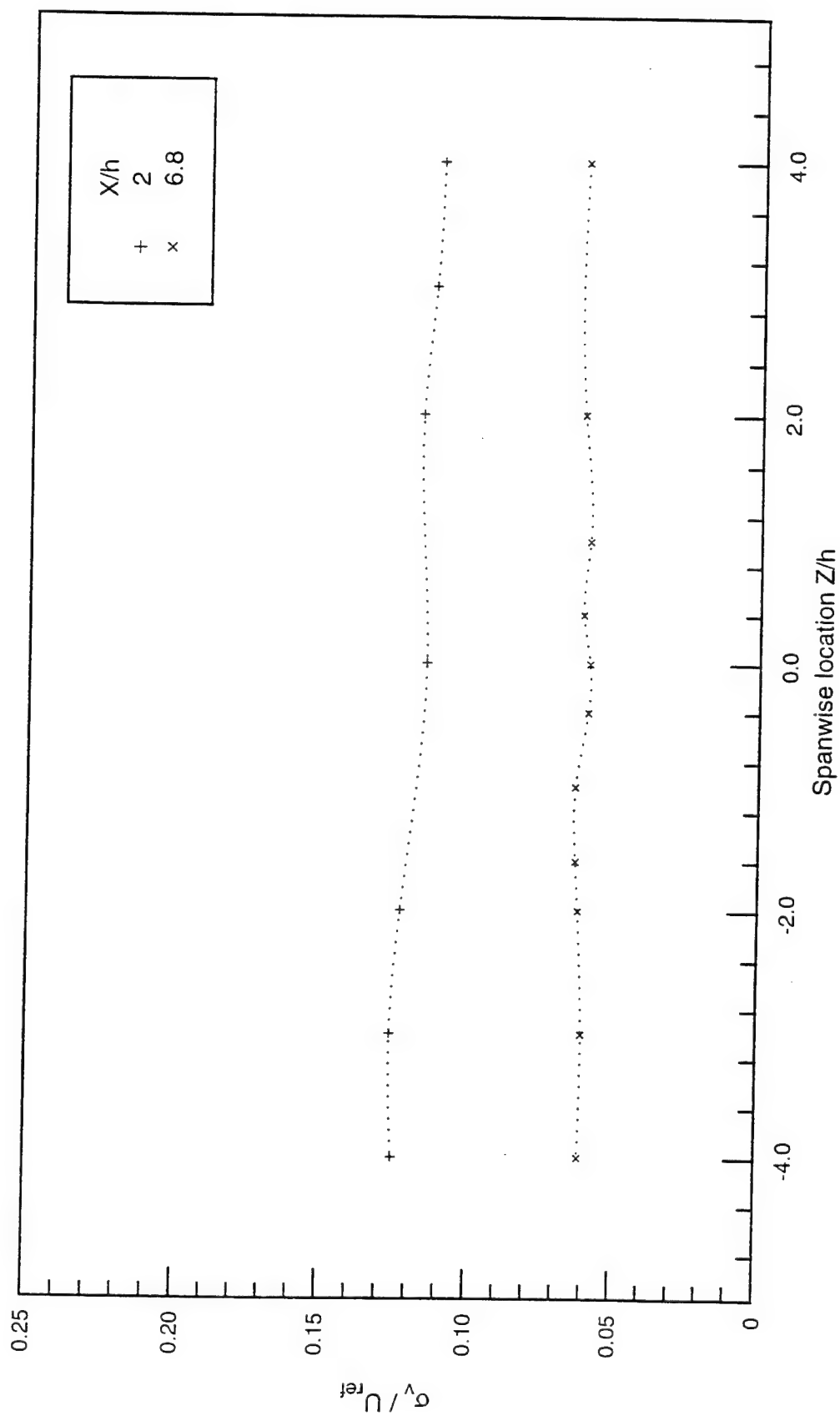


Figure 5.63 Transverse turbulence intensity in (X,Z) plane for the no injection (N) case.

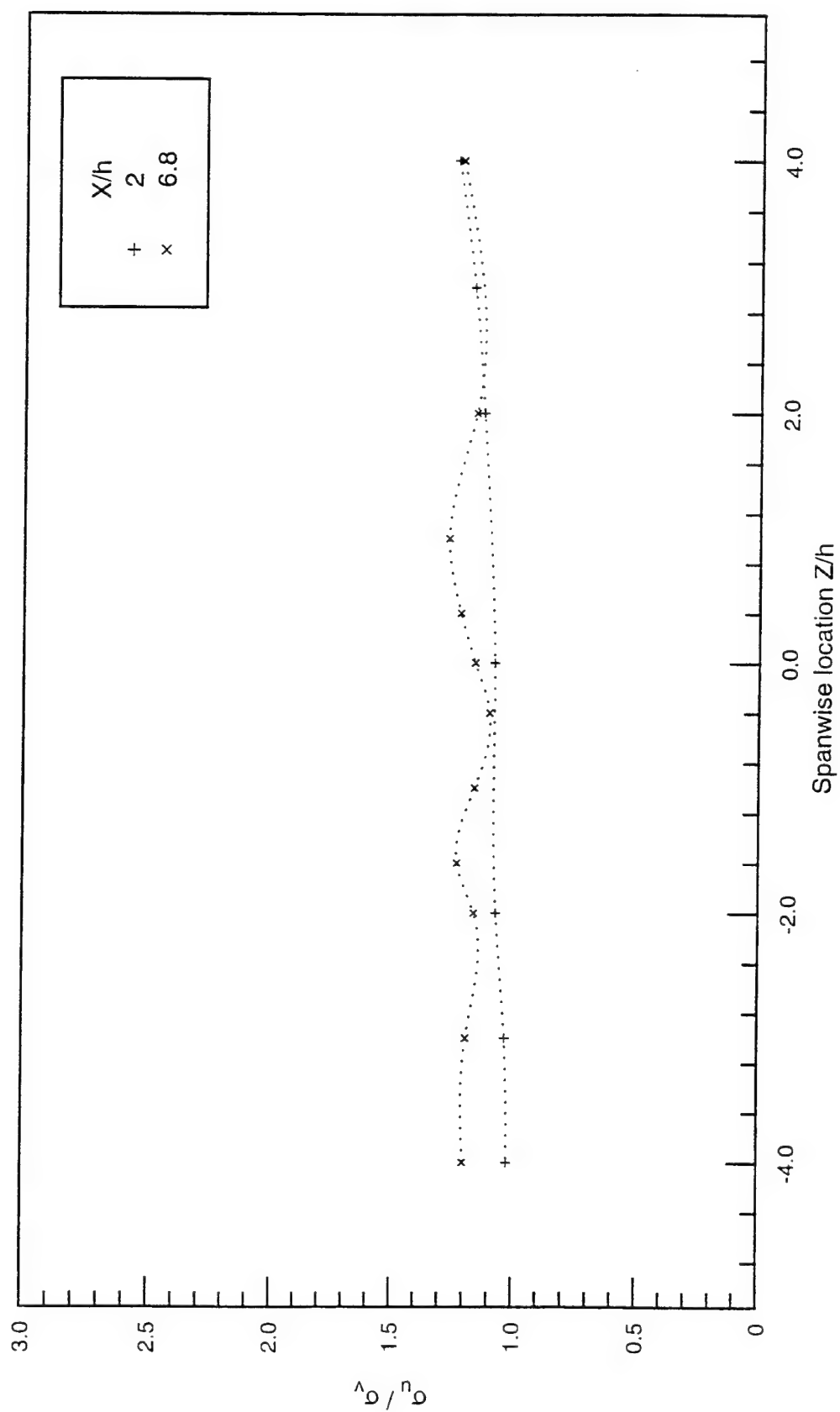


Figure 5.64 Ratio of streamwise to transverse turbulence intensities in (X,Z) plane for the no injection (N) case.

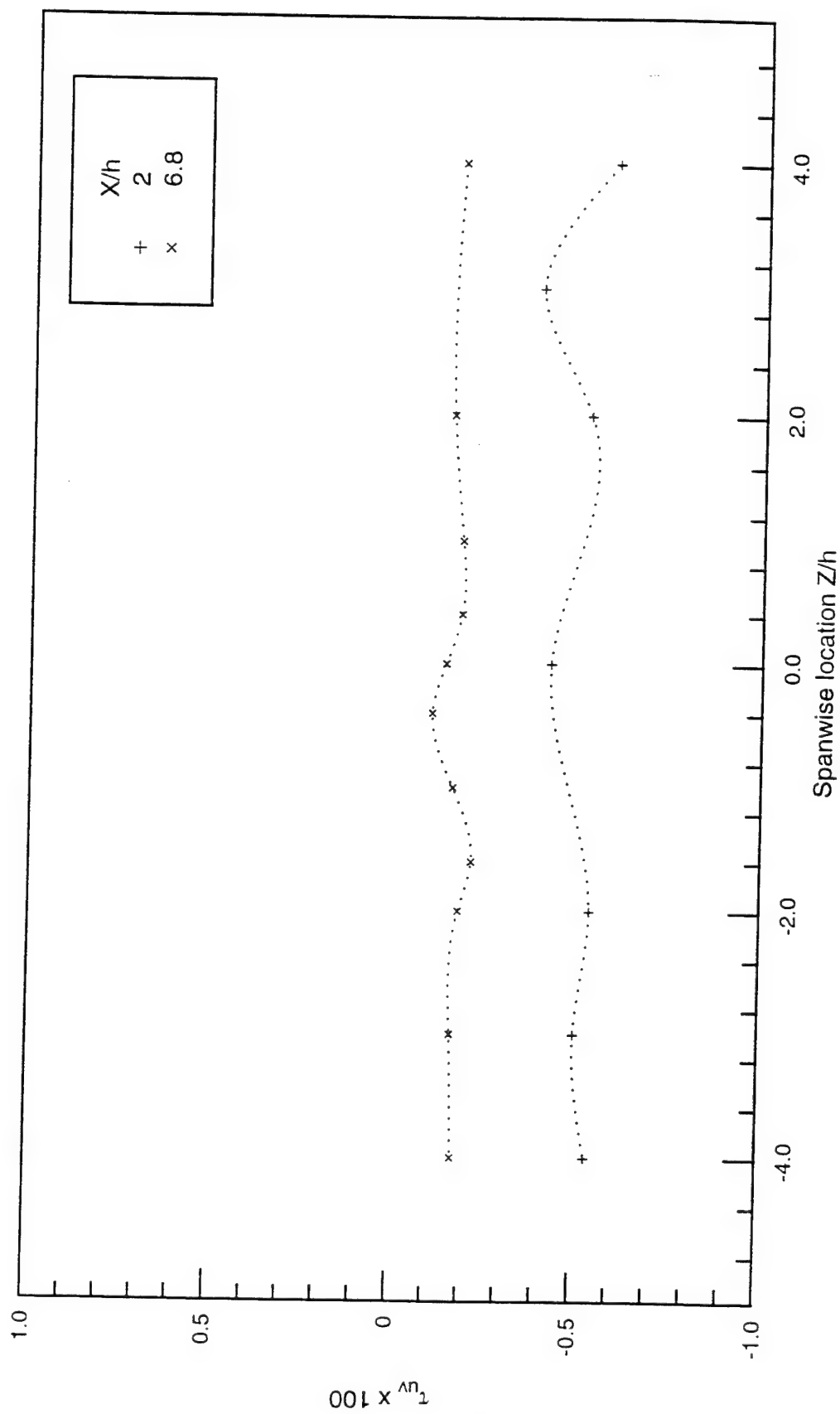


Figure 5.65 Turbulent shear stress in (X,Z) plane for the no injection (N) case.

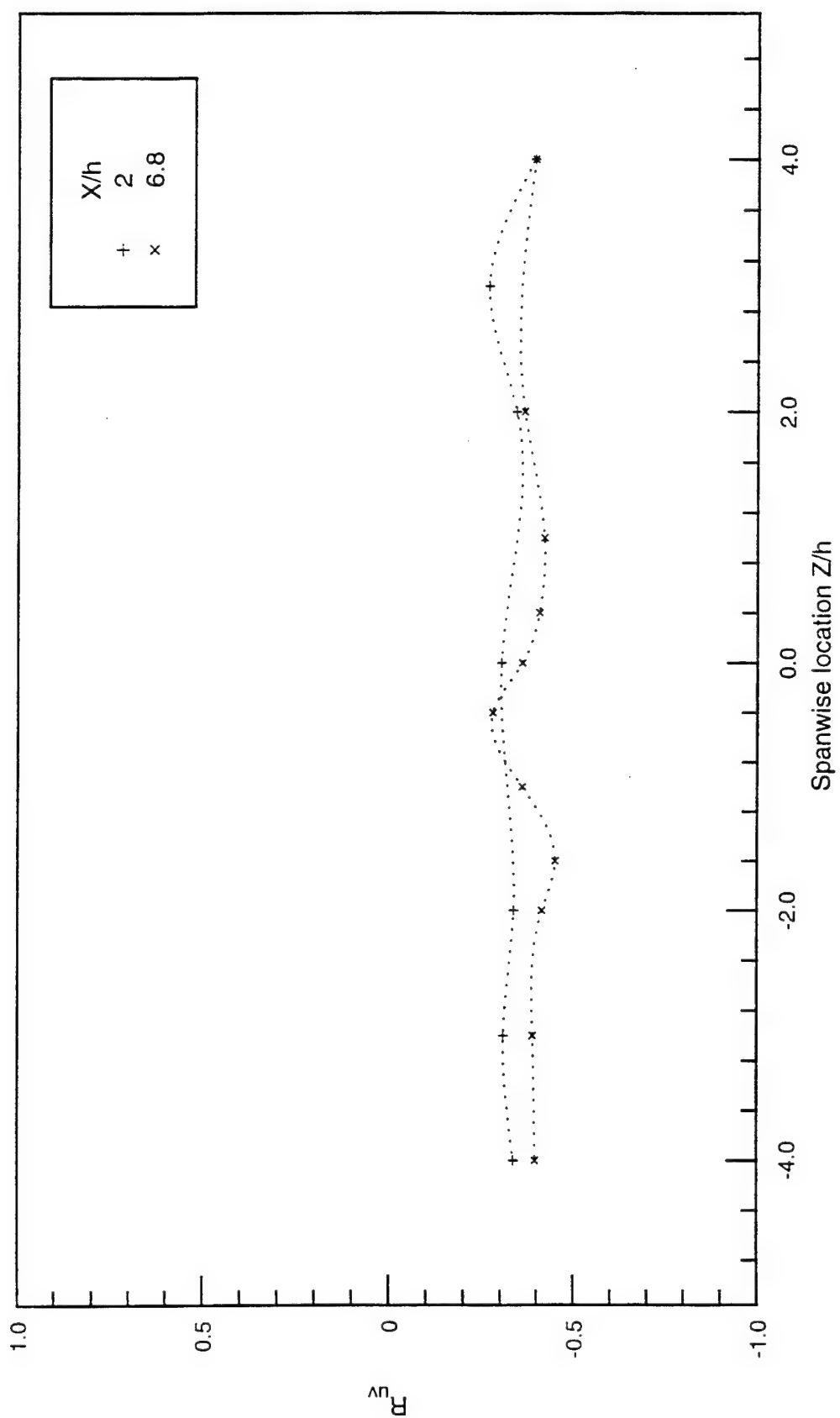


Figure 5.66 Turbulent shear stress correlation coefficient in (X,Z) plane for the no injection (N) case.

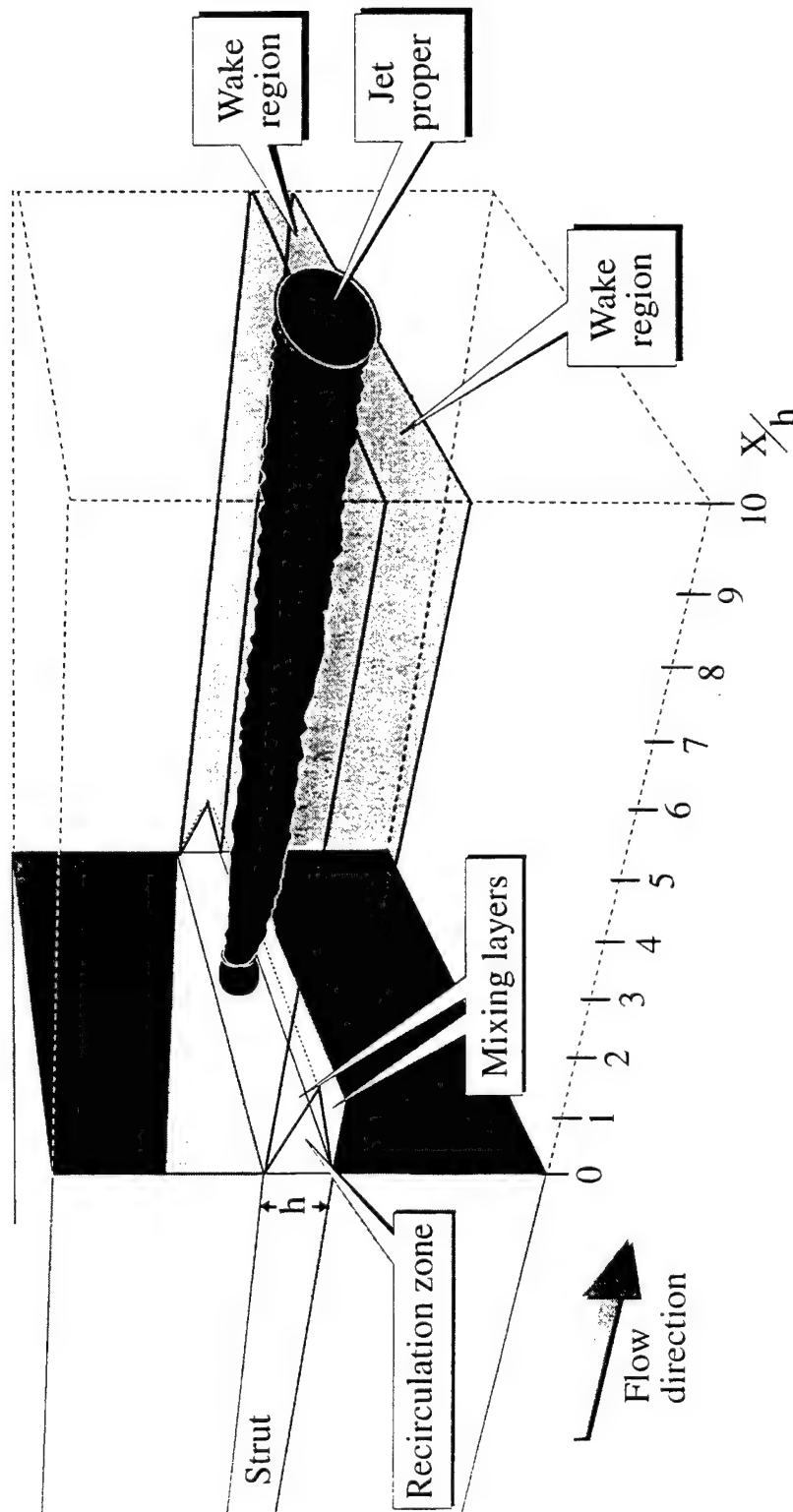


Figure 5.67 Illustration of the mixing interaction of the helium jet and the mixing layers formed between the primary flow and the recirculating flow.

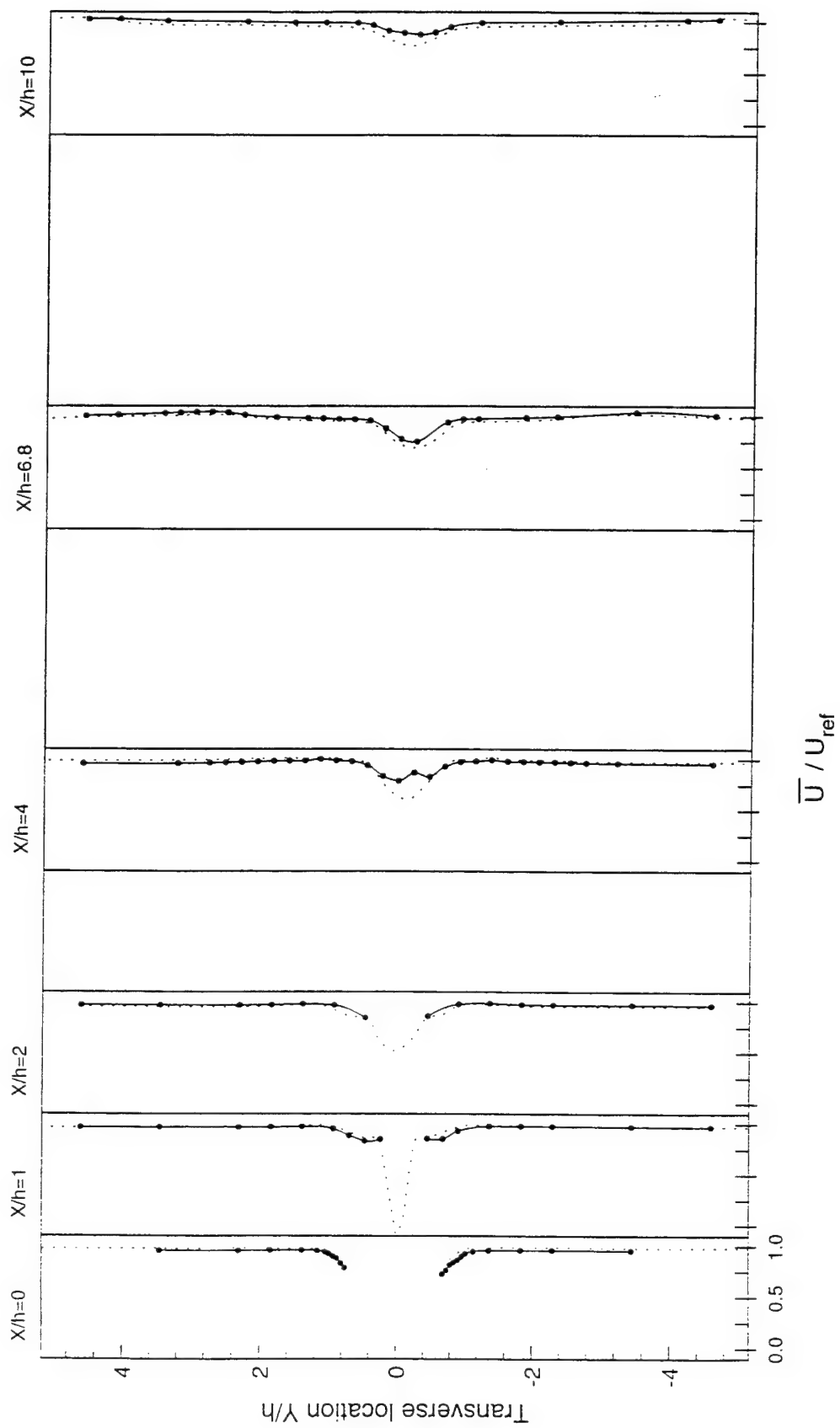


Figure 5.68 Normalized mean streamwise velocity in (X, Y) plane for the no injection (N) case (---) and the helium injection case using circular (C) nozzle (●).

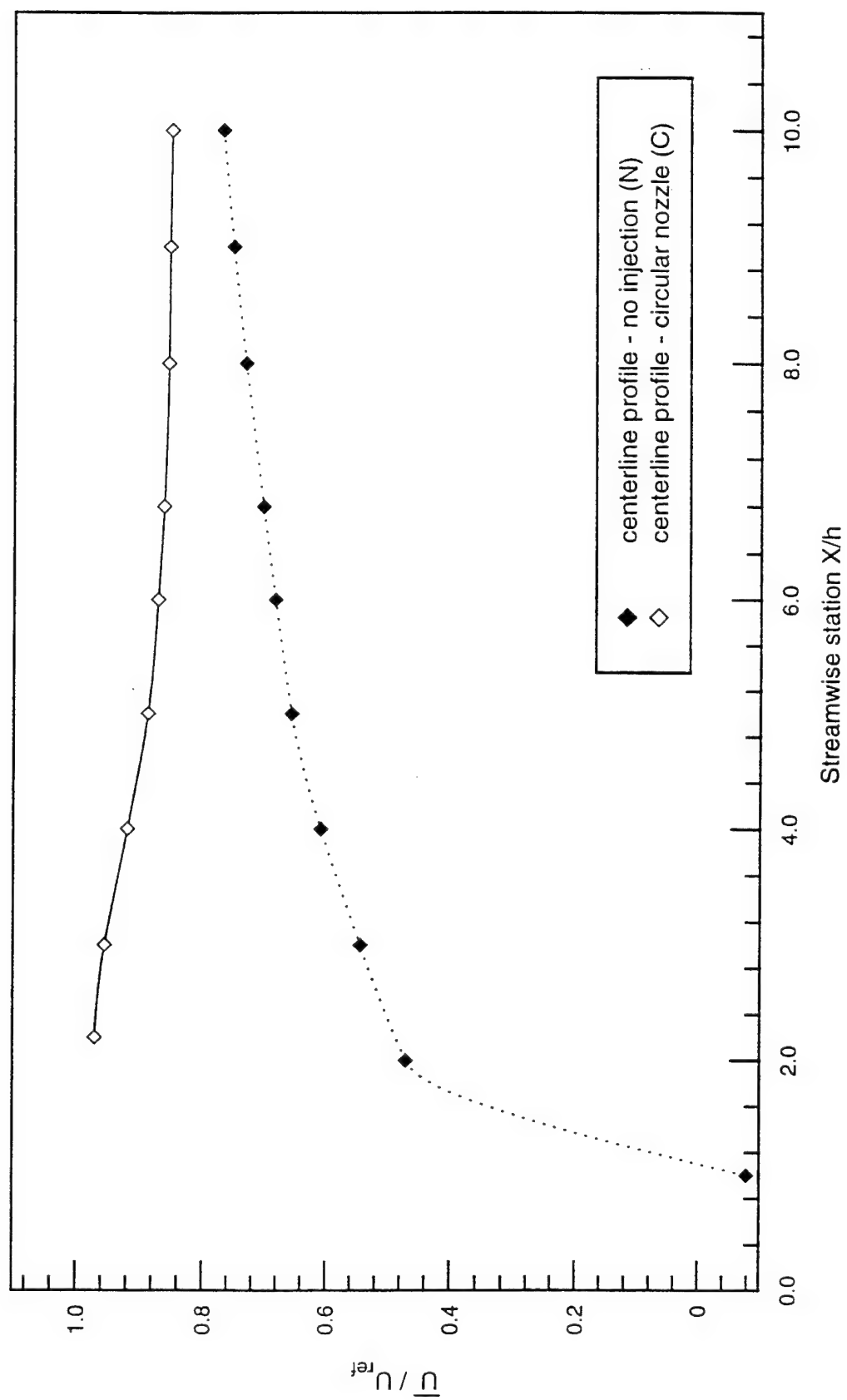


Figure 5.69 Normalized mean streamwise velocity on centerline of strut (X-axis) for the no injection (N) case.

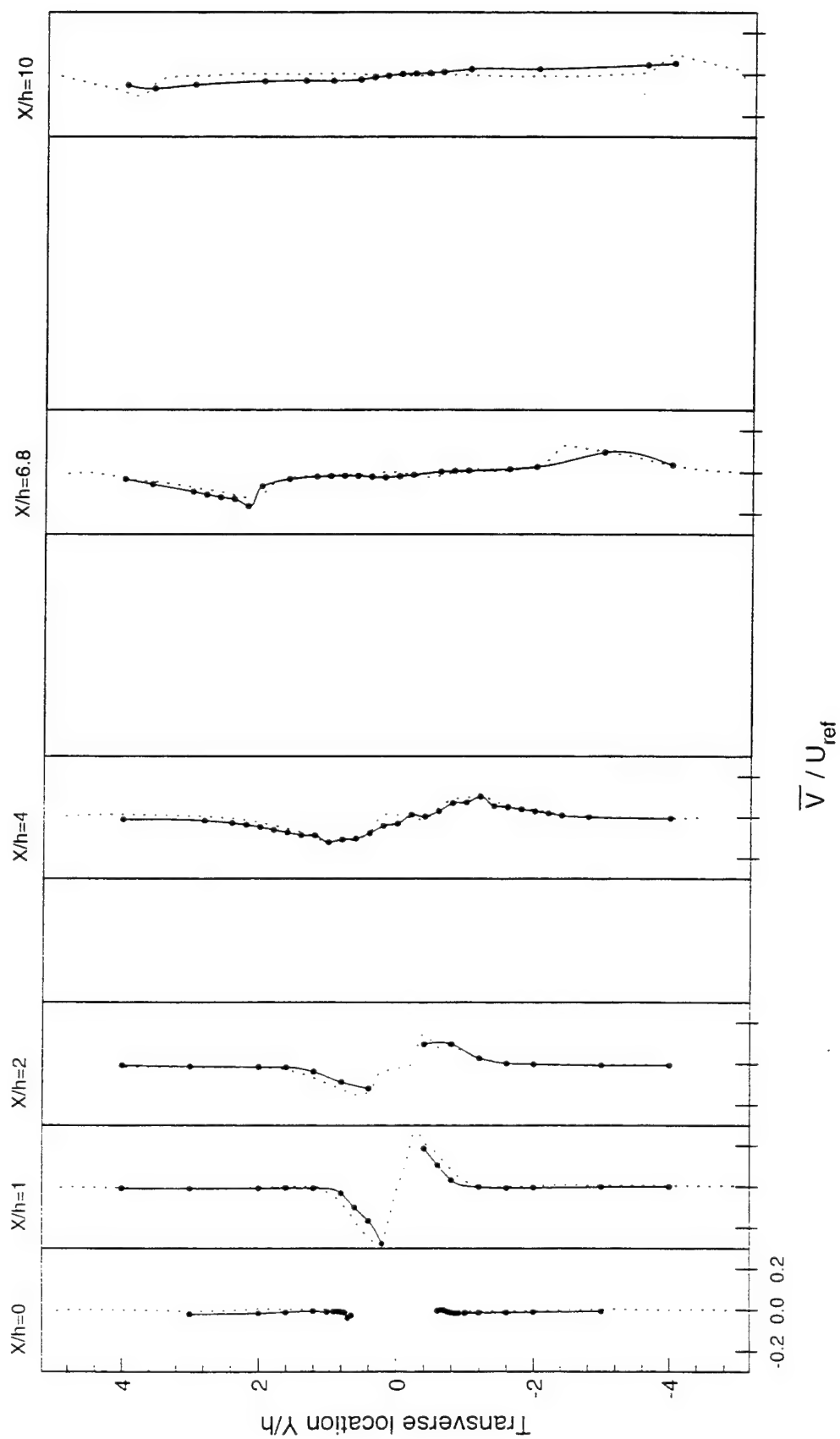


Figure 5.70 Normalized mean transverse velocity in (X, Y) plane for the no injection (N) case (---) and the helium injection case using circular (C) nozzle (●).

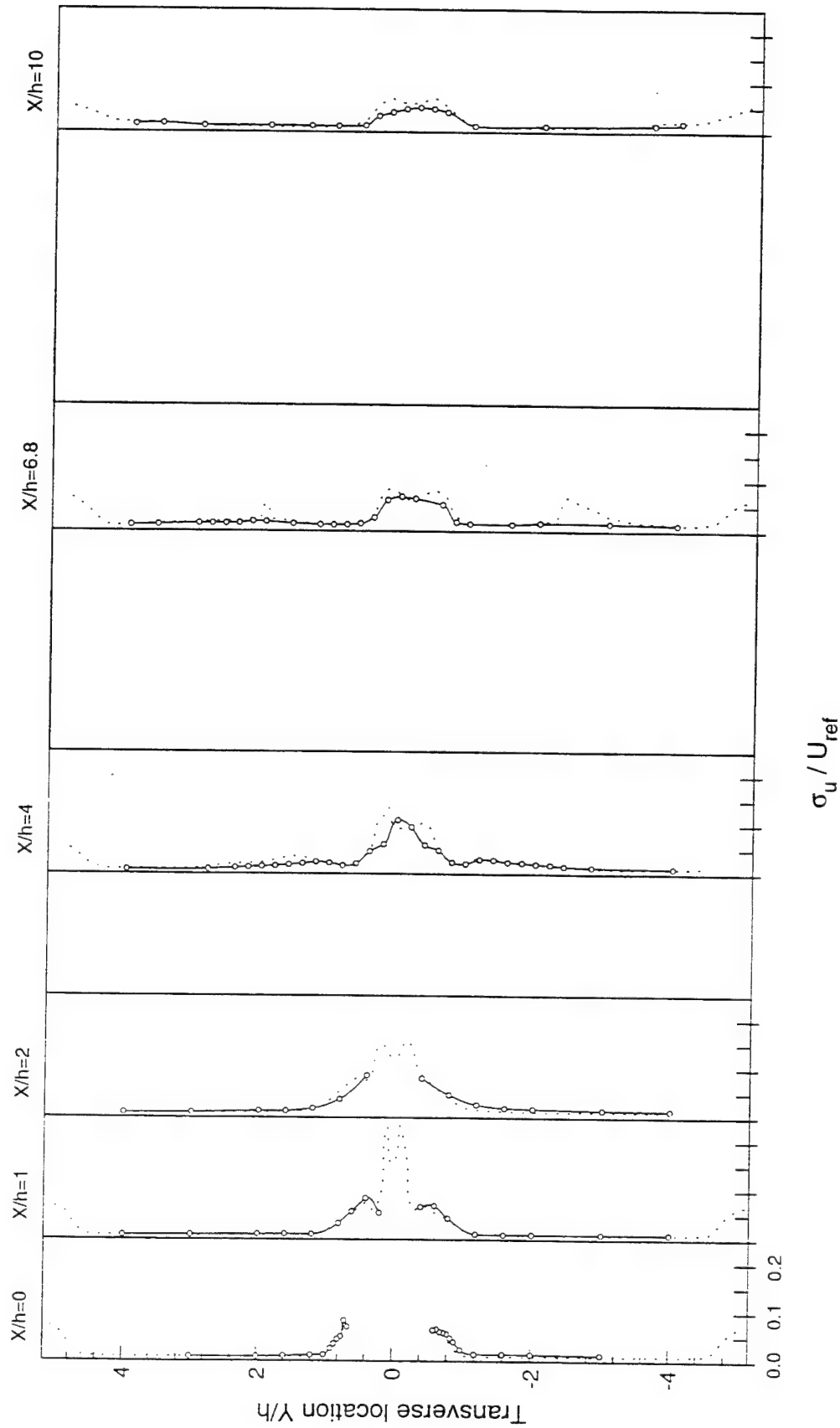


Figure 5.71 Streamwise turbulence intensity in (X,Y) plane for the no injection (N) case (- - -) and the helium injection case using circular (C) nozzle (●).

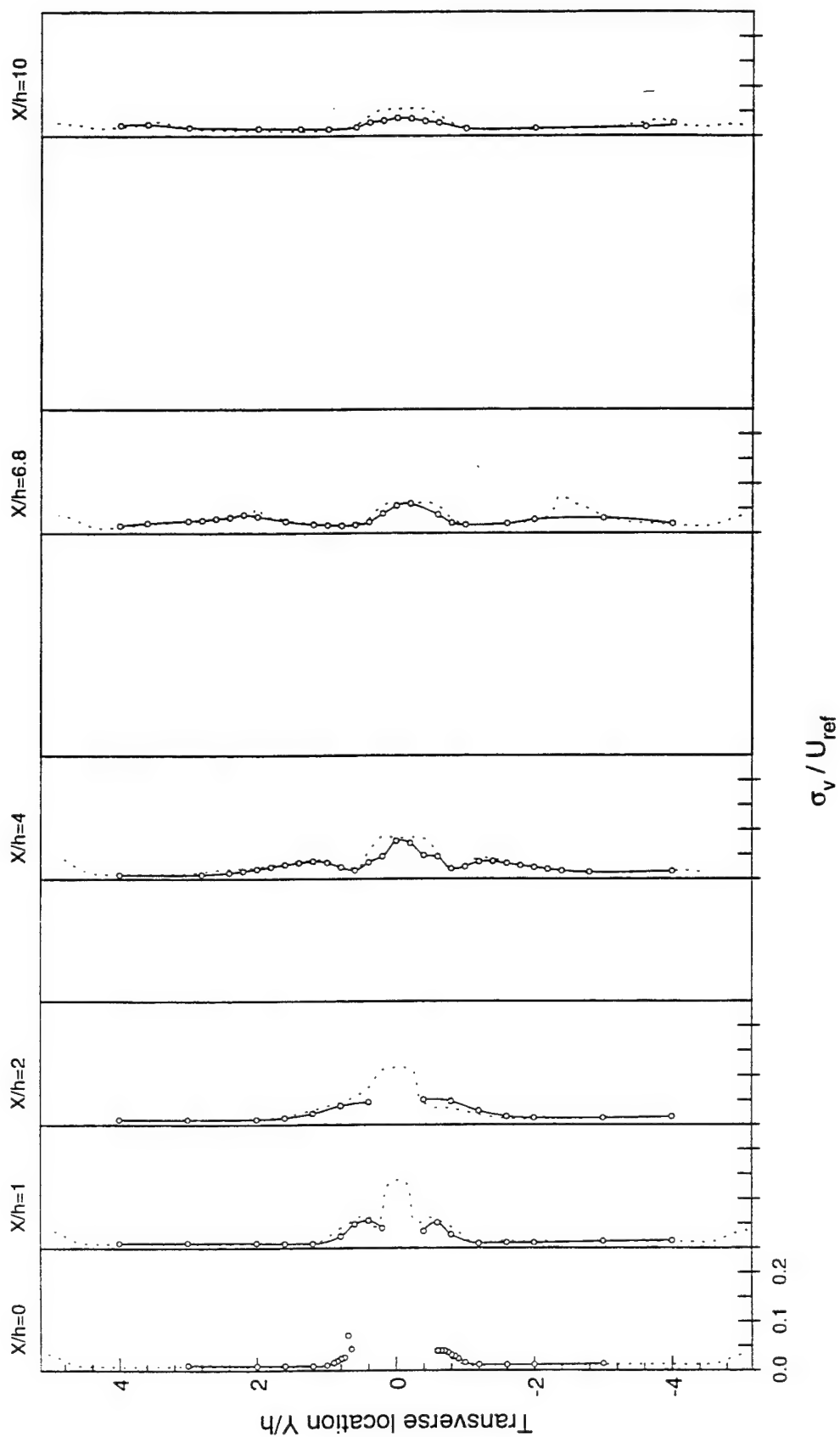


Figure 5.72 Transverse turbulence intensity in (X, Y) plane for the no injection (N) case (---) and the helium injection case using circular (C) nozzle (\bullet).

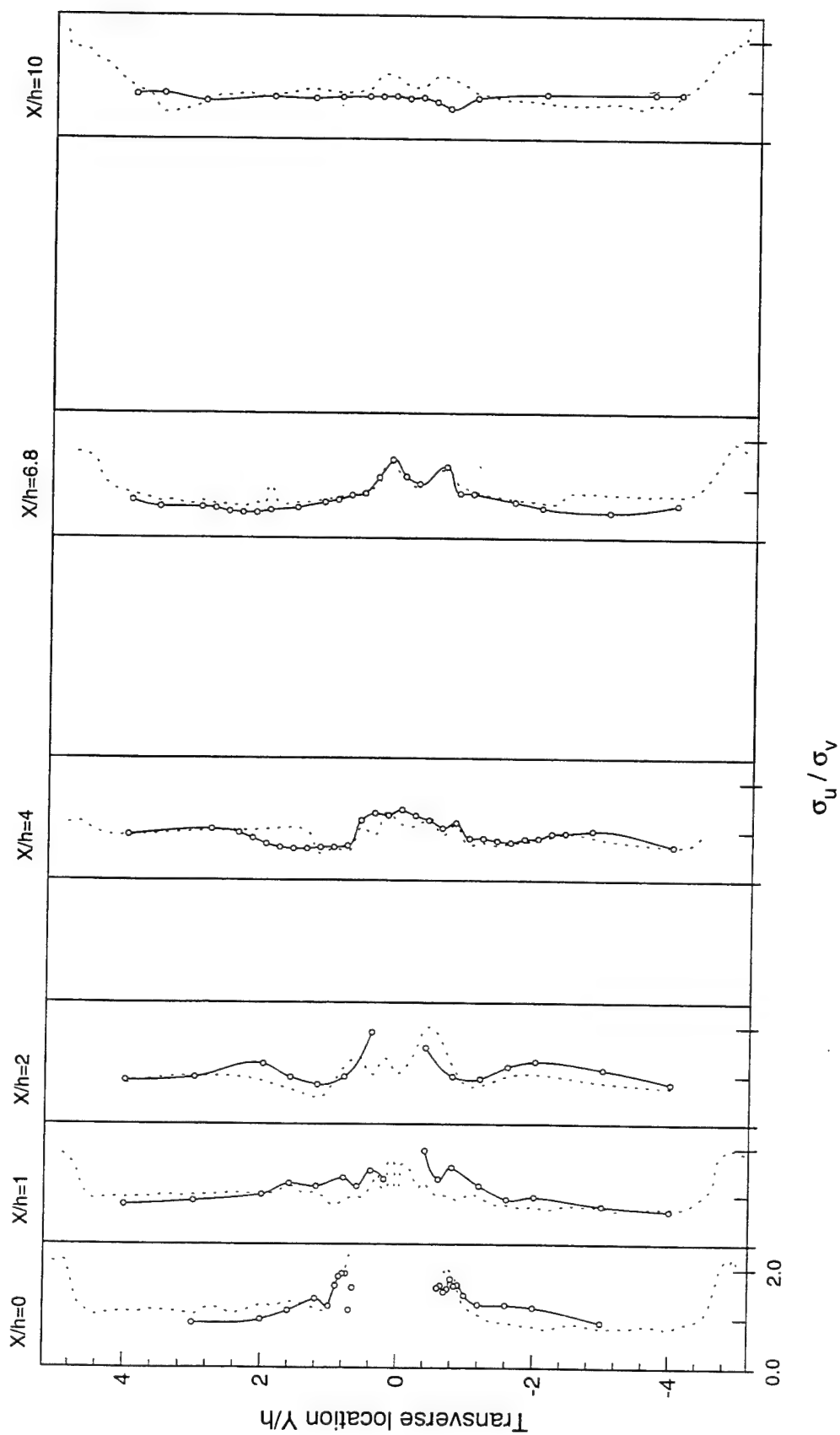


Figure 5.73 Ratio of streamwise to transverse turbulence intensities in (X, Y) plane for the no injection (N) case (---) and the helium injection case using circular (C) nozzle (○).

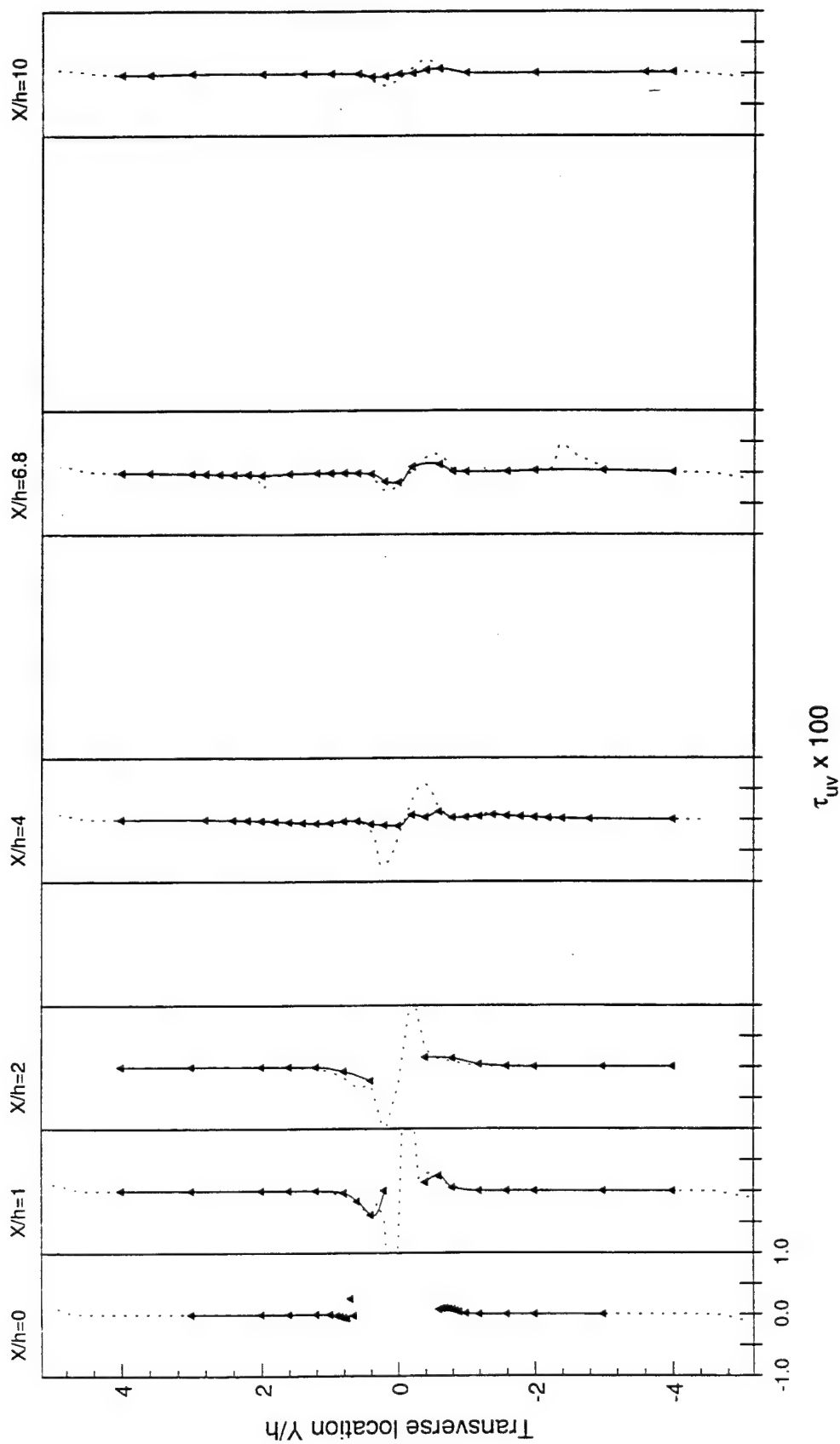


Figure 5.74 Turbulent shear stress in (X, Y) plane for the no injection (N) case (---) and the helium injection using circular (C) nozzle (\blacktriangle).

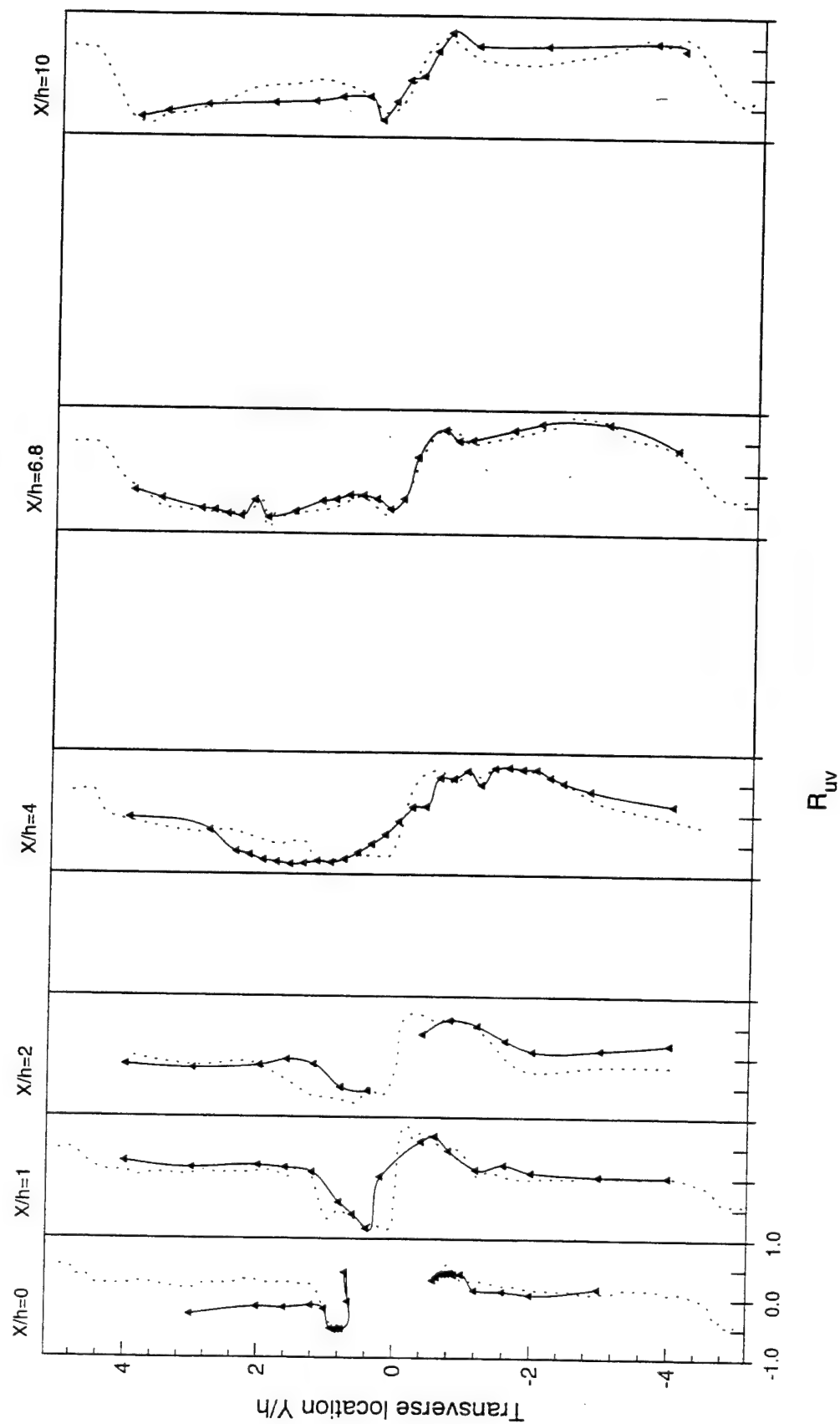


Figure 5.75 Turbulent shear stress correlation coefficient in (X, Y) plane for the no injection (N) case (---) and the helium injection case using circular (C) nozzle (\blacktriangle).

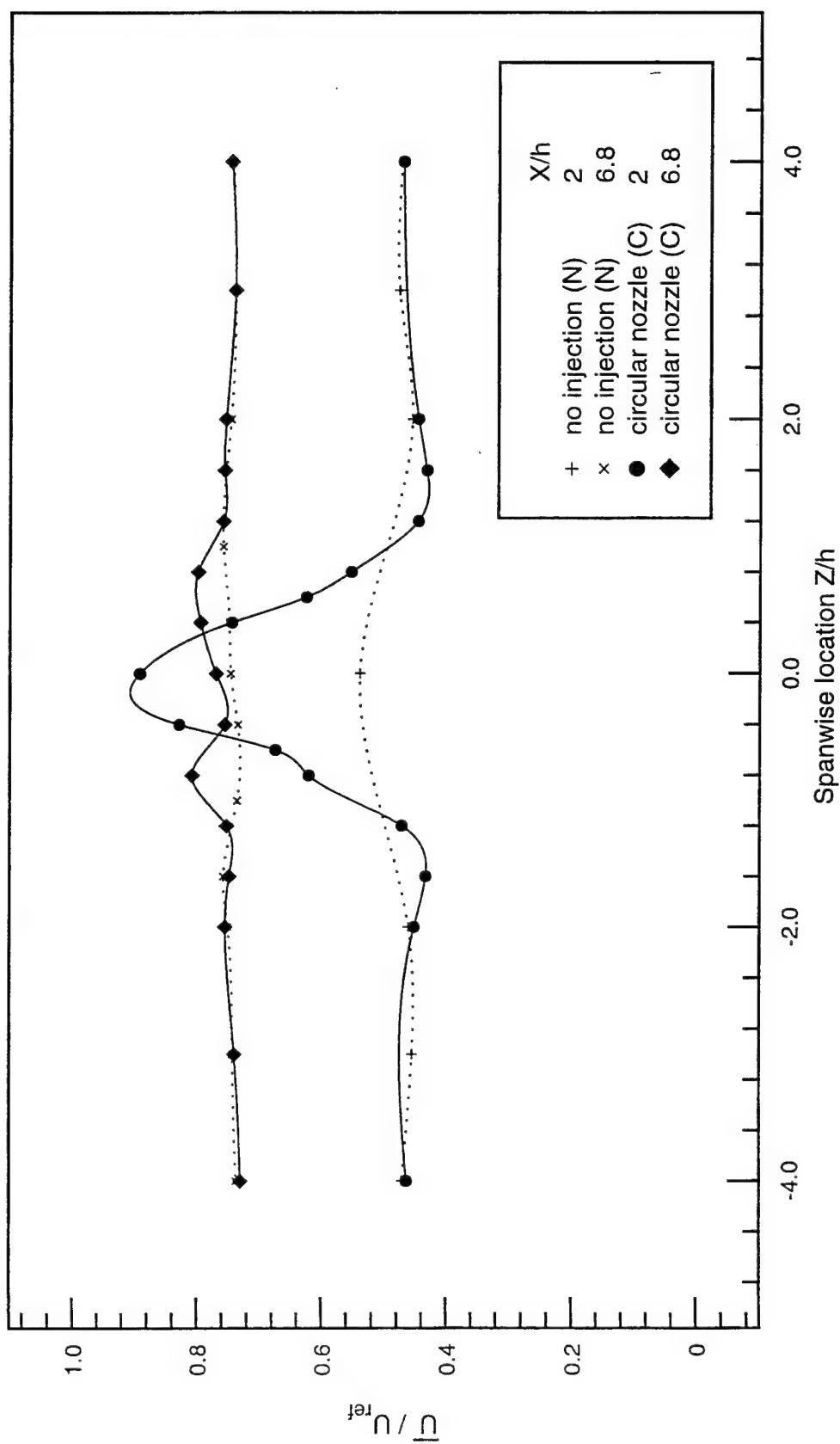


Figure 5.76 Normalized mean streamwise velocity in (X,Z) plane for the no injection (N) case and the helium injection case using circular (C) nozzle.

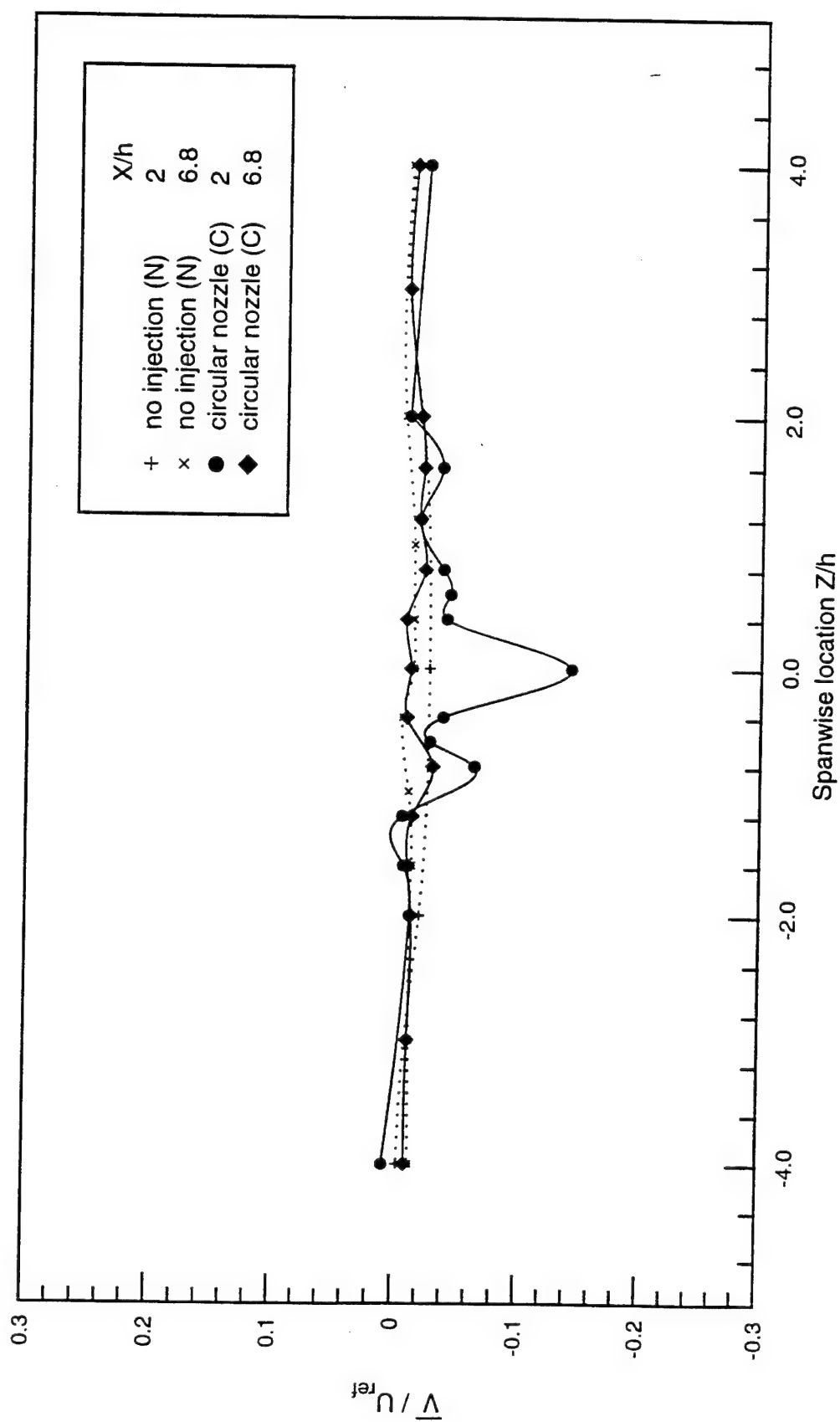


Figure 5.77 Normalized mean transverse velocity in (X,Z) plane for the no injection (N) case and the helium injection case using circular (C) nozzle.

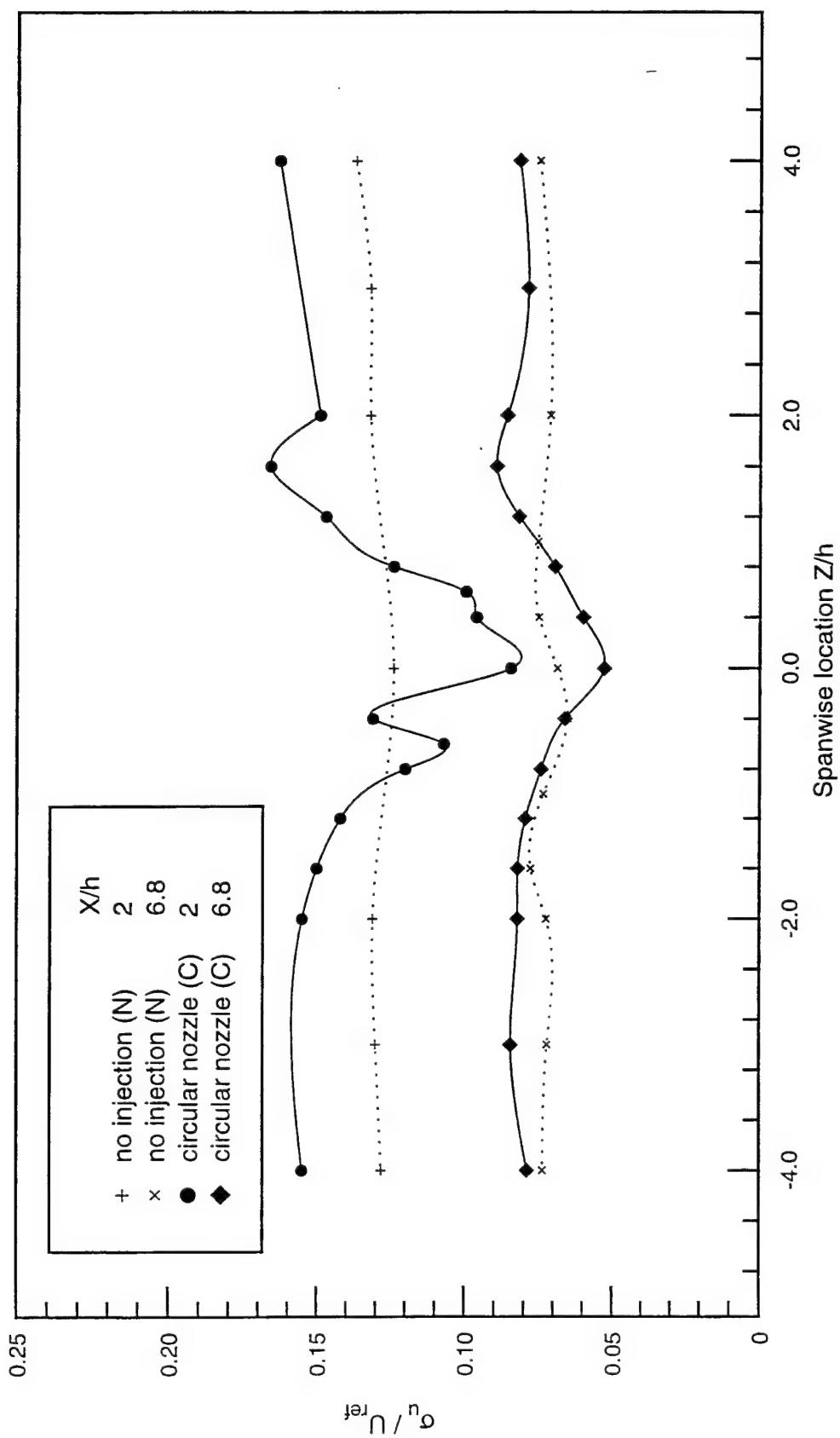


Figure 5.78 Streamwise turbulence intensity in (X,Z) plane for the no injection (N) case and the helium injection case using circular (C) nozzle.

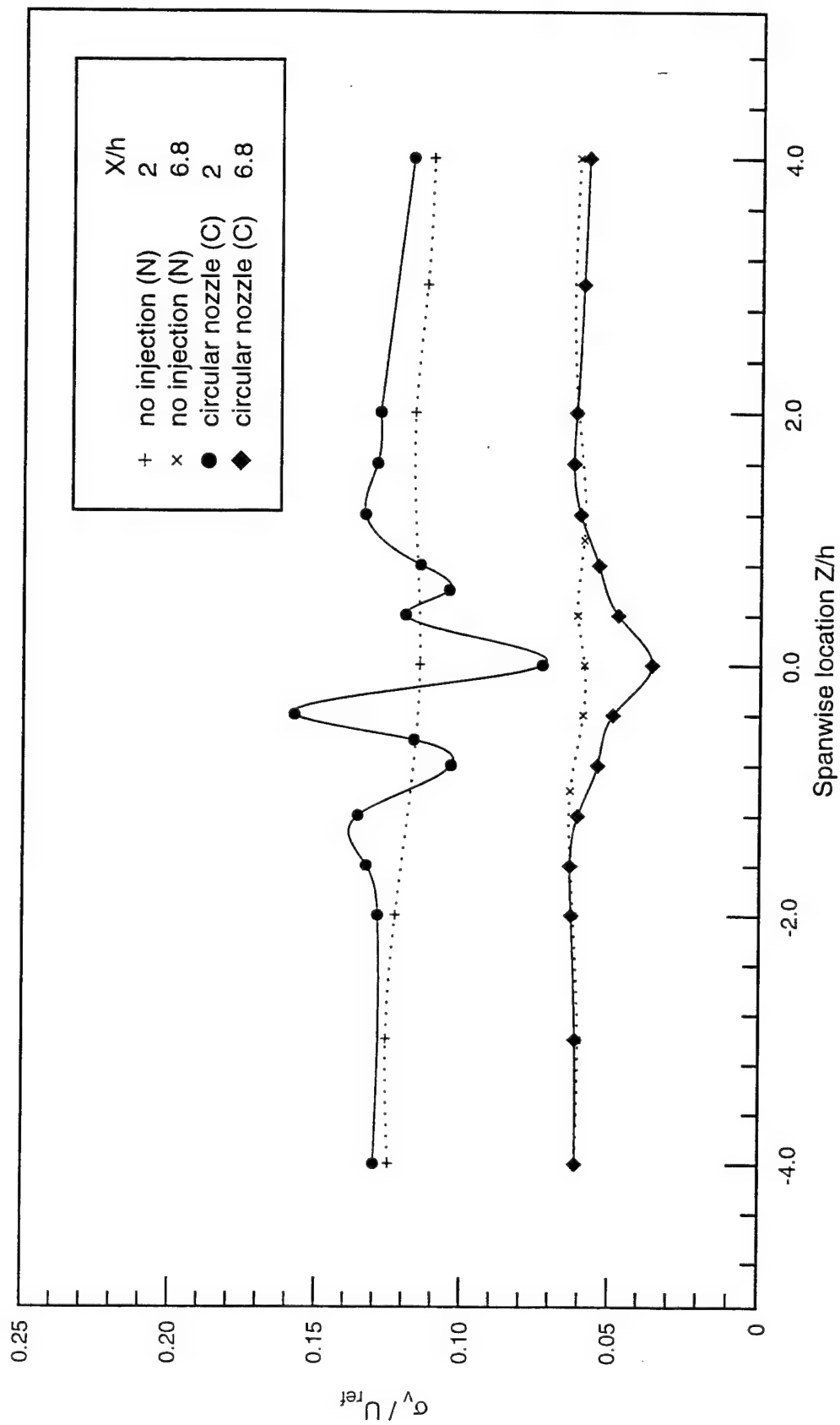


Figure 5.79 Transverse turbulence intensity in (X,Z) plane for the no injection (N) case and the helium injection case using circular (C) nozzle.

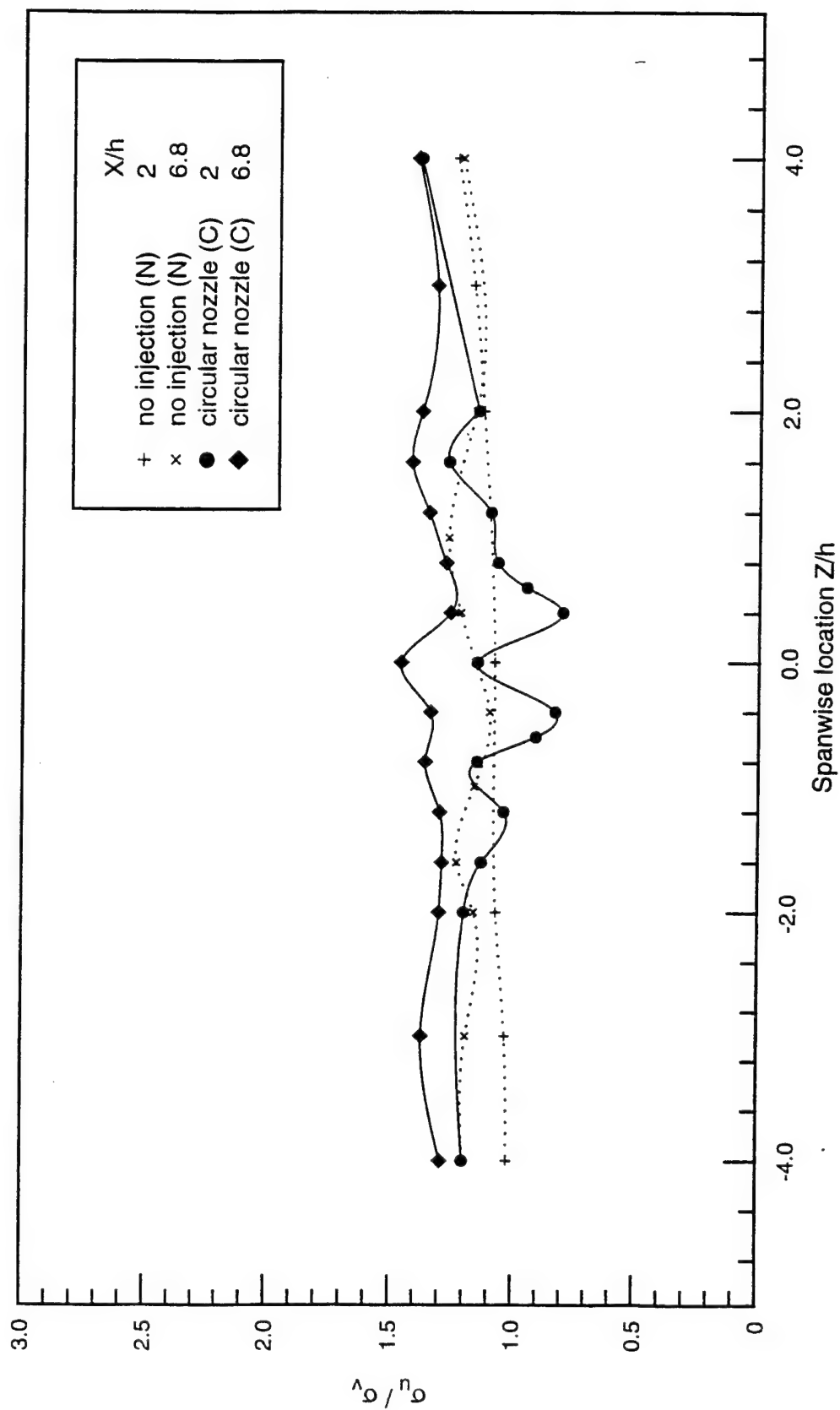


Figure 5.80 Ratio of streamwise to transverse turbulence intensities in (X,Z) plane for the no injection (N) case and the helium injection case using circular (C) nozzle.

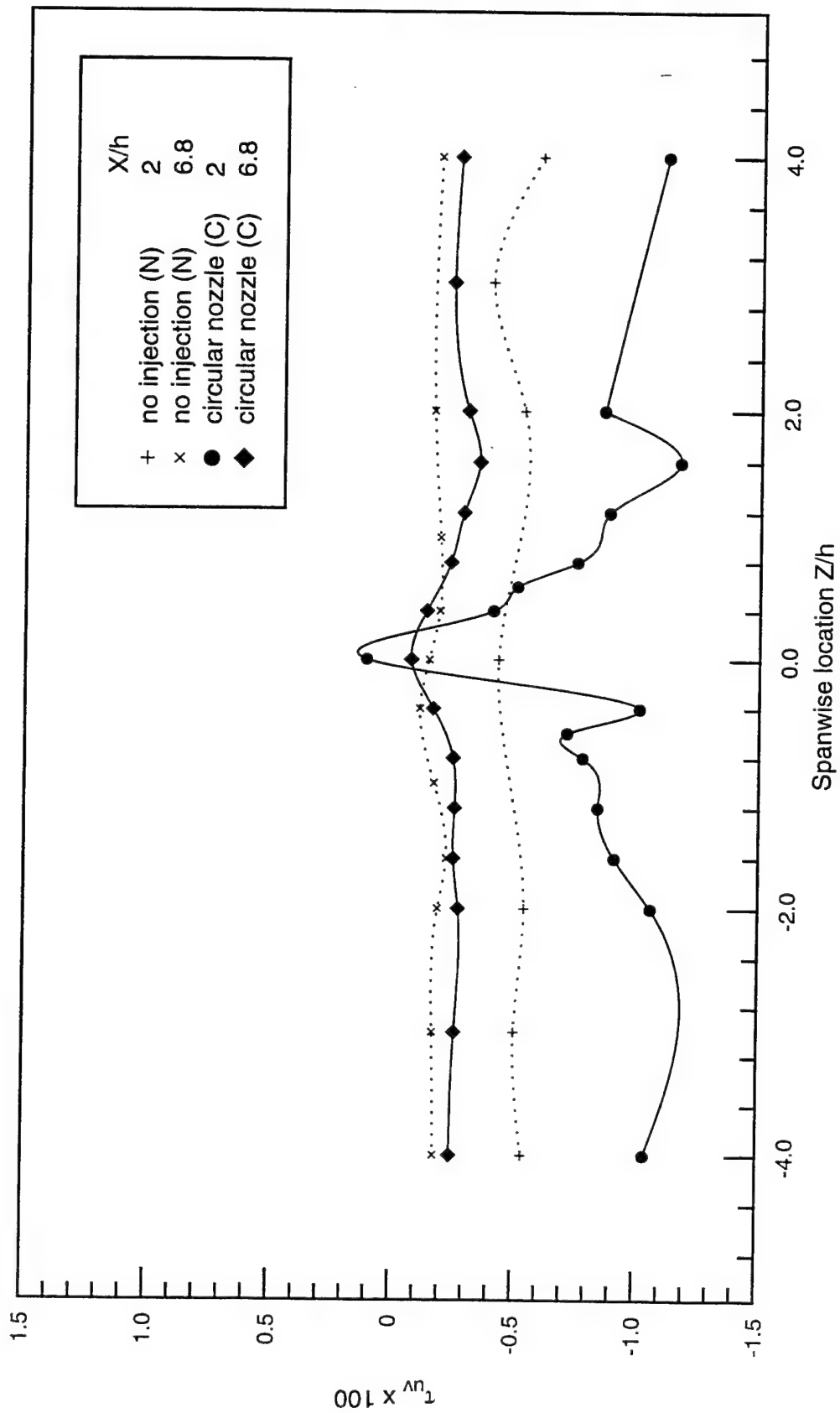


Figure 5.81 Turbulent shear stress in (X,Z) plane for the no injection (N) case and the helium injection case using circular (C) nozzle.

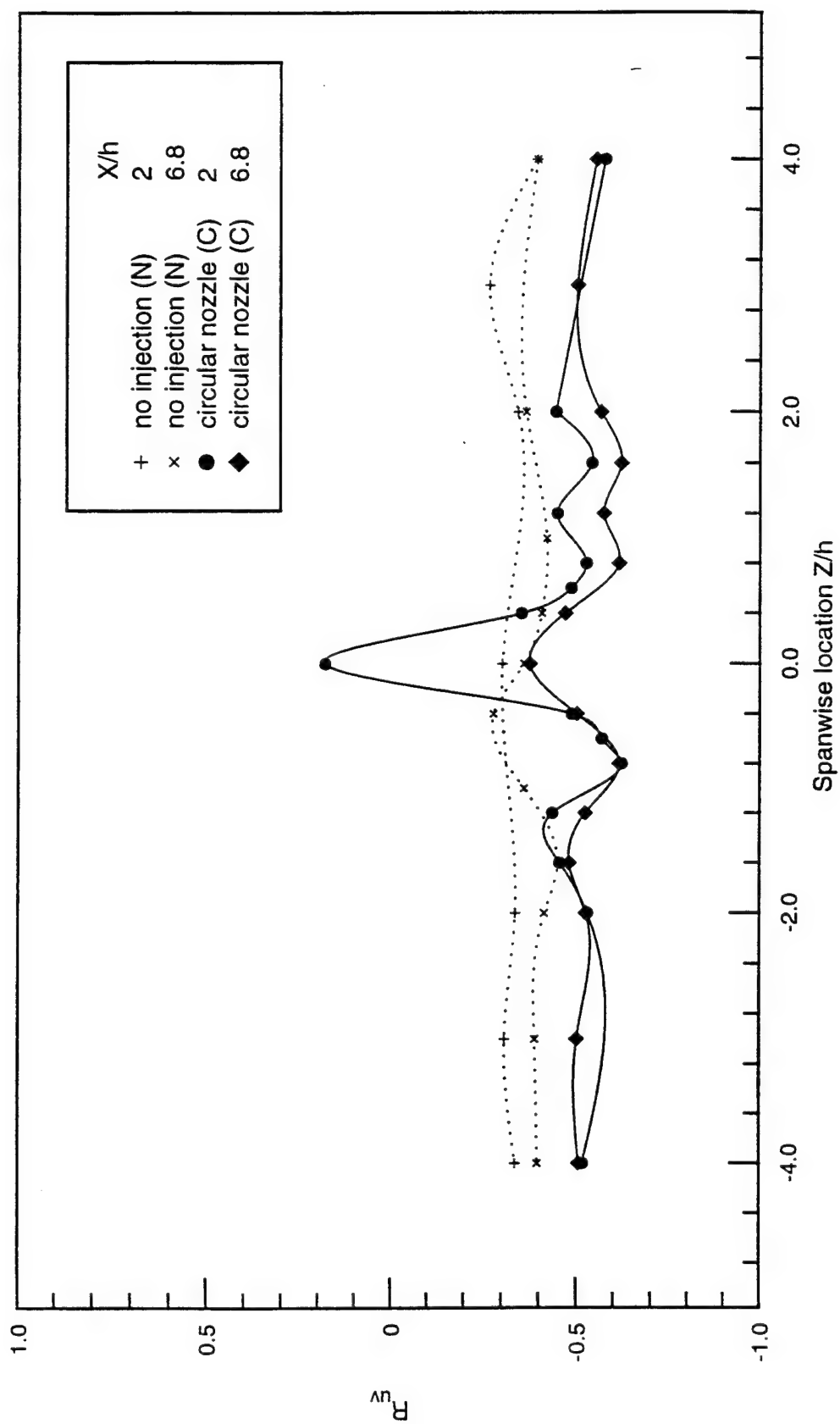


Figure 5.82 Turbulent shear stress correlation coefficient in (X,Z) plane for the no injection (N) case and the helium injection case using circular (C) nozzle.

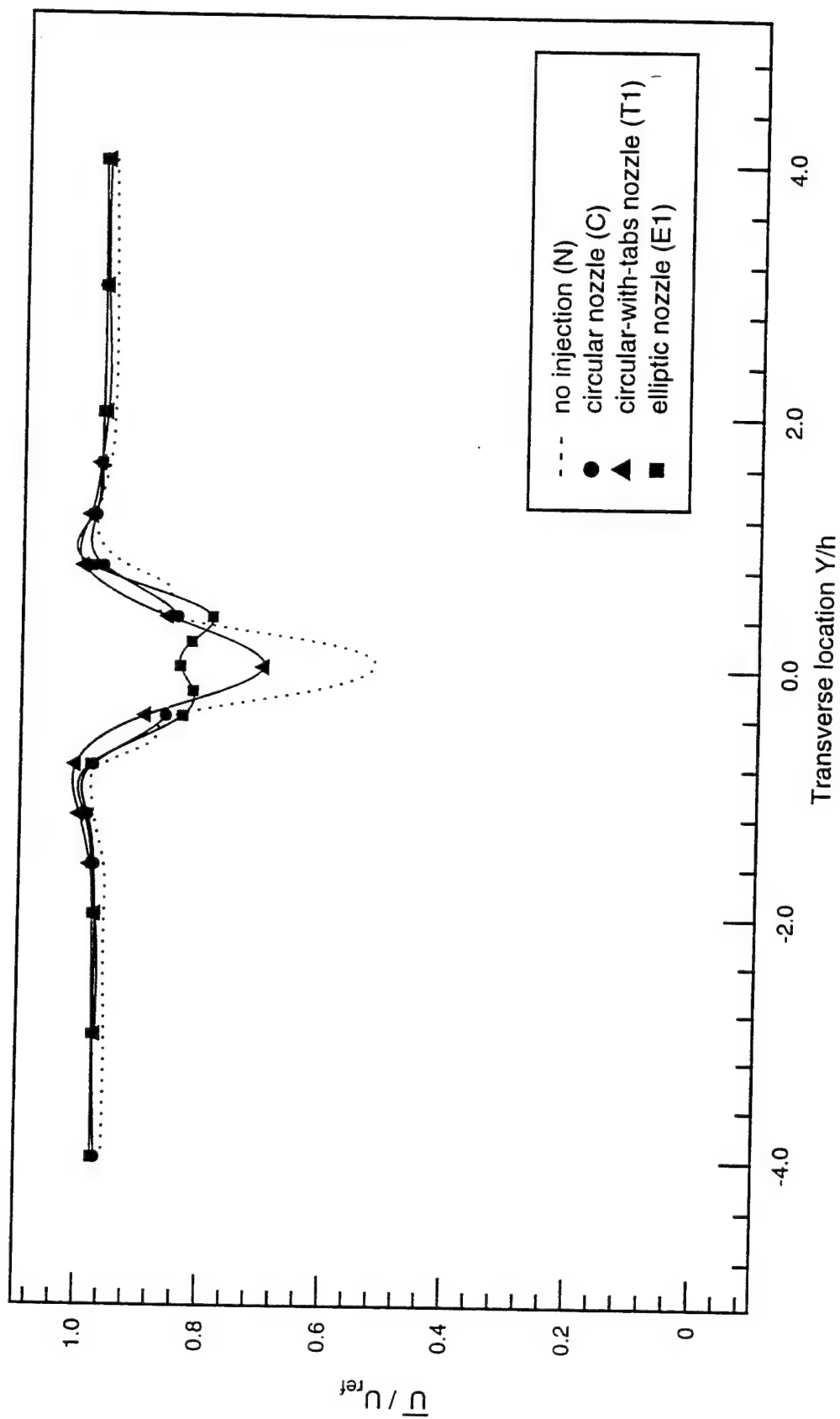


Figure 5.83 Normalized mean streamwise velocity in (X,Y) plane at $X/h=2$ for all cases.

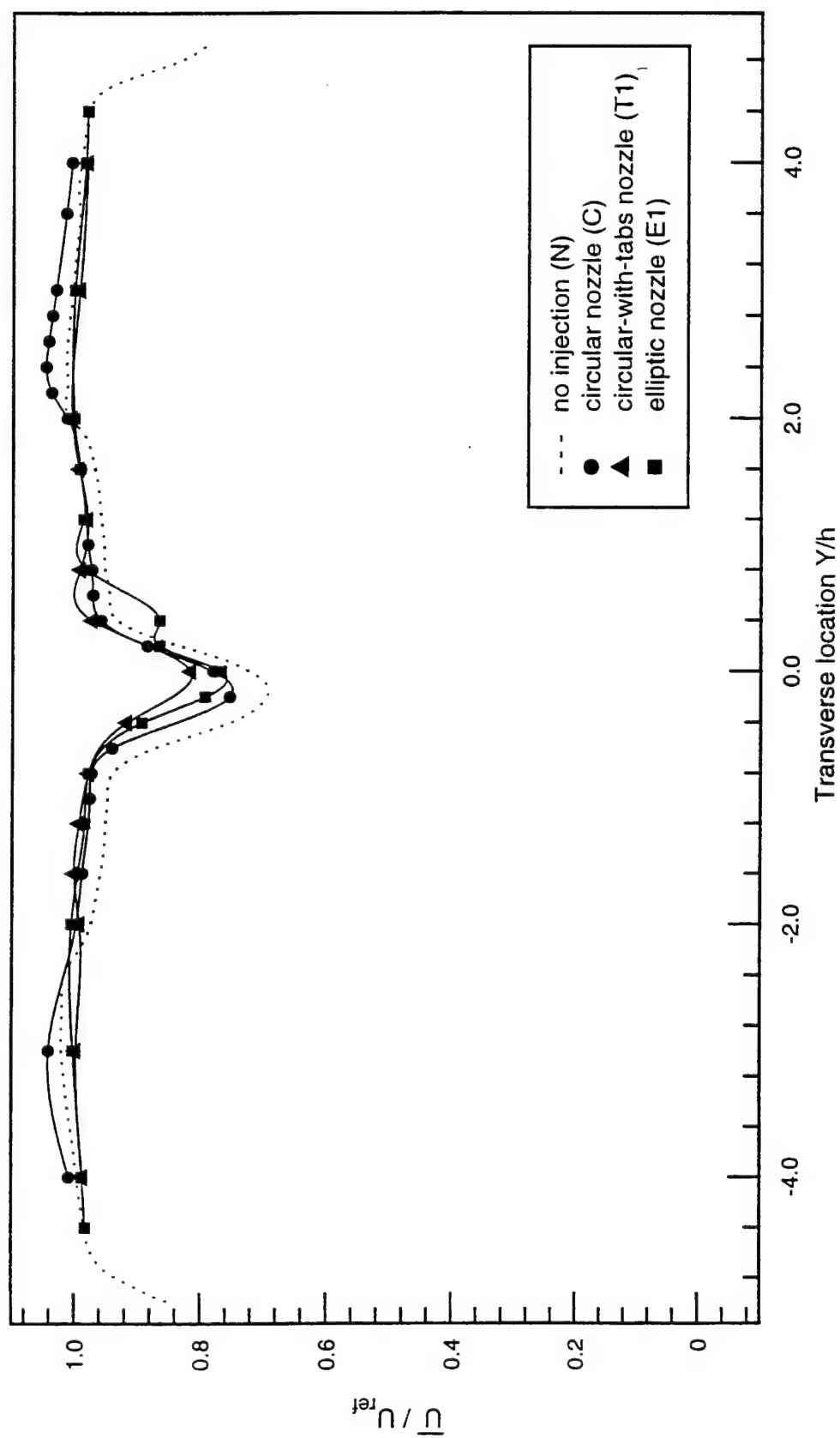


Figure 5.84 Normalized mean streamwise velocity in (X,Y) plane at $X/h=6.8$ for all cases.

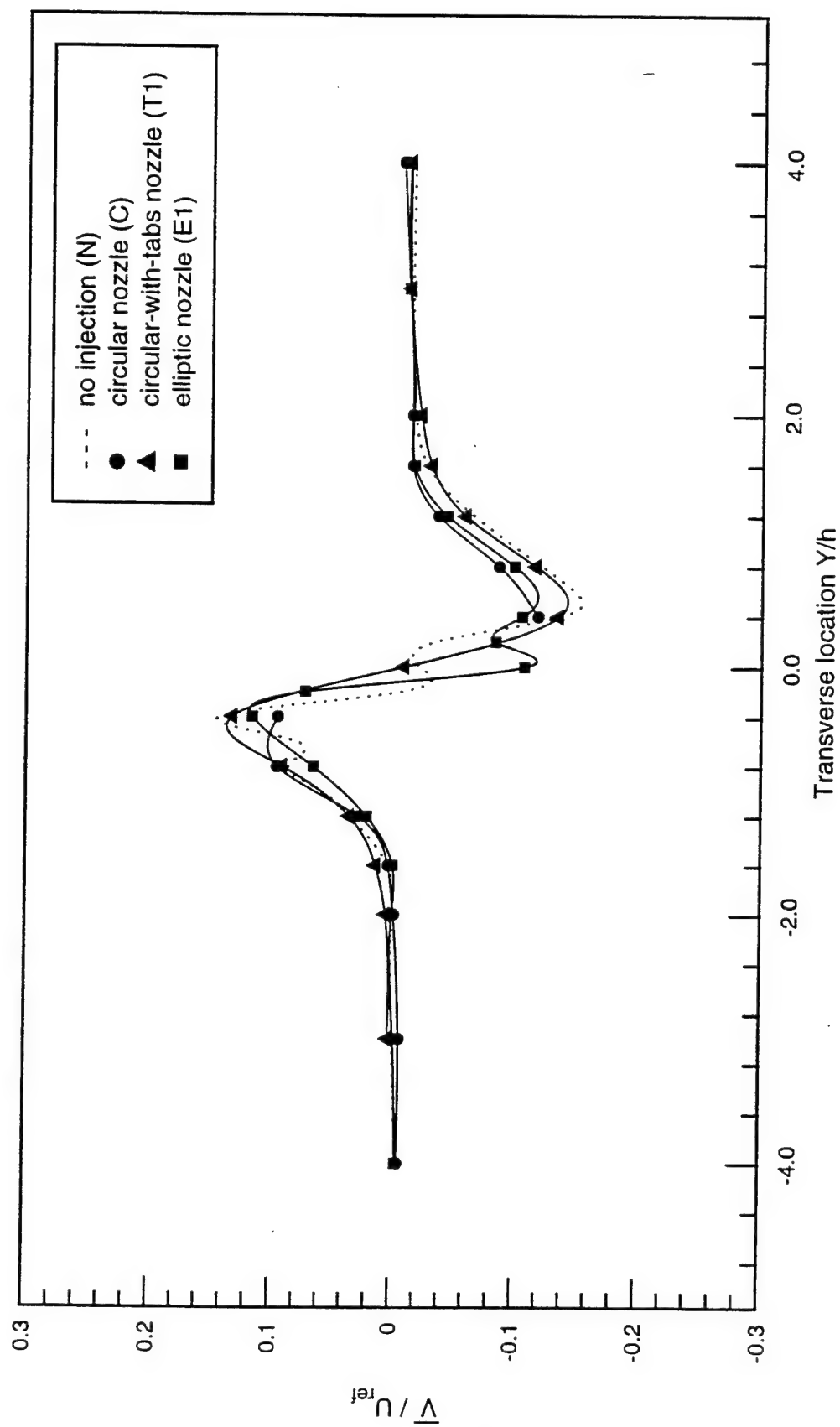


Figure 5.85 Normalized mean transverse velocity in (X, Y) plane at $X/h=2$ for all cases.

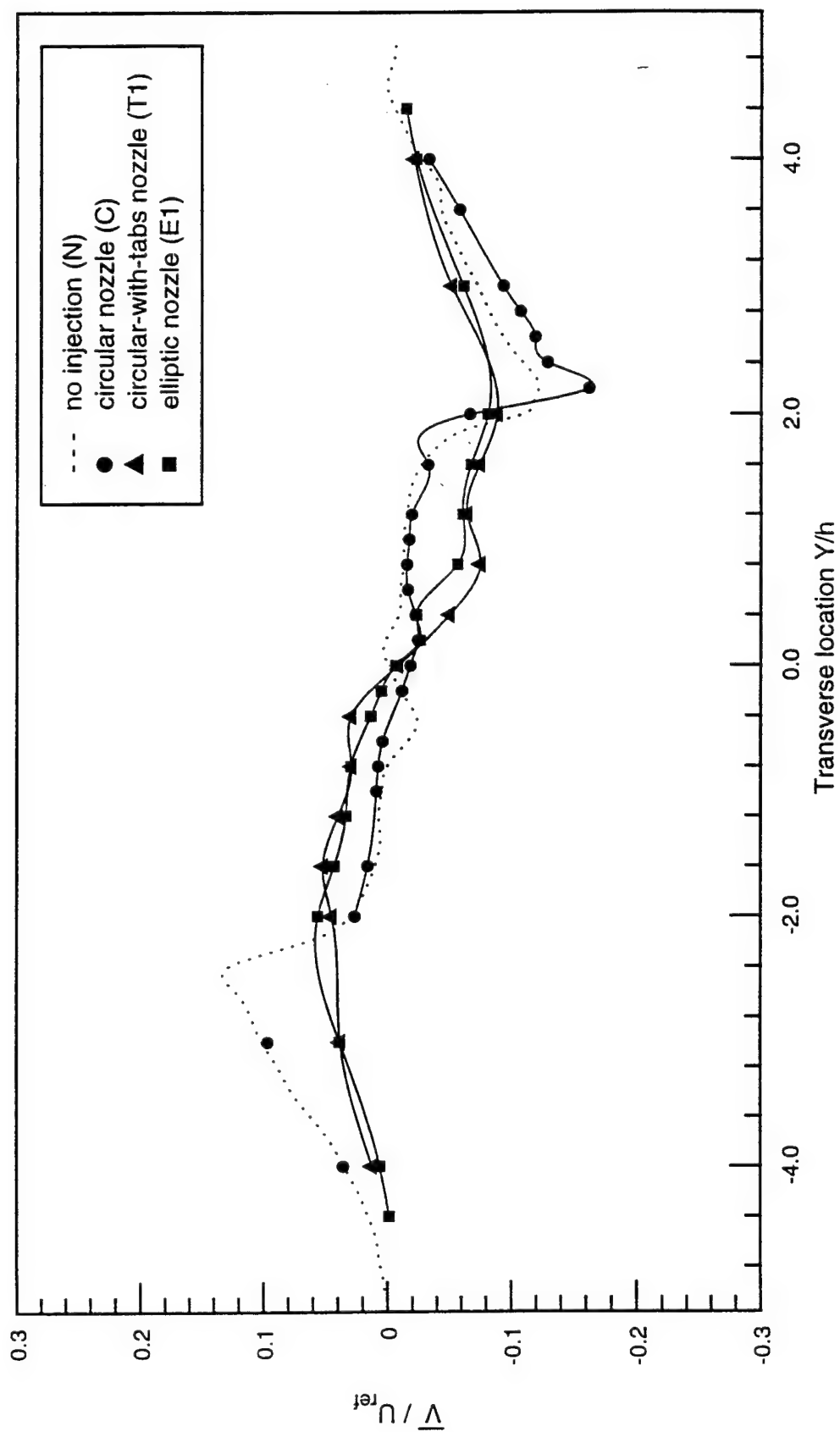


Figure 5.86 Normalized mean transverse velocity in (X,Y) plane at $X/h=6.8$ for all cases.

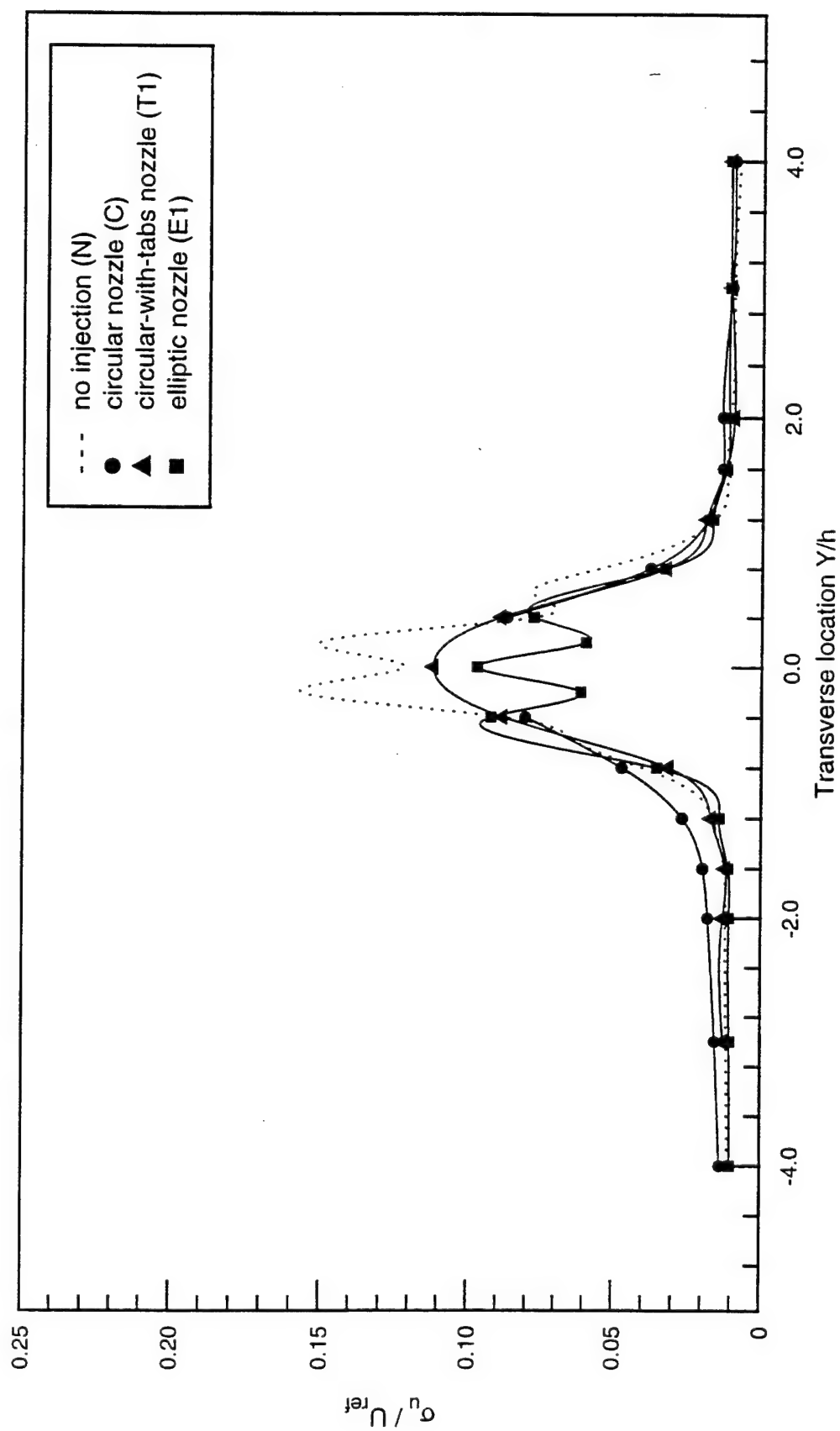


Figure 5.87 Streamwise turbulence intensity in (X, Y) plane at $X/h=2$ for all cases.

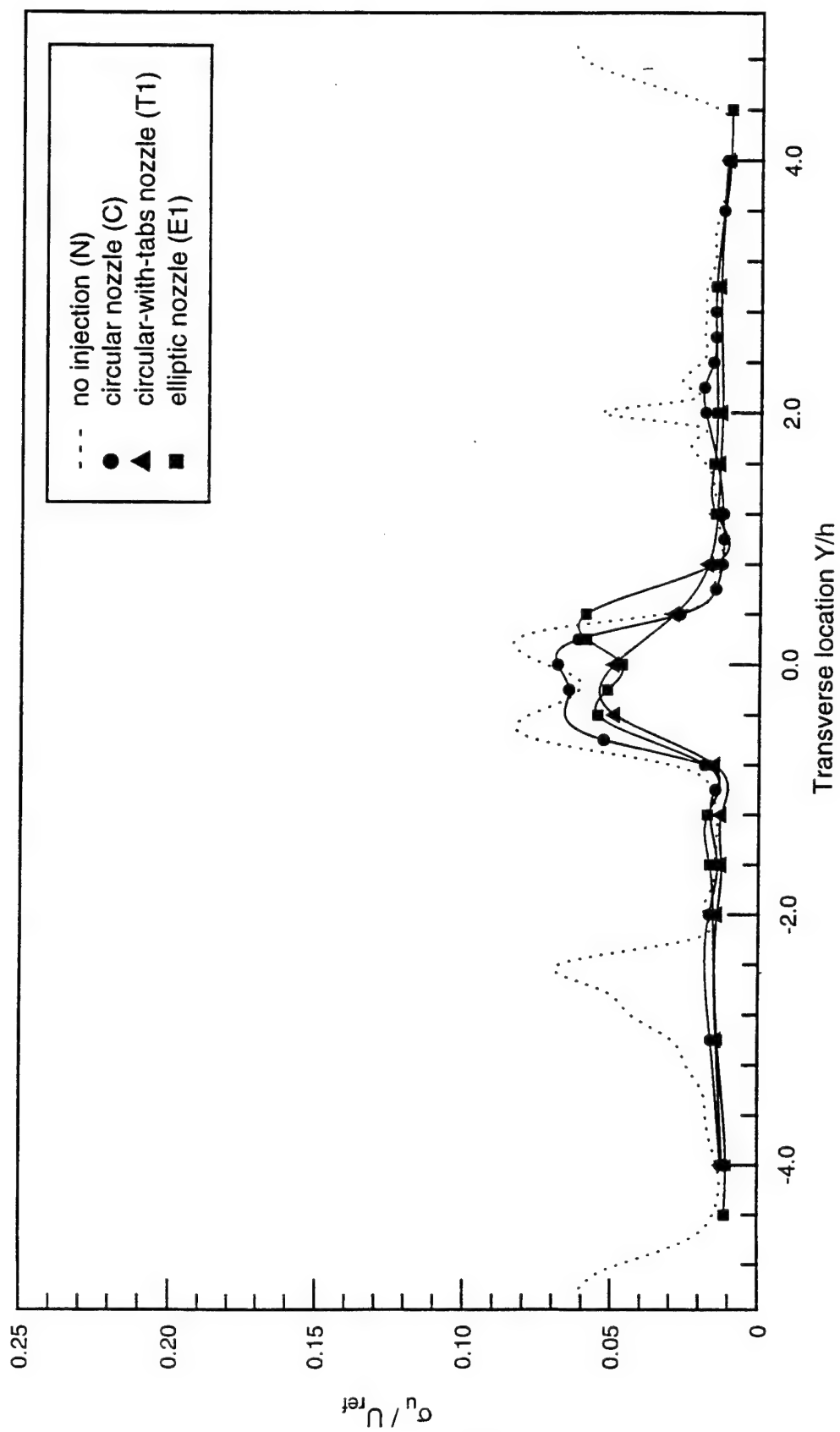


Figure 5.88 Streamwise turbulence intensity in (X,Y) plane at $X/h=6.8$ for all cases.

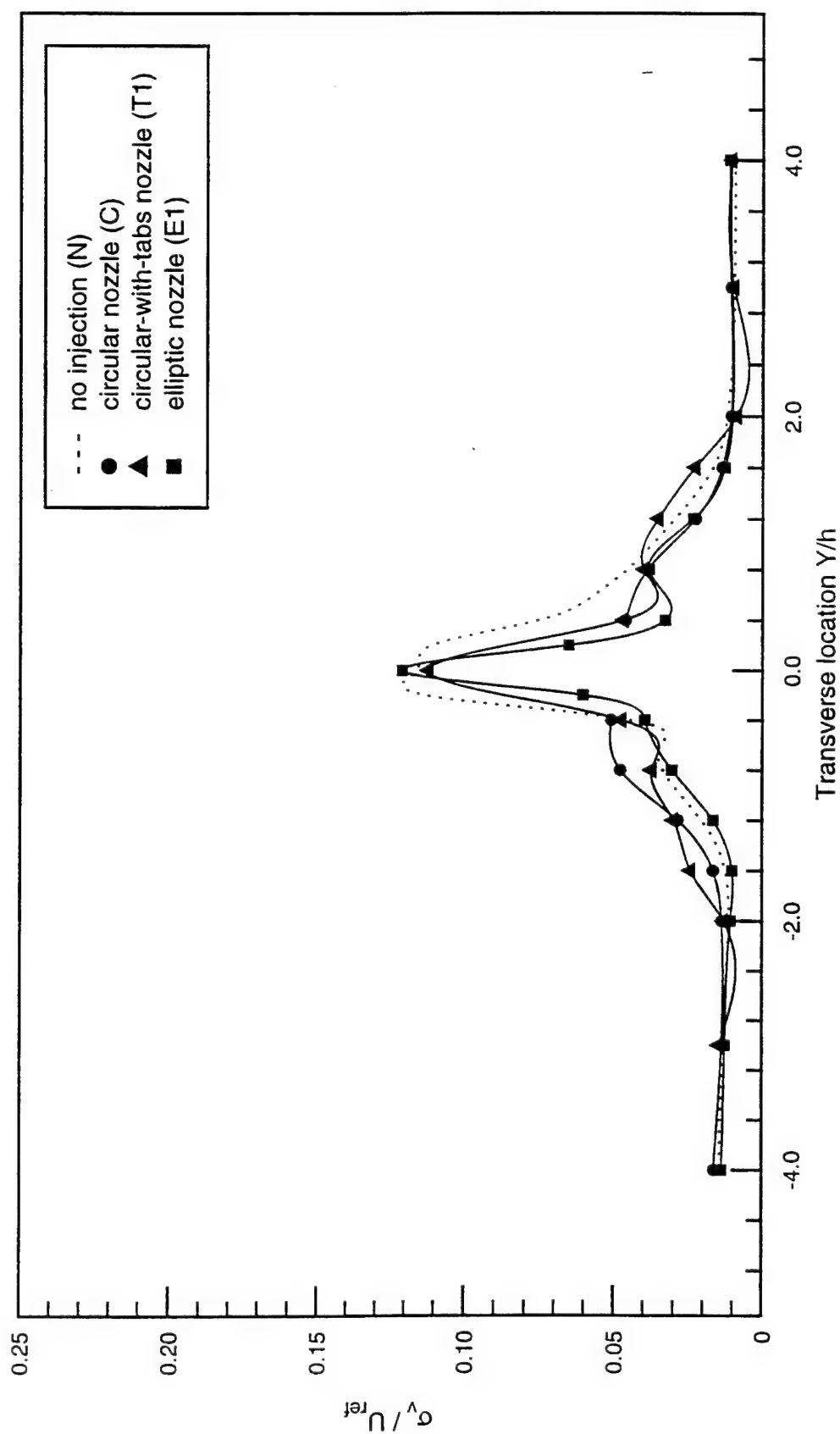


Figure 5.89 Transverse turbulence intensity in (X,Y) plane at $X/h=2$ for all cases.

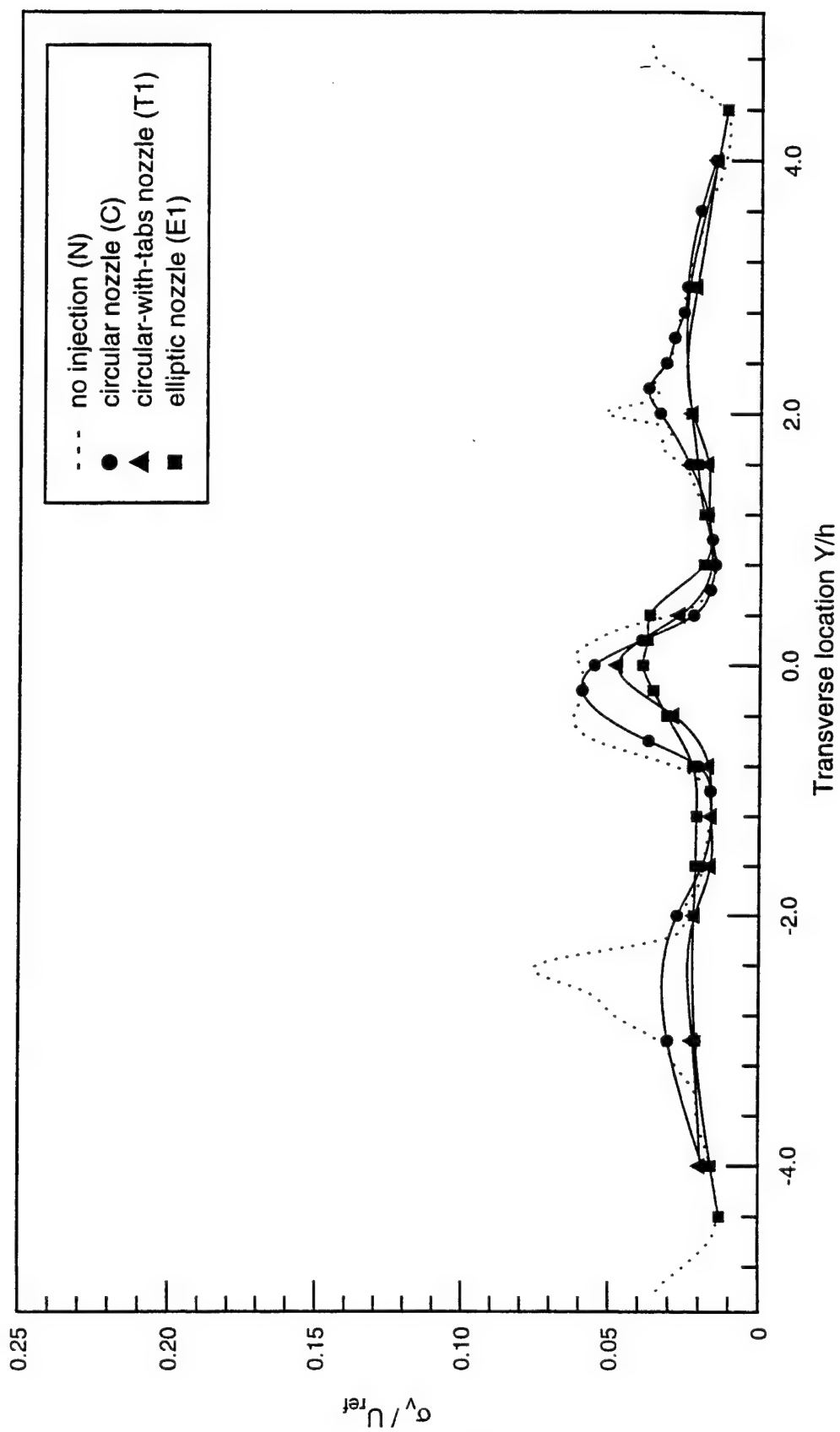


Figure 5.90 Transverse turbulence intensity in (X,Y) plane at $X/h=6.8$ for all cases.

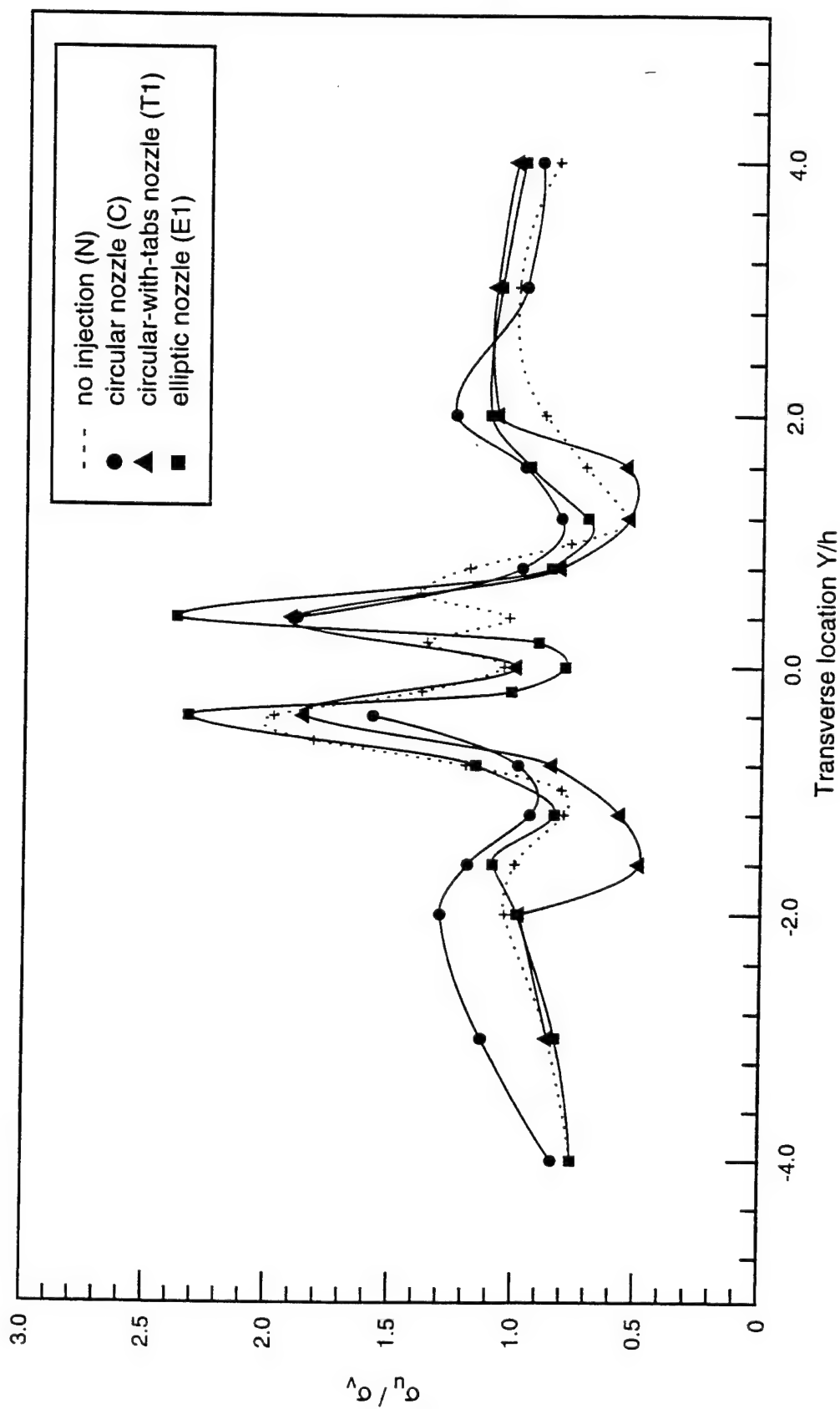


Figure 5.91 Ratio of streamwise to transverse turbulence intensities in (X, Y) plane at $X/h=2$ for all cases.

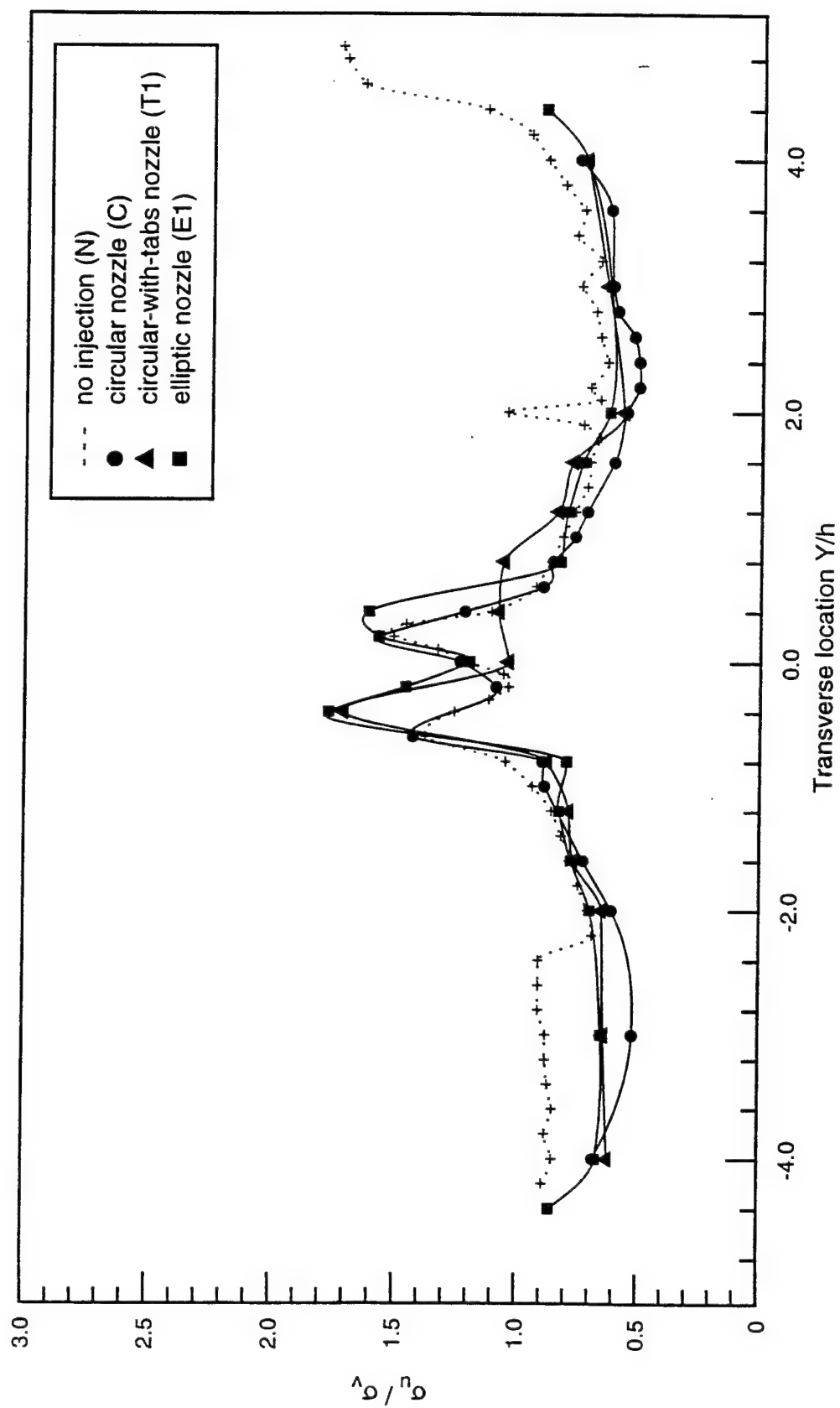


Figure 5.92 Ratio of streamwise to transverse turbulence intensities in (X, Y) plane at $X/h=6.8$ for all cases.

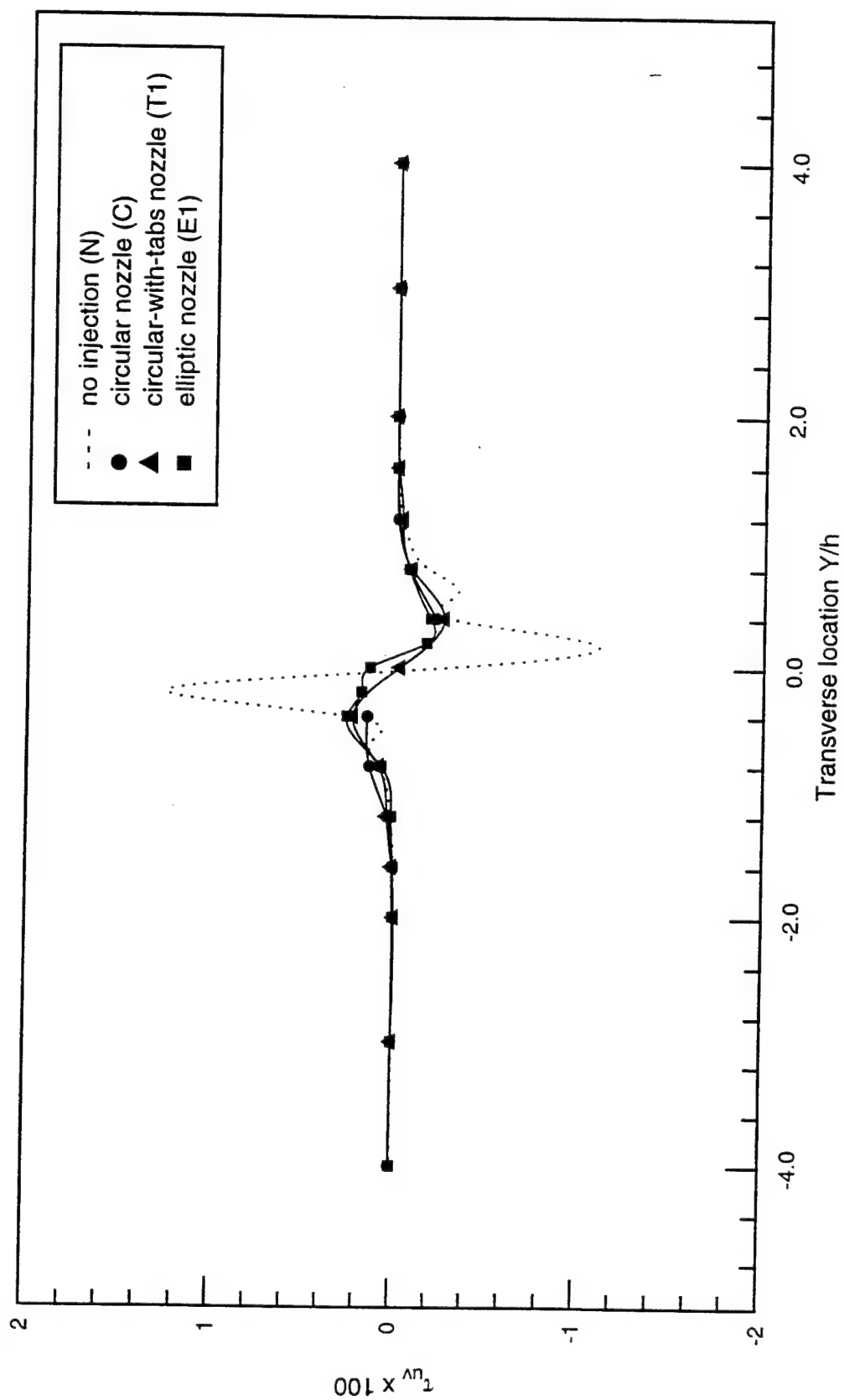


Figure 5.93 Turbulent shear stress in (X, Y) plane at $X/h=2$ for all cases.

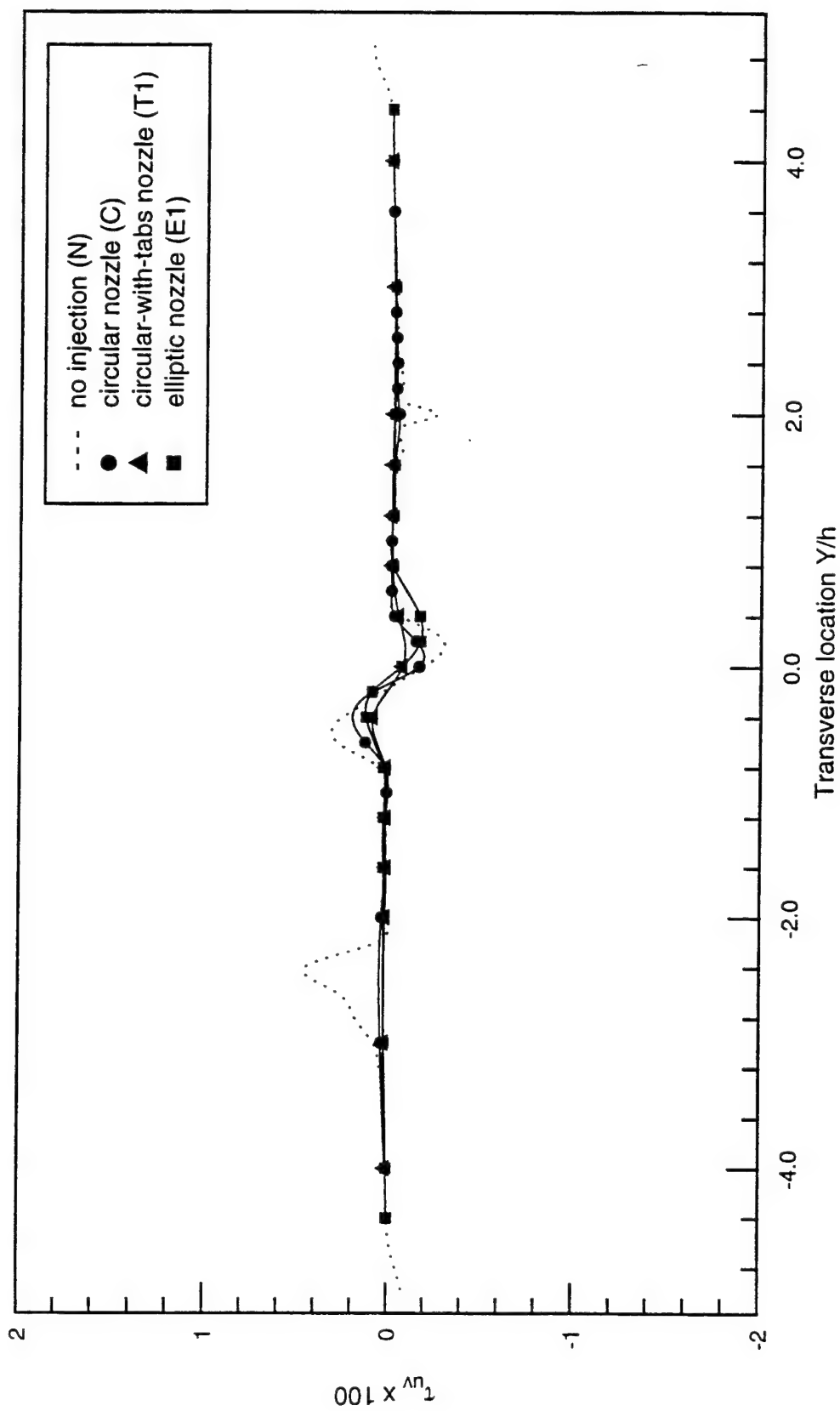


Figure 5.94 Turbulent shear stress in (X,Y) plane at $X/h=6.8$ for all cases.

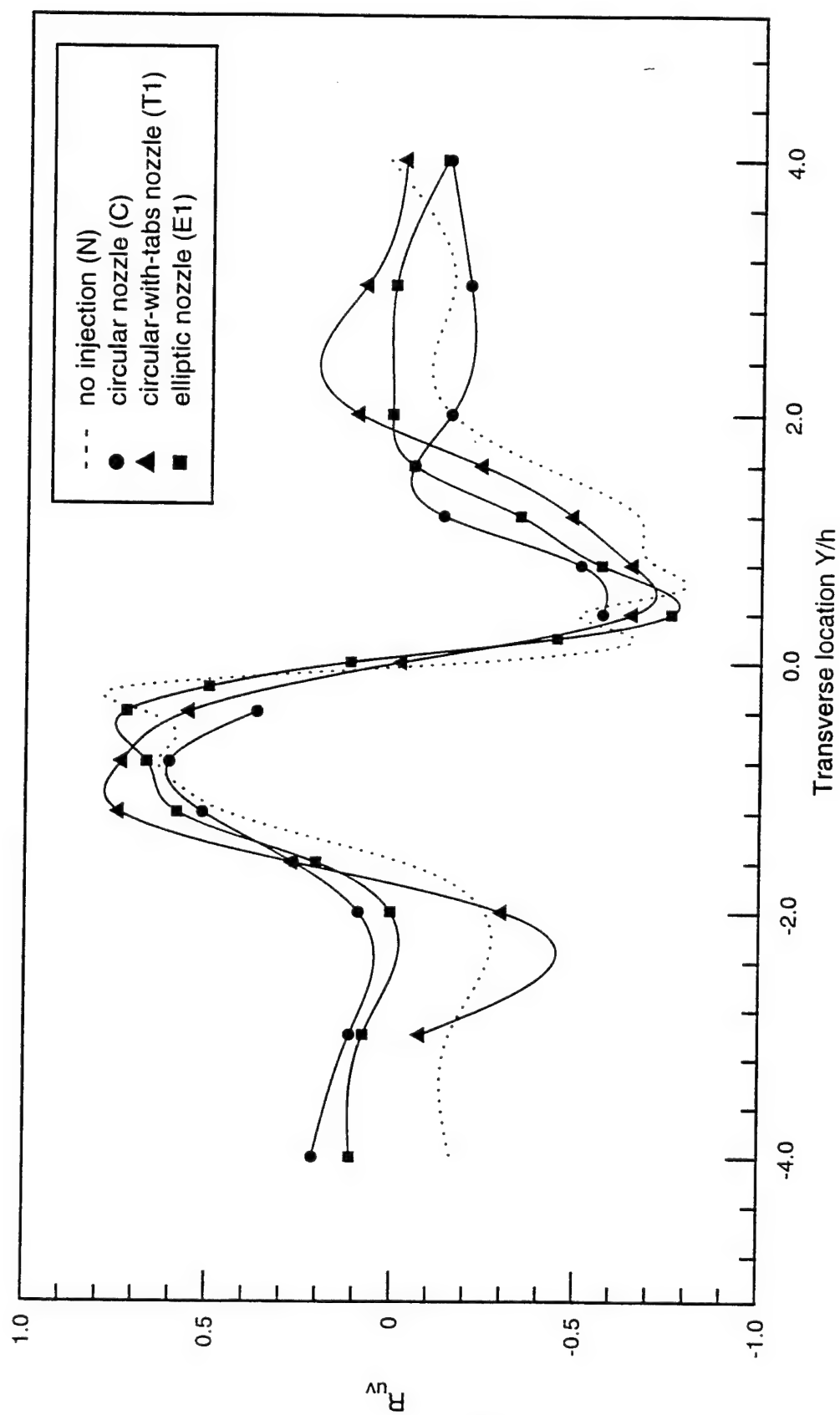


Figure 5.95 Shear stress correlation coefficient in (X,Y) plane at $X/h=2$ for all cases.

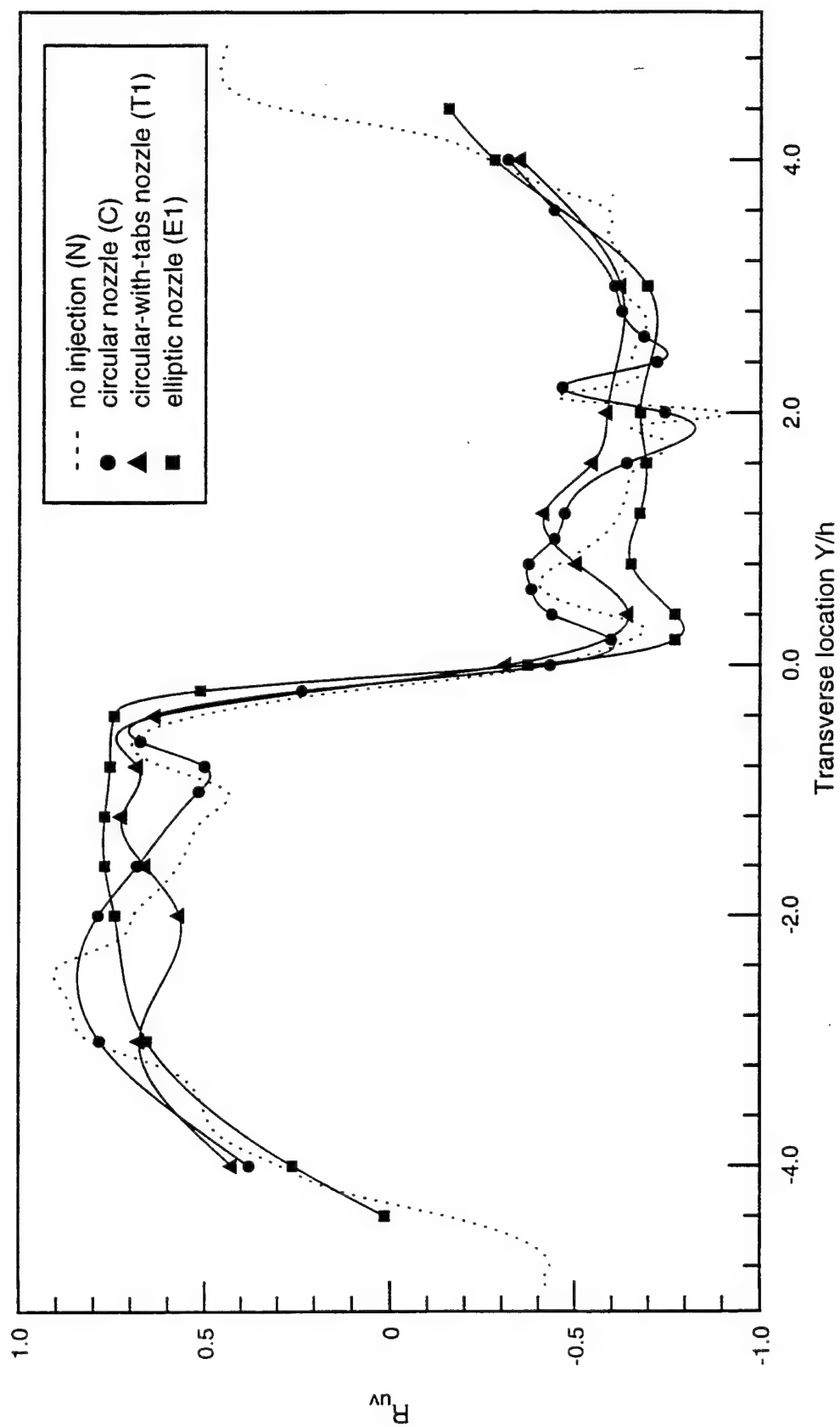


Figure 5.96 Shear stress correlation coefficient in (X,Y) plane at $X/h=6.8$ for all cases.

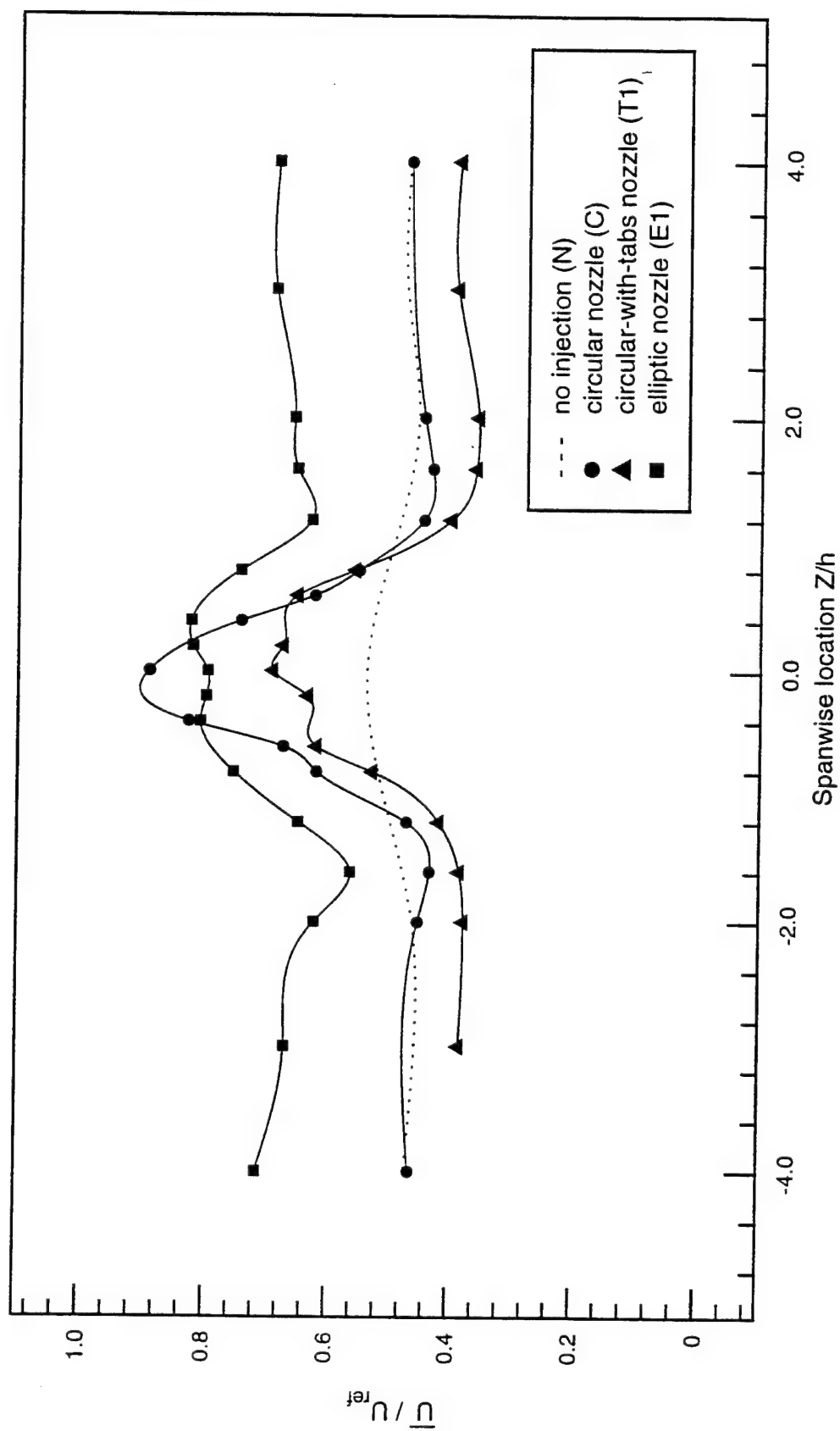


Figure 5.97 Normalized mean streamwise velocity in (X,Z) plane at $X/h=2$ for all cases.

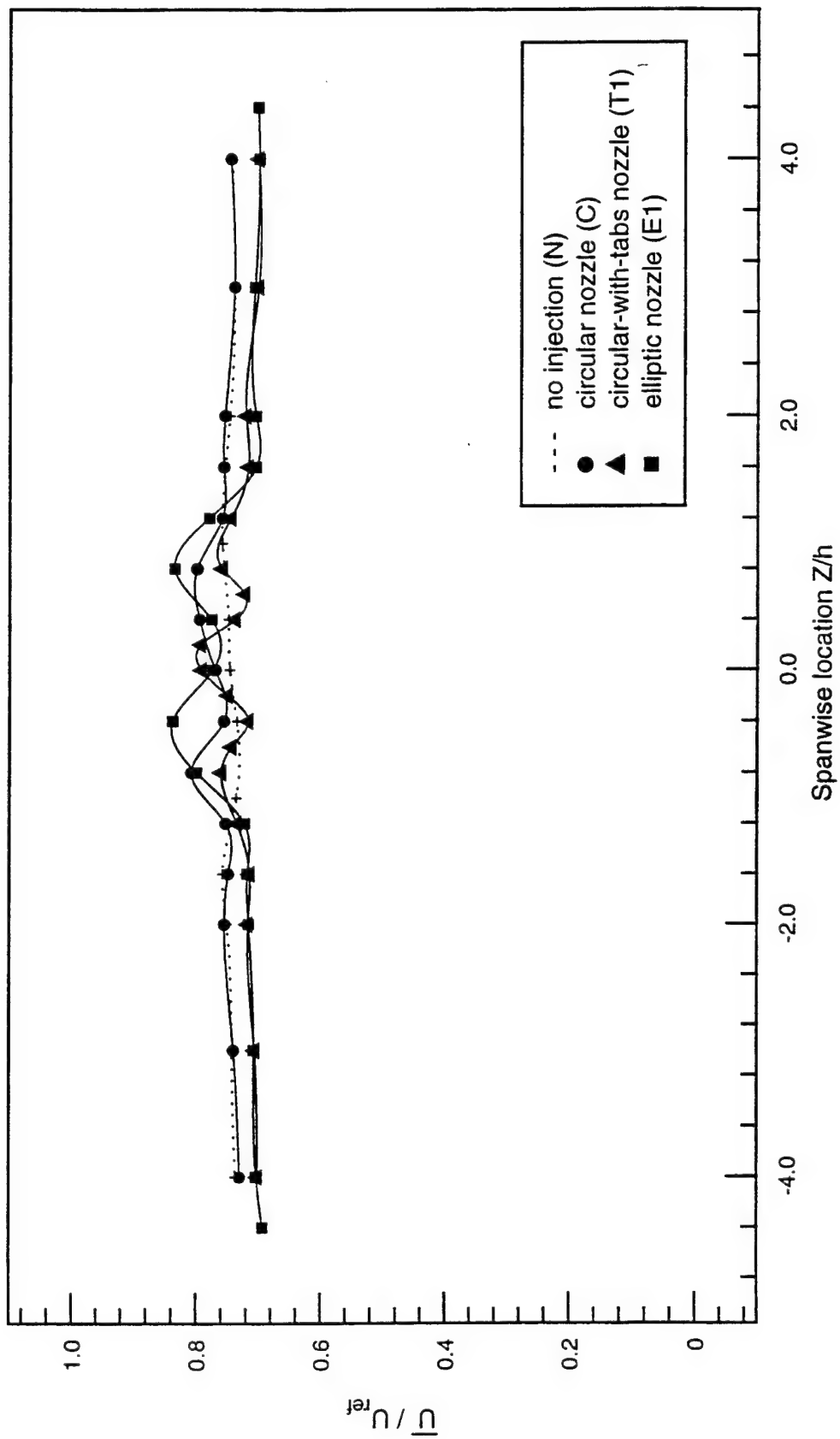


Figure 5.98 Normalized mean streamwise velocity in (X,Z) plane at $X/h=6.8$ for all cases.

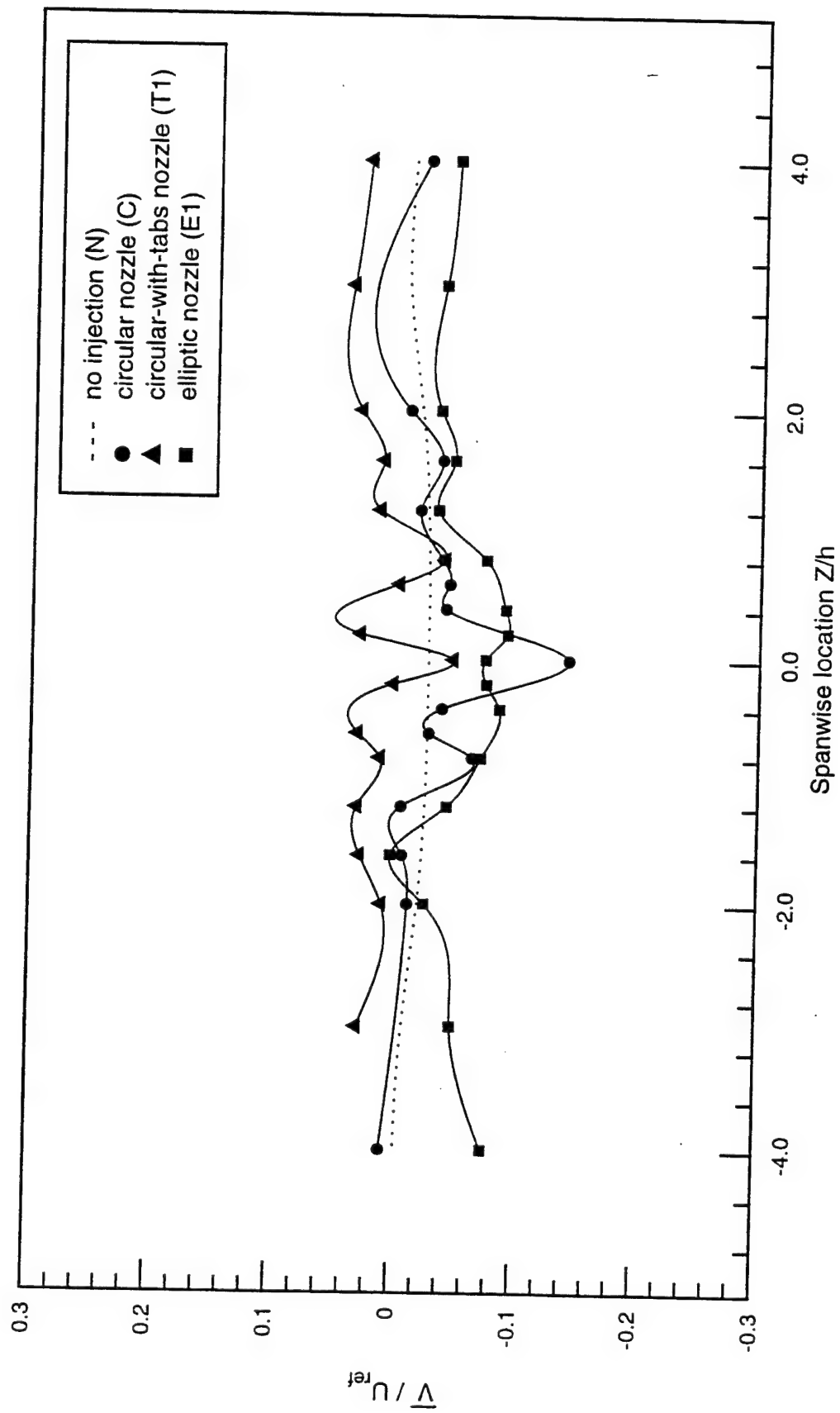


Figure 5.99 Normalized mean transverse velocity in (X,Z) plane at $X/h=2$ for all cases.

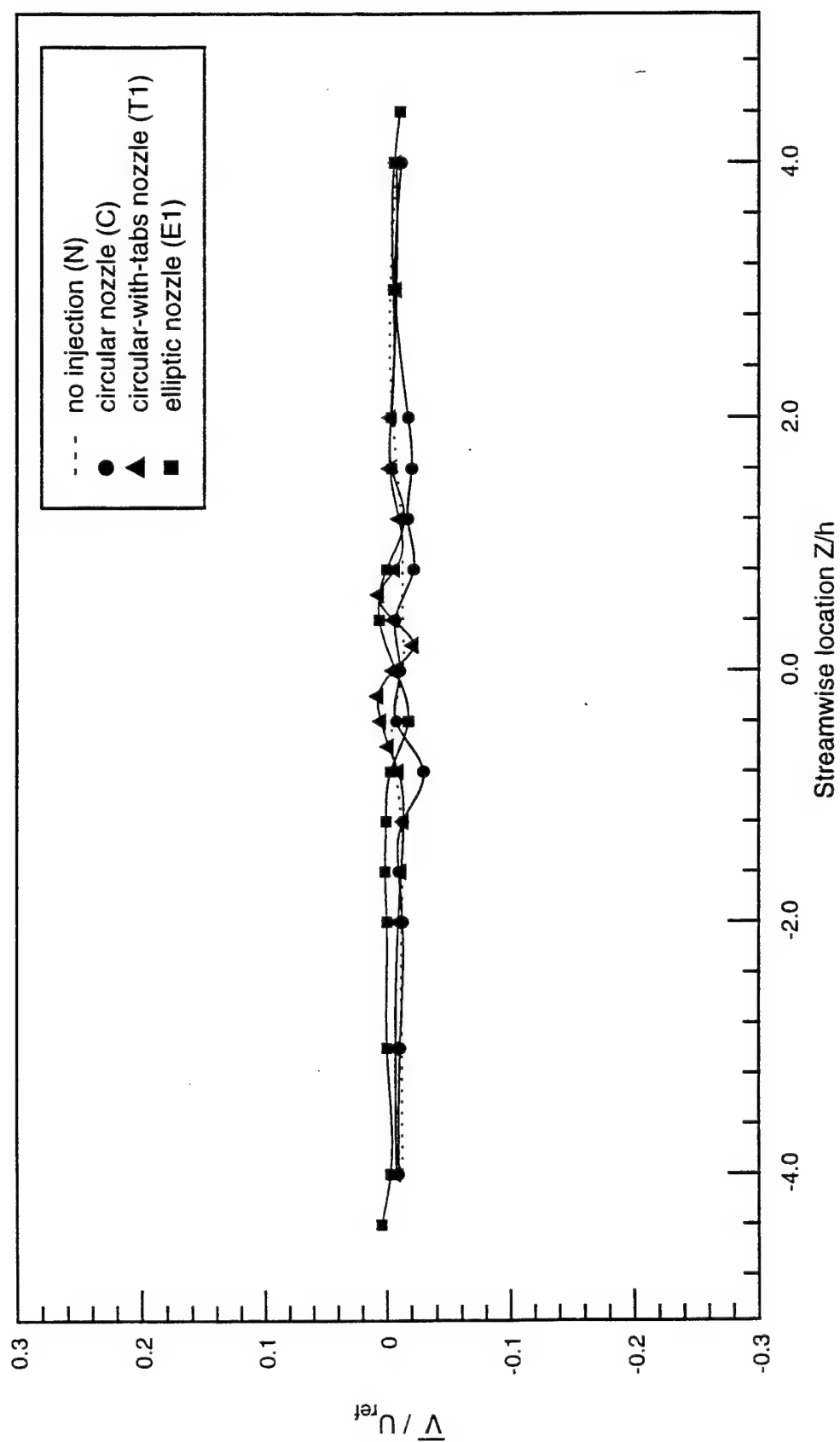


Figure 5.100 Normalized mean transverse velocity in (X,Z) plane at $X/h=6.8$ for all cases.

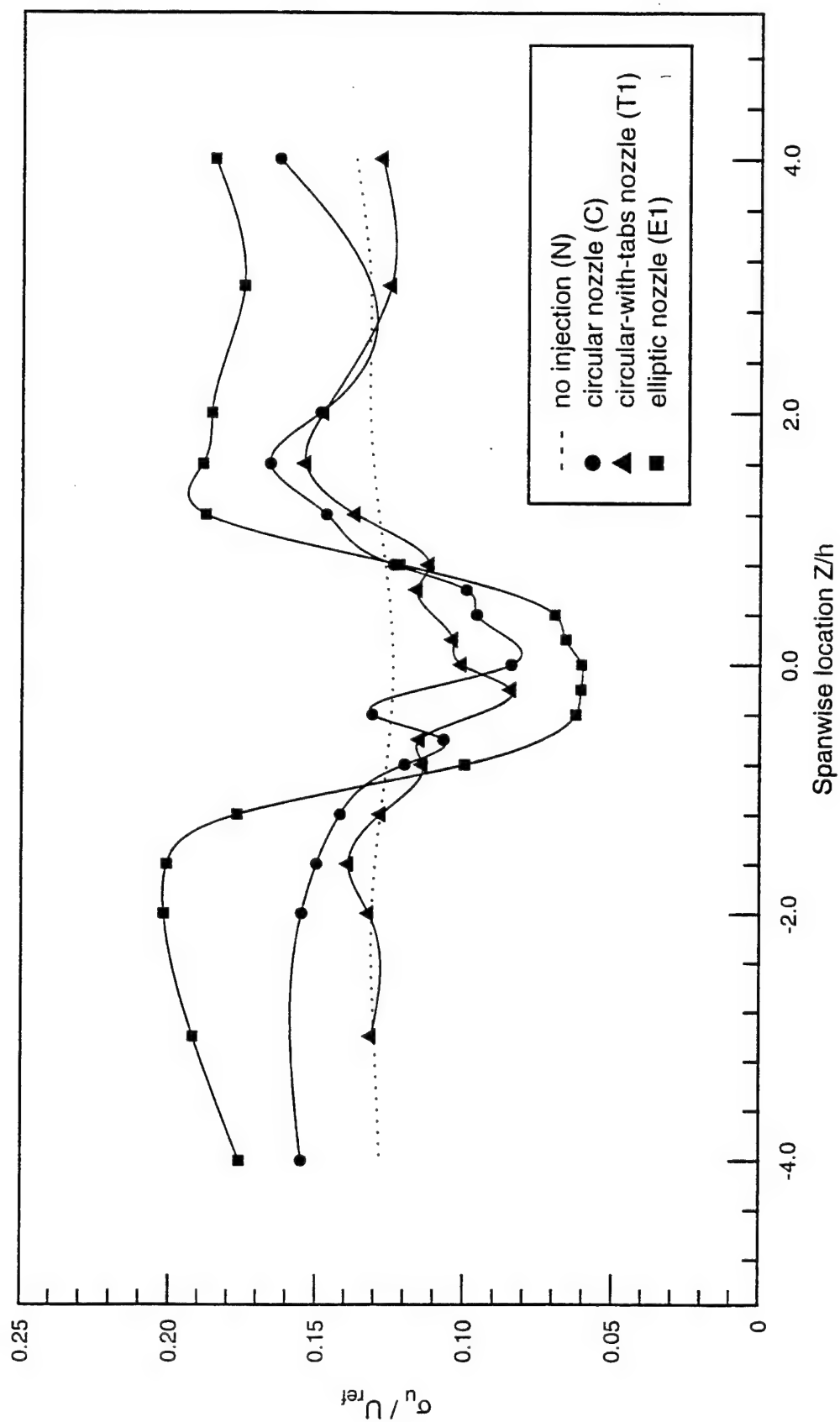


Figure 5.101 Streamwise turbulence intensity in (X,Z) plane at $X/h=2$ for all cases.

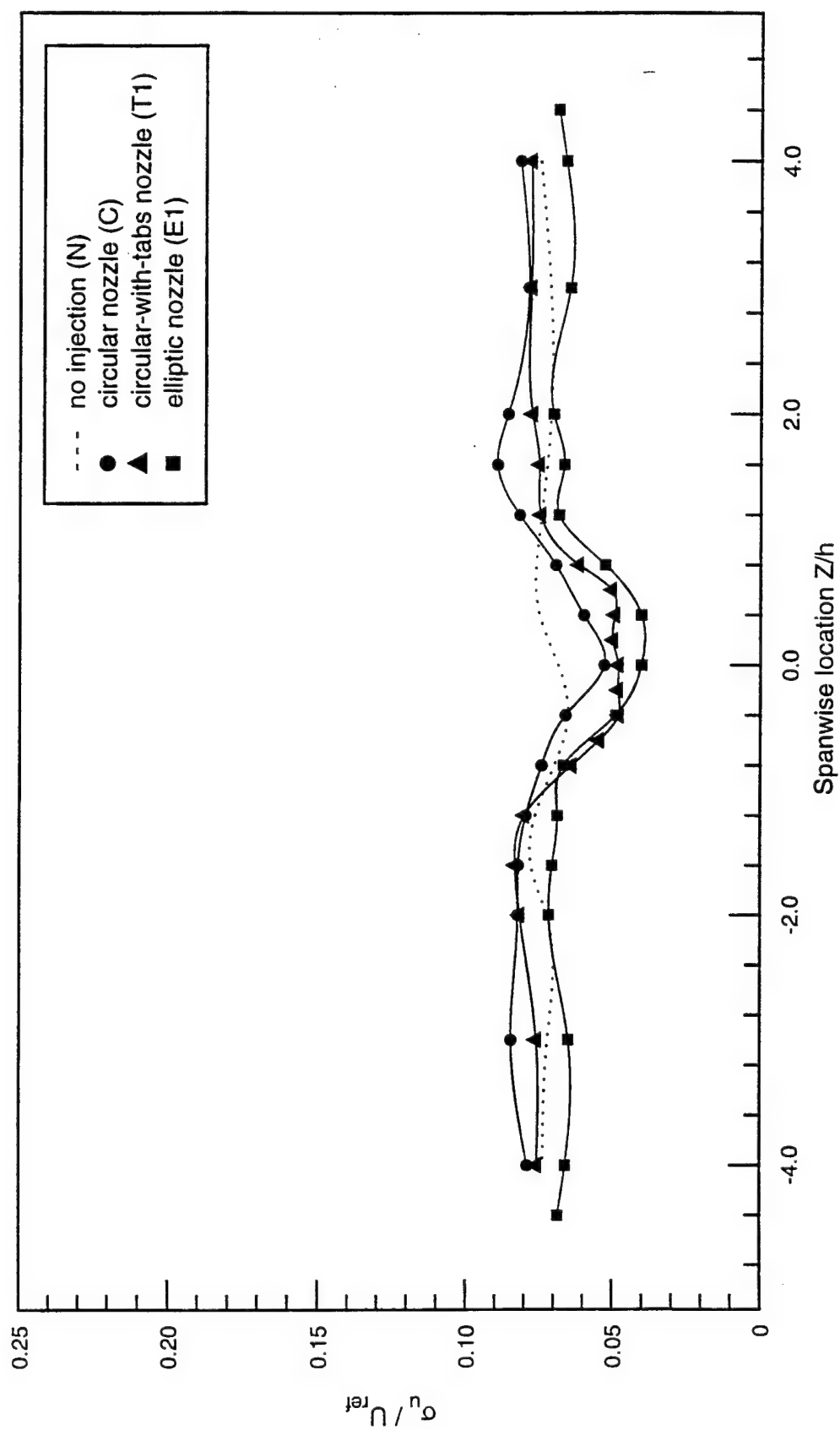


Figure 5.102 Streamwise turbulence intensity in (X,Z) plane at $X/h=6.8$ for all cases.

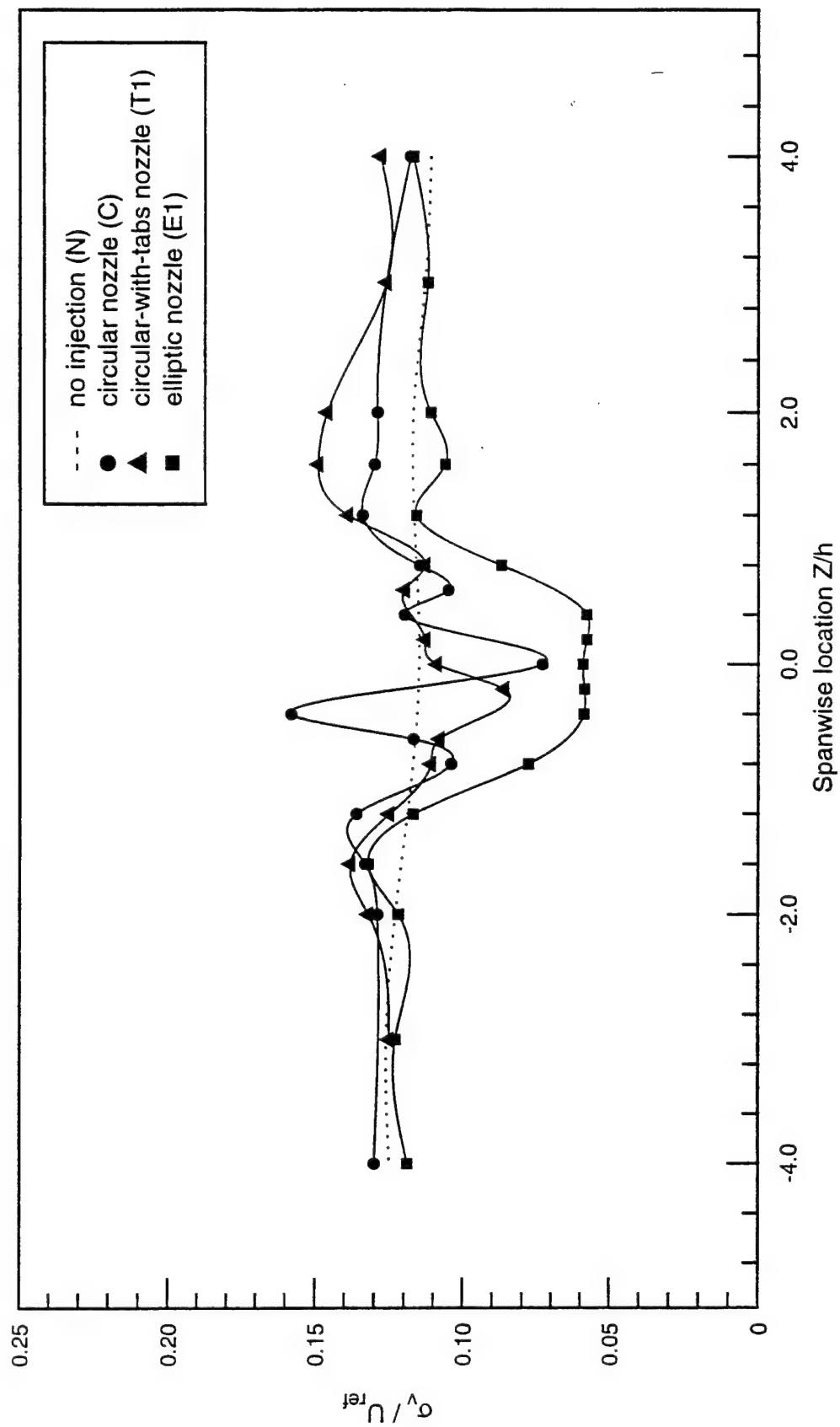


Figure 5.103 Transverse turbulence intensity in (X,Z) plane at $X/h=2$ for all cases.

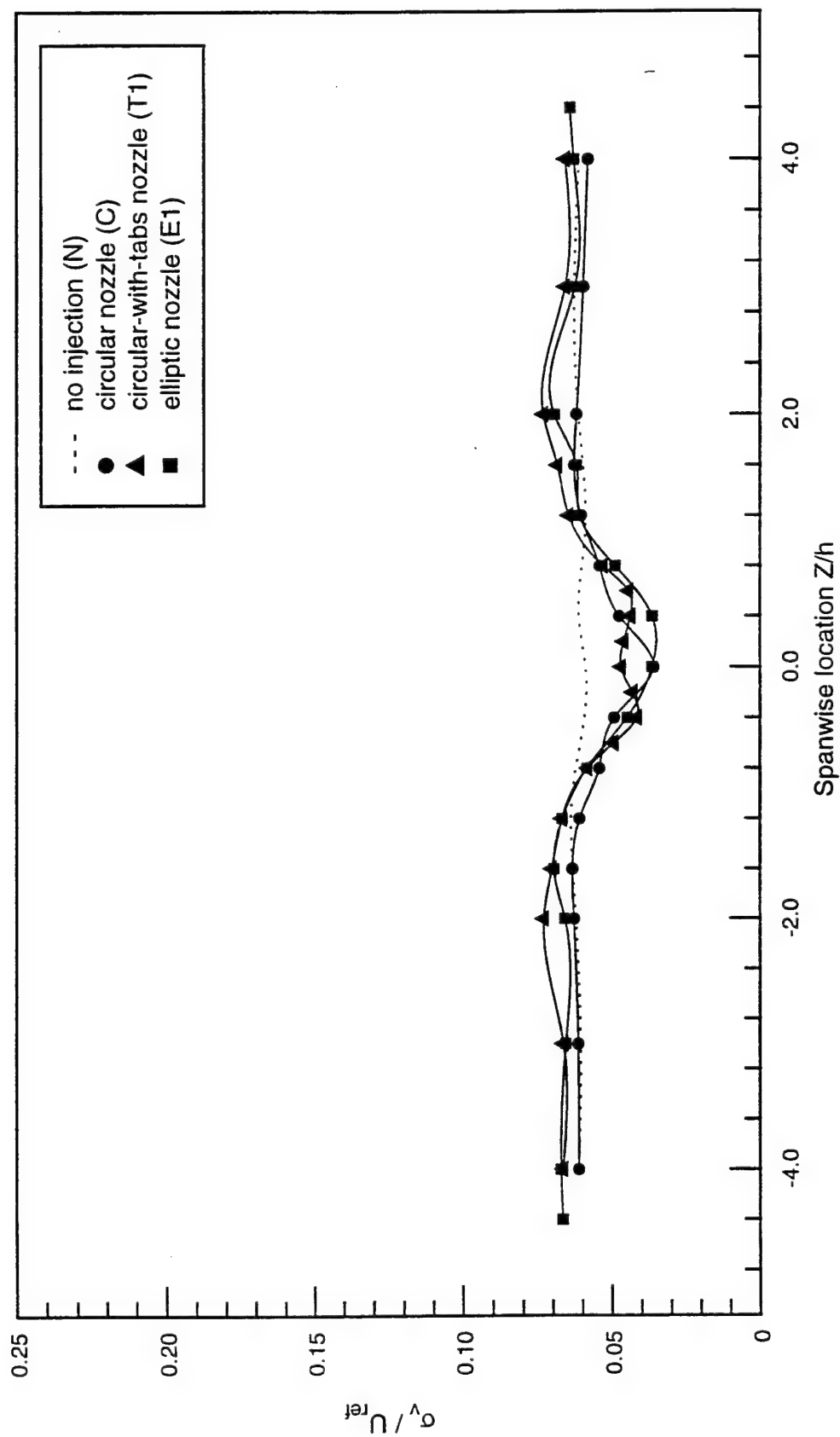


Figure 5.104 Transverse turbulence intensity in (X,Z) plane at $X/h=6.8$ for all cases.

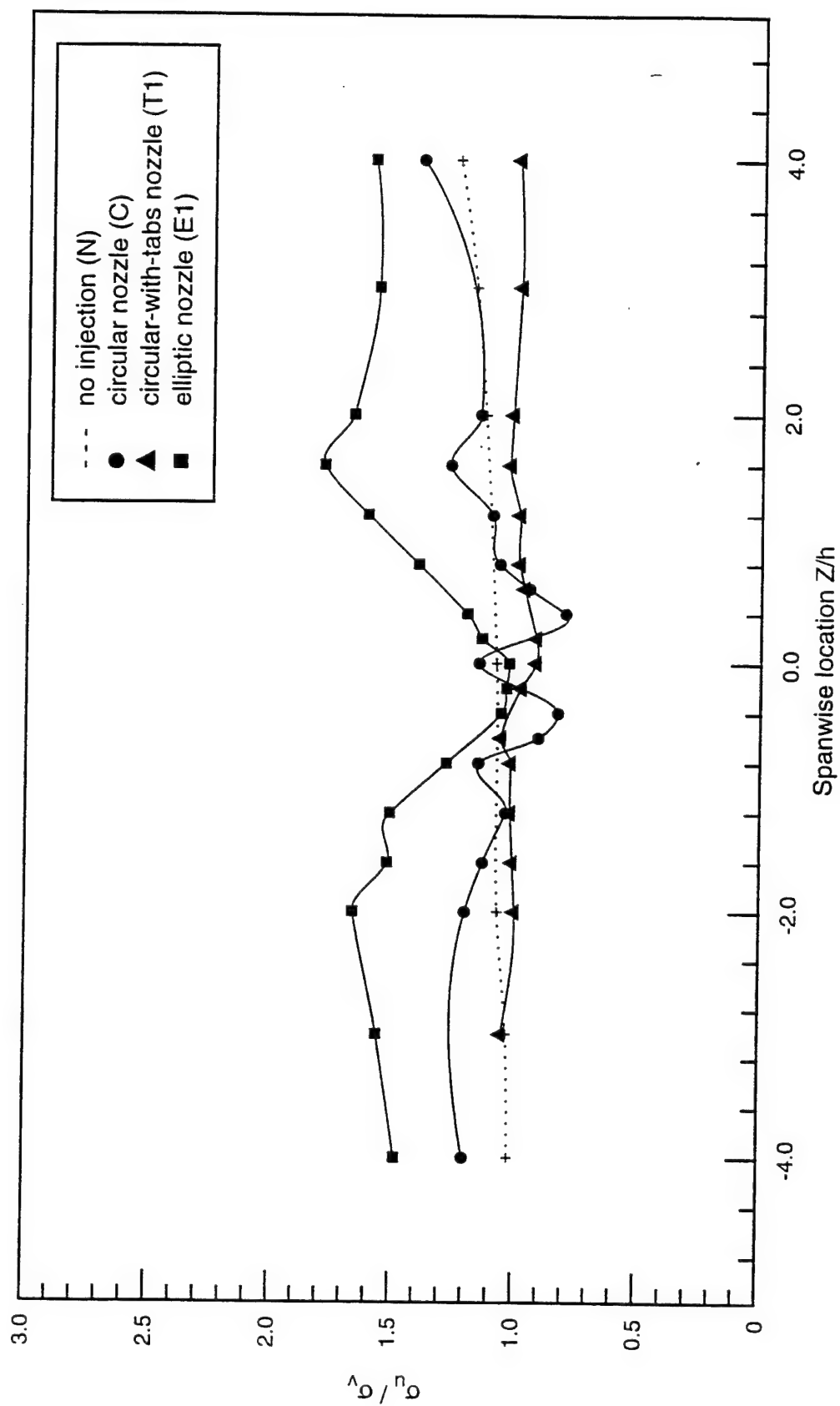


Figure 5.105 Ratio of streamwise and transverse turbulence intensities in (X,Z) plane at $X/h=2$ for all cases.

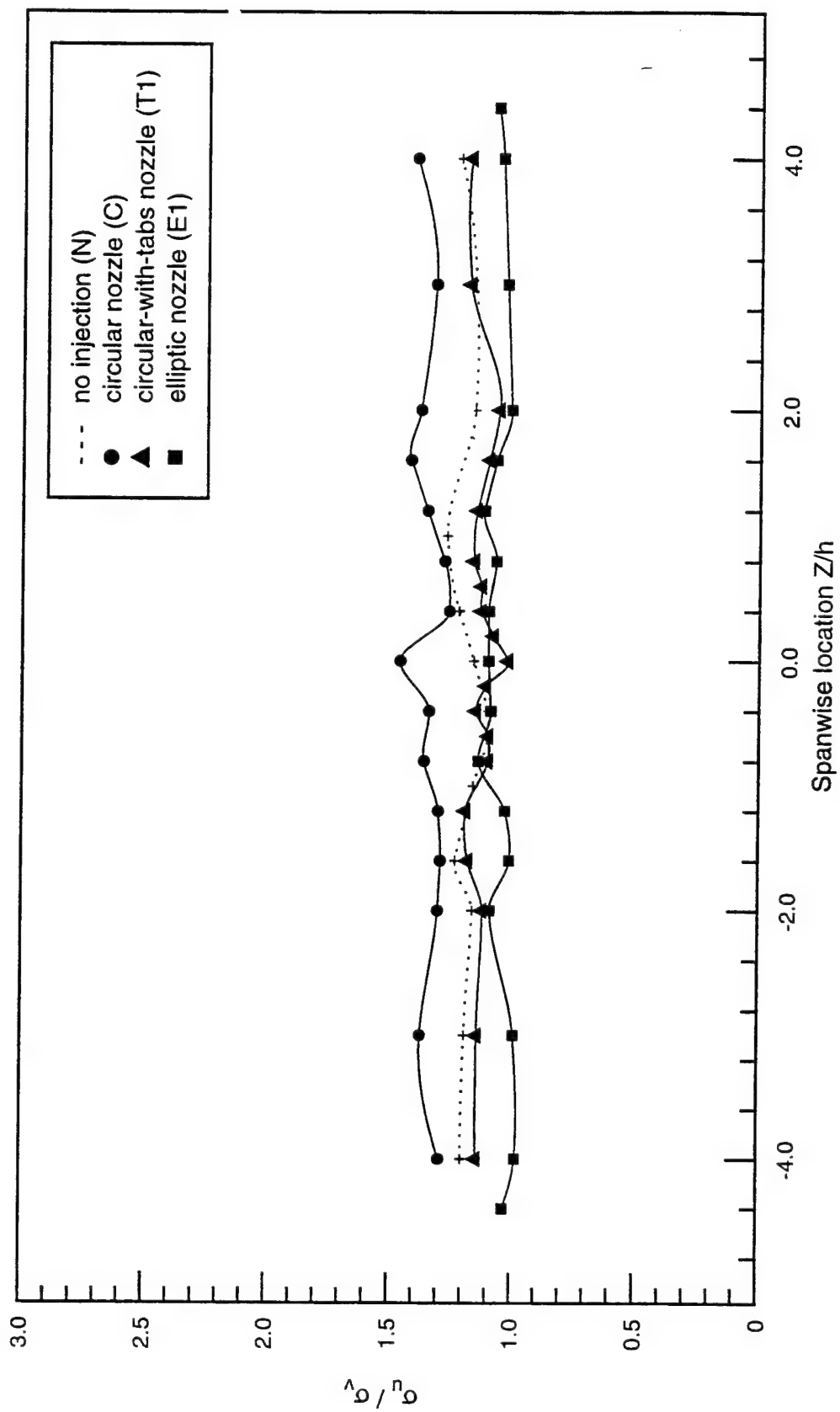


Figure 5.106 Ratio of streamwise and transverse turbulence intensities in (X,Z) plane at $X/h=6.8$ for all cases.

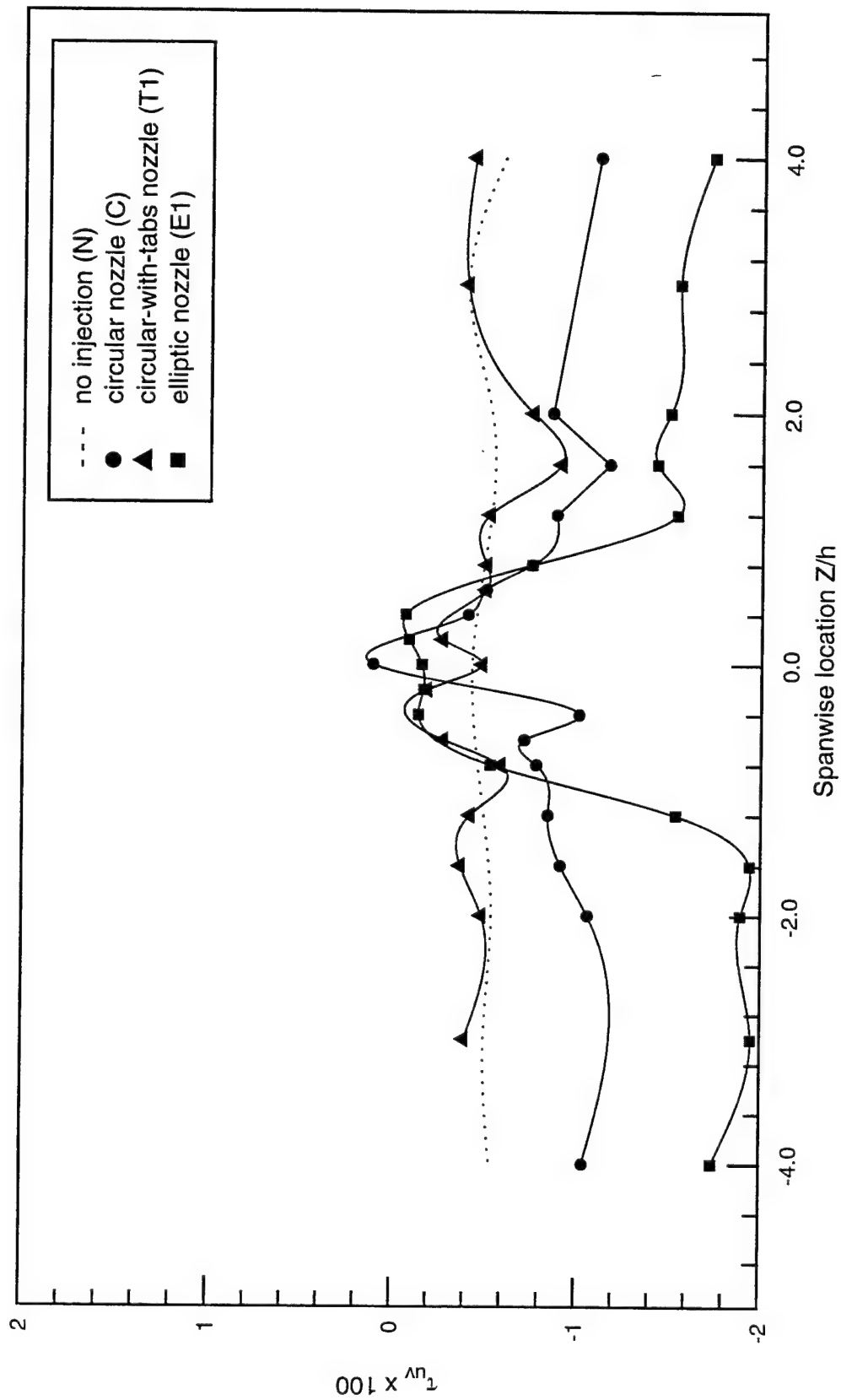


Figure 5.107 Turbulent shear stress in (X,Z) plane at $X/h=2$ for all cases.

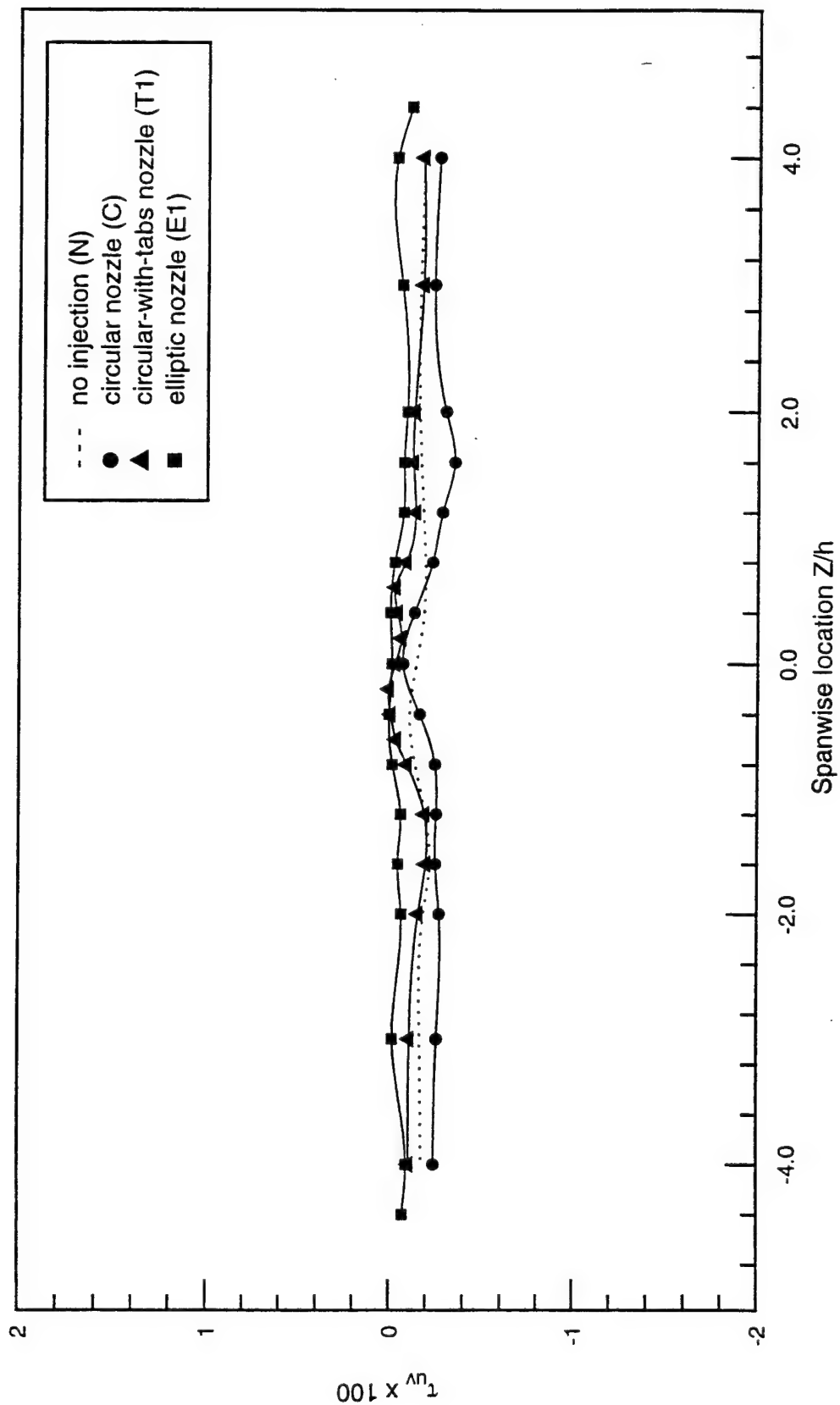


Figure 5.108 Turbulent shear stress in (X,Z) plane at $X/h=6.8$ for all cases.

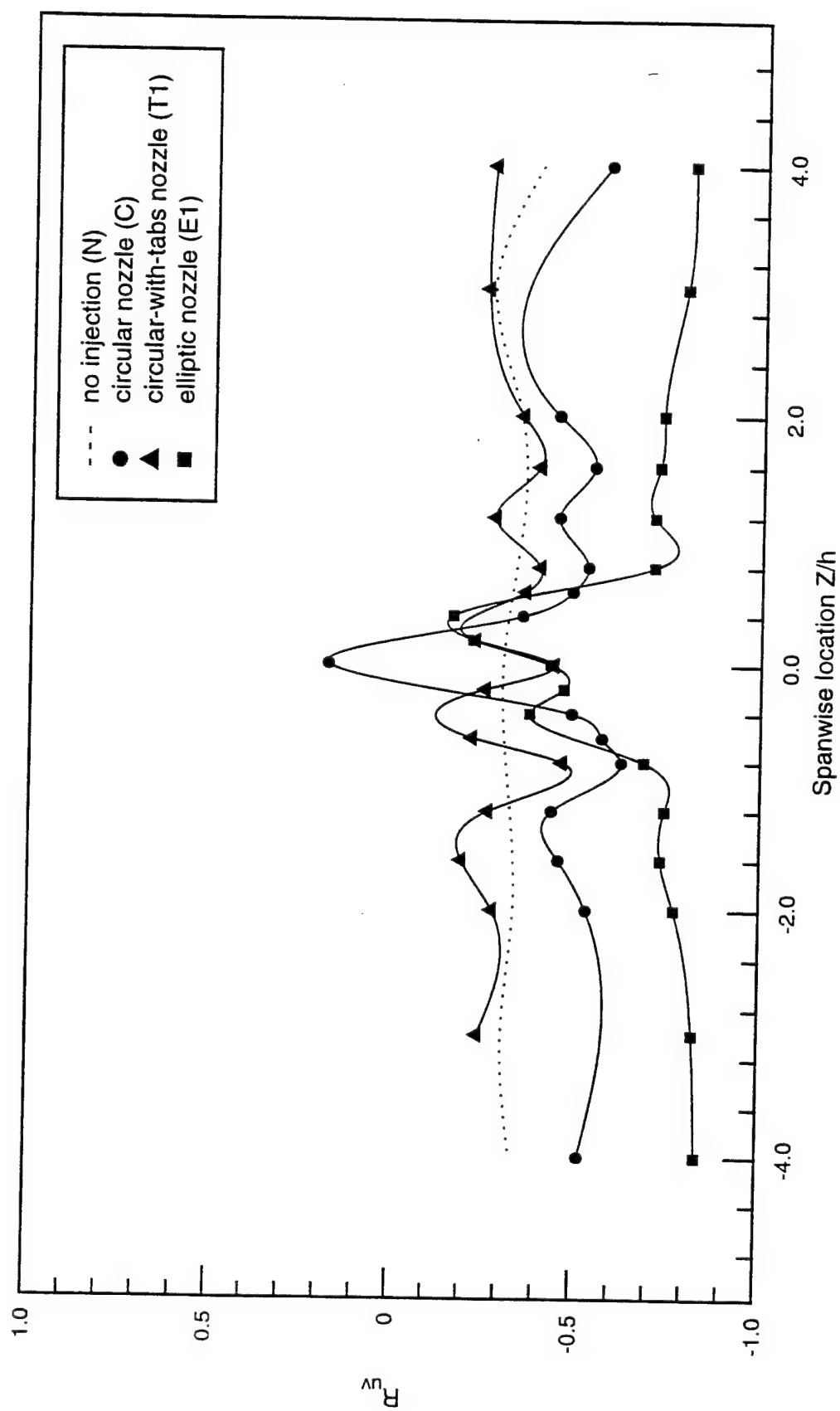


Figure 5.109 Shear stress correlation coefficient in (X,Z) plane at $X/h=2$ for all cases.

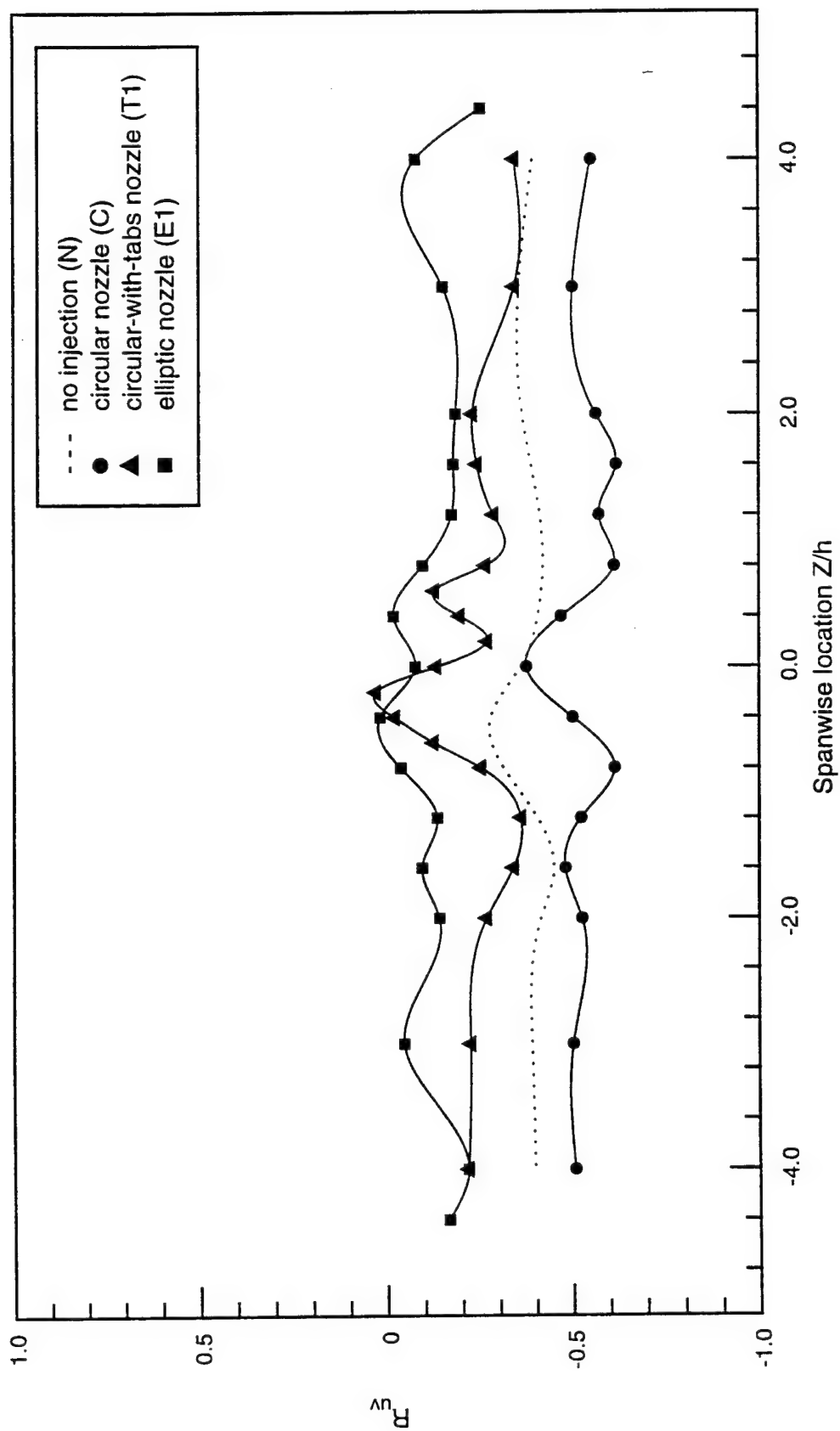


Figure 5.110 Shear stress correlation coefficient in (X,Z) plane at $X/h=6.8$ for all cases.

CHAPTER 6

SUMMARY AND CONCLUSIONS

The flow field without injection was examined to establish a reference case against which the flow field with helium injection from the various nozzle geometries could be evaluated. Laser Doppler Velocimetry (LDV) measurements show the incoming freestream flow to be uniform and symmetric above and below the strut with a calculated Mach number of 1.92 and turbulence intensity of roughly 1%. The boundary layer thickness (δ) was determined to be 5.6 mm with a peak streamwise turbulence intensity of about 7%. Reverse streamwise velocities up to 8% of the freestream velocity were detected in the recirculation zone at $X/h = 1$. Due to a coarse measurement grid a maximum reverse velocity was not obtained. The recirculation zone extends to about $X/h = 1.1$, where the two mixing layers formed between the primary freestream flow and the recirculating flow merge. The angle of the slipline at the boundary of the recirculation zone detected from the LDV data (18°) matches the angle visually approximated from Rayleigh/Mie scattering images. As the mixing layers merge, the flow is compressed and two recompression shock waves are formed. The flow field behind the base of the strut exhibits high turbulence intensities (maximum $\sigma_u/U_{ref} = 0.23$) in the recompression region and a drastic decrease in turbulence intensities downstream. Also present are expansion waves emanating from the top and bottom shoulder of the base of the strut. The predicted angles of the leading and trailing expansion waves, emanating from the top and bottom shoulders of the base, using Prandtl-Meyer theory match the angles apparent on the schlieren photograph.

For the injection cases, helium exits the nozzle into a low velocity, low pressure recirculation zone which approximates underexpanded free jet conditions. When the jet encounters the mixing layers formed between the primary freestream flow and the recirculating fluid at the base of the strut, it experiences azimuthal variation in pressure and velocity gradients, as well as turbulent mixing around its perimeter. This is unlike the free jet case, where gradients are axisymmetric. Azimuthal variation is illustrated by the mean streamwise velocity profiles in the (X,Y) and (Y,Z) planes. The velocity in the freestream adjacent to the top and bottom segments of the jet is higher than the velocity in the jet proper, while the velocity in the wake flow on the spanwise sides of the jet is lower than the velocity in the jet proper.

The mixing interaction between the jet and the primary flow occurs within the confines of the region which is marked by the wake in the flow without injection. Thus the jets exhibit limited spread in the transverse (Y) direction, which limits mixing with the primary freestream flow. It is likely that compressibility affecting the top and bottom segments of the jet is responsible for the limited transverse spread of the jet into the freestream flow. However, the various nozzle geometries [circular (C), circular-with-tabs (T1, T2, T3) and elliptic (E1, E2, E3)] create different mixing dynamics, which affects the overall mixing of the helium in the jet with the air of the primary flow.

The axis-switching phenomenon apparent in free jets issuing from oblong nozzle geometries is apparent for the jets issuing from the elliptic nozzle (E1, E2, E3) in this study. However, interaction of the mixing layers with the jet appears to accelerate an axis switch in the E1 case, distort the axis switch in the E2 case, and retard the axis switch in the E3 case. The effect of the mixing layer on axis switching can be understood by considering an oblong free jet where the development of vorticity around the perimeter is believed to be primarily responsible for axis-switching. Likewise, bifurcation similar to that occurring in free jets issuing from a nozzle with two tabs is

clearly seen in the case of the elliptic jet in this study with the T1 orientation. The effect of the mixing layers on the bifurcation of the jet can be understood by considering the development of the pair of counter rotating, streamwise vortices which are generated by each tab and which engulf surrounding fluid, and by considering the ejection of jet fluid into the surrounding fluid by the radial component of velocity perpendicular to the nozzle diameter connecting the two tabs. The orientation of the nozzle relative to the mixing layer dictates whether the mixing layer characteristics reinforces or suppresses the jet development observed in free jets.

Visual inspection of the instantaneous and average Rayleigh/Mie scattering images, particularly those of the face-on (Y,Z) plane of view, suggests that the T1 jet mixes most effectively, followed by the E1 case with the T3, T2 and C cases incurring the least effective mixing. In agreement with the LDV streamwise velocity profiles, the Rayleigh/Mie images show the E1 case to spread the most in the spanwise (Z) direction but the E1 jet remains coherent as compared to the T1 case, which incurs more mixing. The LDV profiles in the (X,Z) plane at $X/h = 2$ for the E1 case show noticeably elevated values of \overline{U} , σ_u/U_{ref} and τ_{uv} in the wake region on the spanwise sides of the jet proper. This suggests that the jet in the E1 case has a substantial effect on the wake flow near the base of the strut, which may enhance age mixing or back mixing of whole or partially burned gases into the fuel/air mixture to sustain combustion, i.e., flame holding.

The mixing effects of the various nozzle geometries were evaluated using a shape factor and mixedness index. A shape factor parameter was used to describe the convolutedness of the jet perimeter relative to a circular jet. The value of the shape factor indicates the mixing potential of the jet in terms of the presence of large-scale structures and the area of the interface between the jet and the primary fluid. Large-scale structures impart energy to smaller structures through the energy cascade process, and the interfacial area provides the opportunity for small scale viscous mixing -- both ultimately

leading to the small-scale mixing required for efficient combustion. The shape parameter at $X/h = 2$ and 4 , in conjunction with values of jet area, showed that the T1 jet offered the most mixing potential and that the T3 and E3 offered the least mixing potential of the cases in this study. These results are consistent with the conclusions drawn from the Rayleigh/Mie scattering images.

The shapes of the jets are very distinct at $X/h = 1, 2$, and 4 and become less distinct downstream at $X/h = 6.8$ and 10 , as the large mixing structures break down into smaller scale structures. Therefore, a mixedness index was developed and used to characterize the small-scale mixing at the furthest downstream station in order to compare relative mixing between the jets. The T1 and E1 cases appeared to approach full mixing, while the T3 and E3 cases remain fairly unmixed. Thus the case exhibiting the highest mixing potential just downstream of the base (largest shape factor) can be seen to produce the most fully mixed jet downstream. Likewise, the cases exhibiting low mixing potential (small shape factor) produce unmixed jets.

The LDV results show that the streamwise turbulence intensity is larger than the transverse turbulence intensity in the mixing regions of both the flow without injection and the injection cases. This signifies that the turbulent transport in the streamwise direction is superior to that in the transverse direction. Although transport in the streamwise direction may be beneficial to back mixing in combustion, turbulent transport in the transverse direction is desirable for mixing between the jet and the primary freestream flow. Thus the nature of the mixing regions in this study is not conducive to effective mixing of the jet with the freestream.

The transition between mixing dominated by large-scale effects near the base of the strut and mixing dominated by small-scale effects further downstream is suggested by several factors. First, the distinct LDV profiles at $X/h = 2$ become uniform by $X/h = 6.8$, signifying that the bulk of the mixing occurs upstream of $X/h = 6.8$. Second, the velocity

distribution for the circular (C) case shows a transition point somewhere between $X/h = 6$ and 7, signifying a decrease in mixing activity. Similarly, a large structure appearing as a “lobe” on the circular (C) jet in the face-on view Rayleigh/Mie scattering images at $X/h = 1, 2,$ and 4 is not apparent at $X/h = 6.8$, signifying that the large scale structures diminish by $X/h = 6.8$.

The complex interaction of the jet and the surrounding primary flow, especially in the spanwise direction, behind the strut near the base, warrants further study. Three-component LDV would be a promising candidate for such data collection. Since the wake formed by the strut is such an overwhelming factor in the mixing of the jet with the freestream in this configuration, the modification of the strut to alter the wake flow may prove fruitful. Furthermore, a detailed set of experiments in a simple free shear layer would permit further characterization of the mixedness index.

CHAPTER 7

REFERENCES

Abbitt, J.D. III, Hartfield, R.J., McDaniel, J.C. [1991] "Mole fraction imaging of transonic injection in a ducted supersonic flow," AIAA J., Vol. 29, No. 3, pp. 431-435.

Amatucci, V.A., Dutton, J.C., Kuntz, D.W., and Addy, A.L. [1992] "Two-stream, supersonic, wake flow field behind a thick base, part I: general features," AIAA J., Vol. 30, No. 8, pp. 2039-2046.

Arnette, S.A., Samimy, M., and Elliott, G.S. [1993a] "The effect of expansion on the large-scale structure of a compressible turbulent boundary layer," AIAA Paper 93-2991.

Arnette, S.A., Samimy, M., and Elliott, G.S. [1993b] "On streamwise vortices in high Reynolds number supersonic axisymmetric jets," Phys. Fluids A, Vol. 5, No. 1, pp. 187-202.

Barnsley, M. [1988] Fractals Everywhere. Academic Press, Inc., San Diego, CA.

Bell, J.H. and Mehta, R.D. [1990] "Development of a two-stream mixing layer from tripped and untripped boundary layers," AIAA J., Vol. 28, No. 12, pp. 2034-2042.

Bernal, L.P. [1981] "The coherent structure of turbulent mixing layers," Ph.D. dissertation. California Institute of Technology, CA.

Bernal, L.P., and Roshko, A. [1986] "Streamwise vortex structure in plane mixing layers," J. Fluid Mech., Vol. 170, pp. 499-525.

Bogdanoff, D.W. [1983] "Compressibility effects in turbulent shear layers," AIAA J., Vol. 21, No. 6, pp. 926-927.

Bradshaw, P. (ed.) [1987] Turbulence: topics in applied physics - Volume 12, Springer-Verlag, New York.

Breidenthal, R.E. [1981] "Structure in turbulent mixing layers and wakes using a chemical reaction," J. Fluid Mech., Vol. 109, pp. 1-24.

Brodkey, R.S. [1967] The phenomena of fluid motions, Chapter 14, Addison-Wesley, Reading, Massachusetts.

Brown, G.L., and Roshko, A. [1974] "On density effects and large structure in turbulent mixing layers," J. Fluid Mech., Vol. 64, pp. 775-816.

Carrol, B.F., Dutton, J.C., and Addy, A.L. [1986] "NOZCS2: a computer program for the design of continuous slope supersonic nozzles," University of Illinois at Urbana-Champaign, UILU ENG 86-4007.

Chandrsuda, C., and Bradshaw, P. [1981] "Turbulent structure of a reattaching mixing layer," J. Fluid Mech., Vol. 110, pp. 171 - 194.

Chen, M.H., Gaffney, R. Wu, P.K., and Nejad, A.S. [1995] "Numerical simulations of axisymmetric sonic He and H₂ injections into a Mach 2 airstream," AIAA Paper 95-0873.

Clemens, N.T. and Mungal, M.G. [1991] "A planar Mie scattering technique for visualizing supersonic mixing flows," Exp. in Fluids, Vol. 11, pp. 175-185.

Clemens, N.T., and Mungal, M.G. [1992] "Two- and three-dimensional effects in the supersonic mixing layer," AIAA J., Vol. 30, No. 4, pp. 973-981.

Coles, D. [1981] "Prospects for useful research on coherent structure in the turbulent shear flow," Proc. Indian Acad. Sci., Vol. 4, pp. 111-127.

Copeland, R.A., and Crosley, D.R. [1985] "Radiative, collisional and dissociate processes in triplet acetone," Chem. Physics Letters, Vol. 115, No. 4,5, pp. 362-368.

Cox, S.K., Fuller, R.P., and Schetz, J.A. [1994] "Vortical interactions generated by an injector array to enhance mixing in supersonic flow," AIAA Paper 94-0708.

Curran, E. and Stull, F. [1963] "The potential performance of the supersonic combustion ramjet engine," Technical documentary report No. ASD-TDR-63, pp. 1-2.

Davis, D.O., and Hingst, W.R. [1991] "Progress toward synergistic hypermixing nozzles," AIAA Paper 91-2264.

Dimotakis, P.E., Miake-Lye, R.C. and Papantoniou, D.A. [1983] "Structure and dynamics of round turbulent jets," *Phys. Fluids*, Vol. 26, pp. 3185 - 3192.

Drain, L.E. [1980] The Laser Doppler Technique. John Wiley & Sons, Great Britain, 1980.

Dutton, J.C., Herrin, J.L., Molezzi, M.J., Mathur, T., and Smith, K.M. [1995] "Recent progress on high-speed separated base flows," AIAA Paper 95-0472.

Eaton, J.K., and Johnston, J.P. [1981] "A review of research on subsonic turbulent flow reattachment," *AIAA J.*, Vol. 19, No. 9, pp. 1093 - 1100.

Elliott, G.S. and Samimy, M. [1990] "Compressibility effects in free shear layers," *Phys. Fluids A*, Vol. 2, No. 7, pp. 1231-1240.

Elliott, G.S., Samimy, M., and Arnette, S.A., [1992] "Study of compressible mixing layers using filtered Rayleigh scattering based visualizations," *AIAA J.*, Vol. 30, No. 10, pp. 2567-2569.

Elliott, G.S., Samimy, M., and Arnette, S.A. [1995] "The characteristics and evolution of large-scale structures in compressible mixing layers," *Phys. Fluids*, Vol. 7, No. 4, pp. 864-876.

Fuller, E.J., Mays, R.B., Thomas, R.H., Schetz, J.A. [1992] "Mixing studies of helium in air at high supersonic speeds," *AIAA J.*, Vol. 30, No. 9, pp. 2234-2243.

Glawe, D.D., Samimy, M., Nejad, A.S., and Chen, T.H. [1995] "Effects of nozzle geometry on parallel injection from the base of an extended strut into a supersonic flow," AIAA Paper 95-0522.

Glassman, I. [1987] Combustion. Academic Press, Inc., San Diego, California.

Goebel, S.G., and Dutton, J.C., [1990] "Experimental study of compressible turbulent mixing layers," *AIAA J.*, Vol. 29, No. 4, pp. 538-546.

Gouldin, F.C. and Dandekar, K.V. [1984] "Time-resolved density measurements in premixed turbulent flames," *AIAA J.*, Vol. 22, No. 5, pp. 655-663.

Greenblatt, G.D., Ruhman, S., and Haas, Y. [1984] "Fluorescence decay kinetics of acetone vapor at low pressures," *Chem. Physics Letters*, Vol. 112, No. 3, pp. 200-206.

Gruber, M.R. [1995] "An experimental investigation of transverse injection from circular and elliptical nozzles into a supersonic crossflow," University of Illinois, Ph.D. Dissertation, Urbana, Illinois.

Gruber, M.R., and Nejad, A.S. [1994] "Development of a large-scale supersonic combustion research facility," AIAA Paper 94-0544.

Gruber, M.R., Nejad, A.S., Chen, T., and Dutton, J.C. [1995] "Mixing and penetration studies of sonic jets in a Mach 2 freestream," J. Propulsion, Vol. 11, No. 2, pp. 315-323.

Gutmark, E., Schadow, K.C., Parr, D.M., Harris, C.K., and Wilson, K.H. [1985] "The mean and turbulent structure of non circular jets," AIAA Paper 85-0543.

Gutmark, E., Schadow, K.C., and Wilson, K.J. [1989] "Noncircular jet dynamics in supersonic combustion," J. Propulsion, Vol. 5, No. 5, pp. 529-533.

Gutmark, E., Schadow, K.C., and Wilson, K.J. [1991] "Effect of convective Mach number on mixing of coaxial circular and rectangular jets," Phys. Fluids A, Vol. 3, No. 1, pp. 29-36.

Haimovitch, Y., Gartenberg, E. Roberts, S.A., Jr., and Northgam, G.B. [1994] "An investigation of wall injectors for supersonic mixing enhancement," AIAA Paper 94-2940.

Heiser, W.H., and Pratt, D.T. [1994] Hypersonic airbreathing propulsion. AIAA, Inc., Washington D.C..

Heppenheimer, T.A. [1989] "Keepers of the flame," Air & Space, December, pp. 88-95.

Hermanson, J.C., and Winter M. [1993] "Mie scattering imaging of a transverse, sonic jet in supersonic flow," AIAA J., Vol. 31, No. 1, pp. 129-132.

Ho, C.M., and Huerre, P. [1984] "Perturbed free shear layers," Ann. Rev. Fluid Mech., Vol. 16, pp. 365.

Ho, C.M., and Gutmark, E. [1987] "Vortex induction and mass entrainment in a small-aspect-ratio elliptic jet," J. Fluid Mech., Vol. 179, pp. 383-405.

Holman, J.P. [1994] Experimental methods for engineers. 6th ed. McGraw-Hill, Inc. New York, pp. 297-299.

Husain, H.S., and Hussain, F. [1991] "Elliptic jets. Part 2. Dynamics of coherent structures: pairing," J. Fluid Mech., Vol. 233, pp. 439-482.

Husain, H.S., and Hussain, F. [1993] "Elliptic jets. Part 3. Dynamics of preferred mode coherent structure," J. Fluid Mech., Vol. 248, pp. 315-361.

Hussain, F., and Husain, H.S. [1989] "Elliptic jets. Part 1. Characteristics of unexcited and excited jets," J. Fluid Mech., Vol. 208, pp. 257-320.

Hussain, A.K.M.F., and Zedan, M.F. [1978] "Effects of the initial condition of the axisymmetric free shear layer: Effects of the initial momentum thickness," Phys. Fluids, Vol. 21, No. 7, pp. 1100-1112.

Jacobs, J.W. [1992] "Shock-induced mixing of a light-gas cylinder," J. Fluid Mech., Vol. 234, pp. 629-649.

Jimenez, J. [1983] "A spanwise structure in the plane shear layer," J. Fluid Mech., Vol. 132, pp. 319-336.

King, C.J., Krothapalli, A., and Strykowski, P.J. [1994] "Streamwise vorticity generation in supersonic jets with minimal thrust loss," AIAA Paper 94-0661.

King, P.S., Thomas, R.H., Schetz, J.A., Billig, F.S. [1989] "Combined tangential-normal injection into a supersonic flow," AIAA Paper 89-0622.

Konrad, J.H. [1976] "An experimental study of mixing in two-dimensional turbulent shear flows with applications to diffusion limited chemical reactions," Project SQUID Tech. Rep. CIT-8-PU.

Koshigoe, S., Gutmark, E., Schadow, K.C., and Tubis, A. [1989] "Initial development of noncircular jets leading to axis switching," AIAA J., Vol. 27, No. 4, pp. 411-419.

Krothapalli, A., Baganoff, D., and Karamcheti, K. [1981] "On the mixing of a rectangular jet," J. Fluid Mech., Vol. 107, pp. 201-220.

Krothapalli, A., Buzyna, G. and Lourenco, L. [1991] "Streamwise vortices in an underexpanded axisymmetric jet," Phys. Fluids A, Vol. 3, No. 8, pp. 1848-1851.

Kuntz, D.W., Amatucci, V.A., and Addy, A.L. [1987] "Turbulent boundary-layer properties downstream of the shock-wave/ boundary-layer interaction," AIAA J., Vol. 25, No. 5, pp. 668 - 675.

Lasheras, J.C., Cho, J.S., and Maxworthy, T. [1986] "On the origin and evolution of streamwise vortical structures in a plane, free shear layer," J. Fluid Mech., Vol. 172, pp. 231-258.

Lasheras, J.C., and Choi, H. [1988] "Three-dimensional instability of a plane free shear layer: an experimental study of the formation and evolution of streamwise vortices," J. Fluid Mech., Vol. 189, pp. 53-86.

Lee, S.J., and Baek, S.J. [1993] "Near-field turbulent structure of elliptic jets," Ninth Symposium on "Turbulent Shear Flows," Kyoto, Japan, August, pp. 9.2.1-9.2.5.

Lepicovsky, R., Ahuja, K.K., Brown, W.H., and Burrin, R.H. [1987] "Coherent large-scale structures in high Reynolds number supersonic jets," AIAA J., Vol. 25, No. 11, pp. 1419-1425.

Liepmann, D. [1991] "Streamwise vorticity and entrainment in the near field of a round jet," Phys. Fluids A, Vol. 3, No. 5, pp. 1179-1185.

Longmire, E.K., Eaton, J.K., and Elkins, C.J. [1992] "Control of jet structure by crown-shaped nozzles," AIAA J., Vol. 30, No. 2, pp. 505-512.

Lozano, A., Yip, B., and Hanson, R.K. [1992] "Acetone: a tracer for concentration measurements in gaseous flows by planar laser-induced fluorescence," Exp. in Fluids, Vol. 13, pp. 369-376.

Maise, G. and McDonald, H. [1968] "Mixing length and kinematic eddy viscosity in a compressible boundary layer," AIAA J. Vol. 6., No. 1, pp. 73-80.

Mays, R.B., Thomas, R.H., Schetz, J.A. [1989] "Low angle injection into a supersonic flow," AIAA Paper 89-2461.

McCartney, E.J. [1976] Optics of the Atmosphere. John Wiley and sons, New York.

McClinton, C.R. [1972] "The effect of injection angle on the interaction between sonic secondary jets and a supersonic free stream," NASA Tech. Report TN D-6669.

Melling, A.[1986] "Seeding gas flows for laser anemometry," AGARD-CP-399, pp. 8.1-8.11.

Messersmith N.L., Dutton, J.C., and Krier, H. [1991] "Experimental investigation of large-scale structures in compressible mixing layers," AIAA Paper 91-0244.

Miles, R. and Lempert W. [1990] "Two-dimensional measurement of density, velocity and temperature in turbulent high-speed air flows by UV Rayleigh scattering," Appl. Phys. B, Vol. 51, pp. 1-7.

Novopashin, S.A., and Perepelkin, A.L. [1989] "Axial symmetry loss of a supersonic preturbulent jet," Phys. Lett. a, Vol. 135, pp. 290-293.

Papamoschou, D., Hubbard, D.G., and Lin, M. [1991] "Observations of supersonic transverse jets," AIAA Paper 91-1723.

Papamoschou, D., and Roshko, A. [1988] "The compressible turbulent shear layer: an experimental study," J. Fluid Mech., Vol. 197, pp. 453-477.

Petrie, H.L, Samimy, M. and Addy, A.L. [1986] "Compressible separated flows," AIAA J., Vol. 24, No. 12, pp. 1971-1978.

Pratt, D.T. [1975] "Mixing and chemical reaction in continuous combustion," Prog. Energy Combust. Sci., Vol. 1, pp. 73-86.

Quinn, W.R. [1989] "On mixing in an elliptic turbulent free jet," Phys. Fluids A, Vol. 1, No. 10, pp. 1716-1722.

Raffoul, C.N. [1995] "A three component laser velocimetry investigation of the flow field downstream of a bluff body," Ph.D. Dissertation, University of Dayton, Dayton, Ohio.

Reeder, M.F.[1994] "An experimental study of mixing enhancement in jets with vortex generating tabs," Ph.D. Dissertation, The Ohio State University, Columbus, Ohio.

Reeder, M.F., and Zaman, K.B.M.Q. [1994] "The impact of 'tab' location relative to the nozzle exit on jet distortion," AIAA Paper 94-3385.

Reynolds, W.C., and Bouchard, E.E. [1981] In Unsteady Turbulent Shear Flows. (ed. R. Michel, J. Cousteix and R. Houdeville), p. 402, Springer.

Samimy, M. [1984] "An experimental study of compressible turbulent reattaching free shear layers," Ph.D. dissertation, University of Illinois, Urbana, Illinois.

Samimy, M., and Addy, A.L. [1986] "Interaction between two compressible, turbulent free shear layers," AIAA J., Vol. 24, No. 12, pp. 1918-1923.

Samimy, M., and Elliott, G.S. [1990] "Effects of compressibility on the characteristics of free shear layers," AIAA J., Vol. 28, pp. 439-445.

Samimy, M., and Lele, S.K. [1991] "Motion of particles with inertia in a compressible free shear layer," Phys. Fluids A, Vol. 3, pp. 1915-1923.

Samimy, M., Reeder, M.F., and Elliott, G.S. [1992] "Compressibility effects on large structures in free shear flows," Phys. Fluids A, Vol. 4, pp. 1251-1258.

Samimy, M., Zaman, K.B.M.Q., and Reeder, M.F. [1993] "Effect of tabs on the flow and noise field of an axisymmetric jet," AIAA J., Vol. 31, No. 4, pp. 609-619.

Schadow, K.C., and Gutmark, E. [1989] "Review of passive shear flow control research for improved subsonic and supersonic combustion," AIAA Paper 89-2786.

Schadow, K.C., Gutmark, E., Koshigoe, S., and Wilson, K.J. [1989a] "combustion-related shear-flow dynamics in elliptic supersonic jets," AIAA J., Vol. 27, No. 10, pp. 1347-1353.

Schadow, K.C., Gutmark, E., Parr, D.M., and Wilson, K.J. [1988] "Selective control of flow coherence in triangular jets," Experiments in Fluids, Vol. 6, pp. 129-135.

Schadow, K.C., Gutmark, E., and Wilson, K.J. [1989b] "Passive mixing control in supersonic coaxial jets at different convective Mach numbers," AIAA Paper 89-0995.

Schetz, J.A. [1993] Boundary Layer Analysis. Prentice-Hall, Inc., Englewood Cliffs, New Jersey.

Schetz, J.A., and Billig F.S. [1966] "Penetration of gaseous jets injected into a supersonic stream," J. Spacecraft, Vol. 3, No. 11, pp. 1658-1665.

Shih, C., Krothapalli, A., and Gogineni, S. [1992] "Experimental observations of instability modes in a rectangular jet," AIAA J., Vol. 30, No. 10, pp. 2388-2394.

Sreenivasan, K.R. [1991] "Fractals and multifractals in fluid turbulence," *Annu. Rev. Fluid Mech.*, Vol. 23, pp. 539 - 600.

Sullins, G.A., and Anderson, J.D., Jr., and Drummond, J.P., [1982] "Numerical investigation of supersonic base flow with parallel injection," AIAA Paper 82-1001.

Sun, C.C., and Childs, M.E. [1973] "A modified wall wake velocity profile for turbulent compressible boundary layers," *J. Aircraft*, Vol. 10, No. 6, pp. 381 - 383.

Tait, N.P. and Greenhalgh, D.A. [1992] "2D laser induced fluorescence imaging of parent fuel fraction in non premixed combustion," 24th International Symposium on Combustion, The Combustion Institute, pp. 1621-1628.

Tang, S.K., and Ko, N.W.M. [1993] "A study on the noise generation mechanism in a circular air jet," *J. Fluids Eng.*, Vol. 115, pp. 425-435.

Tennekes, H.T., and Lumley, J.L. [1972] A first course in turbulence. The MIT Press, Cambridge, Massachusetts.

TSI, Incorporated [1992] "Model IFA 750 digital burst correlator," P.O. Box 64394, St. Paul, Mn 55164 USA (Ph: 612-483-4711).

Waitz, I.A., Marble, F.E., and Zukoski, E.E. [1991] "An investigation of a contoured wall injector for hypervelocity mixing augmentation," AIAA Paper 91-2265.

Waitz, I.A., Marble, F.E., and Zukoski, E.E. [1992a] "A systematic experimental and computational investigation of a class of contoured wall fuel injectors," AIAA Paper 92-0625.

Waitz, I.A., Marble, F.E., and Zukoski, E.E. [1992b] "Vorticity generation by contoured wall injectors," AIAA Paper 92-3550.

Wegener, P.P., and Parlange, J.Y. [1967] "Non-equilibrium nozzle flow with condensation," AGARD Proceedings No. 12, Recent Advances in Aerothermochemistry, Vol. 2, pp. 607-634.

Wegener, P.P., and Pouring, A.A. [1964] "Condensation of water by homogeneous nucleation in nozzles," *Physics of Fluids*, Vol. 7, No. 3, pp. 352-361.

Wlezien, R.W., and Kibens, V. [1987] "Influence of nozzle asymmetry on supersonic jets," *AIAA J.*, Jan., pp. 27-33.

Yoda, M., Hesselink, L., and Mungal, M.G. [1992] "The evolution and nature of large-scale structures in the turbulent jet," *Phys. Fluids A*, Vol. 4, pp. 803 - 811.

Yu, K., Kraeutle, K., Wilson, K., Parr, T., Smith, R., Gutmark, E., Schadow, K. [1992] "Supersonic flow mixing and combustion using ramp nozzle," AIAA Paper 92-3840.

Yule, A.J. [1978] "Large-scale structure in the mixing layer of a round jet," *J. Fluid Mech.*, Vol. 89, No. 3, pp. 413-432.

Zapryagaev, V.I., and Solotchin, A.V. [1988] "Spatial structure of flow in the initial section of a supersonic underexpanded jet," Academy of Sciences USSR, Siberian Section, Institute of Theoretical and Applied Mechanics, Preprint No. 23-88, UDK 533.6.011.

Zaman, K.B.M.Q., Reeder, M.F., and Samimy, M. [1994] "Control of an axisymmetric jet using vortex generators," *Phys. Fluids*, Vol. 6, No. 2, pp. 778-793.

APPENDIX A

FREESTREAM MACH NUMBER

True freestream Mach number calculated from freestream velocity values measured using the LDV system and stagnation temperature measured in the stagnation chamber.

$U = 506 \text{ m/s}$ (measured at $X = -1.27 \text{ cm}$ in freestream air flow)

$T_0 = 300 \text{ K}$ (measured in stagnation chamber)

$P_0 = 345 \text{ KPa}$

$R = 287 \text{ kJ/kg}\cdot\text{K}$

$\gamma = 1.4$

$$\text{Isentropic flow:} \quad T/T_0 = 1 + \frac{\gamma-1}{2} M^2 = 1 + \frac{\gamma-1}{2} \left(\frac{U^2}{a^2} \right) \quad \text{AA-1}$$

$$T = T_0 - \frac{\gamma-1}{2\gamma R} U^2 \longrightarrow T_\infty = 172 \text{ K} \quad \text{AA-2}$$

$$\frac{P_0}{P} = \left(1 + \frac{\gamma-1}{2} M^2 \right)^{\gamma/\gamma-1} \quad \text{AA-3}$$

$$P_0/P_\infty = 6.91 \longrightarrow P_\infty = 49.9 \text{ KPa} \quad \text{AA-4}$$

$$a = \sqrt{\gamma R T} \longrightarrow a_\infty = 263 \text{ m/s} \quad \text{AA-5}$$

$$M = U/a \longrightarrow M_\infty = 1.92 \quad \text{AA-6}$$

$$\rho = \frac{P}{RT} \longrightarrow \rho_\infty = 1.01 \text{ kg/m}^3 \quad \text{AA-7}$$

$$\ddot{P} = \frac{1}{2} \rho U^2 \longrightarrow \ddot{P}_\infty = 1.29 \times 10^5 \text{ kg/m}\cdot\text{s}^2 \quad \text{AA-8}$$

$$\mu = \frac{(0.000001458) T^{1.5}}{110.4 + T} \longrightarrow \mu_\infty = 1.16 \times 10^{-5} \text{ Pa}\cdot\text{s} \text{ (Sutherlands law)} \quad \text{AA-9}$$

$$\text{Re}/l = \frac{U\rho}{\mu} \longrightarrow (\text{Re}/l)_\infty = 4.4 \times 10^7 \text{ m}^{-1} \text{ (unit Reynolds number)} \quad \text{AA-10}$$

APPENDIX B

HELIUM EXIT PRESSURE

Calculations of helium thermodynamic conditions at the nozzle exit for static helium-to-freestream air pressure ratios $\Psi = 1, 2$, and 4 .

$T_0 = 300 \text{ K}$ (measured in stagnation chamber)

$M = 1$

$R = 2077 \text{ kJ/kg}\cdot\text{K}$

$\gamma = 1.67$

$$\text{Isentropic acceleration: } \frac{T_o}{T} = 1 + \frac{\gamma-1}{2} M^2 \quad \text{AB-1}$$

$$\frac{P_o}{P} = \left(1 + \frac{\gamma-1}{2} M^2 \right)^{\gamma/\gamma-1} \quad \text{AB-2}$$

$$\text{At nozzle exit (M = 1) gives: } \frac{T_o}{T_e} = 1.335 \longrightarrow T_e = 225 \text{ K} \quad \text{AB-3}$$

$$\frac{P_o}{P_e} = 2.055 \quad \text{AB-4}$$

$$U = Ma = \sqrt{\gamma RT} \longrightarrow U_e = 883 \text{ m/s} \quad \text{AB-5}$$

$$\rho = \frac{P}{RT} \quad \text{AB-6}$$

$$\ddot{P} = \frac{1}{2} \rho U^2 \text{ (momentum)} \quad \text{AB-7}$$

For $\Psi = 1$, $P_0 = 97 \text{ KPa} \rightarrow P_e = 47 \text{ KPa}$, $\rho_e = 0.01 \text{ kg/m}^3$, $\ddot{P}_e = 39.0 \times 10^3 \text{ kg/m}\cdot\text{s}^2$

For $\Psi = 2$, $P_0 = 207 \text{ KPa} \rightarrow P_e = 101 \text{ KPa}$, $\rho_e = 0.22 \text{ kg/m}^3$, $\ddot{P}_e = 85.7 \times 10^3 \text{ kg/m}\cdot\text{s}^2$

For $\Psi = 4$, $P_0 = 414 \text{ KPa} \rightarrow P_e = 201 \text{ KPa}$, $\rho_e = 0.44 \text{ kg/m}^3$, $\ddot{P}_e = 171.5 \times 10^3 \text{ kg/m}\cdot\text{s}^2$

APPENDIX C

LDV DATA REDUCTION EQUATIONS

Mean:
$$\bar{U} = \frac{1}{n} \sum_{k=1}^n U_k \quad \text{or} \quad \frac{1}{n} (U_1 + U_2 + U_3 + \dots + U_n)$$
 AC-1

Standard Deviation:
$$\sigma_u = \sqrt{\frac{\sum_{k=1}^n U_k^2}{n} - \left(\frac{\sum_{k=1}^n U_k}{n} \right)^2}$$
 AC-2

where n is the number of samples in the data set.

Turbulence intensity (%):
$$100 \sigma_u / U_{ref}$$
 AC-3

Second Moments:
$$\begin{aligned} \overline{uv} &= \frac{1}{n} \sum_{k=1}^n ((U_k - \bar{U})(V_k - \bar{V})) \\ &= \left(\frac{\sum_{k=1}^n U_k V_k}{n} \right) - \left(\frac{\sum_{k=1}^n U_k}{n} \right) \left(\frac{\sum_{k=1}^n V_k}{n} \right) \end{aligned}$$
 AC-4

Similarly,
$$\overline{uu} = \left(\frac{\sum_{k=1}^n U_k U_k}{n} \right) - \left(\frac{\sum_{k=1}^n U_k}{n} \right) \left(\frac{\sum_{k=1}^n U_k}{n} \right) = \sigma_u^2$$
 AC-5

Turbulent (Reynolds) shear stress:
$$\tau_{uv} = \frac{\overline{uv}}{U_{ref}^2}$$
 AC-6

Correlation coefficient:
$$R_{uv} = \frac{\overline{uv}}{\sigma_u \sigma_v}$$
 AC-7

APPENDIX D

BOUNDARY LAYER CALCULATIONS

Van Driest II [Schetz 1993]

$$\frac{U_\infty}{B_1'} \left[\sin^{-1} \left(\frac{2B_1' \left(\frac{\bar{U}}{U_\infty} \right) - B_2'}{\sqrt{(B_2')^2 + 4(B_1')^2}} \right) + \sin^{-1} \left(\frac{B_2'}{\sqrt{(B_2')^2 + 4(B_1')^2}} \right) \right] = U^* \left[\frac{1}{K} \ln(y^+) + c \right] \quad \text{AD-1}$$

The left hand side of the above equation is denoted U_{eff} for convenience, where
 $T_0 = 300 \text{ K}$, $P_0 = 345 \text{ KPa}$, $U_\infty = 506 \text{ m/s}$, $M_\infty = 1.92$, $T_\infty = 172 \text{ K}$, $P_\infty = 49.9 \text{ KPa}$.

$$B_1' = \sqrt{\frac{\frac{(\gamma-1)}{2} M_\infty^2 r}{T_w/T_\infty}} = 0.629 \quad \text{AD-2}$$

$$B_2' = \frac{1 + \frac{(\gamma-1)}{2} M_e^2 r}{T_w/T_e} - 1 = 0 \quad \text{AD-3}$$

$$U^* = \sqrt{\tau_w / \rho_w} = 18 \quad \text{AD-4}$$

$$\tau_w = \frac{1}{2} \rho_\infty U_\infty^2 C_f = 205 \text{ Pa} \quad \text{AD-5}$$

$$\frac{C_{f_c}}{C_{f_i}} = 0.78 \text{ from Figure 10-7 [Schetz 1993]} \quad \text{AD-6}$$

$$C_{f_i} = 0.0456 \text{Re}_\delta \quad \text{AD-7}$$

$$\text{Re}_\delta = \frac{\rho_\infty U_\infty \delta}{\mu_\infty} = 2.4 \times 10^5 \quad \text{AD-8}$$

$$y^+ = \frac{\rho_w U^* y}{\mu_w} \quad \text{AD-9}$$

$$P_w = P_\infty = 49.77 \text{ KPa} \quad \text{AD-10}$$

$$T_w = T_\infty \left(1 + \frac{\gamma - 1}{2} M_\infty^2 \zeta \right) = 285 \text{ K} \text{ adiabatic wall temperature} \quad \text{AD-11}$$

$$\mu_w = 1.458 \times 10^{-6} \frac{T_w^{1.5}}{T_w + 110.4} = 1.774 \times 10^{-5} \text{ Pa}\cdot\text{s} \quad \text{AD-12}$$

$$\text{Pr} = \frac{\mu c_p}{K} = 0.70 \text{ (approximately)} \quad \text{AD-13}$$

$$\zeta = \sqrt[3]{\text{Pr}} = 0.89 \quad \text{AD-14}$$

APPENDIX E
STANDARD DEVIATION FOR A STREAM-SEPARATED FLOW

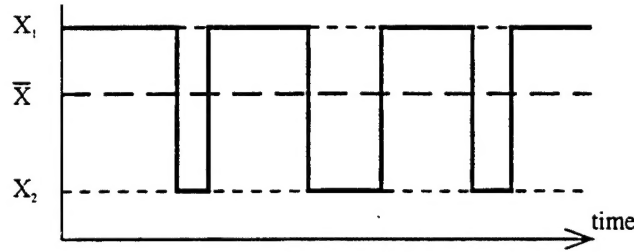


Figure AE-1. Time-varying concentration trace in a stream-segregated flow.

$$\bar{\chi} = \alpha\chi_1 + \beta\chi_2, \quad \text{AE-1}$$

where

α = fraction of time when $\chi = \chi_1$

β = fraction of time when $\chi = \chi_2$

$$\alpha + \beta = 1 \quad \text{AE-2}$$

$$\sigma_x = \left[\alpha(\chi_1 - \bar{\chi})^2 + \beta(\chi_2 - \bar{\chi})^2 \right]^{\frac{1}{2}}. \quad \text{AE-3}$$

Substituting

$$\alpha = \frac{\bar{\chi} - \chi_2}{\chi_1 - \chi_2} \quad \text{AE-4}$$

and

$$\beta = \frac{\chi_1 - \bar{\chi}}{\chi_1 - \chi_2} \quad \text{AE-5}$$

into equation AE-3 gives

$$\sigma_x = \left[\frac{\bar{\chi} - \chi_2}{\chi_1 - \chi_2} (\chi_1 - \bar{\chi})^2 + \frac{\chi_1 - \bar{\chi}}{\chi_1 - \chi_2} (\chi_2 - \bar{\chi})^2 \right]^{\frac{1}{2}}, \quad \text{AE-6}$$

$$\sigma_x = \left\{ \frac{1}{\chi_1 - \chi_2} [(\bar{\chi} - \chi_2)(\chi_1 - \bar{\chi})((\chi_1 - \bar{\chi}) - (\chi_2 - \bar{\chi}))] \right\}^{\frac{1}{2}}, \quad \text{AE-7}$$

$$\sigma_x = [(\chi_1 - \bar{\chi})(\bar{\chi} - \chi_2)]^{\frac{1}{2}}. \quad \text{AE-8}$$